Universität Bremen

Space Engineering Fachbereich 04

Badgasteiner Straße
28359 Bremen
https://www.fb4.uni-bremen.de

Master Thesis

Design and Simulation of an Orbit Control Systems

Pradhyuman Singh Shekhawat

Matriculation Number: 3207374
15.07.2024

Supervised by
Dr.-Ing. Stephan Theil

Second reviewer
Dr.-Ing. Benny Rievers

Abstract

The contemporary era of satellite deployment, characterized by an unprecedented increase in the number of satellites in Low Earth Orbit (LEO), underscores the importance of advanced orbit control systems. These systems are vital for the sustainable and precise operation of satellite and satellite constellations across various applications. This thesis enhances this aspect of space technology by focusing on the design and analysis of orbit control systems for satellite station-keeping, a critical task for ensuring the operational longevity and reliability of satellites in LEO.

Addressing the challenge of developing a robust control system, this research navigates through the complexities of space dynamics to propose a solution that enhances the efficiency of satellite maneuvers in LEO. The study introduces an array of functional models created in Scilab, including models for positioning sensors utilizing Global Navigation Satellite System (GNSS) measurements, orbit determination algorithms, and thruster systems encompassing electric propulsion. These models are specifically designed to simulate real-world space conditions by incorporating realistic errors and variabilities.

Subsequently, the thesis simulates these models within a comprehensive Scilab environment, examining both individual and collective satellite operations. This leads to the formulation and optimization of control algorithms dedicated to maintaining precise orbit trajectories, particularly focusing on two advanced control strategies: the Linear Quadratic Regulator (LQR) and Clohessy-Wiltshire (CW) based trajectory control. These methodologies are analysed for their effectiveness in precise trajectory management and fuel efficiency.

A thorough evaluation of the proposed control systems is conducted, assessing fuel consumption, manoeuvre accuracy, and the frequency of necessary adjustments. Through detailed comparative analysis, the study elucidates the efficacy of the electric thruster and its corresponding control strategies, offering valuable insights into their applicability for diverse satellite missions.

The findings of this research illuminate the complexities of orbit control systems and significantly contribute to the field of satellite engineering. By demonstrating potential enhancements in efficiency and sustainability for satellite operations, this thesis lays the groundwork for future innovations in orbit control systems. The implications of this work are broad, suggesting a transformative impact on the management and operation of satellite constellations in LEO.

Contents

List of Abbreviations

CW Clohessy-Wiltshire

ECI Earth-Centered Inertial

EKF Extended Kalman Filter

FIR Finite Impulse Response

GEO Geostationary Orbit

GNSS Global Navigation Satellite System

GPS Global Positioning System

IIR Infinite Impulse Response

LEO Low Earth Orbit

LQR Linear Quadratic Regulator

LVLH Local Vertical Local Horizontal

MEO Medium Earth Orbit

MPC Model Predictive Control

PID Proportional Integral Derivative

POD Precise Orbit Determination

PQW Perifocal Coordinate System

RCS Reaction Control System

RMSE Root Mean Square Error

SMA Simple Moving Average

UKF Unscented Kalman Filter

List of Figures

List of Tables

1. Introduction

The expansion of satellite constellations orbiting Earth has brought to the forefront the need for sophisticated, efficient, and precise orbit control systems. These satellites are crucial across various domains, including communication networks, global positioning systems, and Earth observation, profoundly impacting modern societal functions. As depicted in Figure 1.1, adapted from (Armstrong, 2022), there has been a substantial increase in the number of satellite launches since the era of Sputnik, with an exponential rise observed over the past decade. This trend highlights not only the escalating reliance on satellite technology but also underscores the increasing complexities involved in space traffic management.

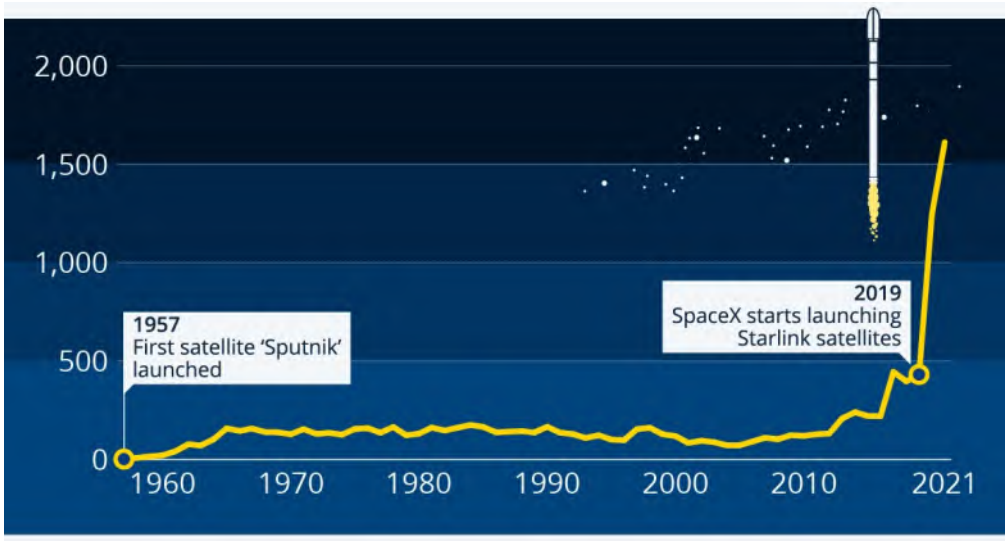

Figure 1.1.: Number of satellites launched from Sputnik (1957) to Starlink (2021). Source: Statista. Available at: https://www.statista.com/chart/28308/satellite-payloads-launched-into-space-timeline/

The necessity for precise orbit determination has become a paramount concern. (Selvan et al., 2023) provide a thorough review of the developments in Low Earth Orbit (LEO) determination techniques, Global Navigation Satellite System (GNSS) systems, and satellite missions over the last two decades. Despite these advancements, maintaining accurate orbital paths, especially in the dynamically challenging environment of LEO, poses significant operational hurdles.

This thesis addresses the technological and methodological advancements in spacecraft trajectory control.It delves into the utilization of the Clohessy-Wiltshire (CW) equations for relative motion control in orbit and examines various control techniques such as Linear

Quadratic Regulators (LQR) and Monte Carlo simulations to enhance the accuracy and efficiency of satellite maneuvers.

1.1. Background and Motivation

In the rapidly evolving field of space exploration and satellite deployment, the exponential increase in the number of satellites encircling the Earth marks a significant technological and operational milestone. This surge is primarily fuelled by the escalating demand for satellite-facilitated services, encompassing telecommunications, global positioning systems, and Earth observation. Such an upsurge underscores the imperative for a robust Orbit Control System (OCS), designed to mitigate collision risks and manage spatial traffic effectively in the increasingly crowded orbital lanes. OCS technologies are pivotal in ensuring the operational safety and efficacy of satellites within this densely populated space environment (Gatlin, 2019).

The sophistication and mission complexity of contemporary satellites have concurrently advanced. Modern satellites are engineered for prolonged operational life spans and are tasked with multifaceted mission objectives, significantly straining traditional ground-based control methodologies. In this context, OCS emerges as an indispensable solution, offering real-time, autonomous navigational management essential for fulfilling these complex mission parameters (Vaddiparty & Chandrasekhar, 2017).

Operational cost reduction remains a paramount objective in satellite management. Conventional ground-based controls, albeit effective, are associated with substantial financial and temporal expenditures. The deployment of OCS can substantially alleviate these costs by automating operations traditionally manned by ground operators, thus enhancing operational efficiency. Furthermore, OCS facilitates the optimization of orbital maneuvers, promoting fuel economy and further diminishing operational expenses (B. Li et al., 2018).

Certain satellite missions demand exceptional agility and responsiveness, a quintessential example being Earth observation satellites that necessitate rapid sensor orientation towards targets of interest. OCS is crucial in enabling the high-precision and swift control required for such operations, ensuring mission success (Kumar, 2011).

OCS technology extends its utility across various satellite categories, offering specific benefits tailored to each:

- **Communication Satellites:** OCS enhances antenna pointing accuracy, crucial for improving signal strength and data throughput.
- **Navigation Satellites:** It ensure the maintenance of precise orbits, vital for the accuracy of positioning and navigation services.
- **Earth Observation Satellites:** OCS enables precise sensor orientation, essential for targeted Earth surveillance.
- **Scientific Satellites:** It facilitates exact pointing and attitude control, necessary for the collection of scientific data.

The field of OCS is characterized by swift technological advancements and the ongoing introduction of novel solutions, marking it as a dynamic and evolving domain. As OCS systems grow more sophisticated and cost-effective, their significance in the future landscape of space exploration and satellite operations is poised to increase markedly.

Notable applications of OCS in current and envisaged spacecraft missions include:

1. **The International Space Station (ISS):** The ISS employs OCS for maintaining its orbit and orientation, utilizing an advanced system of thrusters and reaction wheels controlled by complex computational algorithms.
2. **The European Space Agency's (ESA) Galileo Constellation:** This navigation satellite constellation leverages OCS for precise orbital maintenance, designed for high autonomy with minimal ground intervention.
3. **The SpaceX Starlink Constellation:** This internet satellite constellation utilizes OCS to sustain formation flying and provide global internet coverage, showcasing the scalability of such systems for extensive satellite networks.

In summation, OCS represents a foundational technology in modern and future spacecraft operations. By automating critical navigational tasks, it significantly enhances mission autonomy, efficiency, safety, and cost-effectiveness. The ongoing advancement of OCS technology is expected to further revolutionize spacecraft mission capabilities, underscoring its pivotal role in the next frontier of space exploration.

1.2. Objective

The objective of this thesis is twofold, encompassing both theoretical exploration and practical application within the domain of satellite orbit control, specifically targeting LEO operations. The research aims to bridge the gap between the dynamic simulation of satellite orbits and the practical implementation of a control system for precise station-keeping and maneuvering.

Part One: Plant Simulation and Testing - The initial phase of the thesis is dedicated to the comprehensive simulation of a satellite's operational environment in orbit. This involves the development and integration of several critical models:

- A *Thruster Model* to simulate the propulsion mechanisms available for orbit adjustments.
- A *Translation Motion Model* for capturing the satellite's movement through space.
- A *GNSS Receiver Model* to provide accurate positioning data through satellite navigation systems.
- An *Orbit Determination Model* for assessing the satellite's current trajectory and identifying any deviations from its intended path.

This part aims to simulate the real-time dynamics of satellite orbit, facilitating a deeper understanding of how various factors influence its trajectory and how these can be effectively managed through controlled interventions.

Part Two: Control System Design and Implementation - Expanding on the insights derived from the initial simulation phase, the second part of this thesis is dedicated to the development and implementation of specialized control systems. These systems are engineered specifically for satellite station keeping and rendezvous tasks, utilizing

the principles of CW theory. At the heart of this effort are two sophisticated control mechanisms: the LQR controller and the CW-based trajectory controller. Both controllers are meticulously crafted to enhance the satellite's ability to maintain or adjust its orbit with high precision, catering to specific mission objectives or addressing unintended deviations. The focus is on optimizing the balance between control effectiveness and resource conservation — primarily fuel and thruster usage — through the employment of short, impulsive maneuvers.

The efficacy of these controllers is rigorously tested against the demanding criteria of satellite station-keeping and rendezvous operations, with particular emphasis on system stability and robustness. These evaluations are aimed at verifying the control system's proficiency in executing precise orbit corrections and maintaining critical orbital parameters.

In essence, this thesis endeavours to contribute significantly to the field of space engineering by advancing the capabilities and understanding of orbit control systems. Through detailed modelling, simulation, and practical implementation of advanced control strategies, it seeks to pave the way for more sophisticated, efficient, and reliable satellite operations in the near future.

1.3. Outline

This thesis is meticulously structured to explore the design and analysis of orbit control systems, specifically emphasizing the aspect of station-keeping for satellites in LEO. The document unfolds across five principal chapters, each dedicated to a distinct yet interconnected facet of the research. Below is an outline that specifies the structure and thematic focus of each chapter:

1. **Chapter 1: Introduction** - This opening chapter introduces the subject matter, highlighting the significance of autonomous orbit control for satellite station-keeping in LEO. It outlines the research motivation and objectives of the study. The chapter concludes by presenting an overview of the thesis structure, setting the stage for the detailed exploration that follows.

2. **Chapter 2: Literature Review** - This chapter offers an exhaustive examination of the scholarly works and technological advancements pertinent to orbit control systems, with a keen focus on station-keeping mechanisms. It delves into the historical progression of orbit control strategies, critically assesses contemporary technologies, and highlights the research voids that the current study aims to address. Additionally, this section includes a thorough literature survey conducted to select appropriate thruster types for station-keeping tasks, as well as a review of various control methodologies.

3. **Chapter 3: Methodology and System Design** - This chapter presents the research methodology and details the development of Scilab models for GNSS receivers, orbit determination, motion dynamics, and thruster systems. It elaborates on system design and the simulation approaches employed. The chapter also covers the verification of the thruster model, which includes applying thrust in the radial,

orbital normal, and flight directions. Results are corroborated with analytical calculations. Verification processes involve conducting specific maneuvers to assess the simulation's accuracy, presenting the expected outcomes, and analysing the test results to confirm the reliability of the modelled components.

4. **Chapter 4: Control Design and Implementation** — This chapter details the design and validation of the LQR and CW-based trajectory control systems, anchored in the CW model for orbital dynamics. It thoroughly examines how LQR principles and the inverse CW matrix are adapted to achieve high-precision satellite station-keeping and orbit adjustment in LEO. Through exhaustive Monte Carlo simulations and a series of test cases, the chapter highlights the control system's ability to adeptly manage satellite trajectories, showcasing its robustness against real-world disturbances and uncertainties inherent in the model. Additionally, this chapter delves into the integration of specific parameters such as high-velocity and control effort weights for the LQR, and varying time-to-target ($delta_t$) settings for the CW-based controller within the control matrix. These integrations are critically analyzed to assess the system's response across different operational scenarios.
5. **Chapter 5: Conclusion** - The concluding chapter synthesizes the key findings of the thesis, reflecting on the research objectives and the contributions made to the field of orbit control systems. It discusses the limitations encountered during the study, offers conclusions drawn from the research, and proposes directions for future work in the domain of satellite technology and orbit control.

This structured approach ensures a logical progression through the thesis, from the foundational introduction and literature review to the detailed methodology, analysis of results, and concluding reflections. Each chapter is crafted to build upon the insights of the preceding sections, culminating in a comprehensive narrative that not only addresses the technical intricacies of autonomous orbit control but also situates the study within the larger context of advancing satellite technology and space exploration.

2. Literature Review

The era of satellite orbit control began with the launch of Sputnik in 1957, marking humanity's first foray into space. This event marked humanity's inaugural venture into the cosmos. Figures 2.1a and 2.1b showcase images of the Sputnik satellite. Initially, the primary challenge was to achieve and maintain stable orbits. Early satellite missions focused on understanding the basics of orbital mechanics and the effects of various environmental factors, such as gravitational forces and atmospheric drag, on satellite trajectories.

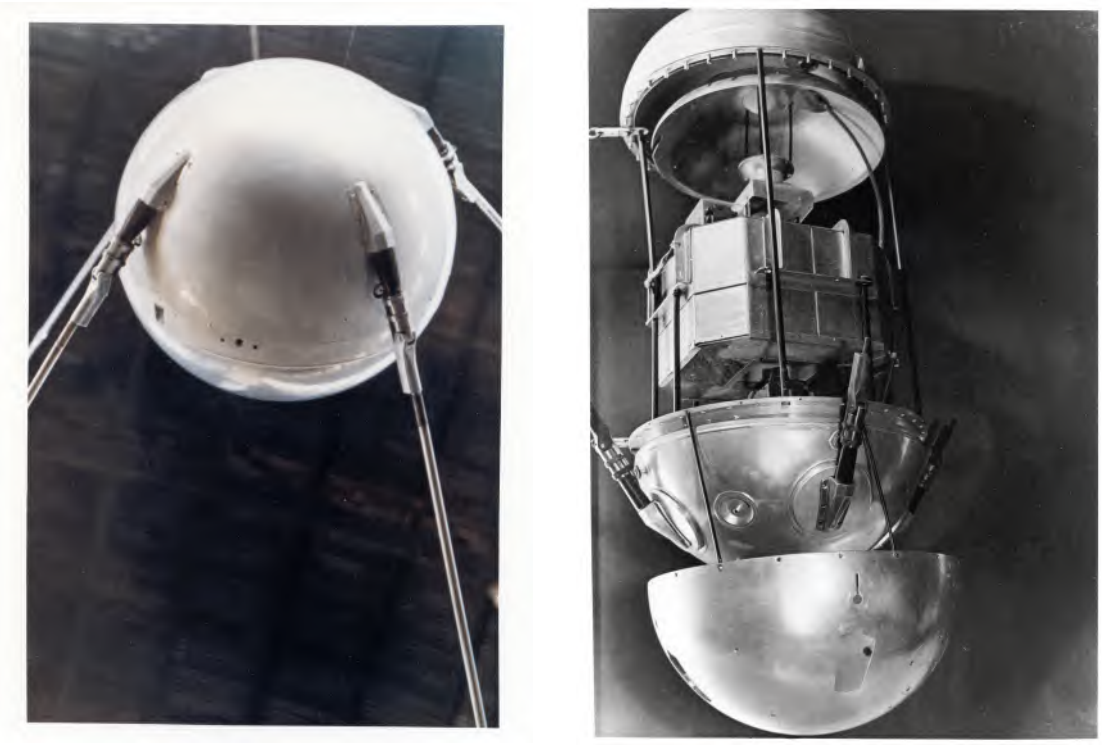

(a) A replica of Sputnik 1, the first artificial Earth satellite, launched by the Soviet Union on October 4, 1957.

(b) Detailed exploded view of Sputnik 1, illustrating its internal components and construction.

Figure 2.1.: Photographic representations of Sputnik 1: (a) a replica showcasing the exterior, and (b) an exploded view highlighting the satellite's internal structure.

During these early years, scientists and engineers faced numerous challenges maintaining satellite orbits, especially due to a limited understanding of factors like the Earth's gravitational anomalies and solar radiation pressure. The tracking of satellites was primarily

done using ground-based optical and radio tracking systems, and orbit adjustments were a manual and labor-intensive process.

Significant early missions, such as Explorer 1 and Vanguard 1, provided crucial data that helped refine orbital models and deepen the understanding of space environment effects on satellite orbits. These missions laid the groundwork for more advanced satellite operations in subsequent decades.

2.1. Orbit Control Systems for Satellites

OCS play a critical role in the modern era of satellite operations, enabling satellites to conduct precise and efficient maneuvers essential for the maintenance of satellite formations and constellations. By automating tasks that were traditionally dependent on ground control, OCS introduced a paradigm shift in satellite management, enhancing operational autonomy and efficiency. The advantages of incorporating OCS into satellite systems include:

- **Increased mission autonomy**: By minimizing the need for continuous ground intervention, OCS allow satellites to respond more dynamically to operational demands and environmental changes. This autonomy enhances the capability of satellite missions to adapt in real-time, improving responsiveness and mission effectiveness (Gurfil, 2013).
- **Enhanced mission efficiency**: OCS optimizes the execution of maneuvers, ensuring optimal use of fuel and resources. This optimization leads to significant reductions in fuel consumption and, consequently, operational costs, contributing to more sustainable and cost-effective mission profiles (Vallado & McClain, 2017).
- **Improved mission safety**: The ability to autonomously maintain precise orbital paths and execute collision avoidance maneuvers significantly mitigates the risk of in-orbit collisions. This capability is especially crucial in densely populated orbits, where the potential for interaction with other spacecraft and space debris is high (B. Li et al., 2018).
- **Lower mission costs**: By reducing the dependency on extensive ground-based infrastructure and personnel for routine operations, contributing to lower overall mission costs. This reduction allows for the allocation of resources to other critical mission aspects, further enhancing the mission value (Iqbal et al., 2020).

2.1.1. Components of Orbit Control System

This section details the architecture of an OCS developed for precise satellite maneuvering and orbit maintenance. Specifically engineered to control a satellite's six degrees of freedom, the system integrates a meticulously designed array of six thrusters with state-of-the-art control algorithms. The unique role and specifications of each component are discussed, highlighting their contribution to the overall effectiveness and efficiency of the OCS.

1. **Sensors**: Position sensors are fundamental to the OCS, providing essential data for orbit and attitude adjustments. Primarily, the system utilizes GNSS receivers, capable of delivering precise real-time positioning and velocity information. This data is crucial for accurately determining the satellite's orbital state, enabling the precise calculation of necessary adjustments to maintain the desired trajectory and orientation. According to Fortescue et al. (2011), "the accuracy of GNSS systems has been pivotal in enhancing the reliability of orbit determinations and adjustments" (Fortescue et al., 2011).

2. **Onboard Computer**: Acting as the central processing unit, the onboard computer processes input from the position sensors to calculate control commands. It is tasked with the real-time analysis of satellite positioning data, determination of optimal maneuvering strategies, and execution of commands to adjust the satellite's orbit and attitude. Eickhoff (2012) highlights that onboard computers integrate multiple sensor inputs to synthesize coherent command structures for maneuver execution (Eickhoff, 2012).

3. **Thrusters**: Equipped with six strategically placed thrusters, the OCS controls the satellite's six degrees of freedom. These thrusters execute fine-tuned adjustments in both orbit and attitude, responding to commands generated by the onboard computer. The selection and placement of thrusters are optimized for maximum control authority and fuel efficiency, allowing for precise maneuvering and orientation control throughout the mission's duration. Pisacane (2005) emphasize that "the strategic placement of thrusters plays a crucial role in the dynamic control of satellite motion."

4. **Control Algorithms**: Central to the OCS, control algorithms transform sensor data into precise thruster commands, balancing mission objectives with efficiency. The suite ranges from simple PID controllers to advanced LQR and CW models. LQR optimizes control efforts against deviations, ensuring fuel efficiency and trajectory accuracy. Meanwhile, CW equations aid in maneuver planning by modeling relative motion. Wertz (2011) discusses the efficacy of LQR in "minimizing control effort while maintaining desired trajectory adherence" (Wertz, 2011).

The advanced OCS design represents a significant contribution to the field of satellite navigation and control, embodying the integration of precision engineering, advanced mathematics, and computer science. Its development and implementation address the challenges of modern satellite operations, emphasizing the importance of each component in achieving the system's overall functionality and performance.

2.1.2. Control Algorithms for OCS

Control strategies in OCS range from simple Proportional-Integral-Derivative (PID) control for robustness (Franklin et al., 2010) to more sophisticated approaches like LQR for optimal performance in linear systems, Model predictive control (MPC) for managing complex dynamics and constraints (Qin & Badgwell, 2003), and nonlinear control for handling the complex nonlinearities in satellite dynamics (Gurfil, 2013).

2.1.3. Challenges and Future Directions

Despite advancements, OCS development faces challenges such as limited onboard resources, environmental disturbances, and collision avoidance in crowded orbits. Future research could focus on distributed control for constellations, adaptive control based on real-time data, and enhanced fault detection for maintaining operation even under failure conditions.

2.2. Modeling of GNSS Receivers and Orbit Determination

Accurate orbit determination is critical for the successful operation of spacecraft, especially in the context of OCS. GNSS, such as Global Positioning System (GPS) or Galileo, are pivotal in providing essential positioning and timing data conducive to onboard orbit determination efforts. However, leveraging raw GNSS measurements directly introduces challenges due to satellite ephemeris inaccuracies, atmospheric disturbances, and sensor noise, which can significantly impact the accuracy of the measurements.

2.2.1. Modeling GNSS Receivers

The development of precise and efficient models for GNSS receivers is a key area of research within space applications. The comprehensive model includes aspects of signal acquisition, tracking, pseudorange measurements, and error modeling for various sources. This model is crucial for enhancing precision in GNSS-based orbit determination.

Advances in GNSS receiver modeling have introduced sophisticated methods to mitigate specific error sources such as multipath effects and receiver noise, significantly improving measurement accuracy. Recent studies highlight the importance of epoch-parallel processing strategies for real-time precise orbit determination (POD), enhancing the efficiency of GNSS data processing and reducing computational load (Teunissen & Montenbruck, 2017). These strategies allow for the real-time adjustment of satellite orbit parameters, thereby providing highly accurate orbit determination that is crucial for mission-critical applications (M. Li et al., 2019).

(Montenbruck & Gill, 2018) discusses the integration of advanced error modeling techniques in GNSS receivers, which include handling ionospheric and tropospheric delays, thereby further refining the precision of orbit determination. The combination of these advancements contributes to the robustness and reliability of modern GNSS receiver systems, making them indispensable for contemporary space missions.

2.2.2. Orbit Determination Techniques

Upon acquiring GNSS measurements and establishing error models, the next step is to accurately estimate the satellite's true orbital state. Orbit determination techniques are varied, each with unique advantages and limitations. (Leick, 2004) provides an in-depth exploration of these methods, noting the Kalman filter's popularity due to its suitability for linear systems with Gaussian noise (Gelb, 1974). The Extended Kalman Filter (EKF), as discussed by (Maybeck, 1979)], adapts the Kalman filter for nonlinear

systems, such as those encountered in satellite dynamics, making it highly relevant for practical applications. Additionally, the Unscented Kalman Filter (UKF) introduced by (Julier & Uhlmann, 1997) addresses linearization errors, offering potentially more accurate estimates for highly nonlinear systems.

Implementation and Performance Analysis

Effective implementation and performance analysis of the selected filtering technique are paramount. Given the constraints of on-board applications, computational efficiency is crucial. (Iqbal et al., 2020) highlight the need to balance the complexity of filtering techniques with the available on-board computing resources. Moreover, real-time algorithm efficiency is essential for successful deployment (Gurfil, 2013). Performance evaluations typically involve metrics such as Root Mean Square Error (RMSE) and convergence time, facilitating the optimization of parameters and comparison of different filtering approaches (Vallado & McClain, 2017).

Specific Considerations for OCS

Integrating GNSS receiver models and orbit determination techniques into OCS requires careful consideration of additional factors. (Vallado & McClain, 2017) stress the significance of accounting for environmental disturbances and actuator imperfections to ensure robust control performance. (B. Li et al., 2018) emphasize the necessity for efficient and reliable orbit determination methods, especially critical in densely populated orbital environments where collision avoidance is paramount. This demands fast convergence and precise state estimation to facilitate timely and effective control decisions.

Future Directions and Open Challenges

Despite notable advancements in the field, several challenges remain, presenting opportunities for further research and development:

- (Ren et al., 2018) investigate distributed control strategies for satellite constellations, highlighting the complexity of coordinating multiple satellites for orbit determination.
- (Luo et al., 2020) propose the adoption of machine learning and artificial intelligence techniques for adaptive control, aiming to enhance orbit determination efficiency and flexibility.
- The development of robust fault detection and isolation algorithms is crucial for maintaining operational reliability, even in the presence of sensor or actuator failures (Guan et al., 2022).

The ongoing research and development in modeling GNSS receivers and robust orbit determination algorithms are foundational to enabling sophisticated orbit control for satellites. By addressing error sources, selecting suitable filtering techniques, and efficiently implementing these models, satellites can achieve reliable orbital state estimation. This accuracy is instrumental for the control algorithms that maneuver the satellite

to fulfil its mission objectives. The field's continuous advancement promises to further unlock efficient, reliable, and autonomous spacecraft operations.

2.3. Types of Thruster Systems

Satellites utilize a variety of thruster systems, each characterized by unique operational principles and performance metrics. (Vallado & McClain, 2017) offers an exhaustive overview of prevalent thruster types, including:

- **Hot Gas Thrusters**: Hot gas thrusters, also known as chemical propulsion systems, operate on the principle of combusting propellant to generate thrust. The combustion process produces high-temperature gas, which is expelled through a nozzle to create forward momentum (Wertz & Larson, 2011). These systems are characterized by their ability to deliver medium to high levels of thrust, making them ideal for maneuvers requiring significant delta-v, such as orbit insertion or major course corrections. However, they tend to have moderate specific impulse values (250–350 seconds), indicating a compromise between thrust output and fuel efficiency (Fortescue et al., 2011).

- **Cold Gas Thrusters**: Cold gas thrusters rely on the expulsion of stored inert gases, such as nitrogen or helium, under pressure. These systems are celebrated for their mechanical simplicity and high reliability, attributed to the absence of complex combustion mechanisms (Turner, 2008). While they offer very low thrust levels and a lower specific impulse (40–70 seconds) compared to hot gas thrusters, their simplicity and reliability make them suitable for fine-tuning satellite orientation and position.

- **Electric Propulsion Systems**: Electric propulsion systems harness electric or magnetic fields to accelerate charged particles, generating thrust. This method achieves exceptionally high specific impulse ratings (1000–3000 seconds), indicating superior fuel efficiency, especially beneficial for long-duration missions requiring sustained thrust (Choueiri, 2009). Though the thrust output is relatively low, the efficiency of electric propulsion systems in terms of fuel consumption is unmatched, making them increasingly popular for deep space missions and satellite station-keeping (Goebel & Katz, 2008).

Thruster Type	Thrust	Specific Impulse (Isp)	Efficiency	Complexity	Reliability	Cost
Electric Thrusters	Low	1000–3000 seconds	Very high	High	Moderate	High
Cold Gas Thrusters	Very low	40–70 seconds	Low	Very low	Very high	Low
Hot Gas Thrusters	Medium to high	250–350 seconds	Moderate to high	Moderate	Moderate	Moderate

Table 2.1.: Comparative Analysis of Satellite Thruster Systems: This table delineates the key performance and operational characteristics of different thruster types used in satellite technology. Each type is evaluated based on thrust capability, specific impulse, efficiency, system complexity, reliability, and cost, providing a comprehensive overview essential for selecting the appropriate thruster type based on mission requirements.

The selection of a thruster system is influenced by various mission-specific requirements, including the desired thrust level, fuel efficiency, operational complexity, and cost considerations. Accurate modelling of the selected thruster system is crucial for predicting its performance under different operational conditions. For this research, an electric thruster system has been selected due to its relevance and potential advantages. Accurate modeling of this electric thruster is essential to predict its performance across varying operational conditions.

2.3.1. Modeling Approaches

The modelling of thruster systems encompasses several approaches, each with its advantages and limitations. (B. Li et al., 2018) categorizes these into three main types:

- **Black-box models**: These models view the thruster as a system with known input-output relationships, often relying on empirical data or simplified theoretical constructs. While computationally efficient, they may not fully capture the thruster's dynamic behavior.

- **Gray-box models**: Combining physical principles with empirical data, gray-box models strike a balance between model fidelity and computational demand, offering a more nuanced representation of thruster operations.

- **White-box models**: Rooted in detailed physical principles, these models provide the most accurate depiction of thruster internals but require extensive computational resources.

The choice among these modeling approaches hinges on the required accuracy, available computational resources, and the specific needs of the mission. For real-time control applications onboard satellites, (Gurfil, 2013) recommends computationally lean models like black-box or gray-box variants, whereas white-box models are preferable for in-depth performance analysis and optimization in the development phase.

2.3.2. Key Modeling Considerations

The development of accurate thruster system models for orbital maneuvers necessitates a comprehensive understanding of several key factors. These elements are integral to predicting the performance and operational capabilities of thrusters in space. Addressing these factors with precision ensures the reliability and effectiveness of satellite missions.

1. **Thrust Magnitude and Direction**: The cornerstone of thruster system modeling is the precise calculation of thrust output. This includes an in-depth analysis of propellant flow rate, combustion efficiency, and nozzle design dynamics. Accurately simulating these parameters is essential for predicting the actual thrust a system can deliver in space operations (Hofmann-Wellenhof et al., 2008).

2. **Thrust Response Time**: To realistically simulate the control system's behavior, the model must account for the temporal delay between the issuance of a command and the generation of actual thrust. This latency, or thrust response time, is critical for understanding the agility and responsiveness of the thruster system in executing commanded maneuvers (Luo et al., 2020).

3. **Fuel Consumption**: An accurate estimation of fuel consumption during operations is pivotal for mission planning and resource allocation. Modeling fuel usage with high fidelity allows for the optimization of thruster operations, ensuring that the mission objectives can be achieved within the constraints of available propellant resources (Iqbal et al., 2020).

4. **Environmental Influences**: The model must also incorporate the effects of external environmental factors, such as atmospheric drag and gravitational perturbations (notably the J2 effect), which can significantly impact thruster performance and efficiency. Including these factors in simulations enhances the realism and predictive accuracy of thruster behavior in the variable conditions of space (Vallado & McClain, 2017).

Through meticulous attention to these modeling considerations, the design and execution of orbital maneuvers can be optimized. This approach ensures that satellite missions are planned and conducted with a high degree of precision and efficiency, directly contributing to their success and the overall advancement of space technology.

2.3.3. Recent Advancements and Future Directions

The field of thruster system modeling is continuously evolving, with recent studies addressing new challenges and incorporating innovative technologies. (Ren et al., 2018) investigate the development of hybrid models that merge various thruster types within a single framework, necessitating sophisticated modeling approaches to accurately represent their interactions. Furthermore, the application of machine learning and artificial intelligence to thruster modeling presents opportunities for adaptive control and performance optimization in real-time scenarios (Luo et al., 2020).

Moving forward, the trajectory of future investigations into thruster system modeling could include:

- Developing high-fidelity, physics-based models that delve into the intricate internal processes of emerging thruster technologies, such as plasma thrusters and Hall-effect thrusters.
- Exploring data-driven approaches that utilize operational telemetry and sensor data to construct dynamic thruster models, enhancing their accuracy and adaptability.
- Integrating uncertainty quantification methods into thruster models to account for variations in manufacturing, environmental conditions, and sensor inaccuracies, thereby improving the reliability of control system designs.

As the demand for precise and efficient satellite maneuvers continues to grow, the advancement of thruster system modeling remains a critical area of research, underpinning the development of next-generation control algorithms and satellite technologies.

2.4. Control Strategies for Orbit Maintenance

Recent advancements in control strategies for spacecraft have significantly influenced operational efficiency and precision, with the LQR and CW trajectory models standing out for their robustness in dynamic space environments.

2.4.1. Linear Quadratic Regulator (LQR)

The LQR strategy optimizes a cost function to balance state deviation and control efforts effectively, making it ideal for various aerospace applications, including satellite formation flying and precise attitude control (Anderson & Moore, 2005; Wu & Chen, 2010). The combination of LQR with real-time state estimation techniques, like the Kalman filter, enhances autonomous operations by adapting to dynamic conditions effectively (Brown & Smith, 2019; Matsumoto, 2016). This adaptive LQR approach, utilizing real-time dynamic programming, showcases significant improvements in control responsiveness and efficiency (Wu & Chen, 2010).

2.4.2. CW Based Trajectory Control

Developed from the foundational theories by Clohessy and Wiltshire (Clohessy & Wiltshire, 1960a), CW equations are pivotal in managing relative motion in orbit, essential for spacecraft rendezvous and docking operations (Schaub & Junkins, 2004; Sullivan & Atkins, 2013). Modifications of the CW model to support elliptical orbits have expanded its utility for broader mission profiles (Breger & How, 2008).

2.4.3. Integrative Approaches and Computational Advances

The integration of LQR and CW models with advanced computational strategies like genetic algorithms and machine learning revolutionizes spacecraft control systems, optimizing parameters dynamically to suit varying space conditions (Wang et al., 2019). Furthermore, advancements in electric propulsion technology enhance the granularity of

control adjustments necessary for the intricate operations dictated by these sophisticated models (de Bruijn, 2016).

2.4.4. Challenges and Prospects

Despite their proven capabilities, advanced control strategies like LQR and CW face challenges such as high computational demands and the complexity of managing non-linear dynamics in intricate orbital environments. Future research directions focus on improving computational algorithms and expanding the control models for interplanetary missions (Damico et al., 2015; Lee & Richards, 2018).

2.4.5. Conclusion

The continuous evolution of control strategies such as LQR and CW-based models is crucial to the success of both contemporary and future space missions. These strategies provide the necessary robustness, efficiency, and adaptability to meet the rigorous demands of space travel, highlighting their significance in the field of aerospace engineering.

2.5. Chapter Summary

This chapter has explored the critical role of Autonomous Orbit Control Systems in enabling efficient and precise spacecraft operations. From the challenges of orbit maintenance and the intricacies of GNSS receiver modeling to the complexities of thruster system behavior and control strategy design, the discussion has highlighted the importance of advanced modeling and control in overcoming operational constraints and achieving mission objectives. The continuous advancement of OCS technologies, fueled by research and innovation, promises to enhance the capabilities of future space missions, ensuring their success in the increasingly crowded and complex space environment.

3. Modelling and Simulation

3.1. Frame Conversion

This section delineates the frame transformations employed throughout this thesis, specifically converting from the Local Vertical, Local Horizontal (LVLH) frame to the Earth-centered Inertial (ECI) frame, and from the Perifocal (PQW) frame to the ECI frame. The conversion from LVLH to ECI is essential for translating the thrust force from LVLH to ECI, as the translation model operates with the position and velocity vectors in the ECI frame.

The conversion of orbital elements into Cartesian coordinates is achieved by transitioning from the PQW frame, which aligns with the plane of the orbit, to the ECI frame. This section details the mathematical processes involved in this transformation, utilizing orbital elements such as semi-major axis (a), eccentricity (e), inclination (i), right ascension of the ascending node (Ω), argument of periapsis (ω), and true anomaly (ν).

3.1.1. Position and Velocity in PQW Frame

The position ($\vec{r}_{PQW}$) and velocity ($\vec{v}_{PQW}$) vectors in the perifocal coordinate system are described by the equations below:

$$\vec{r}_{\mathrm{PQW}} = \frac{h^2/\mu}{1 + e\cos\nu} \begin{bmatrix} \cos\nu \\ \sin\nu \\ 0 \end{bmatrix} \tag{3.1}$$

$$\vec{v}_{\mathrm{PQW}} = \frac{\mu}{h} \begin{bmatrix} -\sin\nu \\ e + \cos\nu \\ 0 \end{bmatrix} \tag{3.2}$$

where $h = \sqrt{\mu \cdot a \cdot (1 - e^2)}$ denotes the specific angular momentum, and μ is the standard gravitational parameter of the central body. These vectors pinpoint the object's location and motion within the orbital plane.

To transition these vectors to the ECI frame, a transformation matrix (R) composed of the orbital elements is utilized. This matrix is an amalgamation of three rotation matrices:

$$R = R_3(-\Omega) \cdot R_1(-i) \cdot R_3(-\omega) \tag{3.3}$$

where the rotation matrices $R_3(\theta)$ and $R_1(\theta)$ around the z-axis and x-axis are defined as follows:

$$\mathrm{R}_3(\theta) = \begin{bmatrix} \cos(\theta) & \sin(\theta) & 0 \\ -\sin(\theta) & \cos(\theta) & 0 \\ 0 & 0 & 1 \end{bmatrix} \qquad \mathrm{R}_1(\theta) = \begin{bmatrix} 1 & 0 & 0 \\ 0 & \cos(\theta) & \sin(\theta) \\ 0 & -\sin(\theta) & \cos(\theta) \end{bmatrix} \tag{3.4}$$

Ω, i, and ω represent the right ascension of the ascending node, inclination, and argument of periapsis, respectively. These rotations align the PQW frame with the ECI frame, facilitating the vector conversions.

By applying the transformation matrix to the PQW vectors, the position and velocity in the ECI frame ($\vec{r}_{ECI}$ and $\vec{v}_{ECI}$) are derived:

$$_{ECI} = R \cdot \vec{r}_{PQW} \qquad _{ECI} = R \cdot \vec{v}_{PQW} \tag{3.5}$$

This method effectively transforms the orbital elements, which delineate the orbit's geometry and orientation, into Cartesian coordinates. These coordinates are vital for various space mission analysis tasks, such as orbit prediction, spacecraft tracking, and mission planning.

3.1.2. LVLH to ECI

The LVLH frame is integral for discerning the orientation and position of a spacecraft relative to its trajectory around Earth. This frame is derived from the position and velocity vectors known in the ECI frame, providing a direct method for frame conversion that adheres to standard definitions.

The axes of the LVLH frame, expressed in the ECI frame, are defined using a clear and simplified notation:

- $o3_I$: LVLH Z-axis - Opposite to the spacecraft's geocentric position vector.
- $o2_I$: LVLH Y-axis - Aligned with the negative orbit-normal.
- $o1_I$: LVLH X-axis - Complements the right-hand rule triad, ensuring an orthogonal coordinate system.

Given the spacecraft's position vector (r_I) and velocity vector ($\dot{r}_I = v_I$), both expressed in the ECI frame, the axes vectors of the LVLH frame can be mathematically depicted as follows:

$$o3_I = -\frac{r_I}{\|r_I\|} \tag{3.6}$$

$$o2_I = -\frac{r_I \times v_I}{\|r_I \times v_I\|} \tag{3.7}$$

$$o1_I = o2_I \times o3_I \tag{3.8}$$

The transformation from the LVLH frame to the ECI frame entails constructing a rotation matrix (A_{IO}) composed of the LVLH frame axes vectors as columns:

$$A_{IO} = [o1_I \quad o2_I \quad o3_I] \tag{3.9}$$

This rotation matrix acts as a conduit for translating vectors between the LVLH and ECI frames, aiding the comprehension of spacecraft dynamics in relation to Earth.

Below is the graphical depiction of the LVLH frame, illustrating its orientation relative to Earth and the spacecraft's trajectory.

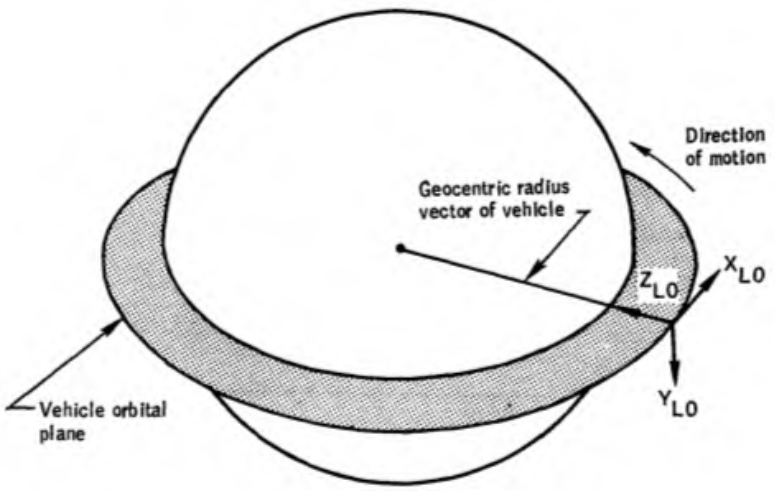

Figure 3.1.: Illustration of the LVLH Coordinate System used to define the orientation and movement of a satellite in orbit. The LVLH frame is defined such that the X_{LO} axis points along the orbit's velocity vector (direction of motion), the Z_{LO} axis points towards the center of the Earth (geocentric radius vector), and the Y_{LO} axis completes the right-handed coordinate system, normal to the orbital plane. Source: Adapted from NASA Technical Reports Server (NTRS), available at: https://ntrs.nasa.gov/api/citations/19740026178/downloads/19740026178.pdf

This illustration, along with the described mathematical formulations, emphasizes the systematic approach to transitioning between the LVLH and ECI frames, accentuating

their importance in the context of orbital mechanics and spacecraft navigation. Detailed discussions and frameworks for these conversions can be found in external resources such as the one provided by AI Solutions on attitude reference frames (AI Solutions, n.d.).

3.1.3. ECI to CW Frame Conversion

The ECI to CW frame conversion is pivotal for scenarios involving relative motion, such as rendezvous and proximity operations. The CW frame's axes are defined relative to a target's orbit:

- Radial ($\vec{r}_{\text{hat}}$): Aligns with the target's position vector.
- Along-track ($\vec{\theta}_{\text{hat}}$): Perpendicular to the orbital plane and radial direction.
- Normal ($\vec{n}_{\text{hat}}$): Completes the right-hand system with the orbital angular momentum.

The transformation matrix from ECI to CW, $R_{\text{eci\_to\_cw}}$, involves these unit vectors:

$$R_{\text{eci\_to\_cw}} = \begin{bmatrix} \vec{r}'_{\text{hat}} \\ \vec{\theta}'_{\text{hat}} \\ \vec{n}'_{\text{hat}} \end{bmatrix}, \tag{3.10}$$

facilitating the conversion of position and velocity from ECI to CW:

$$\vec{r}_{\text{cw}} = R_{\text{eci\_to\_cw}} \cdot \vec{r}_{\text{vec}}, \tag{3.11}$$

$$\vec{v}_{\text{cw}} = R_{\text{eci\_to\_cw}} \cdot \vec{v}_{\text{vec}} - \vec{\omega}_{\text{vec}} \times \vec{r}_{\text{cw}}, \tag{3.12}$$

where $\vec{\omega}_{\text{vec}}$ is the orbital angular velocity vector. This frame conversion is crucial for executing precise maneuvers and understanding the relative dynamics in a two-body problem.

This thorough explanation of frame conversions provides a solid foundation for understanding spacecraft dynamics in various reference frames, which is essential for accurate mission analysis and operations planning.

3.2. Simulation Framework and Configuration

For this thesis, Scilab, a powerful open-source software, served as the primary simulation platform. The development of simulation models was facilitated through the creation of Scilab scripts, specifically tailored to each model.(Eaton et al., 2013; Overton, 2015)

This process involved the drafting of two distinct scripts per model: an interface script and a simulation script. The interface script is designed to define the model parameters, establishing the foundational settings for the simulations. In the context of large-scale projects, the utilization of the Scilab toolbox is highly recommended, offering

enhanced functionality and efficiency. Guidance on configuring this toolbox for extended applications is available for further consultation.(Mottelet, 2012; Team, 2020)

The simulation script is intricately structured to manage various scenarios through the implementation of flags, which signify different computational tasks or states. These flags are important in guiding the computational functions towards the appropriate actions, based on the specific requirements of each task and the triggering event number.(Enterprises, 2021)

Prominent flags utilized in the thesis include:

- Flag 4: Initiates the simulation environment.

- Flag 6: Triggers the re-initialization process for the simulation.

- Flag 1: Engages in the computation of output variables.

- Flag 2: Computes discrete state variables.

- Flag 0: Calculates the derivatives of continuous state variables.

For an in-depth understanding of scripting within Scilab and the utilization of the xcos environment, the official Scilab website provides comprehensive resources and documentation. Further exploration of these tools is encouraged to leverage the full potential of Scilab in simulation-based research.

3.3. Methodology and Approach

This thesis employs a multifaceted methodology to design and analyze OCS for station-keeping. The approach integrates theoretical analysis with software modeling and simulation, leveraging the capabilities of Scilab and its graphical interface, Xcos, for dynamic simulation.

The core of the methodology involves the development of plant simulations, essential for understanding satellite behavior in orbit. Each simulation encompasses a series of models, including but not limited to:

- Kinematic and dynamic models for satellite motion.
- Environmental models to account for external forces.
- Control algorithms for station-keeping and maneuvering.

For each model within the plant simulation, a mathematical foundation is established, detailing the equations and algorithms governing satellite motion and control. These formulations serve as the basis for implementation in Scilab scripts, with the Xcos environment utilized for visual simulation.

The execution of simulations through Scilab scripts and Xcos diagrams facilitates an immersive analysis of satellite dynamics under various conditions. Key aspects of simulation setup, execution, and result interpretation include:

- Configuring initial conditions and simulation parameters based on realistic assumptions.
- Analyzing the impact of different control strategies on satellite station-keeping.
- Evaluating the results to understand variations and discrepancies, with a focus on the implications of assumptions and simplifications made during model development.

This comprehensive approach ensures a deep understanding of OCS for satellite station-keeping, highlighting the synergy between theoretical insights and practical simulation outcomes.

Limitations and Future Work

- The research presented herein concentrates on autonomous orbit control within the LEO regime. Its applicability to other orbital regimes or spacecraft configurations may be limited.
- The developed models are simplified representations of their real-world counterparts, potentially omitting certain complexities and nuances.
- Performance assessments conducted through simulations may not fully encapsulate the behavior of actual space-borne systems.
- Future investigations could delve into more sophisticated control algorithms, incorporate a broader range of environmental disturbances, and integrate hardware-in-the-loop simulations for a more grounded evaluation.

Through a comprehensive methodological approach, this thesis endeavors to fulfill its goal of devising and scrutinizing efficient systems for satellite station-keeping. The devised models, control strategies, and analytical frameworks are poised to offer valuable perspectives for the design and enhancement of future satellite control systems, thereby facilitating more effective, reliable, and economically viable satellite operations.

Key Contributions and Expected Outcomes

This thesis propounds significant advancements in the realm of autonomous orbit control for satellite formations and constellations. Employing intricate system modeling, refined control algorithms, and exhaustive performance evaluations, the study yields insightful and utilitarian outcomes:

Key Contributions

- **Enhanced System Modeling:** Elaboration of precise and computationally efficient Scilab models for GNSS receivers, orbit determination, and diverse thruster configurations. These models reflect essential attributes and constraints, offering a very similar portrayal of satellite control components.
- **Effective Controller Design:** Formulation and realization of control algorithms within Scilab for managing both singular and collective satellite operations. These

algorithms are tailored to maintain accurate orbit trajectories, mindful of fuel economy and operational limitations.

- **Comparative Insights:** Delineation of optimal propulsion and control pairings based on analytical outcomes, furnishing critical guidance for subsequent mission planning and control system selection.

Expected Outcomes

- **Improved Control System Design:** The methodologies and analytical tools developed contribute towards advancing control systems for satellite groupings, aiding engineers in crafting more effective and economically viable solutions.

- **Enhanced Mission Performance:** Optimizations in fuel efficiency, orbit accuracy, and formation coherence as facilitated by the proposed control solutions may result in superior mission efficacy and diminished operational expenditures.

- **Advancement in Scilab Applications:** The successful employment of Scilab for this research underscores its potential for complex control system analysis and simulation, encouraging its broader utilization in aerospace engineering.

- **Foundation for Future Research:** The established methodologies and derived findings lay the groundwork for further explorations into advanced control strategies, incorporation of additional environmental variables, and the pursuit of hardware-in-the-loop experiments for more exhaustive analyses.

In essence, this thesis aims to make a substantial contribution to the autonomous orbit control discipline, setting the stage for future endeavors in satellite mission optimization.

3.3.1. GNSS Receiver Model

The GNSS receiver model employs a straightforward approach to approximate the observed position and velocity of a satellite. It utilizes mathematical equations to account for the actual position and velocity of the receiver, and incorporates constant biases that reflect the systematic errors typically found in GNSS systems. These biases signify the common inaccuracies in the measurements of position and velocity.

Figure 3.2 depicts how this model is set up within the Xcos simulation environment. The model is structured to accept inputs for position and velocity and outputs the simulated values, incorporating errors. These adjustments include compensations for known biases in position and velocity, as well as considerations for noise.

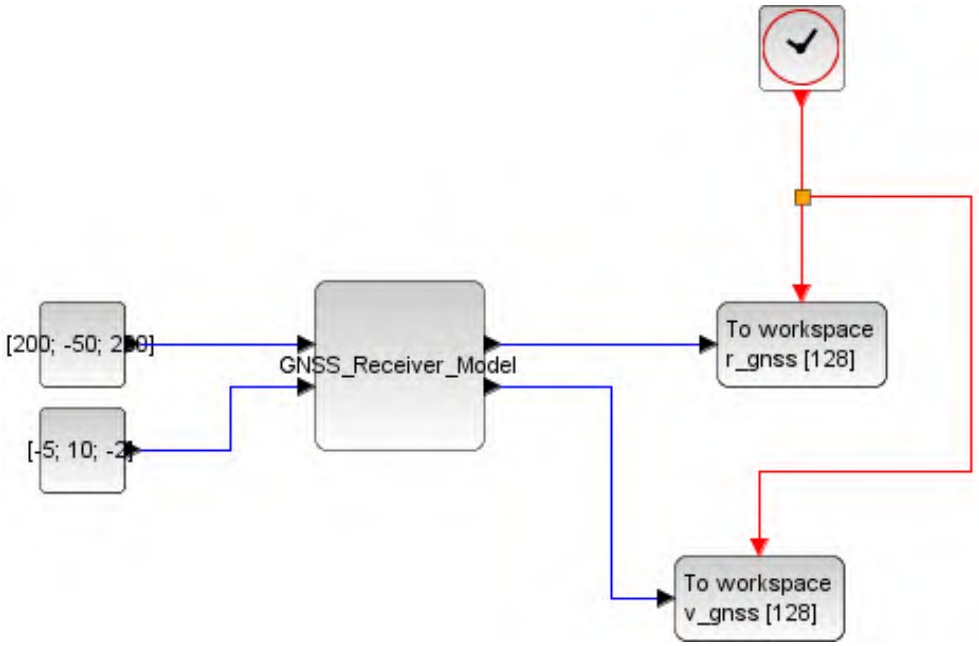

Figure 3.2.: This diagram shows the simulation setup for the GNSS Receiver Model, highlighting how positional and velocity inputs are processed with error adjustments. It illustrates the operation of a GNSS receiver in real-time scenarios, demonstrating the processing and correction of GNSS signals for inaccuracies.

The GNSS receiver's observed position ($\vec{r}_{\text{gnss}}$) and velocity ($\vec{v}_{\text{gnss}}$) are influenced by the true position ($\vec{r}$) and velocity ($\vec{v}$), along with constant biases ($\vec{b}_r$ for position and $\vec{b}_v$ for velocity), and the uncertainties in these measurements. The uncertainties are denoted by noise σ_r for position and σ_v for velocity. The formulas to represent these relationships are:

$$\vec{r}_{\text{gnss}} = \vec{r} + \vec{b}_r + \sigma_r \tag{3.13}$$

$$\vec{v}_{\text{gnss}} = \vec{v} + \vec{b}_v + \sigma_v \tag{3.14}$$

Where:

- $\vec{r}_{\text{gnss}}$ and $\vec{v}_{\text{gnss}}$ are the GNSS receiver's reported position and velocity, respectively. These values integrate the true values ($\vec{r}$ and $\vec{v}$), systematic biases ($\vec{b}_r$ and $\vec{b}_v$), and the measurement uncertainties (σ_r and σ_v).
- σ_r and σ_v symbolize the noise for position and velocity measurements, reflecting the degree of uncertainty or deviation from the true values due to measurement noise and environmental conditions.

Translation Motion Dynamics of a Spacecraft

The translation motion dynamics of a spacecraft are governed by Newton's second law of motion, which states that the force acting on an object is equal to the mass of the object times its acceleration. This fundamental principle forms the basis for understanding how forces affect spacecraft trajectories and is detailed in classical astrodynamics texts *Fundamentals of Astrodynamics* by Bate, Mueller, and White (Bate et al., 1971). For a spacecraft in Earth's vicinity, the equation can be expressed as:

$$m\dot{\vec{v}} = \vec{F}_{\text{grav}} + \vec{F}_{\text{thrust}} + \vec{F}_{\text{drag}} + \vec{F}_{\text{J2}} \tag{3.15}$$

where:

- m is the mass of the spacecraft,
- $\dot{\vec{v}}$ is the acceleration vector of the spacecraft,
- $\vec{F}_{\text{grav}}$ is the gravitational force,
- $\vec{F}_{\text{thrust}}$ is the thrust force,
- $\vec{F}_{\text{drag}}$ is the atmospheric drag force, and
- $\vec{F}_{\text{J2}}$ is the perturbative force due to Earth's oblateness.

Gravitational Force

The gravitational force exerted by the Earth on the spacecraft can be modeled by Newton's law of universal gravitation, a fundamental concept thoroughly explained in *Classical Mechanics* by Goldstein et al. (Goldstein et al., 2002). The force equation is given by:

$$\vec{F}_{\text{grav}} = -\frac{GM_{\text{e}}m}{r^2}\hat{r} \tag{3.16}$$

where:

- G is the gravitational constant, approximately $6.674 \times 10^{-11}\,\text{m}^3\text{kg}^{-1}\text{s}^{-2}$,
- M_{e} is the mass of the Earth, approximately $5.972 \times 10^{24}\,\text{kg}$,
- m is the mass of the spacecraft,
- r is the distance between the spacecraft and the Earth's center, and
- $\hat{r}$ is the unit vector pointing from the spacecraft to the Earth's center.

This relationship is crucial for understanding the forces at play during the spacecraft's orbital maneuvers and is central to the analysis of orbits and trajectories.

Thrust Force

The thrust force, a critical aspect of spacecraft propulsion, is provided by the spacecraft's propulsion system. The fundamental principles and mathematical formulation of thrust are extensively covered in *Rocket Propulsion Elements* by Sutton and Biblarz (Sutton & Biblarz, 2010). The formula for thrust is given by:

$$\vec{F}_{\text{thrust}} = I_{\text{sp}} g_0 \dot{m} \hat{n} \tag{3.17}$$

where:

- I_{sp} is the specific impulse of the propulsion system,
- g_0 is the standard gravitational acceleration,
- $\dot{m}$ is the rate of mass ejection, and
- $\hat{n}$ is the unit vector in the direction of the thrust.

Atmospheric Drag

The force due to atmospheric drag is critical for spacecraft operating in lower Earth orbits and can be effectively modeled with an equation provided by Howard D. Curtis in his textbook, *Orbital Mechanics for Engineering Students* Curtis, 2013. This model captures the interaction between the spacecraft and the Earth's atmosphere:

$$\vec{F}_{\text{drag}} = -\frac{1}{2} C_{\text{d}} A \rho v^2 \hat{v} \tag{3.18}$$

The parameters of this equation are:

- C_{d}, the drag coefficient, which quantifies the drag force encountered by the spacecraft. For the purposes of these simulations, C_{d} has been selected as 2.7,
- A, the cross-sectional area of the spacecraft perpendicular to the velocity vector,
- ρ, the atmospheric density at the spacecraft's altitude,
- v, the spacecraft's velocity relative to the atmosphere,
- $\hat{v}$, the unit vector in the direction of the velocity.

Curtis's approach to modeling atmospheric drag provides an essential framework for aerospace engineers designing missions that require precision in predicting orbital decay and understanding the aerodynamic forces at play.

J2 Perturbation

The J2 perturbation, which accounts for the oblateness of the Earth and its influence on the gravitational field, is significant for precise orbital calculations. According to Montenbruck

and Gill in *Satellite Orbits: Models, Methods, and Applications* (Montenbruck & Gill, 2000), the force due to J2 perturbation can be mathematically expressed as:

$$\vec{F}_{\mathrm{J2}} = -\frac{3}{2} J_2 \frac{G M_{\mathrm{e}} m R_{\mathrm{e}}^2}{r^4} \left(1 - 5\left(\frac{z}{r}\right)^2\right) \hat{r} + \frac{3}{2} J_2 \frac{G M_{\mathrm{e}} m R_{\mathrm{e}}^2}{r^4} \left(3\left(\frac{z}{r}\right)^2 - 1\right) \hat{z} \tag{3.19}$$

where:

- J_2 is the second zonal harmonic coefficient of the Earth's gravitational potential,
- R_{e} is the mean radius of the Earth, approximately $6,371\,\mathrm{km}$,
- z is the distance of the spacecraft from the Earth's equatorial plane, and
- $\hat{z}$ is the unit vector perpendicular to the equatorial plane.

This formulation provides a comprehensive model for the translational motion dynamics of spacecraft, especially for those in Earth-orbiting missions, underscoring the importance of considering non-spherical Earth effects in precision orbit determination.

CelestLab Integration for Simulation

The CelestLab library in Scilab provides a comprehensive suite of functions to simulate the forces acting on a spacecraft, including gravitational and atmospheric drag forces. Specifically, the `CL_fo_zonHarmAcc` function simulates the acceleration due to Earth's zonal harmonics, and the `CL_fo_dragAcc` function simulates the acceleration due to atmospheric drag. These functions allow for detailed and accurate modeling of spacecraft dynamics, enabling the incorporation of complex gravitational models and atmospheric conditions into simulations.

Zonal Harmonics Acceleration The `CL_fo_zonHarmAcc` function calculates the acceleration due to zonal harmonics:

```
[acc] = CL_fo_zonHarmAcc(pos, [nz, er, mu, j1jn])
```

It considers an array of zonal term numbers (`nz`), the equatorial radius (`er`), the gravitational constant (`mu`), and zonal harmonics coefficients (`j1jn`) to accurately model gravitational perturbations.

Atmospheric Drag Acceleration The `CL_fo_dragAcc` function computes the acceleration due to atmospheric drag:

```
[acc] = CL_fo_dragAcc(vel, rho, coefd)
```

This function uses the velocity relative to the atmosphere (`vel`), the atmospheric density (`rho`), and a coefficient (`coefd`) defined by the drag coefficient, cross-sectional area, and mass of the spacecraft to simulate drag forces.

These CelestLab functions enhance the fidelity of spacecraft dynamics simulations by incorporating detailed models for gravitational and atmospheric effects, crucial for the design and analysis of spacecraft missions.

Thruster Model

The thruster model is designed to simulate the behavior of an electric thruster system. It incorporates several key parameters and dynamic characteristics to accurately represent the thruster's operation. The model is governed by the following equations and considerations.

The thruster model operates based on an input control signal and several predefined parameters:

- $u(t)$: Control signal for the thruster, ranging from 0 (off) to 1 (full power), which scales linearly with the percentage of nominal thrust from 0% to 100%.
- F_{nom}: Nominal thrust, representing the maximum thrust output under ideal conditions.
- $\vec{d}$: Thrust direction vector in the LVLH frame, represented as a unit vector.
- I_{sp}: Specific impulse, indicating the efficiency of the thruster (thrust force per unit mass flow rate).
- T_{delay}: Time constant for the first-order delay, modeling the dynamic response of the thruster's switch-on and switch-off behavior.

The generated thrust and mass flow rate are calculated as follows:

$$F(t) = u(t) \cdot F_{\text{nom}} + \epsilon(t) \tag{3.20}$$

where $F(t)$ is the generated thrust at time t, and $\epsilon(t)$ represents low-frequency noise/error in the thrust output.

$$\dot{m}(t) = \frac{F(t)}{g_0 \cdot I_{\text{sp}}} \tag{3.21}$$

with $\dot{m}(t)$ denoting the mass flow rate at time t, and g_0 being the standard gravity ($9.81\,\text{m/s}^2$).

To model the dynamic response and incorporate a noise model into the thruster operation, the following considerations are made:

$$\tau \frac{dF(t)}{dt} + F(t) = F_{\text{desired}}(t) \tag{3.22}$$

where $\tau = T_{\text{delay}}$ is the time constant of the delay, and $F_{\text{desired}}(t)$ is the desired thrust output based on the control input $u(t)$. This first-order delay models the dynamic response of the thruster for switching on and off.

$$\epsilon(t) \sim \mathcal{N}(0, \sigma^2) \tag{3.23}$$

$\epsilon(t)$ is modeled as a normally distributed random variable with mean 0 and variance σ^2, representing the low-frequency noise affecting the thrust output.

The direction of the thrust force vector in the body-fixed frame is given by:

$$\vec{F}(t) = F(t) \cdot \vec{d} \tag{3.24}$$

where $\vec{F}(t)$ is the thrust force vector, and $\vec{d}$ is the unit direction vector of the thrust in the body-fixed frame.

This model provides a comprehensive framework for simulating the behavior of an electric thruster, incorporating the effects of control inputs, nominal parameters, dynamic responses, and environmental noise.

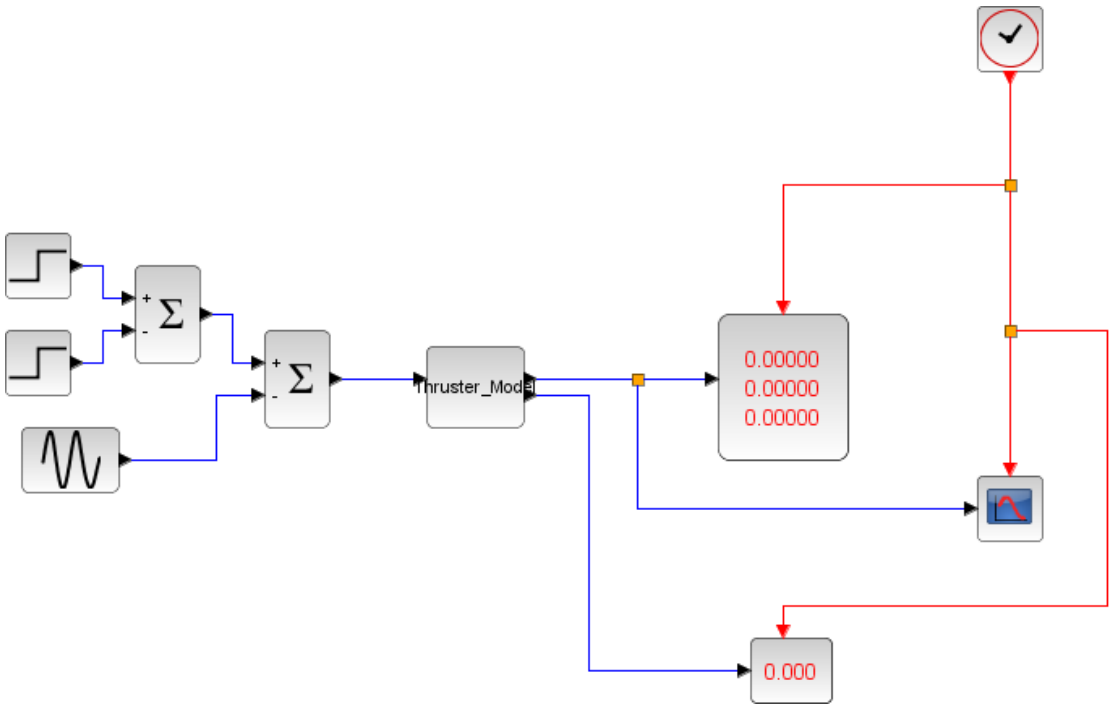

Figure 3.3.: Detailed schematic of the Thruster Model Test Setup. Key components include input signal conditioning, thruster response simulation, and output monitoring, facilitating the evaluation of the thruster's performance.

The utilization of a first-order delay differential equation is pivotal for modeling processes that exhibit time delays between input and response. In the context of the thruster model, such an equation comprehensively captures the physical reality that adjustments in the thruster's output in response to command inputs are not instantaneous. Delays may result from the thruster mechanism's physical constraints or the time taken by the control system to process commands. This mathematical approach is thus instrumental in accurately simulating the dynamics of the thruster's response, facilitating enhanced prediction and control within spacecraft guidance, navigation, and control systems.

3.3.2. Design of the Orbit Determination Model

The Orbit Determination Model (ODM) is integral to satellite navigation, transforming position and velocity data from Cartesian coordinates into Keplerian orbital elements for precise orbit analysis. This process is crucial for understanding the trajectory and behavior of objects in space, ensuring accurate navigation and control. Figure 3.4 demonstrates a simulation setup in xcos environment.

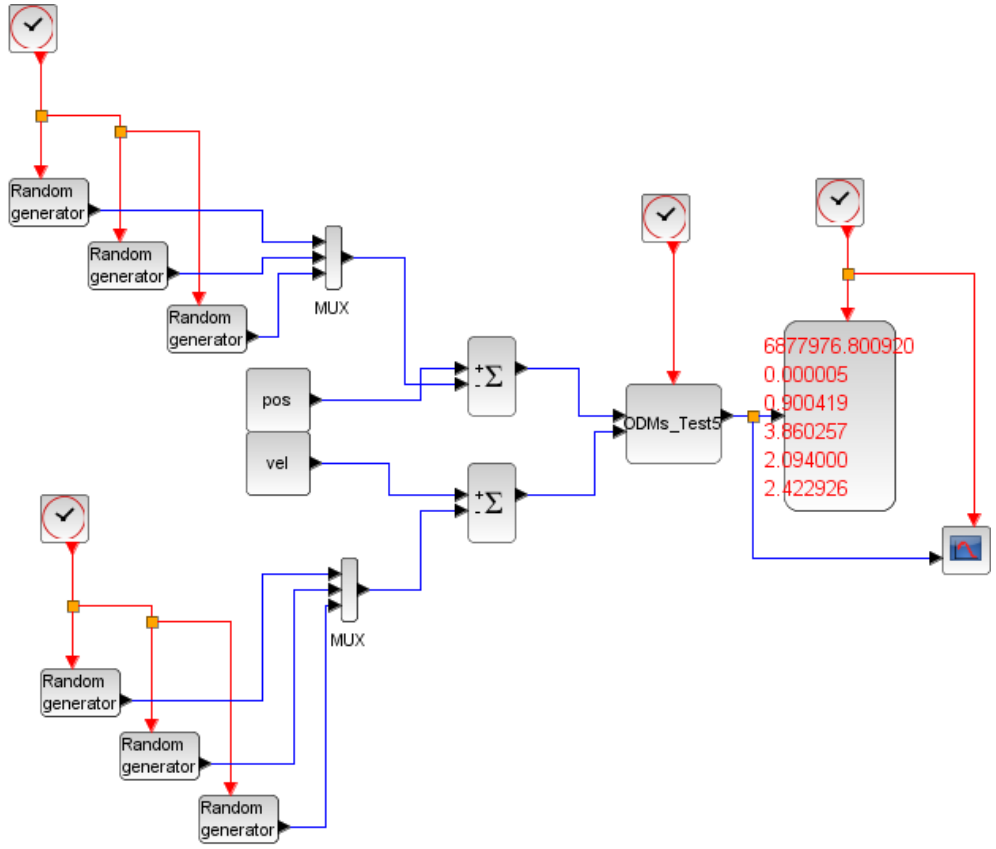

Figure 3.4.: Schematic of the Orbit Determination Model Test Setup. This diagram illustrates the integration of noise simulation via multiple random generators affecting position and velocity inputs, which are processed through a 5th-order filter to simulate real-world satellite tracking errors.

The development of the ODM unfolds through three key stages, evolving from a basic model that directly calculates Keplerian elements to sophisticated versions incorporating filtering techniques for noise reduction and accuracy enhancement. Initially, the model starts without data smoothing, presenting raw orbital characteristics. The second stage introduces a first-order Infinite Impulse Response (IIR) filter, improving data fidelity by mitigating noise. Finally, an advanced model applies a fifth-order filter, significantly refining the output with smooth and stable orbital elements. This evolution underscores a systematic enhancement in processing positional data, culminating in a tool capable of delivering precise orbital analysis for satellite mission planning.

The derivation of orbital elements from position ($\mathbf{r}$) and velocity ($\mathbf{v}$) vectors is a cor-

nerstone of orbital mechanics, thoroughly explained in *Fundamentals of Astrodynamics and Applications* by David A. Vallado (Vallado, 2013). The CelestLab library function `CL_oe_car2kep` facilitates this conversion, particularly focusing on the computation of the mean anomaly (M) as a significant orbital element. The following outlines the fundamental equations employed in this conversion process:

The specific angular momentum ($\vec{\mathbf{h}}$) is derived from the cross product of the position and velocity vectors:

$$\vec{\mathbf{h}} = \vec{\mathbf{r}} \times \vec{\mathbf{v}} \tag{3.25}$$

The eccentricity vector ($\vec{\mathbf{e}}$) is calculated as:

$$\vec{\mathbf{e}} = \frac{\vec{\mathbf{v}} \times \vec{\mathbf{h}}}{\mu} - \frac{\vec{\mathbf{r}}}{|\vec{\mathbf{r}}|} \tag{3.26}$$

where μ is the standard gravitational parameter of the central body.

The inclination (i) is obtained from the angular momentum vector:

$$i = \cos^{-1}\left(\frac{h_z}{|\vec{\mathbf{h}}|}\right) \tag{3.27}$$

where h_z is the z-component of $\vec{\mathbf{h}}$.

The RAAN (Ω) is determined by:

$$\Omega = \cos^{-1}\left(\frac{n_x}{|\vec{\mathbf{n}}|}\right) \tag{3.28}$$

For $n_y < 0$, adjust Ω accordingly, where $\vec{\mathbf{n}}$ denotes the node vector.

The argument of periapsis (ω), also known as ω, is computed using:

$$\omega = \cos^{-1}\left(\frac{\vec{\mathbf{n}} \cdot \vec{\mathbf{e}}}{|\vec{\mathbf{n}}||\vec{\mathbf{e}}|}\right) \tag{3.29}$$

Adjust if $e_z < 0$, with e_z being the z-component of $\vec{\mathbf{e}}$.

The mean anomaly (M) is calculated using Kepler's equation, distinct from the traditional focus on the true anomaly (ν):

$$M = E - e\sin(E) \tag{3.30}$$

where E is the eccentric anomaly, derived from the relationship between e and ν.

This formulation, facilitated by CelestLab's `CL_oe_car2kep` function, exemplifies the conversion from ECI position and velocity vectors to a comprehensive set of orbital elements $(a, e, i, pom, RAAN, M)$, enabling accurate orbital determination and analysis for satellite mission planning.

Conversion from Cartesian to Keplerian Orbital Elements

The model receives position and velocity data from a GNSS and converts these into Keplerian orbital elements. The key function used for this conversion is `CL_oe_car2kep`.

Function Description

- **Function Name:** `CL_oe_car2kep`
- **Purpose:** To convert Cartesian orbital elements (position and velocity) into classical Keplerian orbital elements. It optionally computes the transformation Jacobian.
- **Parameters:**
  - `pos`: Position vector $[x; y; z]$ in meters (3xN).
  - `vel`: Velocity vector $[vx; vy; vz]$ in meters per second (3xN).
  - `mu`: (Optional) Gravitational constant in m^3/s^2 (default value is %CL_mu).
- **Outputs:**
  - `kep`: Classical Keplerian orbital elements $[sma; e; inc; pom; raan; M]$ in meters and radians (6xN).
  - `jacob`: (Optional) Transformation Jacobian.

Implementation in the Model

The following pseudo-code demonstrates how the function is utilized in the orbit determination model:

```
inptr = block.inptr;
r_gnss = inptr(1); // GNSS position
v_gnss = inptr(2); // GNSS velocity
kep = CL_oe_car2kep(r_gnss, v_gnss);
// Converts position and velocity to orbital elements
```

Discrete-Time Realization

In discrete time, the differential equation is approximated as:

$$x_i - y_i = RC \cdot \frac{y_i - y_{i-1}}{\Delta_T} \tag{3.31}$$

where x_i and y_i are the sampled input and output voltages at the i-th interval, and Δ_T is the sampling time interval. This approximation technique and its impact on system behavior are discussed in detail in *Discrete-Time Signal Processing* by Oppenheim and Schafer Oppenheim and Schafer, 1999.

Recurrence Relation

The recurrence relation for the discrete-time filter update is:

$$y_i = \alpha x_i + (1 - \alpha) y_{i-1} \tag{3.32}$$

$$\alpha = \frac{\Delta_T}{RC + \Delta_T} \tag{3.33}$$

where α is the smoothing factor, controlling the amount of smoothing and the filter's response to changes in the input.

Relation to Resistor-Capacitor (RC and Frequency

The time constant RC and the cutoff frequency f_c of the filter are related to the smoothing factor α by:

$$RC = \Delta_T \left(\frac{1 - \alpha}{\alpha} \right) \tag{3.34}$$

$$f_c = \frac{\alpha}{(1 - \alpha)2\pi\Delta_T} \tag{3.35}$$

These relationships define the behavior and characteristics of the orbit determination model's low-pass filter in both continuous and discrete time. Proakis and Manolakis in *Digital Signal Processing: Principles, Algorithms, and Applications* (Proakis & Manolakis, 2007) provide a thorough examination of how this relationship affects filter performance.

Implementation of the Simple Moving Average Filter

The Simple Moving Average (SMA) filter is a type of digital filter used to smooth data by creating a series of averages of different subsets of the full data set. It is commonly applied in signal processing to reduce noise and better reveal the underlying trend.

The SMA of a set of data points $x_1, x_2, \ldots, x_n$ over a window of size N is given by:

$$SMA(k) = \frac{1}{N} \sum_{i=0}^{N-1} x_{k-i}, \tag{3.36}$$

where k is the current time step and N is the total number of points in the window. The output at each point k is the average of the last N inputs up to that point (Wikipedia contributors, 2024).

The Scilab code implements an SMA filter for smoothing Keplerian elements derived from GNSS data. Here's a breakdown of the key steps involved:

1. **Data Insertion:** New Keplerian elements are inserted at the beginning of their respective buffers, shifting previous values to make space.
2. **Moving Average Calculation:** For each Keplerian element, the SMA is calculated using the most recent 5 values (i.e., $N = 5$) in the buffer.
3. **Output Update:** The calculated SMA values are stored and used to update the output, providing smoothed estimates of the Keplerian elements.

The mathematical underpinnings of the SMA are essential for the transformation of position and velocity data into a format that is more readily interpretable, especially in the context of space dynamics. Given a series of n measurements, denoted as $p_1, p_2, \ldots, p_n$, the SMA for the most recent k values was determined by the formula:

$$SMA_k = \frac{p_{n-k+1} + p_{n-k+2} + \cdots + p_n}{k} = \frac{1}{k} \sum_{i=n-k+1}^{n} p_i \tag{3.37}$$

This formula ensured an equilibrium in the data analysis, incorporating an equal number of observations both before and following a midpoint, thus minimizing the potential lag in trend detection.

Simplifications and Assumptions in the Model

This section discusses the simplifications and assumptions integrated into the simulation process and testing procedures.

- The satellite's body frame is aligned with the LVLH frame for simplicity.
- External perturbations such as atmospheric drag and J2 perturbation are not considered in the simulation.
- In scenarios involving both target and chaser satellites, the target is posited at the coordinate origin.
- Translational motion, including gravitational acceleration, is factored into the simulations.
- The satellite's total mass is considered to be 25 kg, with 5 kg allocated for fuel used in propulsion.
- For tests and simulations using the CLSS block, the CW frame is used, eliminating the need for frame conversion in the Thruster Model.
- In the non-linear test setup, inputs to the thruster block are converted from the CW frame to the LVLH frame, subsequently transformed to the ECI frame. The relative motion between the chaser and the target is analyzed in the CW frame.

3.4. Verification and Validation of Thruster operation

The structure of this analysis is methodically organized as follows: the motivation for each test is initially presented, setting the stage for a clear understanding of its relevance and objectives. After this, the expected outcomes are delineated, providing a benchmark against which the simulation's performance can be evaluated. The section then transitions to a detailed exposition of the simulation results, facilitating a direct comparison with the theoretical expectations.

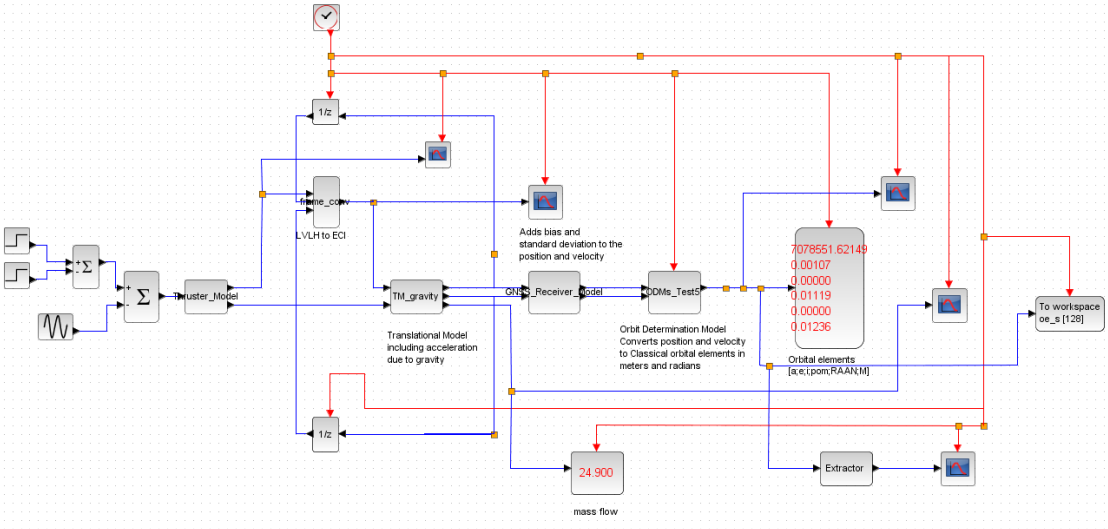

Figure 3.5.: Comprehensive Simulation Framework of the Satellite Control System. This schematic illustrates the interconnected modules of a satellite simulation setup, including thruster models, GNSS receiver simulation, and orbit determination systems. Key components include real-time dynamics modeling, and the translation of navigation data into actionable orbital parameters.

In instances where discrepancies between anticipated and actual outcomes are observed, a thorough examination is undertaken to elucidate the underlying factors contributing to these differences. This exploration is aimed at identifying potential areas for improvement within the simulation framework, ensuring that the model's fidelity and predictive capability are continuously enhanced.

The initial conditions for the test cases are as follows:

Table 3.1.: Initial Conditions for the Spacecraft

Parameter	**Value**
Position (`pos`)	$[7071000, 0, 0]$ meters
Velocity (`vel`)	$[0, 7508.06853975, 0]$ m/s
Spacecraft mass	25 kilograms
Control Parameter $k1$	1
Control Parameter σ	0
Control Parameter $k2$	0

Table 3.2.: Initial conditions for the spacecraft used in the simulation tests. The table specifies key parameters such as position, velocity, mass, and control settings, defining the precise setup for achieving a stable circular orbit.

These initial settings position the spacecraft into a circular orbit with the following characteristics:

Orbital Parameter	Value
Semi-major axis (a)	7070992.16799 m
Eccentricity (e)	0 (circular orbit)
Inclination (i)	0.0 radians
Argument of perigee (ω)	3.14159 radians
Right Ascension of Ascending Node (RAAN)	0.0 radians
Mean anomaly (M)	3.14159 radians

Table 3.3.: Orbit characteristics of the spacecraft, describing the parameters of the circular orbit achieved in the simulation. Values such as the semi-major axis, eccentricity, inclination, argument of perigee, right ascension of the ascending node, and mean anomaly are detailed to outline the specific orbital path maintained throughout the tests.

This configuration ensures the spacecraft maintains a stable circular orbit at an altitude of 700 km, essential for the consistent evaluation of control strategies and the analysis of orbital dynamics.

Test 1: Maneuver in positive flight direction

Test Objective: To assess the ramifications of thrust application in the flight direction on orbital parameters.

It was hypothesized that imparting a nominal thrust of 100 Newtons in the flight direction—aligned along the direction vector [1;0;0] within the LVLH frame, corresponding to the [0;1;0] direction in the ECI frame—would induce significant alterations in the semi-major axis and eccentricity of the orbit. This expectation was underpinned by analytical calculations, anticipating a direct correlation between the applied thrust and the resultant orbital elements.

As depicted in Figure 3.6, the practical application of thrust conspicuously influenced the targeted orbital elements. Panel (a) of the figure delineates a discernible shift in the semi-major axis, diverging from the analytical projections by approximately 1 meter, albeit the eccentricity mirrored the analytical predictions with high fidelity. The methodologies underlying the application of thrust and the conversion between the LVLH and ECI frames are elaborated in Section 3.1.

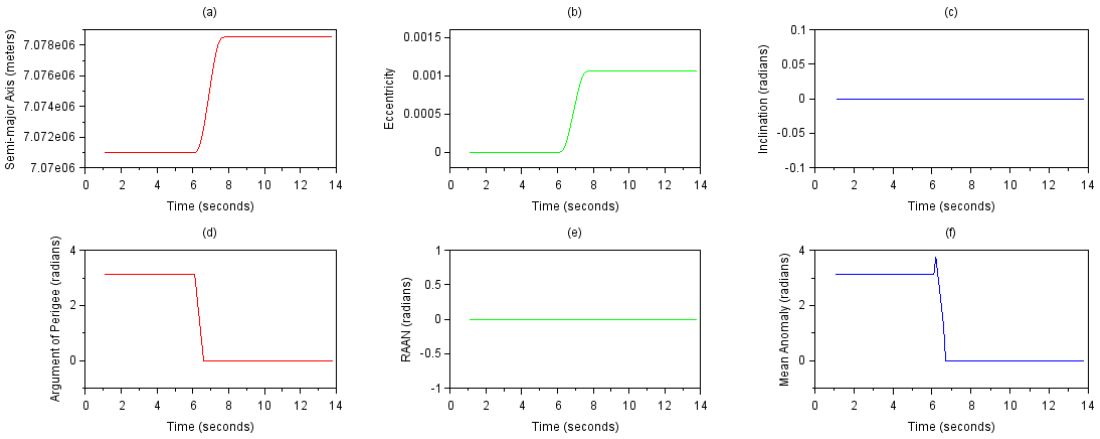

Figure 3.6.: Orbital Element Variations for Test 1: Impact of 100 Newton Thrust in Flight Direction: This table compares the initial, calculated, and simulated orbital elements following a 100 Newton thrust manoeuvre. It details changes in semi-major axis, eccentricity, and other parameters, highlighting deviations from expected values under different specific impulse conditions.

Orbital elements	**a (m)**	**e**	**i (rad)**	**pom (rad)**	**RAAN (rad)**	**M (rad)**
Initial orbital elements	7070992.16799	0.0	0.0	3.14159	0.0	3.14159
Analytical calculation	7078536.485	0.00106	0.0	0.0	0.0	0.0
Simulation results I_{sp} = 10,000 sec)	7078537.995	0.00106	0.0	0.00375	0.0	0.00379
Simulation results I_{sp} = 1,000,000 sec)	7078536.636	0.0106	0.0	0.00375	0.0	0.00379

Table 3.4.: Summary of Orbital Element Changes from Test Case 1 with a 100 Newton Thrust Manoeuvre: This table quantifies the adjustments in orbital parameters under different I_{sp} conditions, contrasting initial conditions with results from analytical and simulation methods.

Despite the largely congruent outcomes, the slight variance observed in the semi-major axis adjustment vis-à-vis the analytical model underscores the complexity of real-world orbital dynamics. This discrepancy, alongside a broader discussion on simulation fidelity, is slated for a comprehensive examination in further test cases.

Test 2: Increased thrust and Isp in flight-direction

The following discussion outlines the outcomes of a targeted experiment that has been designed to evaluate the effects of increased thrust on modifications to orbital elements, with a specific focus on changes to the semi-major axis and eccentricity. Unlike the

previous test, the thrust applied in this instance was increased to 1000 Newtons, and the force was directed along the x-axis of the LVLH frame to simulate propulsion in the direction of flight.

The aim was to observe the impact of the enhanced thrust on the orbit's semi-major axis and eccentricity, reflecting the objectives of the preceding test but under conditions of increased propulsive force.

Referring to the data compiled in Table 3.5, various test scenarios have been evaluated, particularly those conditions where the specific impulse was significantly increased. It was notable that this adjustment had not affected the spacecraft's mass. The outcomes of the simulations have exhibited an exact alignment with the analytical calculations, confirming the model's accuracy under the specified test conditions.

Orbital elements	**a (m)**	**e**	**i (rad)**	**pom (rad)**	**RAAN (rad)**	**M (rad)**
Initial orbital elements	7070992.16799	0.0	0.0	3.14159	0.0	3.14159
Analytical calculation	7147351.34940	0.01068	0.0	0.0	0.0	0.0
Simulation results I_{sp} = 10,000 sec)	7147506.41236	0.01070	0.0	0.00639	0.0	0.00781
Simulation results I_{sp} = 1,000,000 sec)	7147352.89486	0.01068	0.0	0.00639	0.0	0.00781

Table 3.5.: Results for Test 2: Impact of Increased Thrust Directed Along the X-Axis of the LVLH Frame on Orbital Elements: This table showcases the measured changes in orbital parameters following a targeted manoeuvre involving a thrust increase to 1000 Newtons. It reflects how specific orbital elements are affected under enhanced thrust conditions, with comparisons drawn between initial settings, analytical predictions, and simulation outcomes at different I_{sp} settings.

Graphical analyses, as illustrated in the accompanying figure 3.7, showed significant modifications in the semi-major axis and eccentricity as a result of the applied thrust. Interestingly, variations had also been observed in the argument of perigee and the Mean Anomaly. Given the circular nature of the orbit, the filtering algorithm encountered difficulties in accurately discerning the values of these two latter orbital elements, oscillating within the range of 0 to 2π.

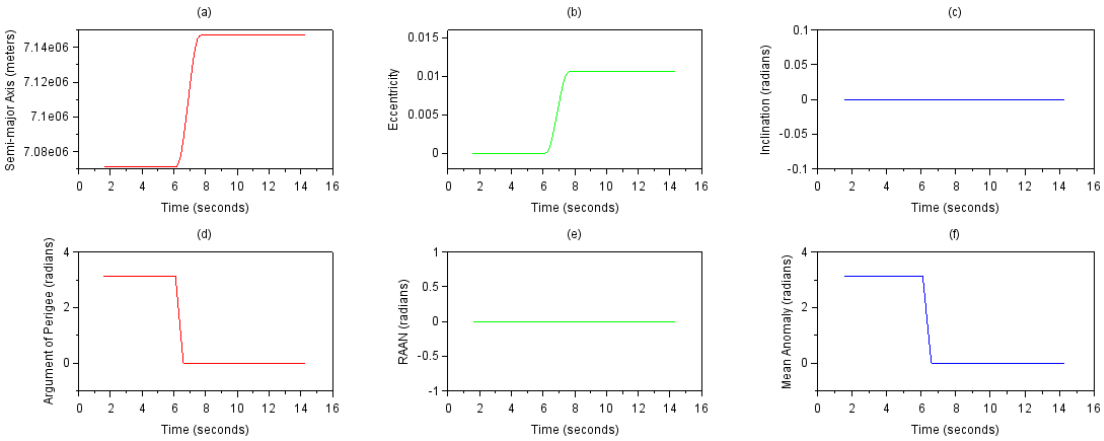

Figure 3.7.: Graphical representation of the semi-major axis and eccentricity changes following a 1000 Newton thrust application in the flight direction.

Test 3: Thrust Application in Negative Orbit Normal Direction

Test 3 involved the application of a nominal thrust of 100 N directed against the orbit normal to evaluate its effects on orbital inclination and the RAAN, while keeping spacecraft parameters consistent with previous experiments. For this test, the I_{sp} was set at 100,000 seconds. The results demonstrated a significant alteration in inclination and RAAN, aligning with theoretical predictions. Remarkably, e remained stable, and only minor deviations were noted in a, as expected due to minimal mass changes.

Specifically, the observed value of a was 7,070,992.68794 meters, compared to the analytical prediction of 7,070,992.5768 meters calculated using a Python script. The negligible discrepancy between these values is attributed to the slight consumption of fuel, leading to a non-constant mass scenario, which deviates from the assumptions used in analytical orbital element computations. The mass decreased by approximately 24.999 kg from an initial total of 25 kg following the thrust application. This minor mass reduction is likely the cause of the small observed variance in a.

Additionally, a slight adjustment in the *pom* was detected, which may result from the mass change or possibly the choice of numerical integrator used in the orbital element computations. A table detailing the comparison between analytical and simulated results is presented in Table 3.6. Furthermore, Figure 3.8 illustrates the variations in classical Keplerian orbital elements before and after the application of thrust.

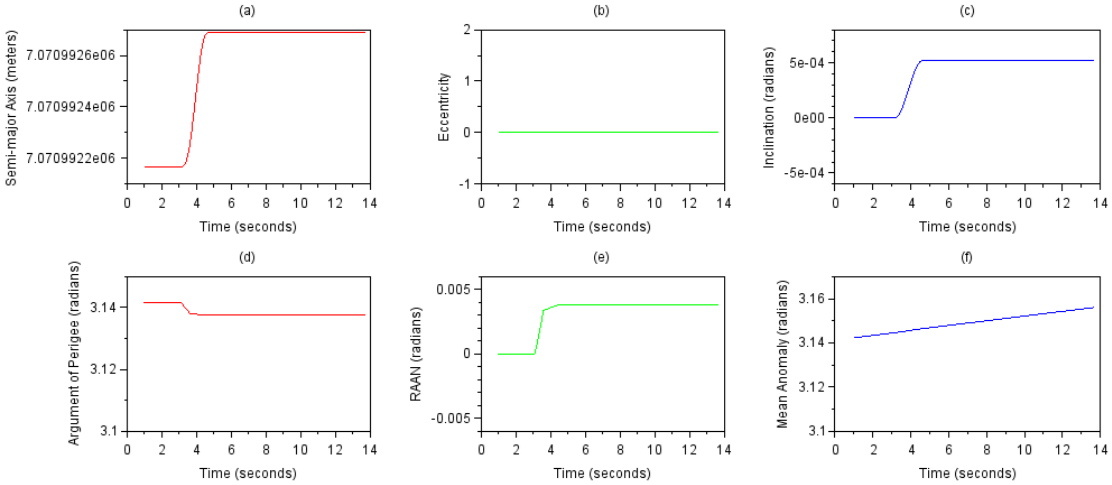

Figure 3.8.: Comparative Analysis of Keplerian Orbital Elements Before and After Applying 100 N Thrust in the Negative Orbit Normal Direction: This graph illustrates the changes in the a, inclination, and RAAN caused by the thrust, highlighting the stability of eccentricity and minor deviations in other orbital parameters due to slight mass variations following fuel consumption.

Orbital elements	**a (m)**	**e**	**i (rad)**	**pom (rad)**	**RAAN (rad)**	**M (rad)**
Initial orbital elements	7070992.17	0.0	0.0	3.14159	0.0	3.14159
Analytical calculation	7070992.5768	0.0	0.000532	3.14159	0.00379	3.14159
Simulation results (Isp = 10^6 seconds)	7070992.68794	0.0	0.00052	3.13751	0.00381	3.15630

Table 3.6.: Comparative Analysis of Orbital Elements Before and After 100 N Thrust Application in Test 3: This table presents the initial conditions, analytical calculations, and simulation results of the orbital parameters under the influence of a nominal 100 N thrust in the negative orbit normal direction. The I_{sp} was set at 1,000,000 seconds for these simulations.

Test 4: Thrust Application in Positive Radial Direction

Test 4 explored the influence of a controlled thrust application of 100 N directed in the positive radial direction. This experiment aimed to assess the effects on eccentricity and slight variations in the semi-major axis while maintaining consistent spacecraft parameters as in previous experiments. The I_{sp} was set exceptionally high at 100,000 seconds to minimize the propellant mass fraction. The outcomes confirmed significant modifications in eccentricity and the *pom*, aligning closely with theoretical predictions. Intriguingly, i remained unchanged, and only minor deviations occurred in the a, as anticipated due to the minimal mass change from fuel consumption.

The observed semi-major axis was 7070995.26251 meters, showing a minute discrepancy

from the analytical value of 7070994.17 meters, derived from a precision Python script. The eccentricity recorded from the simulation was 0.00052, slightly differing from the analytical calculation of 0.00053276. These small differences are attributed to the reduction in spacecraft mass due to fuel usage, leading to a non-constant mass scenario that slightly deviates from the assumptions typically used in analytical orbital computations. Notably, the mass decreased by approximately 24.999 kg from an initial total of 25 kg following the thrust application. Additionally, these discrepancies may stem from mass variations or possibly the numerical integration method employed in the orbital computations.

Significant adjustments were also noted in *pom*. Table 3.7 details a comparative analysis between analytical predictions and simulated results. Figure 3.9 illustrates the changes in classical Keplerian orbital elements before and after the thrust application.

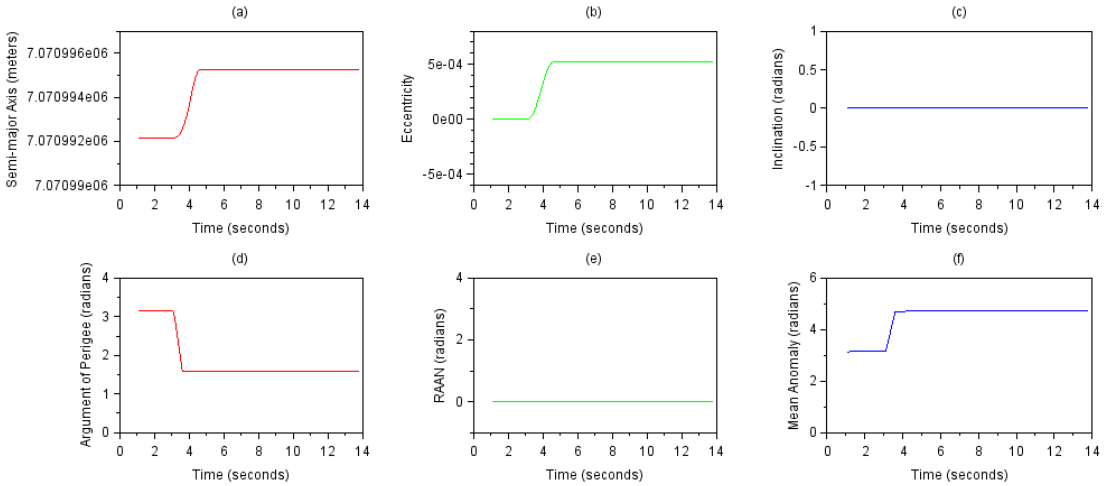

Figure 3.9.: Comparative analysis of Keplerian orbital elements before and after the application of 100 N thrust in the positive radial direction, highlighting the variations in semi-major axis, eccentricity, and longitude of the periapsis.

Orbital Elements	a (m)	e	i (rad)	pom (rad)	RAAN (rad)	M (rad)
Initial Conditions	7070992.17	0.0	0.0	3.14159	0.0	3.14159
Analytical Calculations	7070994.17	0.00053276	0.0	0.0	0.0	2.8906
Simulation Results (Isp = 10^6 seconds)	7070995.26251	0.00052	0.0	1.57641	0.0	4.72215

Table 3.7.: Comparative analysis of orbital elements before and after the application of a 100 N thrust in Test 4. The table presents initial conditions, analytical calculations, and simulation results, illustrating minor changes in semi-major axis and expected adjustments in eccentricity. The variations in *pom* and M are shown, along with their corresponding I_{sp} set at 1,000,000 seconds for these simulations.

Summary of Thruster Operation Tests

Test 1: Maneuver in Positive Flight Direction

- **Objective:** To assess the impact of a 100 Newton thrust in the flight direction on the semi-major axis and eccentricity of the orbit.
- **Expected Outcome:** A significant alteration in the semi-major axis and a nominal change in eccentricity.
- **Results:** The semi-major axis increased by approximately 1 meter from the analytical prediction, confirming the expected influence of the thrust. Eccentricity closely aligned with theoretical expectations.
- **Analysis:** Minor discrepancies in semi-major axis highlight the complexity of real-world orbital dynamics compared to theoretical models.

Test 2: Increased Thrust and Specific Impulse (Isp) in Flight Direction

- **Objective:** To evaluate the effects of a 1000 Newton thrust on orbital elements under increased propulsive force.
- **Expected Outcome:** Significant modifications in the semi-major axis and eccentricity.
- **Results:** Results were consistent with analytical calculations, showing a notable increase in semi-major axis and eccentricity. The adjustments in other orbital elements, such as argument of perigee and mean anomaly, highlighted the sensitivity of orbital dynamics to thrust changes.
- **Analysis:** The results affirmed the model's accuracy under conditions of increased thrust and specific impulse.

Test 3: Thrust Application in Negative Orbit Normal Direction

- **Objective:** To investigate the effects of 100 N thrust against the orbit normal on inclination and RAAN.
- **Expected Outcome:** Significant changes in inclination and RAAN, with minor adjustments to the semi-major axis.
- **Results:** Inclination and RAAN altered significantly as expected, with very slight changes in the semi-major axis and eccentricity remaining stable.
- **Analysis:** The minor variance in semi-major axis from the analytical predictions was attributed to slight mass changes from fuel consumption, demonstrating the non-constant mass scenario's impact on orbital elements.

Test 4: Thrust Application in Positive Radial Direction

- **Objective:** To determine the influence of 100 N thrust in the positive radial direction on eccentricity and semi-major axis.
- **Expected Outcome:** Notable changes in eccentricity with minor deviations in the semi-major axis.
- **Results:** The semi-major axis and eccentricity changed slightly from the analytical predictions. Significant alterations were also noted in the longitude of the periapsis.
- **Analysis:** The discrepancies noted between simulated and analytical results were linked to mass variations and possibly the numerical integration method used, underlining the challenges of applying theoretical models to real-world scenarios.

Several factors could explain the discrepancies between the simulation results and analytical predictions. These discrepancies underscore the complexities involved in dynamically simulating orbital mechanics, particularly when applying theoretical models to practical scenarios.

1. **Mass Variation:** The reduction in spacecraft mass over time due to fuel consumption leads to an increase in acceleration. This dynamic change results in more pronounced variations in the simulation outcomes compared to the static analytical predictions. Such effects were consistently observed across most test scenarios.
2. **Control Delays:** The introduction of a delay block, specifically a 0.1-second delay, likely impacted the application of thrust. This delay causes the transformed thrust vector in the LVLH frame to misalign when translated into the ECI frame. Consequently, there is a 0.1 second lag in thrust application in the ECI frame, affecting the spacecraft's trajectory and velocity.
3. **Thrust Vector Misalignment:** A minor but significant component of thrust was lost in directions where no thrust was intended. This misalignment between the thrust vectors in the LVLH and ECI frames contributed significantly to the deviations observed. The unintended thrust directions typically resulted from inaccuracies in thrust vector transformation or from external perturbations not accounted for in the analytical model.

4. Control Design and Implementation

This chapter is dedicated to the development and analysis of two control strategies designed for the management of spacecraft relative motion: the Linear Quadratic Regulator (LQR) and the Clohessy-Wiltshire (CW) based trajectory control method. The fundamental aim of these control systems is to efficiently regulate the trajectory of a chaser spacecraft relative to a designated target within space, facilitating both rendezvous and station-keeping operations.

The LQR approach is grounded in classical control theory, focusing on optimizing a cost function that judiciously balances the trade-off between state error minimization and control effort. Noted for its robustness and efficacy, LQR ensures optimal performance under strict operational criteria, making it indispensable for precision tasks like target approach and stable relative positioning (Levine, 1996; Ogata, 1998).

Conversely, the CW-based trajectory control method employs inverse matrix computations to accurately determine the velocities needed for the chaser spacecraft to achieve and maintain proximity to the target. This method provides a straightforward approach to control, offering clear solutions to motion planning and control challenges in orbital mechanics for rendezvous and station-keeping (Clohessy & Wiltshire, 1960a; Sullivan & Atkins, 2013).

Recent developments integrate these traditional control methods with modern computational strategies, such as sliding mode control for handling uncertainties and disturbances in system dynamics, enhancing the robustness and reliability of the control systems (Du et al., 2016; Richter, 2011). Moreover, advances in propulsion technology, particularly electric propulsion, have refined the precision of control strategies. These systems offer continuous thrust capabilities, crucial for the fine adjustments required by sophisticated control models like LQR and CW (Brown & Smith, 2019; Michael & Farrar, 1974).

Both control strategies are pivotal in showcasing the effectiveness of advanced control techniques within the domain of complex aerospace applications. They provide a robust framework for achieving precise, reliable, and efficient maneuvering capabilities, which are essential for the success of contemporary and future space missions. This chapter will detail the theoretical foundations of these controllers, elucidate their implementation, and evaluate their performance through simulation studies, highlighting their applicability to both initial approach maneuvers and long-term positional maintenance in orbit.

4.1. Clohessy-Wiltshire Dynamics and LQR Control Design

The Clohessy-Wiltshire (CW) equations, integral to understanding relative motion in orbital mechanics, specifically address spacecraft station-keeping, rendezvous, and

docking maneuvers. Developed by W.H. Clohessy and R.S. Wiltshire in 1960 (Clohessy & Wiltshire, 1960b), these equations extend earlier work by George William Hill in 1878 (Hill, 1878). The CW framework models the motion between a target satellite in a stable circular orbit and a chaser satellite experiencing small deviations (Curtis, 2014), (Starek et al., 2017).

4.1.1. CW Equations and System Dynamics

Defined within a Local Vertical Local Horizontal (LVLH) frame, the CW equations are expressed as:

$$\ddot{x} = 3n^2 x + 2n\dot{y}, \tag{4.1}$$

$$\ddot{y} = -2n\dot{x}, \tag{4.2}$$

$$\ddot{z} = -n^2 z, \tag{4.3}$$

where $n = \sqrt{\mu/a^3}$ represents the mean motion, μ is the gravitational parameter, and a is the orbital radius. The dynamics outlined by these equations demonstrate critical aspects of motion: radial acceleration, Coriolis effects in the tangential direction, and simple harmonic motion out of the orbital plane (Vallado & McClain, 2017).

4.1.2. LQR Strategy for Orbital Rendezvous and Station-Keeping

Building on the CW equations, the LQR provides a robust control approach by minimizing a quadratic cost function of the state errors and control inputs. This section delineates the formulation of an LQR strategy designed to enhance rendezvous and station-keeping operations within the described dynamics.

To implement LQR, the state-space representation is constructed with the state vector $\mathbf{x} = [x, \dot{x}, y, \dot{y}, z, \dot{z}]^T$ and the control inputs $\mathbf{u}$, resulting in:

$$\dot{\mathbf{x}} = A\mathbf{x} + B\mathbf{u}, \tag{4.4}$$

where:

$$A = \begin{bmatrix} 0 & 1 & 0 & 0 & 0 & 0 \\ 3n^2 & 0 & 0 & 2n & 0 & 0 \\ 0 & 0 & 0 & 1 & 0 & 0 \\ 0 & -2n & 0 & 0 & 0 & 0 \\ 0 & 0 & 0 & 0 & 0 & 1 \\ 0 & 0 & 0 & 0 & -n^2 & 0 \end{bmatrix}, \quad B = \begin{bmatrix} 0 & 0 & 0 \\ 1 & 0 & 0 \\ 0 & 0 & 0 \\ 0 & 1 & 0 \\ 0 & 0 & 0 \\ 0 & 0 & 1 \end{bmatrix}. \tag{4.5}$$

The LQR's objective is to minimize:

$$J = \int_0^\infty (\mathbf{x}^T Q \mathbf{x} + \mathbf{u}^T R \mathbf{u})\, dt, \tag{4.6}$$

with Q and R as the state and control input weighting matrices, respectively. The optimal control $\mathbf{u} = -K\mathbf{x}$ is derived where K is computed by solving the Algebraic Riccati Equation (ARE).

Implementing this LQR controller within a spacecraft's guidance system allows for automatic adjustment of thrust commands to maintain precise orbit trajectories. The effectiveness of these combined methodologies in optimizing maneuver performance while minimizing resource expenditure marks a significant advancement in orbital mechanics and control systems design.

4.2. Trajectory Control with Clohessy-Wiltshire Methods

This section discusses the application of the Clohessy-Wiltshire (CW) equations for trajectory control in spacecraft rendezvous and station-keeping, within a real-time simulation environment. The methodology exploits inverse dynamics to compute necessary maneuvers, ensuring the spacecraft achieves and maintains the desired trajectory relative to its target.

The CW equations are pivotal in modeling the relative motion between two spacecraft orbiting within close proximity. These equations serve as the foundation for predicting and controlling relative positions and velocities through state transition matrices.

4.2.1. State Transition Matrices

State transition matrices derived from the CW equations delineate how changes in the spacecraft's position and velocity evolve due to applied thrusts. The spacecraft's state at any time t can be forecasted from its initial state using these matrices:

$$\vec{\gamma}(t) = \Phi_{11}(t)\vec{\gamma}(t_0) + \Phi_{12}(t)\vec{v}(t_0), \tag{4.7}$$

where:

- $\vec{\gamma}(t)$ represents the state vector at time t, comprising position and velocity components,
- $\vec{\gamma}(t_0)$ and $\vec{v}(t_0)$ are the initial position and velocity vectors,
- $\Phi_{11}(t)$ and $\Phi_{12}(t)$ are sub-matrices of the state transition matrix $\Phi(t)$ corresponding to position and velocity transitions.

The relative motion is further characterized by four essential sub-matrices within the CW

framework: $M(t)$, $N(t)$, $S(t)$, and $T(t)$, which relate the initial states to future states:

$$M = \begin{bmatrix} 4 - 3\cos(n\delta t) & 0 & 0 \\ 6(\sin(n\delta t) - n\delta t) & 1 & 0 \\ 0 & 0 & \cos(n\delta t) \end{bmatrix}, \tag{4.8}$$

$$N = \begin{bmatrix} \frac{1}{n}\sin(n\delta t) & \frac{2}{n}(1 - \cos(n\delta t)) & 0 \\ \frac{2}{n}(\cos(n\delta t) - 1) & \frac{1}{n}(4\sin(n\delta t) - 3n\delta t) & 0 \\ 0 & 0 & \frac{1}{n}\sin(n\delta t) \end{bmatrix}, \tag{4.9}$$

$$S = \begin{bmatrix} 3n\sin(n\delta t) & 0 & 0 \\ -6n(1 - \cos(n\delta t)) & 0 & 0 \\ 0 & 0 & -n\sin(n\delta t) \end{bmatrix}, \tag{4.10}$$

$$T = \begin{bmatrix} \cos(n\delta t) & 2\sin(n\delta t) & 0 \\ -2\sin(n\delta t) & 4\cos(n\delta t) - 3 & 0 \\ 0 & 0 & \cos(n\delta t) \end{bmatrix}. \tag{4.11}$$

4.2.2. Optimizing Control for Trajectory Management

The trajectory controller aims to minimize the deviation between the chaser spacecraft's current state and a predefined trajectory. The desired initial velocity $\vec{v}_d(t_0)$ is computed such that the chaser reaches the target position $\vec{\delta r}_d(t_0)$ at a future time $t_0 + \Delta t$:

$$\vec{v}_d(t_0) = N^{-1}(t_0)(\vec{\delta r}_d(t_0) - M(t_0)\vec{\delta r}(t_0)), \tag{4.12}$$

where $M(t_0)$ and $N(t_0)$ are dynamically computed from the CW equations.

The required velocity increment $\Delta\vec{V}$ is then calculated as the difference between this desired velocity and the chaser's current velocity:

$$\Delta\vec{V} = \vec{v}_d(t_0) - \vec{v}_r(t_0), \tag{4.13}$$

where $\vec{v}_r(t_0)$ represents the current velocity of the chaser spacecraft.

In the simulation, this $\Delta\vec{V}$ is used to update the spacecraft's acceleration, ensuring trajectory correction:

$$\vec{a} = \frac{\Delta\vec{V}}{\delta t}, \tag{4.14}$$

where δt is the interval over which the correction is applied.

The control logic is integrated within the Scilab and Xcos simulation environments, providing real-time feedback and updates on the spacecraft's state based on the CW model and computed control inputs.

The trajectory control strategy based on the CW equations and inverse dynamics proficiently navigates the spacecraft to its target, dynamically adjusting its velocity to follow the optimal path. This method significantly enhances the efficiency and safety of space missions, effectively managing both rendezvous and station-keeping maneuvers with minimal deviations.

4.3. Analysis of Non-linear Test Setup

4.3.1. Overview of the Non-linear Test Configuration

The non-linear test configuration has been designed to replicate the dynamics of a chaser spacecraft in relation to a target spacecraft. Figure 4.1 delineates a comprehensive schematic of the test configuration, illustrating both spacecraft equipped with subsystems such as thrusters, frame conversion units, and GNSS receivers, which collectively enhance the simulation's fidelity to actual space conditions. The dynamic interplay between the spacecraft is calculated within the CW frame, pivotal for accurately modelling the relative motions.

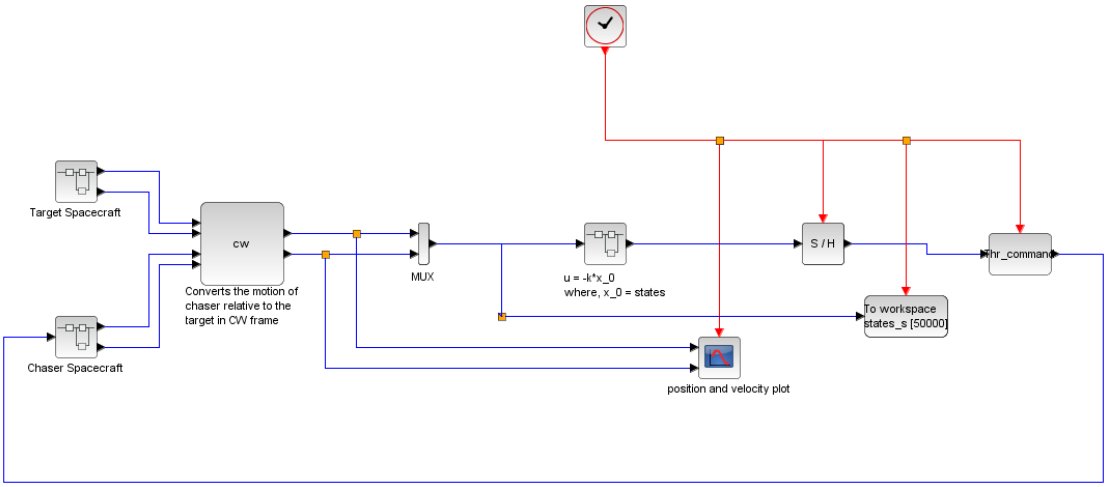

Figure 4.1.: Diagram illustrating the non-linear test set-up for spacecraft interaction analysis, showing subsystems for both the target and chaser spacecraft. This configuration includes GNSS receivers, thruster controls, and frame conversion from LVLH to ECI. The diagram emphasizes the use of the CW frame for simulation of relative motion, with inputs of position and velocity in ECI coordinates and outputs that detail the dynamics within the CW frame.

Inputs to the CW computation block include the position and velocity vectors of both spacecraft in the ECI frame. The outputs are the relative position and velocity of the

chaser with respect to the target, also expressed in the CW frame, which is discussed in detail in section 4.3.2.

The specific configurations of each spacecraft are visually represented in schematics detailing their subsystem layouts, as shown in Figure 4.2. Notably, both spacecraft comprise analogous subsystem blocks such as Thruster Models, Frame Conversion, and GNSS Receivers, yet they differ in their respective orbital positions and velocities, detailed as follows:

- **Target Spacecraft:**
  - Position: [7071000, 0, 0] meters
  - Velocity: [0, 7508.07270064, 0] meters/second
- **Chaser Spacecraft:**
  - Position: [7070929.29, 0, 0] meters
  - Velocity: [0, 7508.14778174, 0] meters/second

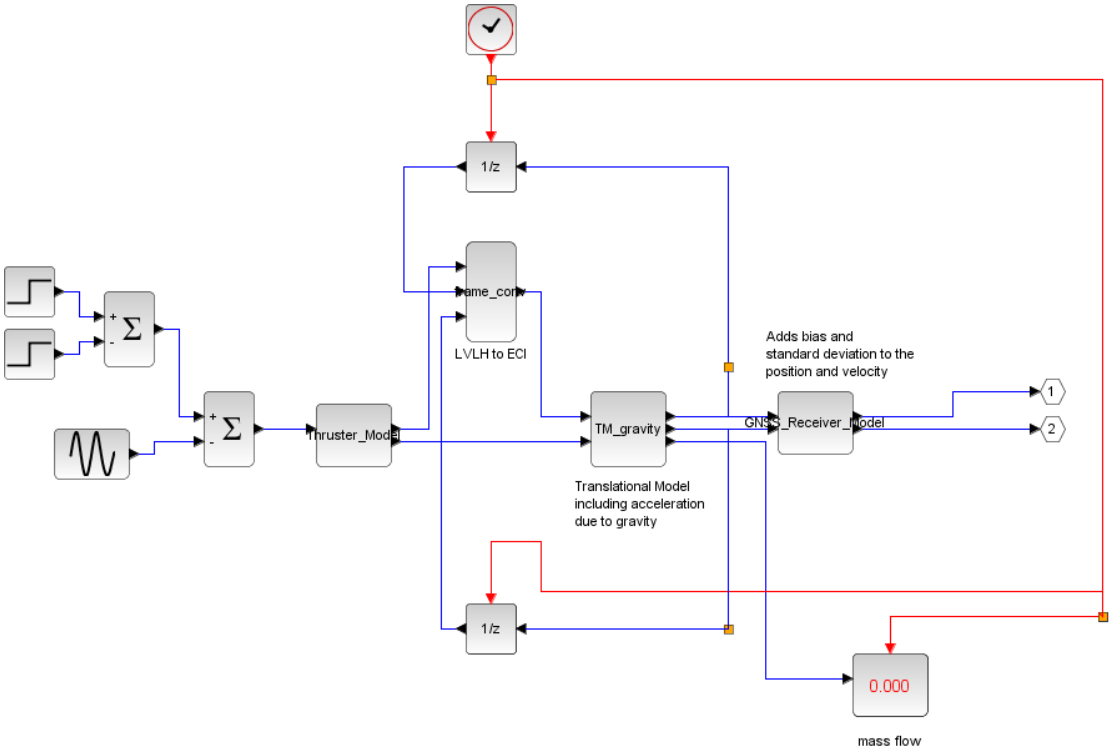

Figure 4.2.: Diagram of the target spacecraft's control architecture, depicting the integration of thruster models, frame transformation from LVLH to ECI, and GNSS receivers. The schematic details the signal and data flow throughout the system.

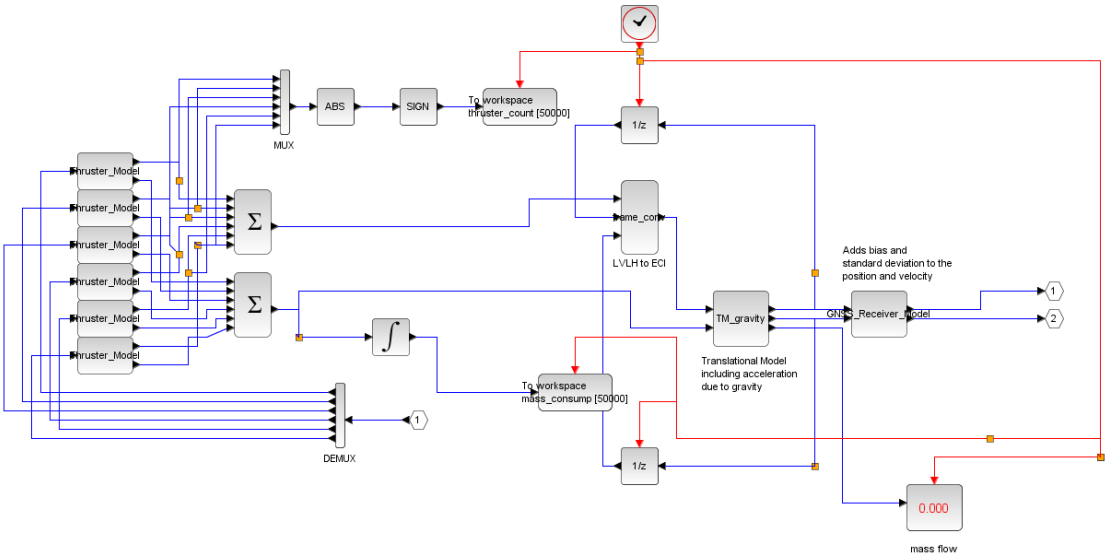

Figure 4.3.: Schematic of the chaser spacecraft's control system depicting the integration of multiple thruster modules, the conversion of coordinate frames from LVLH to ECI, and the incorporation of a GNSS receiver.

4.3.2. Simulation of Relative Motion

Figures 4.4a and 4.4b depict the simulated trajectories of the relative motion between the chaser and target spacecraft, showcasing both two-dimensional and three-dimensional views. These visualizations confirm the expected elliptical paths, indicative of typical orbital dynamics, and are consistent with the representations shown in Figure 4.4.

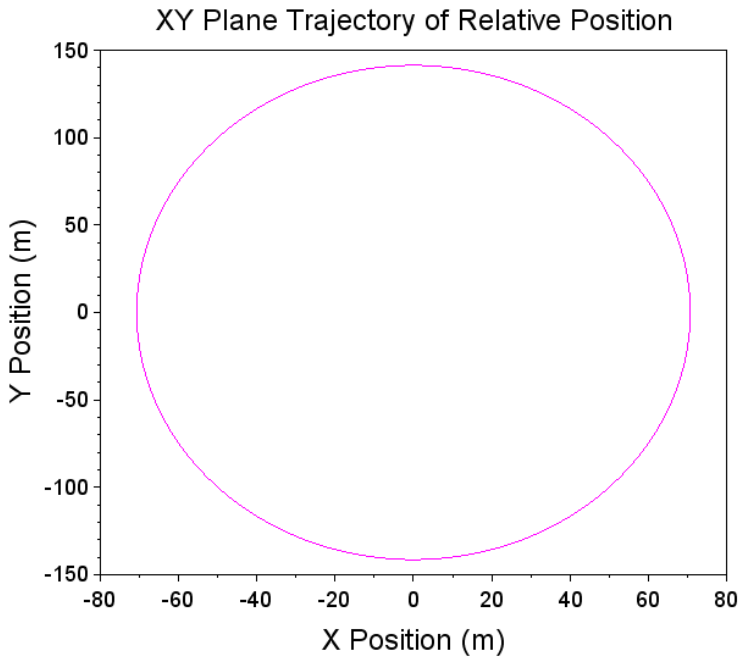

(a) 2D trajectory of the relative position, showing the elliptical path in the XY plane.

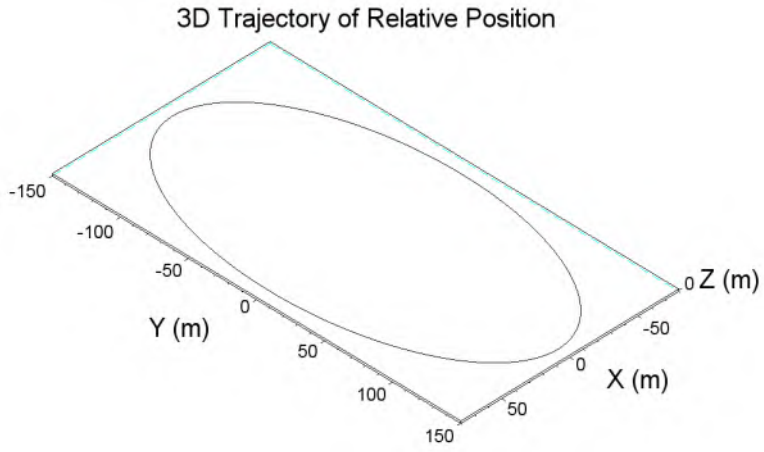

(b) 3D trajectory of the relative position, depicting the orbital path in three-dimensional space.

Figure 4.4.: Simulated trajectories of the relative position in the non-linear test setup: (a) two-dimensional and (b) three-dimensional trajectories.

The plots of relative velocity further elucidate the dynamics of interaction between the chaser and target spacecraft. Figure 4.5 illustrates a consistent orbital velocity pattern, affirming the CW block's effective simulation capabilities.

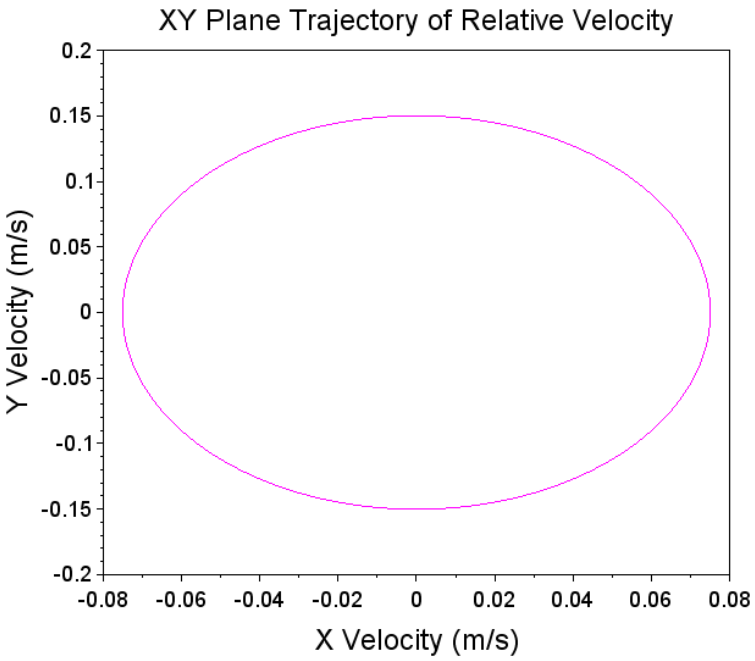

Figure 4.5.: Two-dimensional plot of the relative velocity between spacecraft, demonstrating the cyclical velocity variations within the orbital plane.

4.4. Application of CLSS block in Simulation

This section describes the implementation of the CLSS block in the trajectory control simulation of the spacecraft rendezvous and station-keeping problem. The CLSS block, a fundamental component of the continuous-time systems palette, realizes a continuous-time linear state-space system which is crucial for modeling and simulating dynamic systems in real-time.

4.4.1. Overview of CLSS Block

The CLSS block models the dynamics of a system through the state-space representation where the state equation is given by:

$$\dot{x} = Ax + Bu, \tag{4.15}$$

and the output equation is:

$$y = Cx + Du, \tag{4.16}$$

where:

- x is the vector of state variables (positions and velocities),
- u is the vector of input functions (control inputs or external forces),
- y is the vector of output variables (observable outputs),

- A, B, C, and D are matrices defining the system dynamics and interactions.

4.4.2. System Configuration

In the context of spacecraft trajectory control, the CLSS block is configured to simulate the relative motion of a chaser spacecraft with respect to a target. The configuration of the matrices A, B, C, and D and the initial state X_0 are specifically tailored to reflect the dynamics of spacecraft motion under the influence of control thrusters and the gravitational environment:

- The matrix A is designed based on the linearized relative motion dynamics as described by the Clohessy-Wiltshire equation 4.5:
- The matrix B models the input from the thrusters (Equation: 4.5):
- The matrix C allows the observation of both position and velocity:

$$C = \begin{bmatrix} 1 & 0 & 0 & 0 & 0 & 0 \\ 0 & 1 & 0 & 0 & 0 & 0 \\ 0 & 0 & 1 & 0 & 0 & 0 \\ 0 & 0 & 0 & 1 & 0 & 0 \\ 0 & 0 & 0 & 0 & 1 & 0 \\ 0 & 0 & 0 & 0 & 0 & 1 \end{bmatrix}$$

- The matrix D is typically zero as it represents the direct feed-through of the input to the output, which is not applicable in this scenario.

4.4.3. Initial State and Dynamics

The initial state of the system initialState $= [x_0, y_0, z_0, vx_0, vy_0, vz_0]$ is configured based on the chaser spacecraft's initial position and velocity, derived from its orbital parameters to align with the intended rendezvous and station-keeping trajectory:

- Initial position coordinates x_0, y_0, z_0 are set to zero, aligning the simulation start with the target's reference frame.
- Initial velocity components are defined as follows:

$$\begin{aligned} vx_0 &= \frac{ny_0}{2}, \quad \text{(along x)} \\ vy_0 &= \frac{nx_0}{2}, \quad \text{(along y)} \\ vz_0 &= \frac{nz_0}{2} \quad \text{(along z)} \end{aligned}$$

  These velocities initiate stable orbital movements or corrective maneuvers.

4.4.4. Analysis of Relative Motion

This section highlights the precision of the CLSS block in mirroring the dynamics observed in the non-linear test setup, using identical initial conditions. The trajectory graphs of the chaser spacecraft relative to the target effectively demonstrate the CLSS block's capability to accurately simulate anticipated orbital movements.cv

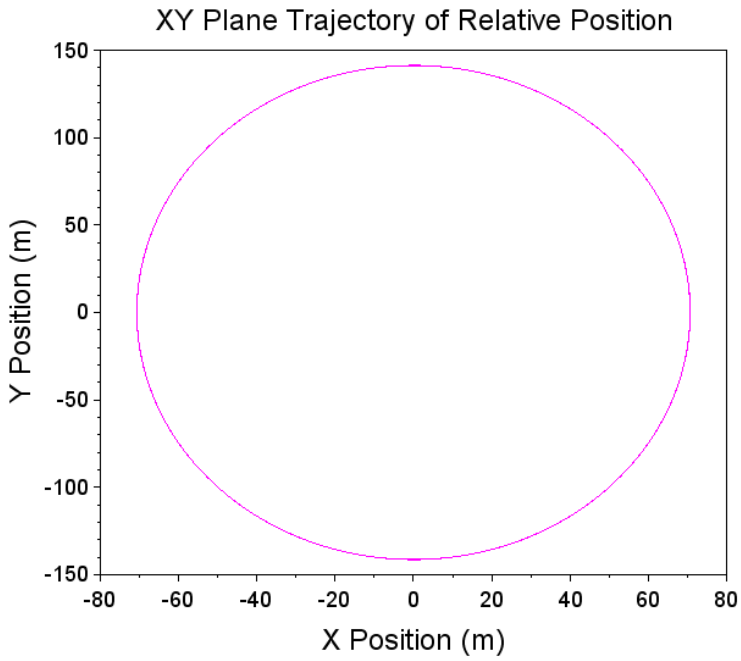

(a) 2D plot of the chaser's trajectory relative to the target, demonstrating the orbital path in the XY plane.

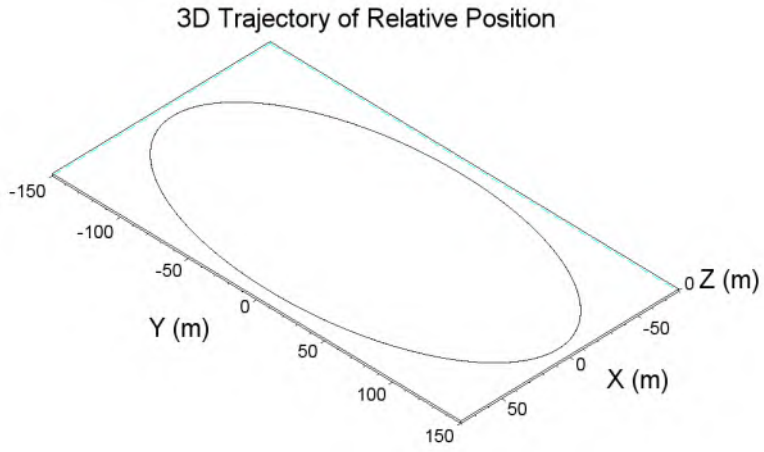

(b) 3D plot of the relative trajectory, illustrating the spatial path of the chaser around the target.

Figure 4.6.: Comparative analysis of the chaser's trajectory relative to the target, displayed in both 2D and 3D plots to highlight the orbital and spatial dynamics involved.

The velocity profile analysis corroborates the model's capability to accurately depict the dynamic response of the chaser spacecraft relative to the target.

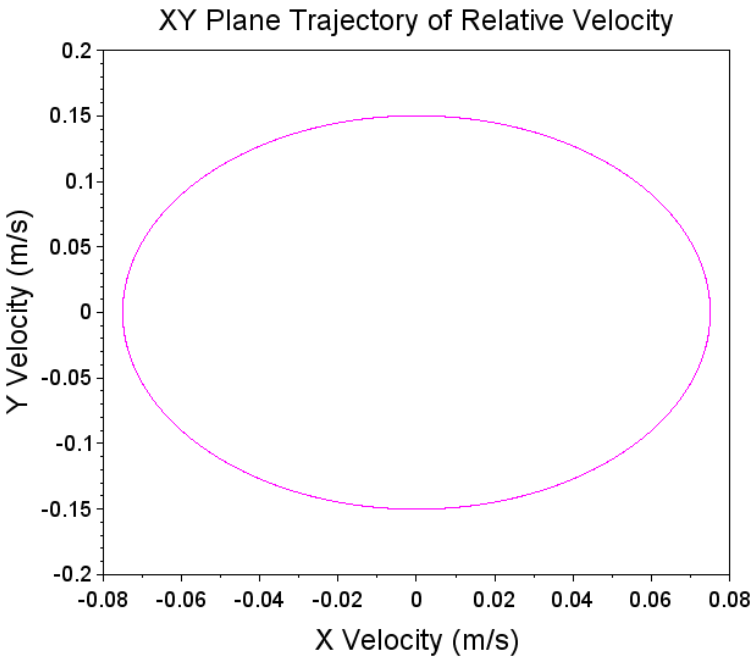

Figure 4.7.: 2D velocity plot of the chaser, showing speed variations over time and validating the control response dynamics.

The position and velocity trajectories observed mirror those in the non-linear setup described in Section 4.3.2. The simulations employing the CLSS block demonstrated a significant reduction in processing time compared to the non-linear test setup. This finding confirms the efficiency of the CLSS block, especially when integrated with LQR and CW-based trajectory controllers, in accelerating simulation processes and enhancing the computational efficiency for dynamic testing environments. Consequently, to further validate the controllers, the CLSS blocks will be utilized for target tests and Monte Carlo simulations, leveraging their speed advantages for more efficient testing outcomes.

4.5. Analysis of Targeted Control Tests

The initial relative position of the chaser satellite, in relation to the target satellite, is established in Cartesian coordinates for individual tests. As detailed in Section 4.4.3, the starting coordinates are set as:

$$[x_0; y_0; z_0] = [200; 100; 100] \text{ meters}$$

This setup positions the chaser satellite 200 meters along the x-axis, 100 meters along the y-axis, and 100 meters along the z-axis relative to the target. Each simulation runs over a duration corresponding to three orbital periods, totaling 17,752.26 seconds. This duration is consistently applied across all simulations in the targeted control tests. The test setup for the individual tests can be seen in Figure 4.8.

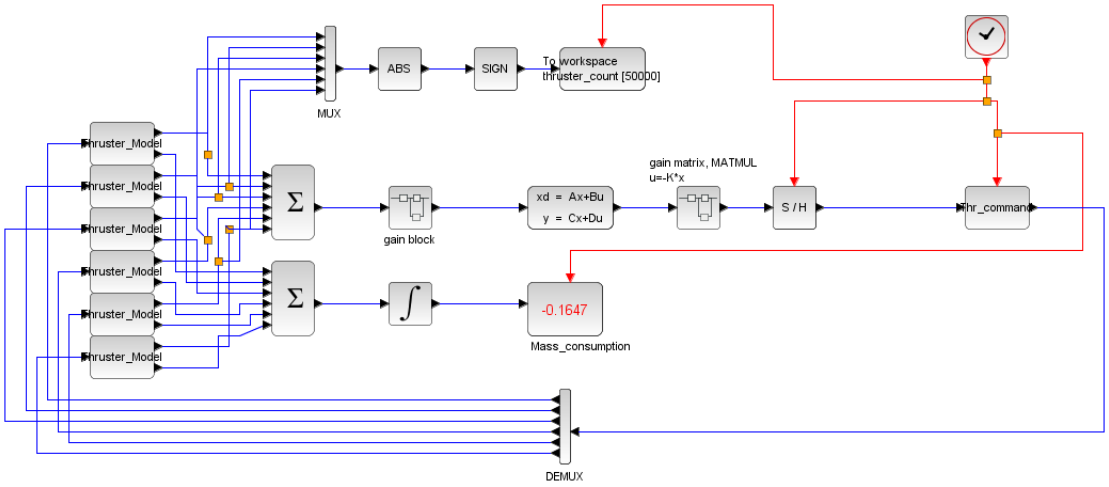

Figure 4.8.: Detailed schematic of the test set-up for evaluating the LQR controller's performance. This diagram illustrates the integration of thruster models, control logic, and signal processing components.

A series of evaluations are conducted on two different controllers to identify the most effective tuning parameters for each. Adjustments to the Q and R matrices are explored within the LQR controller settings, while variations in the time to target (Δt) are tested for the CW controller. The performance of these tests is assessed by measuring fuel consumption and the frequency of thruster activations. These experiments yield valuable insights into the performance and efficiency of the varied controller configurations.

4.5.1. LQR Test Scenarios

Test Case 1

In this test case, the weighting matrices Q and R are configured to prioritize position accuracy over velocity accuracy, with substantial emphasis placed on minimizing control effort. The matrix Q, which assigns higher weights to position components than to velocity components, is defined as:

$$Q = \begin{bmatrix} 10 & 0 & 0 & 0 & 0 & 0 \\ 0 & 10 & 0 & 0 & 0 & 0 \\ 0 & 0 & 10 & 0 & 0 & 0 \\ 0 & 0 & 0 & 1 & 0 & 0 \\ 0 & 0 & 0 & 0 & 1 & 0 \\ 0 & 0 & 0 & 0 & 0 & 1 \end{bmatrix} \qquad R = \begin{bmatrix} 1000 & 0 & 0 \\ 0 & 1000 & 0 \\ 0 & 0 & 1000 \end{bmatrix}$$

Dynamics and Results:

The simulation results indicate that it takes approximately 2000 seconds for the chaser spacecraft to reach the target in the x-direction, 1300 seconds in the y-direction, and 1000 seconds in the z-direction. These dynamics are illustrated in Figures 4.9, 4.10a, and 4.10b.

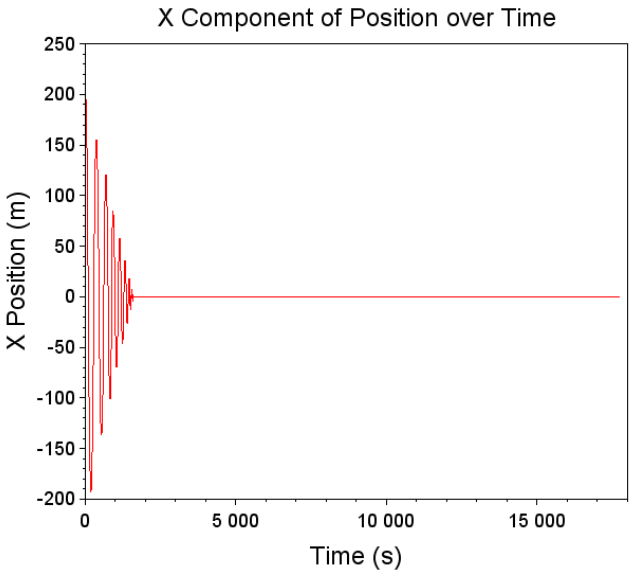

Figure 4.9.: Precision in directional control along the x-axis over time for Test Case 1 using the LQR controller.

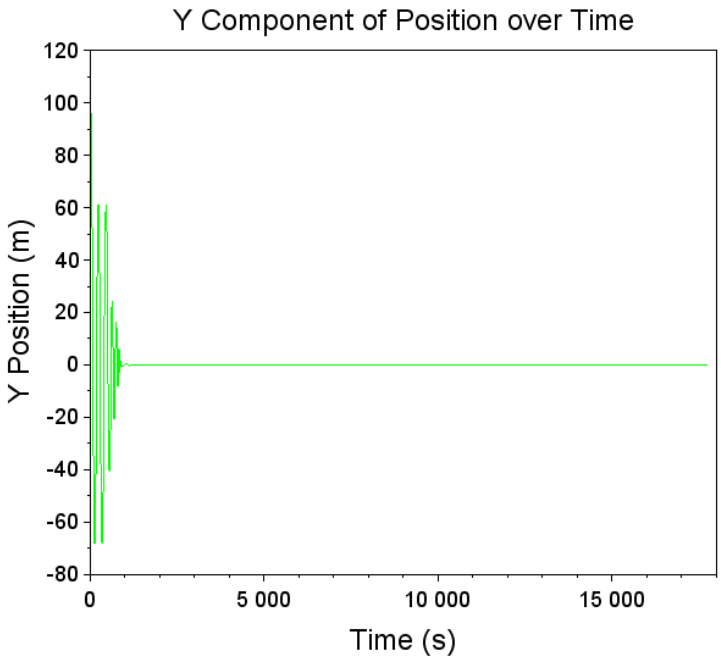

(a) Effective maneuvering adjustments along the y-axis over time for Test Case 1 using the LQR controller.

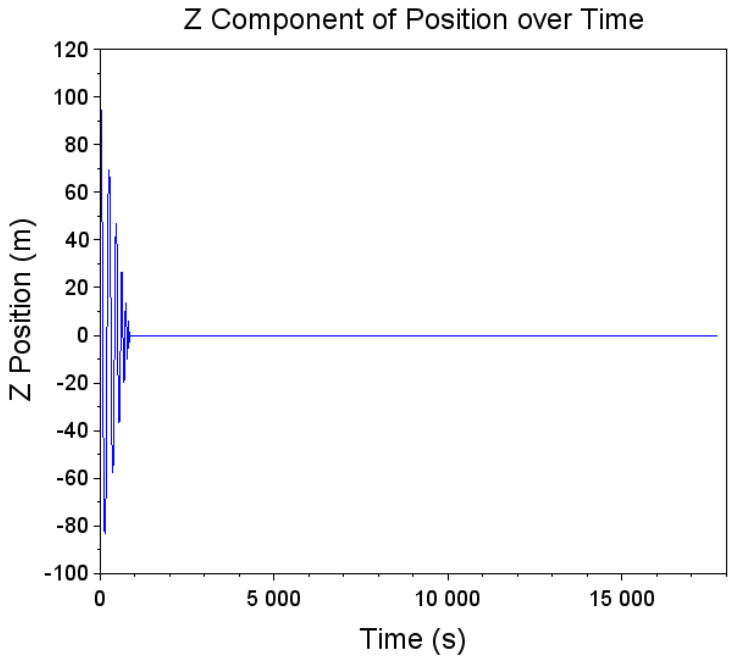

(b) Demonstration of altitude control capabilities along the z-axis over time for Test Case 1 using the LQR controller.

Figure 4.10.: Comparative analysis of maneuvering adjustments and altitude control along the y-axis and z-axis using the LQR controller in Test Case 1, illustrating the controller's effectiveness in multi-axis stabilization.

The 2D plots for position and velocity over three orbital periods are depicted in Figure 4.11, and 4.12, providing insights into the trajectory dynamics and control response. Additionally, the 3D trajectory plot, as shown in Figure 4.13, provides a comprehensive visualization of the spacecraft's path through space.

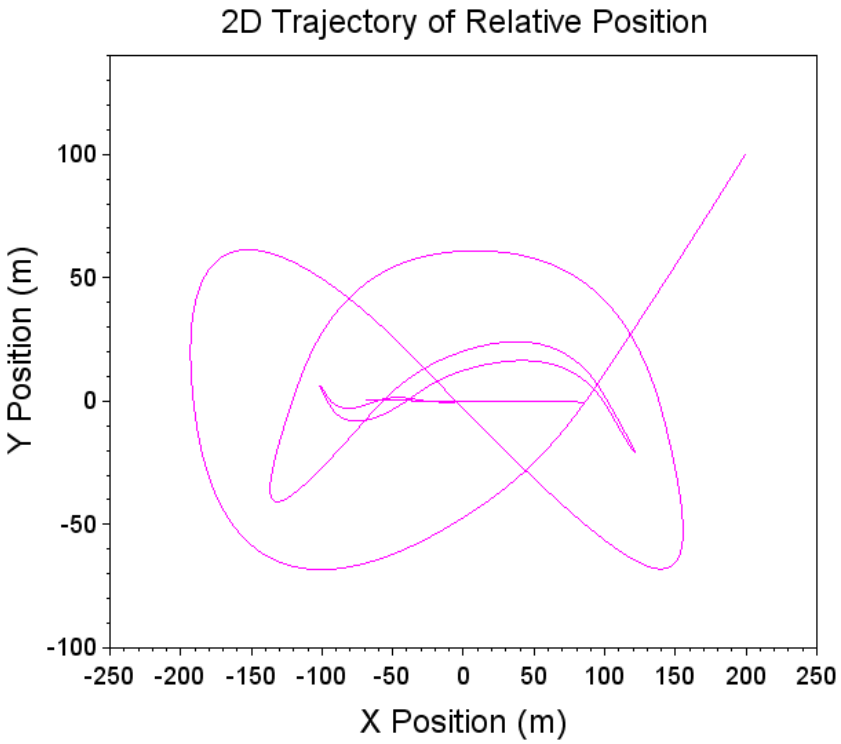

Figure 4.11.: 2D trajectory plot for Test Case 1 under LQR control, demonstrating the spacecraft's positional adjustments.

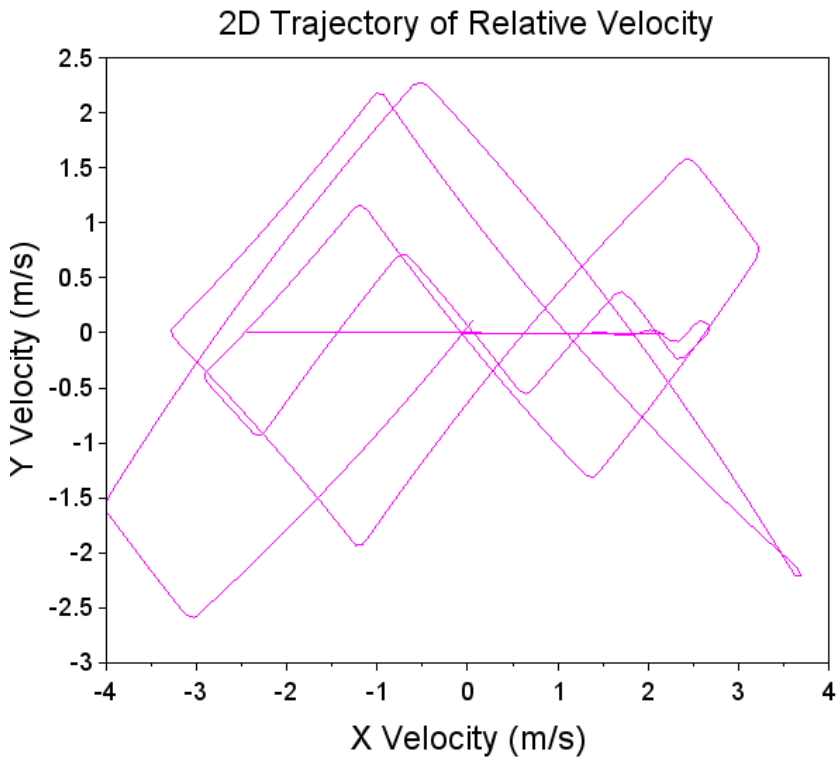

Figure 4.12.: 2D velocity plot for Test Case 1 under LQR control, illustrating the control effects on spacecraft velocity.

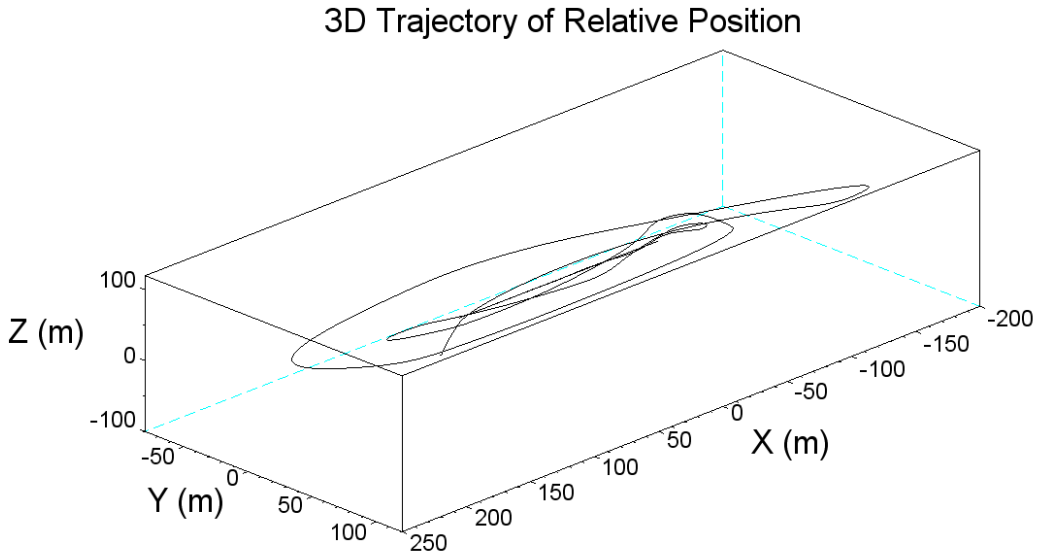

Figure 4.13.: Three-dimensional trajectory visualization for Test Case 1 using the LQR controller, depicting the dynamic path across the x, y, and z coordinates during the control test.

Analysis of the control effort reveals that the maximum thruster firings occur for the positive y-direction thruster, totaling 337 activations. In contrast, the least number of firings is observed for the negative z-direction thruster, with a total of 189 activations, as depicted in the bar plot in Figure 4.14. Overall, the complete array of six thrusters has been activated a cumulative total of 1605 times.

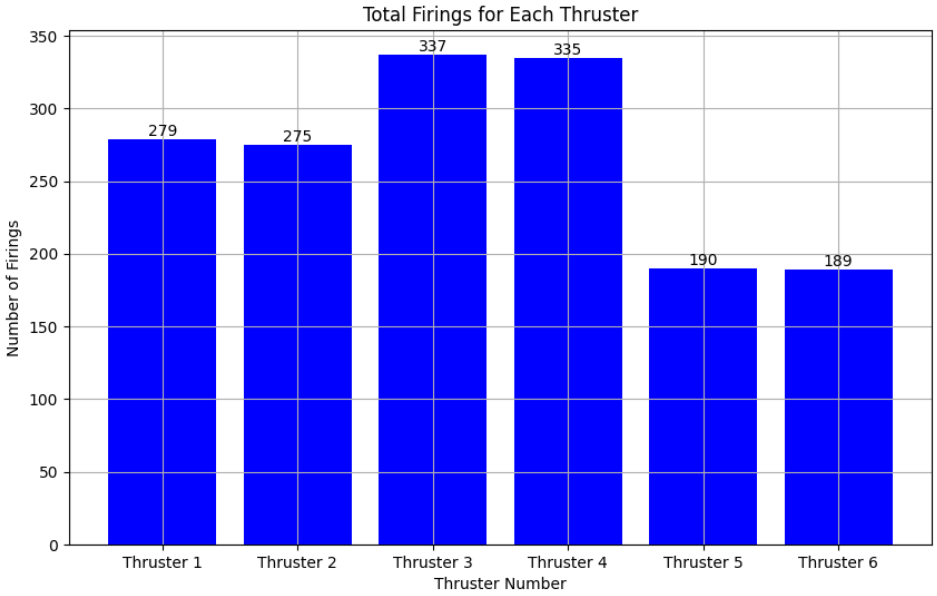

Figure 4.14.: Bar graph detailing the frequency of thruster activations for Test Case 1 under LQR control, illustrating the distribution of control effort across different axes during the simulation.

The fuel consumption for this test case amounts to 3.5 kg, which is 70% of the total 5 kg allocated for the duration of the simulation, lasting 17752.26 seconds. This metric underlines the efficiency and challenges of the control strategy under the defined weight settings.

Test Case 2: Velocity Control Optimization

In contrast to the first test case, Test Case 2 assesses the implications of emphasizing velocity stabilization, with equal emphasis on control effort optimization. The definition of the weighting matrices Q and R is as follows:

$$Q = \begin{bmatrix} 1 & 0 & 0 & 0 & 0 & 0 \\ 0 & 1 & 0 & 0 & 0 & 0 \\ 0 & 0 & 1 & 0 & 0 & 0 \\ 0 & 0 & 0 & 1000 & 0 & 0 \\ 0 & 0 & 0 & 0 & 1000 & 0 \\ 0 & 0 & 0 & 0 & 0 & 1000 \end{bmatrix} \quad R = \begin{bmatrix} 1000 & 0 & 0 \\ 0 & 1000 & 0 \\ 0 & 0 & 1000 \end{bmatrix}$$

Experimental Outcomes:

- *Fuel Efficiency*: Only 0.4 kg of the allocated 5 kg of fuel was consumed during the maneuver.

- *Spacecraft Mass*: Total mass remains constant at 25 kg.

- *Trajectory Characterization*: The spacecraft approached the target through a direct linear path, avoiding the spiral trajectory noted in the previous test case.

The inversion of velocity component weights in the Q matrix relative to Test Case 1 facilitated rapid velocity corrections, advantageous for executing swift maneuvers in less critical trajectory paths. Uniform weights in the R matrix ensured that control efforts were optimized, mitigating excessive fuel expenditure.

- *Temporal Dynamics*: The spacecraft required 200-300 seconds to align with the target along the x-axis, effectively demonstrated in Figure 4.15, and 100-150 seconds for alignments along the y and z-axes, as shown in Figures 4.16 and 4.17 respectively. This temporal analysis highlights the efficiency and precision of the control strategies implemented.

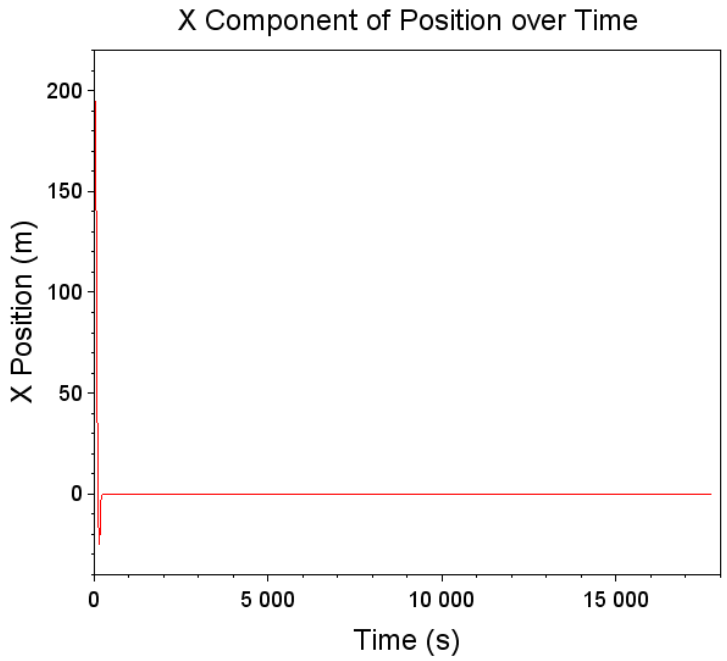

Figure 4.15.: X-axis alignment: Showcases the LQR control's efficiency in stabilizing the spacecraft along the x-direction for Test Case 2.

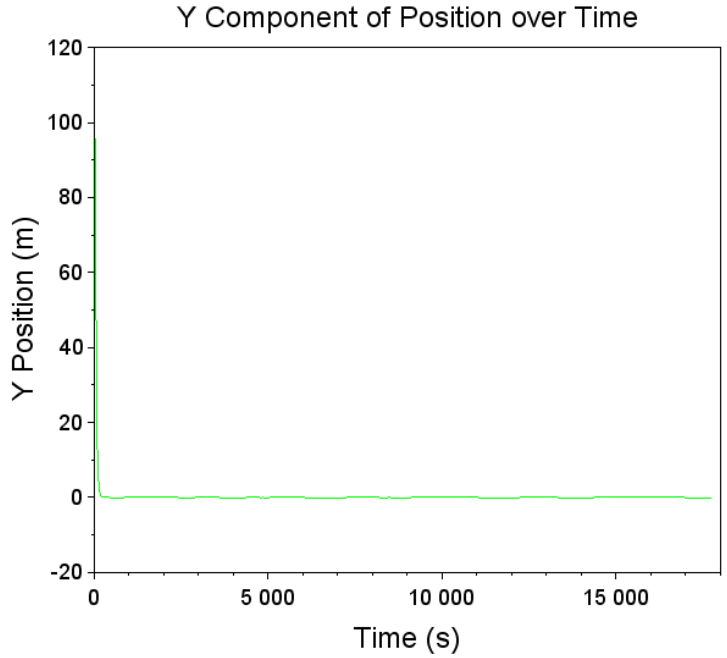

Figure 4.16.: Y-axis response: Depicts the control accuracy along the y-axis, reflecting rapid alignment to the target path for Test Case 2 using LQR.

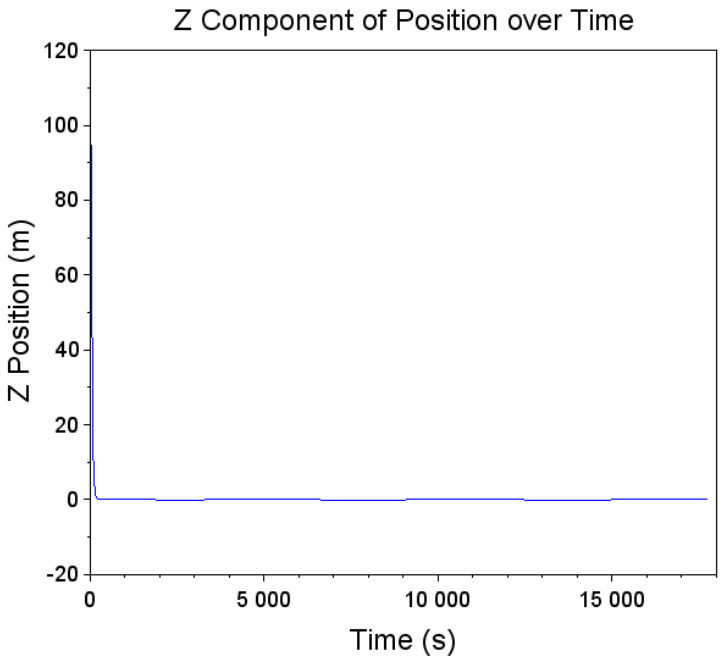

Figure 4.17.: Z-axis dynamics: Visualizes the control along the z-axis, emphasizing smooth trajectory correction for Test Case 2 using LQR.

- *Control Actions*: Over the span of three orbital periods, the thrusters were activated a total of 179 times. Notably, the thruster oriented in the positive y-direction registered the highest number of activations at 44, while the thruster in the negative z-direction recorded the minimal, with only 9 activations.

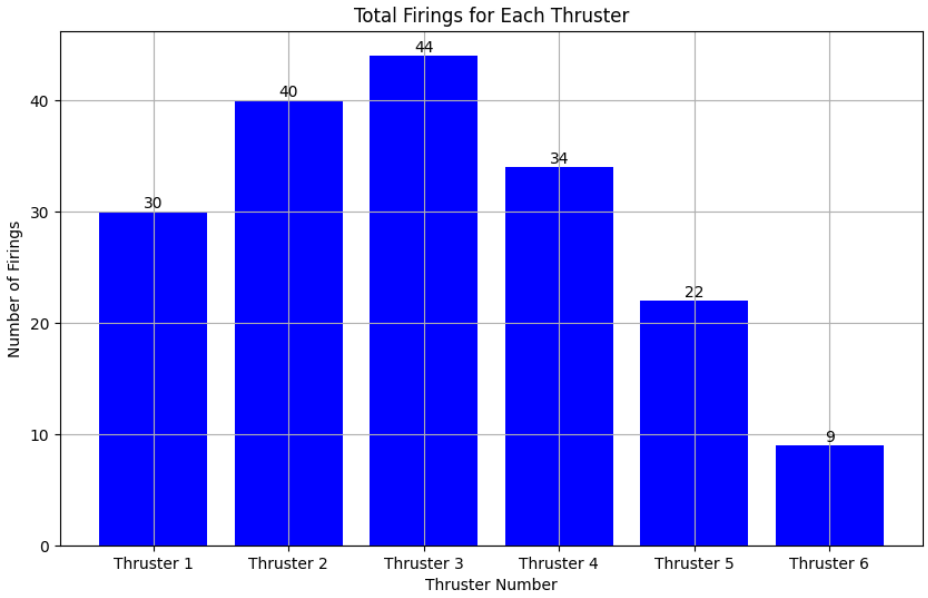

Figure 4.18.: Thrust activity per thruster for Test Case 2, showing each thruster's contribution to maintaining the spacecraft's trajectory under the LQR control setup.

Visualization Data: The following figures provide a comprehensive view of the spacecraft's trajectory and velocity in both two-dimensional and three-dimensional spaces, illustrating the effectiveness of the control strategies employed:

- *2D Trajectory Plot*: Depicts the spacecraft's path in the XY-plane, highlighting trajectory control and stabilization efforts. This is shown in Figure 4.19.

- *3D Trajectory Plot*: Provides a three-dimensional perspective of the spacecraft's navigational path, allowing for an analysis of its spatial maneuvers, as illustrated in Figure 4.20.

- *2D Velocity Plot*: Captures the velocity vector changes in the XY-plane, emphasizing dynamic adjustments and control precision. This is detailed in Figure 4.21.

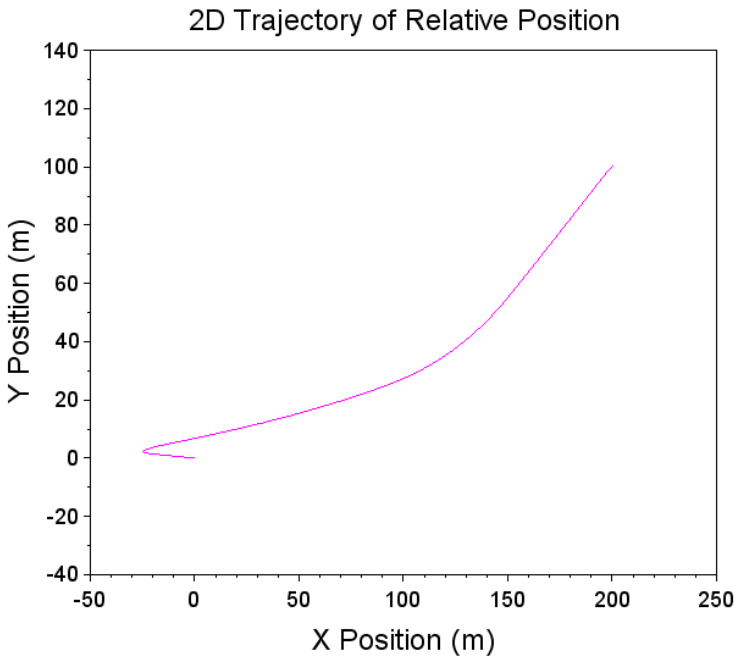

Figure 4.19.: 2D trajectory plot of the spacecraft under Test Case 2, illustrating precise trajectory control and stabilization.

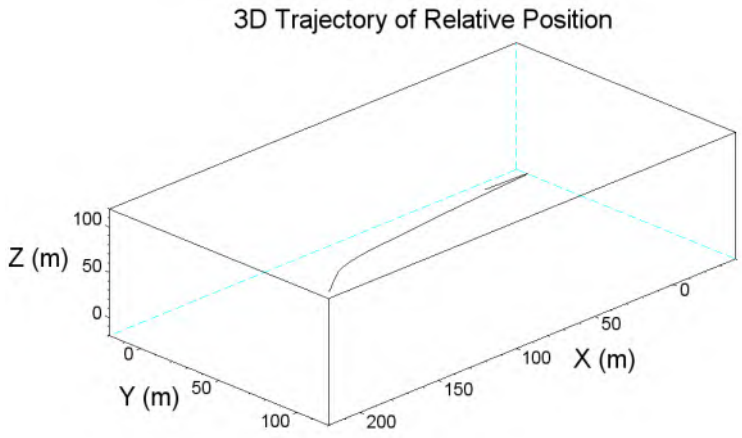

Figure 4.20.: 3D trajectory visualization for Test Case 2, providing a detailed view of the spacecraft's movement and control efficacy in three-dimensional space.

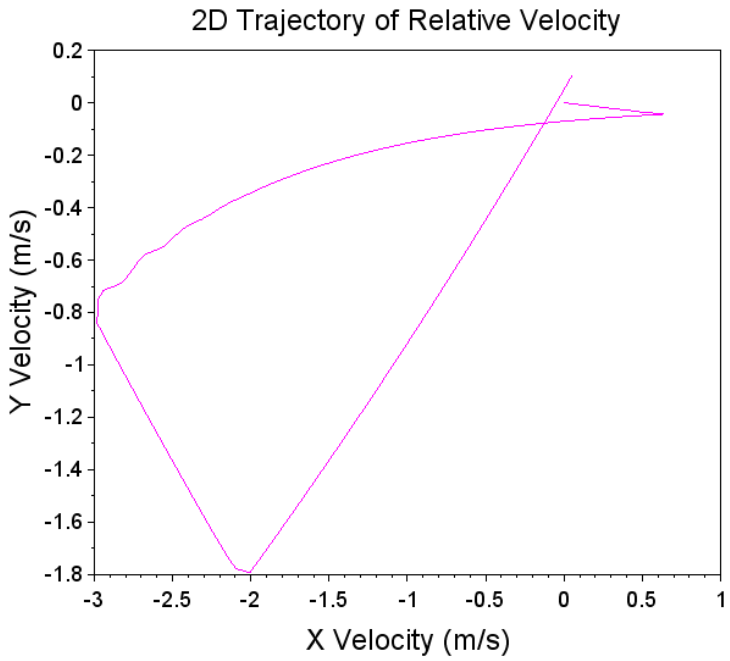

Figure 4.21.: 2D velocity plot for Test Case 2, demonstrating the effectiveness of velocity stabilization and dynamic response throughout the simulation.

Test Case 3: High-Velocity Emphasis with Reduced Control Weight

This test case explores the dynamics of prioritizing velocity control by significantly reducing the emphasis on positional corrections within the control strategy. The weight assigned to control was decreased tenfold from 1000 to 100, shifting the focus towards rapid velocity adjustments rather than maintaining positional stability. This configuration provides insight into the performance limits of the control system when confronted with scenarios that demand quick velocity stabilization under less stringent positional accuracy.

$$Q = \begin{bmatrix} 1 & 0 & 0 & 0 & 0 & 0 \\ 0 & 1 & 0 & 0 & 0 & 0 \\ 0 & 0 & 1 & 0 & 0 & 0 \\ 0 & 0 & 0 & 10000 & 0 & 0 \\ 0 & 0 & 0 & 0 & 10000 & 0 \\ 0 & 0 & 0 & 0 & 0 & 10000 \end{bmatrix} \quad R = \begin{bmatrix} 100 & 0 & 0 \\ 0 & 100 & 0 \\ 0 & 0 & 100 \end{bmatrix}$$

The adoption of this aggressive control strategy resulted in significantly high fuel con-

sumption, totaling 53.2 kg, which starkly contrasts with the spacecraft's operational constraints. This scenario illustrates the challenges and potential pitfalls when excessively prioritizing velocity control over positional accuracy.

Visual Representations and Analysis:

- **2D Plots for Position and Velocity**: Figures 4.22 display the 2D plots for position and velocity, respectively, which detail the dynamic response of the spacecraft to the implemented control strategy throughout the simulation.

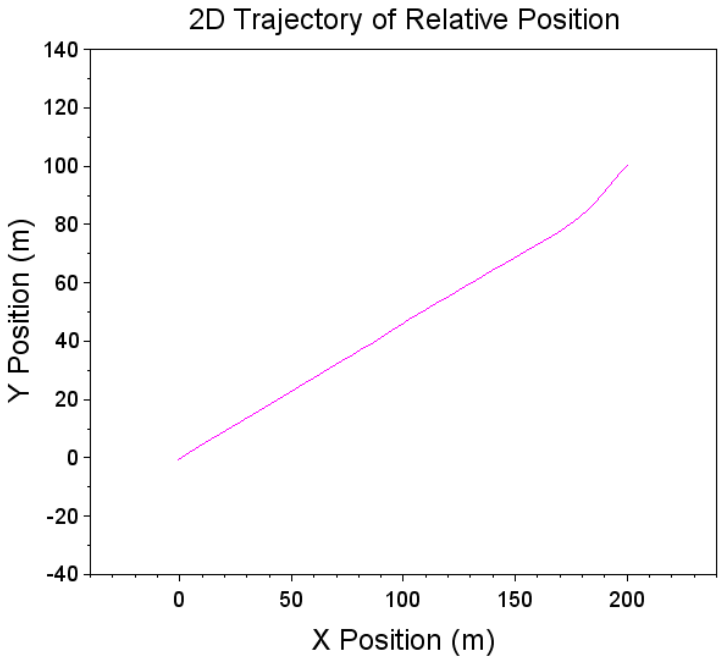

Figure 4.22.: 2D plot showcasing the positional adjustments of the spacecraft under extreme velocity control conditions for Test Case 3.

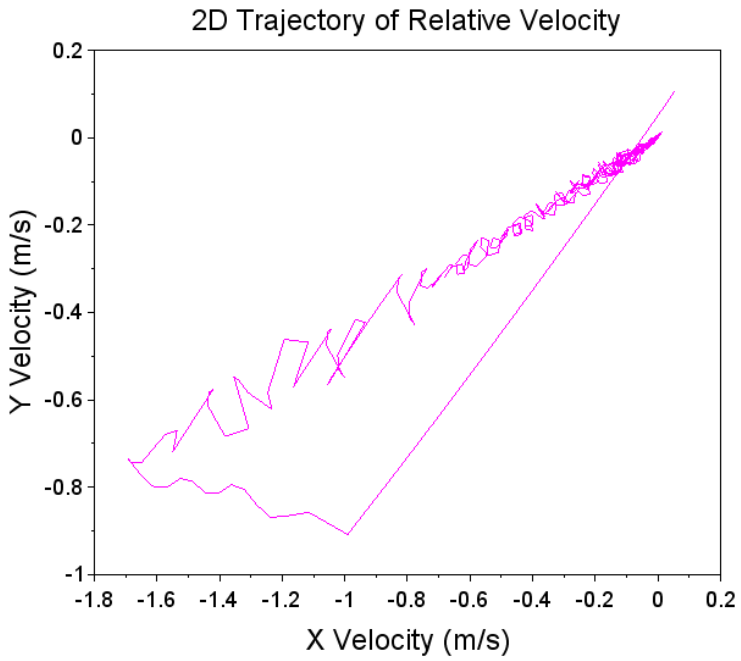

Figure 4.23.: Velocity adjustments of the spacecraft demonstrating the rapid response induced by the high-velocity emphasis for Test Case 3.

- **3D Plot for Position**: Figure 4.24 provides a three-dimensional representation of the spacecraft's trajectory, offering a comprehensive view of the positional adjustments throughout the simulation.

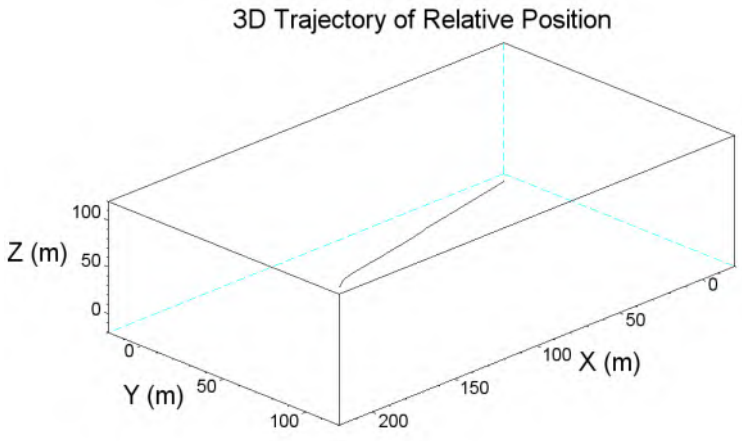

Figure 4.24.: Three-dimensional view of the spacecraft's path, highlighting the trajectory complexities when velocity control is prioritized over positional accuracy for Test Case 3.

- **Thruster Firing**: Figure 4.25 presents a bar plot of the thruster firing frequencies, highlighting the intensive use of control actions required to maintain the desired trajectory under the high-velocity control regime.

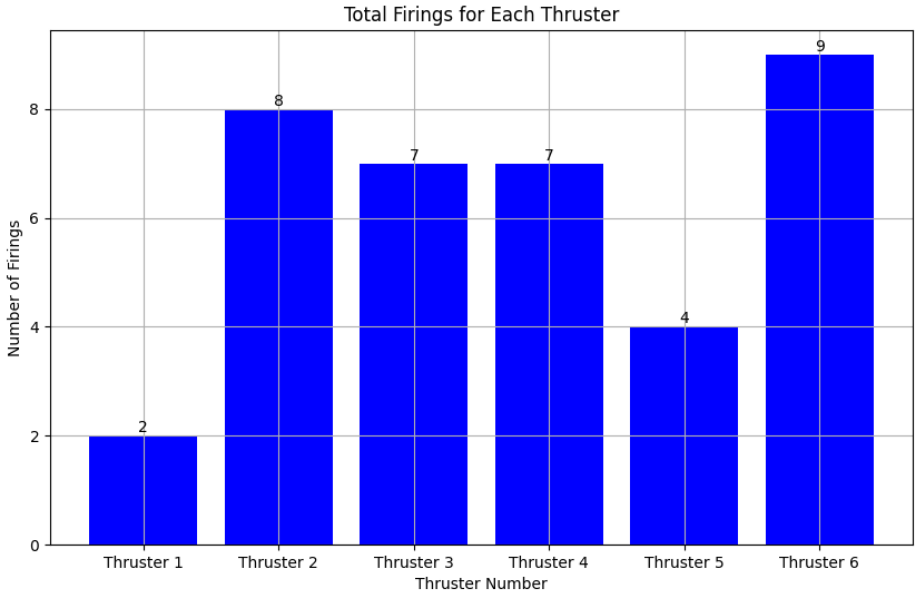

Figure 4.25.: Distribution of thruster firings for Test Case 3, showcasing the intensive control efforts required to stabilize the spacecraft's high-velocity trajectory.

Dynamics and Outcomes:

- *Fuel Consumption*: The control strategy led to an unsustainable fuel usage of 53.2 kg over three orbits, significantly exceeding the total mass of the spacecraft, which is 25 kg.
- *Control Instabilities*: Oscillations of 2-4 meters in the z-direction were observed and persisted without stabilization by the end of the simulation, indicating potential system instabilities.(See figure 4.28)

The drastic reduction in R values, coupled with extremely high weights on velocity in the Q matrix, created a highly aggressive control policy. This policy led to unrealistic fuel usage and introduced control instabilities, as evidenced by the persistent oscillations. Although this setup demonstrated rapid response capabilities, it proved to be impractical for actual mission scenarios due to its unsustainable fuel demands and the resultant instability issues.

Time to Target:

- The spacecraft aligned with the target within approximately 200-400 seconds for the x and y directions, showcasing the rapid control capabilities enabled by the high-velocity emphasis as shown in figures 4.73a, and 4.73b.

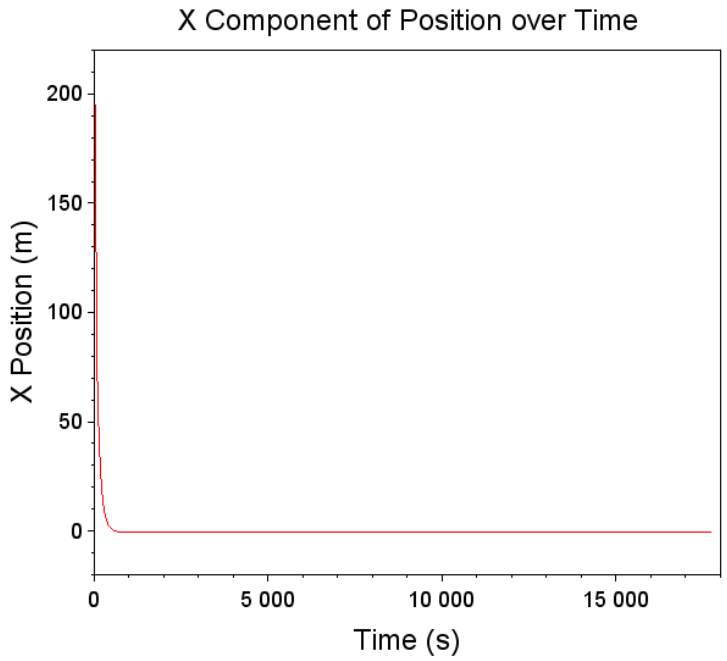

Figure 4.26.: X-axis position over time shows the rapid alignment under the high-velocity emphasis for Test Case 3.

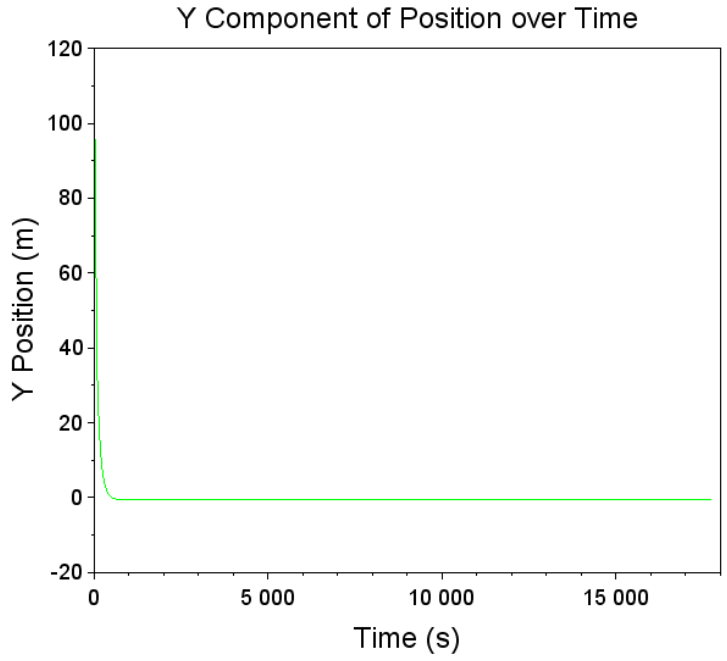

Figure 4.27.: Y-axis response underlines the swift y-direction adjustment for Test Case 3.

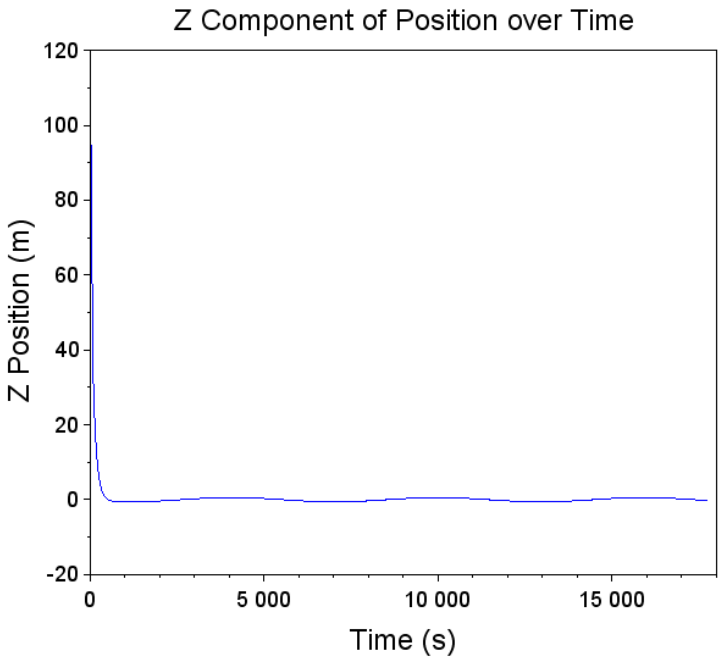

Figure 4.28.: Z-axis dynamics depict the stabilization efforts along the z-axis for Test Case 3.

Test Case 4: High-Control and Velocity Weights for Optimal Efficiency

Test Case 4 explores a control setup where both velocity and control inputs are highly weighted. This scenario investigates the implications of significant prioritization of these parameters within the spacecraft's control system.

$$Q = \begin{bmatrix} 1 & 0 & 0 & 0 & 0 & 0 \\ 0 & 1 & 0 & 0 & 0 & 0 \\ 0 & 0 & 1 & 0 & 0 & 0 \\ 0 & 0 & 0 & 10^5 & 0 & 0 \\ 0 & 0 & 0 & 0 & 10^5 & 0 \\ 0 & 0 & 0 & 0 & 0 & 10^5 \end{bmatrix} \qquad R = \begin{bmatrix} 10^5 & 0 & 0 \\ 0 & 10^5 & 0 \\ 0 & 0 & 10^5 \end{bmatrix}$$

This test strategically focuses on maximizing control fidelity and minimizing deviations by employing extremely high weights on control efforts and velocity components. Remarkably, this setup results in a substantial decrease in fuel usage, consuming only 0.0733 kg of fuel, a minimal amount compared to previous test cases.

The position and velocity of the spacecraft, represented in 2D plots, illustrate an almost linear trajectory toward the target, demonstrating the effectiveness of the control strategy in maintaining a steady course. The 2D plots for position and velocity are shown in Figures 4.29, and 4.30 respectively.

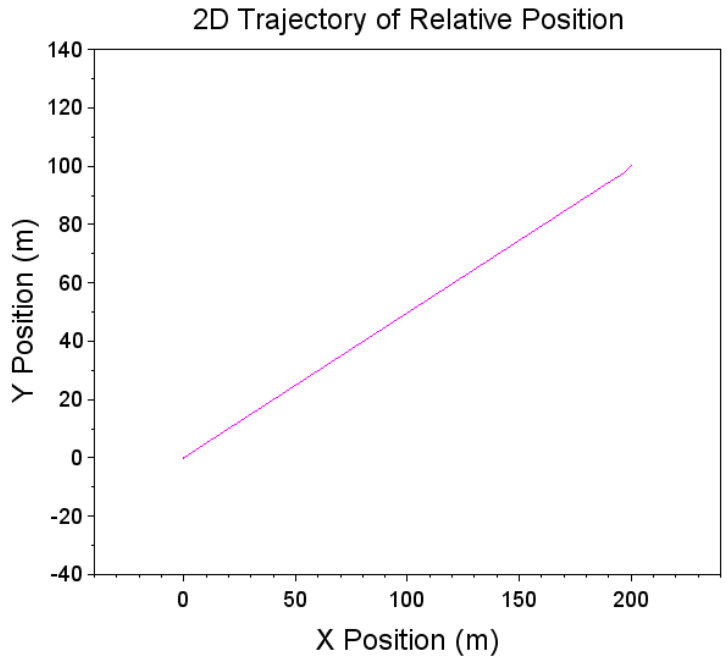

Figure 4.29.: 2D trajectory of the spacecraft's position under LQR control in Test Case 4, demonstrating efficient path control.

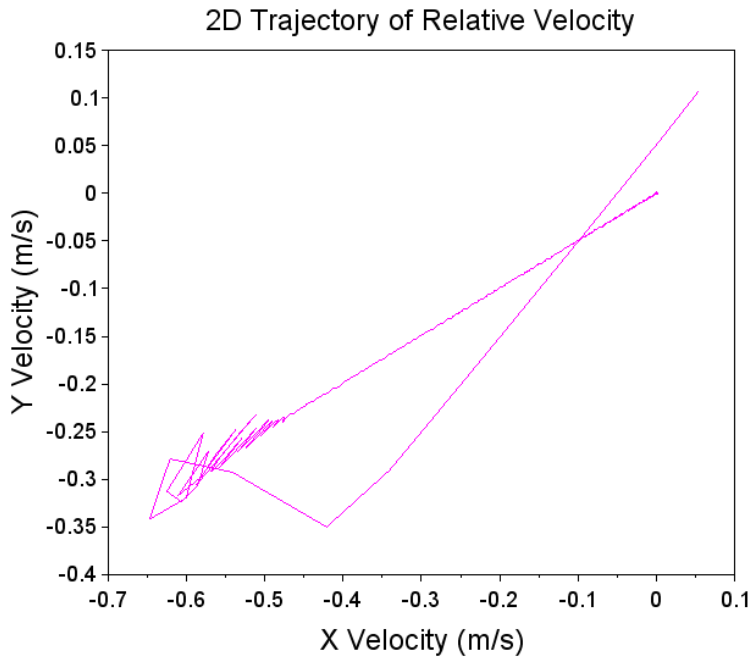

Figure 4.30.: 2D velocity trajectory under LQR control in Test Case 4, highlighting smooth velocity transitions and control stability.

The 3D plot in Figure 4.31 further provides a comprehensive view of the spacecraft's trajectory, offering a detailed perspective on the positional adjustments throughout the mission.

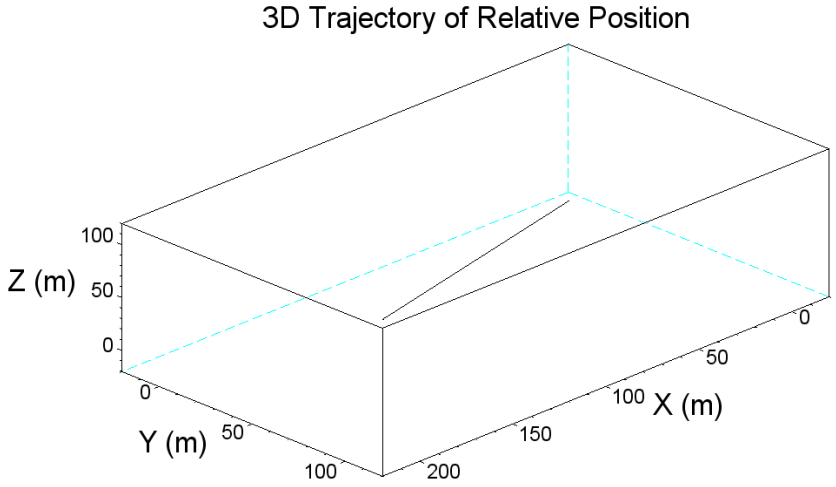

Figure 4.31.: 3D trajectory visualization of the spacecraft's path in Test Case 4, showcasing precise control through high-control weights.

Time to Target:

- The spacecraft reaches its target within approximately 1800-1900 seconds in the x-direction, 2300 seconds in the y-direction, and 1900 seconds in the z-direction, as demonstrated in Figures 4.32, 4.33, and 4.34.

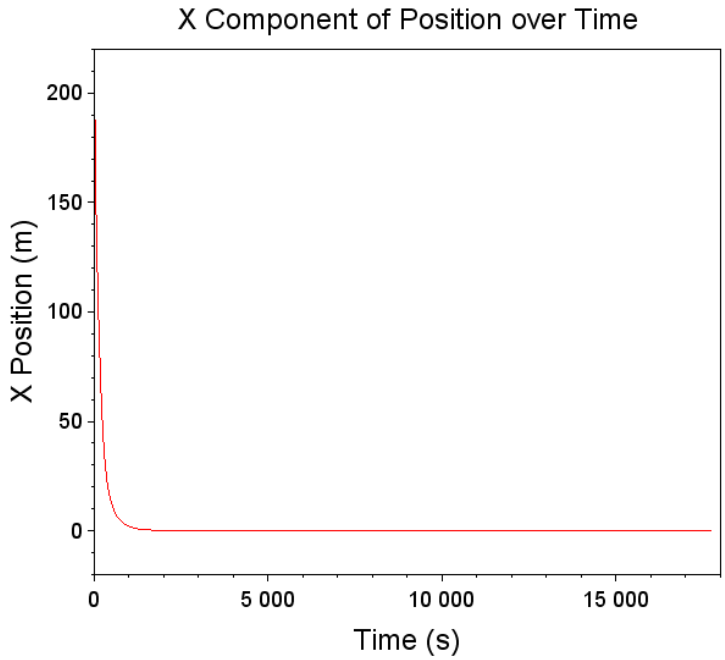

Figure 4.32.: X-axis position over time in Test Case 4, demonstrating the effectiveness of the LQR controller in controlling the x-axis dynamics.

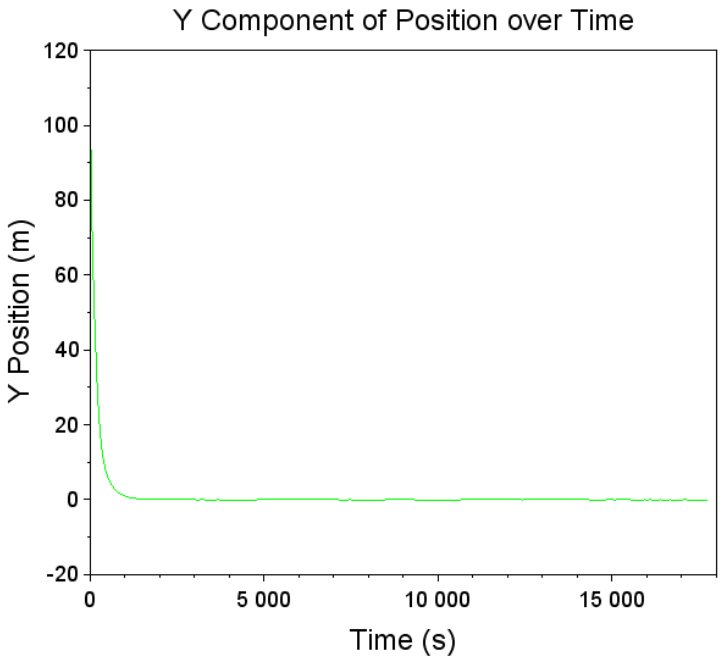

Figure 4.33.: Y-axis position over time in Test Case 4, showing how the LQR controller manages y-axis movements to maintain the desired trajectory.

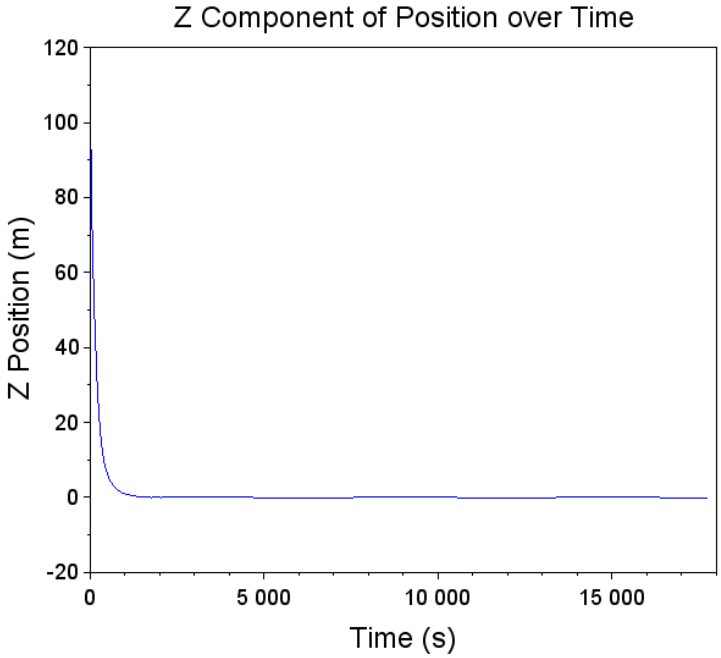

Figure 4.34.: Z-axis position over time in Test Case 4, illustrating the LQR controller's capability in altitude control and z-axis stabilization.

Control Actions:

- The highest frequency of thruster activity is recorded for the positive x-direction with 148 firings while least thruster firing observed for the negative z-direction thruster, contributing to a total of 454 thruster activations across all directions. This is depicted in Figure 4.35.

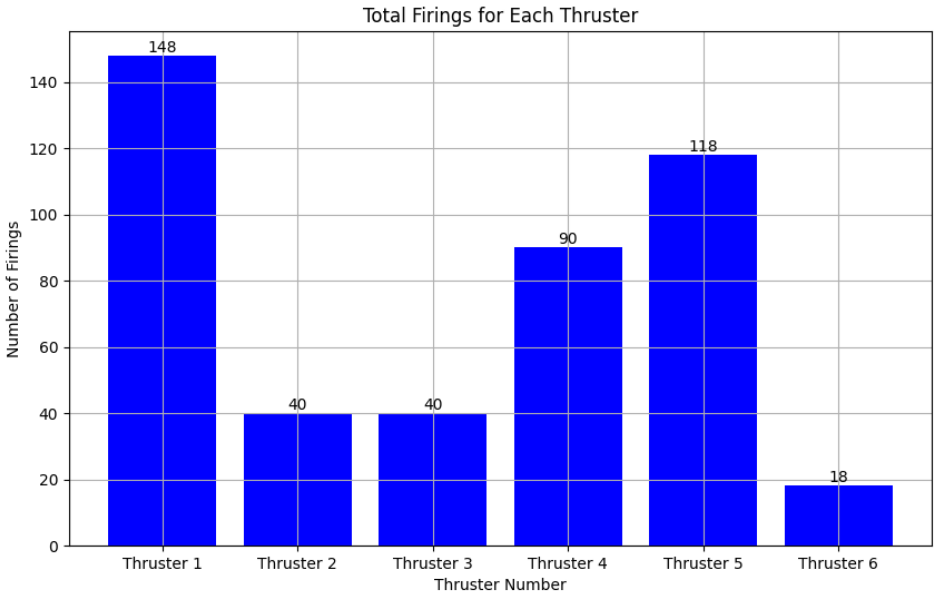

Figure 4.35.: Distribution of thruster firings in Test Case 4, emphasizing the LQR controller's control requirements.

This test demonstrates the capacity of high-control weights to drastically reduce fuel consumption, achieving an efficient operational mode. However, the increased time to reach the target and the high number of thruster firings also indicate potential trade-off in response speed and system wear. The almost linear trajectory and the efficient use of fuel validate the efficacy of the weight settings in the Q and R matrices, showcasing an optimal balance between energy conservation and control precision.

The results from Test Case 4 offer critical insights into the scalability of high-weight control strategies for long-duration missions, where fuel economy is paramount. Further analysis would be required to fully understand the long-term impacts of such high control frequencies on spacecraft systems and mission success.

4.5.2. Summary of Test Results

The table 4.1 presents a comparative overview of the outcomes from four distinct test cases, each designed to evaluate the spacecraft control system under varying operational conditions. Test Case 1, which focused on position accuracy, resulted in moderate fuel consumption of 3.5 kg and the highest number of thruster firings at 1605, indicating a

robust but demanding control strategy. In stark contrast, Test Case 2 emphasized velocity control and achieved significant efficiency, consuming only 0.4 kg of fuel and necessitating 179 thruster activations. Test Case 3, which prioritized rapid velocity adjustments, led to an excessive fuel usage of 53.2 kg, the highest among all cases, but required the fewest thruster firings, only 37. This suggests a highly aggressive but less frequent control approach. Lastly, Test Case 4, which balanced high control and velocity weights for optimal efficiency, demonstrated remarkable fuel economy, consuming a mere 0.0733 kg, while requiring a moderate number of thruster firings at 454. These results highlight the trade-offs between fuel efficiency, control precision, and operational demands, providing valuable insights into the spacecraft's performance across different control settings.

Test Case	**Fuel Consumption (kg)**	**Total Thruster Firings**
1	3.5	1605
2	0.4	179
3	53.2	37
4	0.0733	454

Table 4.1.: Summary of Test Results: Fuel Consumption and Thruster Firings Across Four Test Scenarios.

4.5.3. Evaluation of Clohessy-Wiltshire Based Trajectory Controller

This section systematically evaluates the performance of the spacecraft control system through a series of structured test cases. Each test case applies a specific time-to-target parameter (Δt), serving as a basis to assess the controller's efficacy in optimizing trajectory, improving fuel efficiency, and managing thruster usage under varied operational constraints.

Test Case 1 ($\Delta t = 10$ seconds)

Test Case 1 evaluates the control duration (Δt) set to 10 seconds, investigating the effects of very short control intervals on trajectory accuracy, fuel efficiency, and thruster usage. This scenario aims to understand the controller's performance under highly frequent adjustments and the highest operational demands.

Observations and Results:

1. **Trajectory Analysis:** The 3D trajectory plot (Figure 4.36) shows a controlled path with significant deviations, indicating the challenges of maintaining precise trajectory control with very short control intervals.

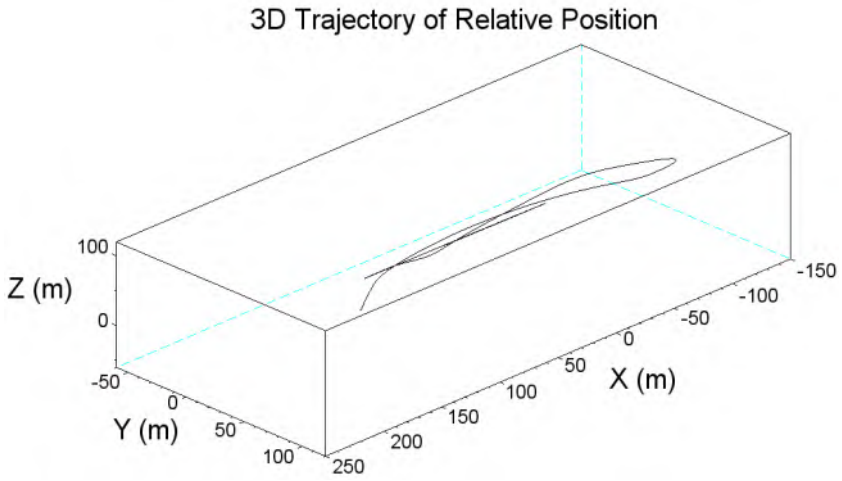

Figure 4.36.: 3D Trajectory of Relative Position for Test Case 1 ($\Delta t = 10$ seconds), showing significant deviations due to short control intervals.

The XY plane trajectory plot (Figure 4.37) further illustrates these dynamics with a highly variable path, reflecting the frequent adjustments required to maintain the trajectory.

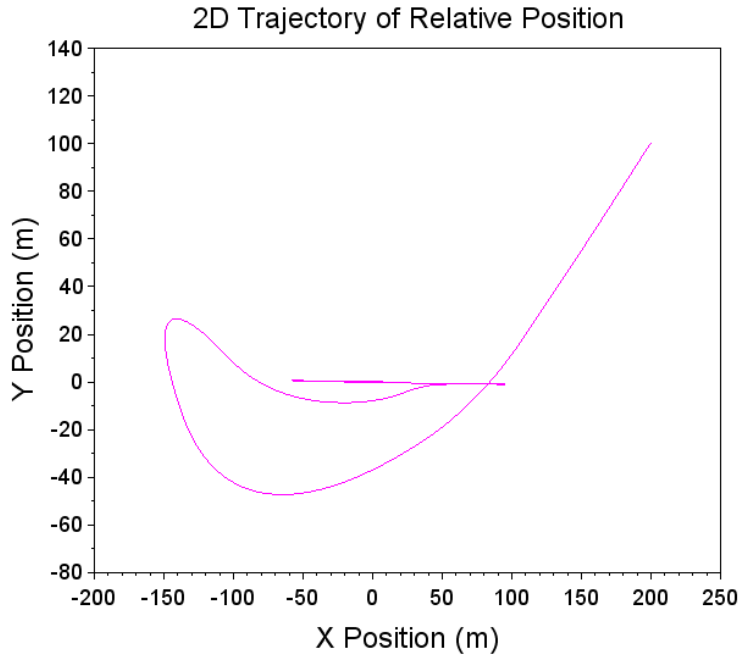

Figure 4.37.: XY Plane Trajectory of Relative Position for Test Case 1 ($\Delta t = 10$ seconds), depicting the frequent adjustments needed under short Δt.

2. **Positional Dynamics:** The position time plots for the X axis (Figure 4.38), Y axis (Figure 4.39), and Z axis (Figure 4.40) indicate highly frequent adjustments,

with the spacecraft struggling to stabilize due to the very short control intervals.

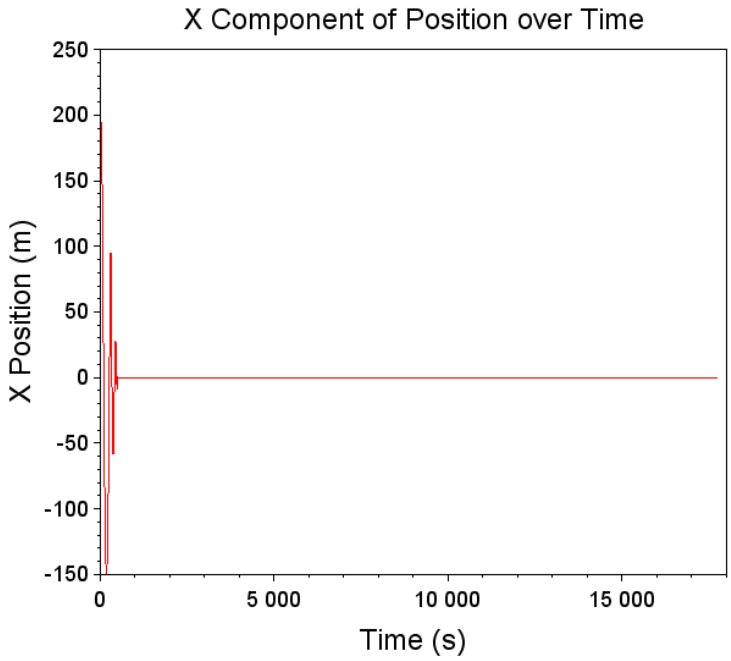

Figure 4.38.: X Component of Position over Time for Test Case 1 ($\Delta t = 10$ seconds) showing rapid fluctuations under stringent control demands, demonstrating the sensitivity of the control system to time discretization.

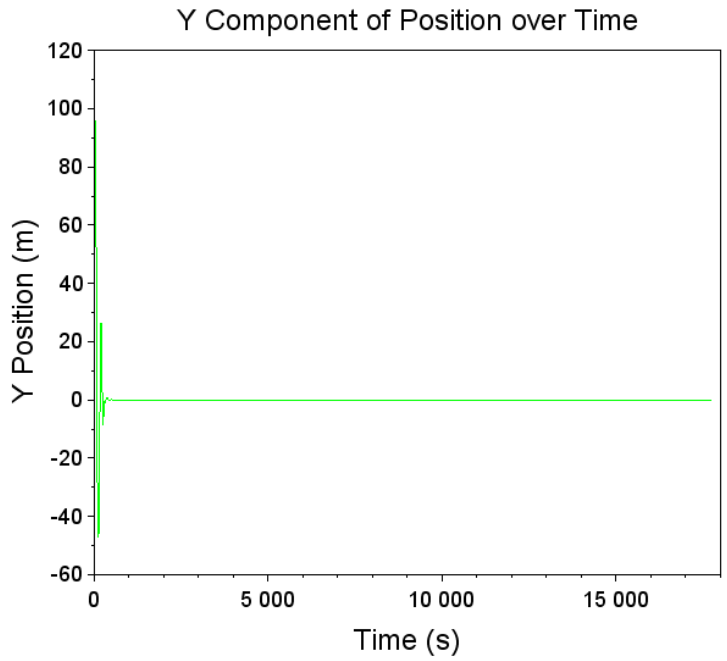

Figure 4.39.: Y Component of Position over Time for Test Case 1 ($\Delta t = 10$ seconds), reveals the dynamic adjustments required to maintain the intended course, illustrating control complexity in lateral movements.

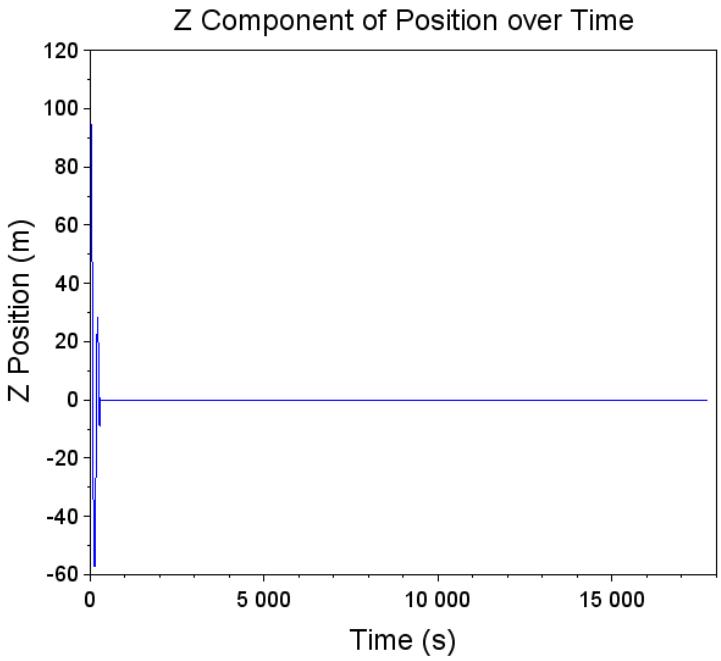

Figure 4.40.: Z Component of Position over Time for Test Case 1 ($\Delta t = 10$ seconds) illustrates the challenges in achieving stability with short control intervals, highlighting the vertical control accuracy issues.

3. **Velocity Control:** The XY plane trajectory of relative velocity (Figure 4.41) displays significant variance and unpredictable behavior, reflecting the difficulty of maintaining stable velocity control with very frequent adjustments.

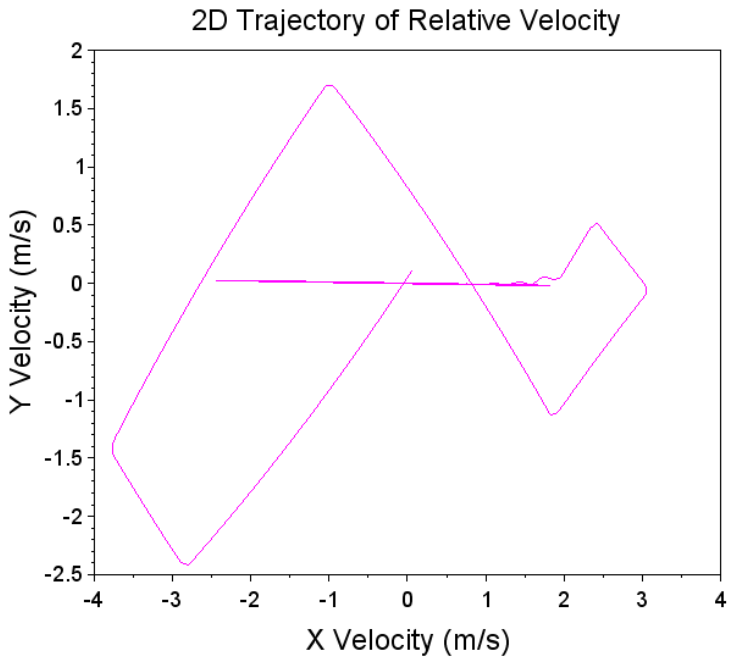

Figure 4.41.: XY Plane Trajectory of Relative Velocity for Test Case 1 ($\Delta t = 10$ seconds), showing unpredictable velocity behavior due to high-frequency control actions.

4. **Thruster Activity:** The distribution of thruster activations, as shown in the bar plot (Figure 4.42), reveals a notably high frequency of activations. Thruster 3 (positive y-direction) and Thruster 4 (negative y-direction) recorded the highest activities with 351 and 352 firings, respectively. In contrast, the thrusters in both the positive and negative z-directions demonstrated the lowest activity, with only 32 activations each. This high frequency of activations reflects the increased operational demands of the very short control interval.

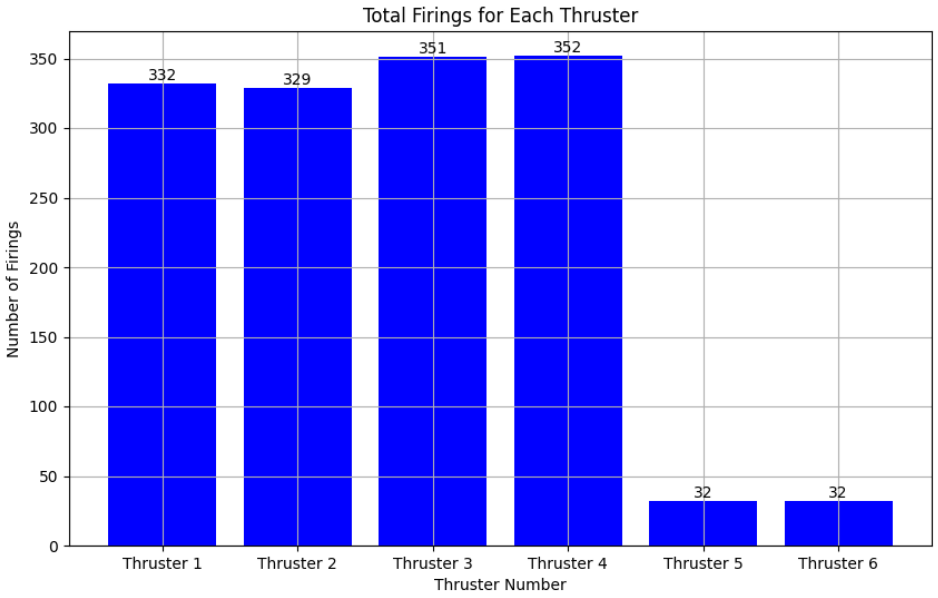

Figure 4.42.: Total Firings for Each Thruster in Test Case 1 ($\Delta t = 10$ seconds), illustrating the high frequency of thruster activations required for tight control intervals.

5. **Fuel Efficiency:** The fuel consumption in this scenario is the highest among all test cases amounting to 1.25467 kg, emphasizing the significant trade-off between control interval and fuel efficiency. The increased number of thruster activations necessitates greater fuel usage to maintain the desired trajectory.

Test Case 1 highlights the substantial challenges of maintaining precise control with very short Δt intervals. While the controller can manage the spacecraft's trajectory, the high frequency of adjustments leads to the highest operational demands and fuel consumption. This scenario underscores the importance of balancing control intervals to optimize fuel efficiency and operational complexity.

Test Case 2 ($\Delta t = 100$ seconds)

Test Case 2 evaluates the control duration (Δt) set to 100 seconds, investigating the effects of shorter control intervals on trajectory accuracy, fuel consumption, and thruster usage. This scenario aims to understand the controller's performance under more frequent adjustments and higher operational demands. The fuel consumption for this test was 0.18472 kg.

Observations and Results:

1. **Trajectory Analysis:** The 3D trajectory plot (Figure 4.43) illustrates a well-regulated path with minimal deviations, highlighting the complexities involved in achieving precise trajectory control under shorter control intervals.

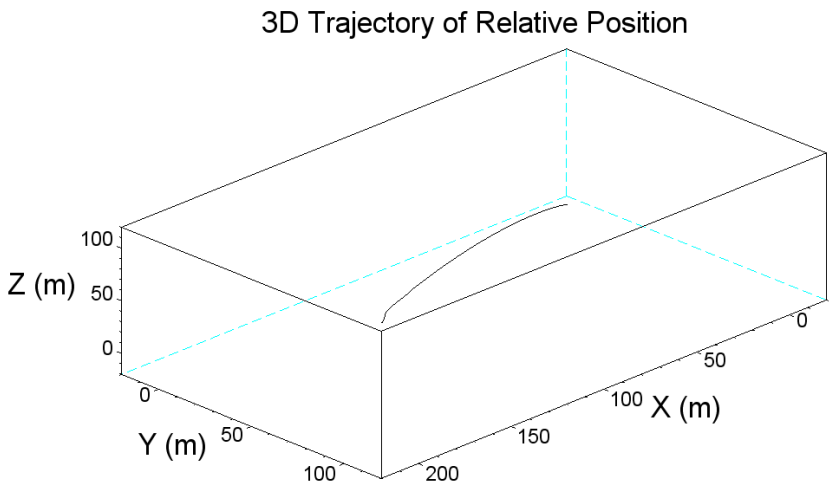

Figure 4.43.: 3D Trajectory of Relative Position for Test Case 2 ($\Delta t = 100$ seconds), depicting controlled but deviating path due to shorter control intervals.

The 2D trajectory plot (Figure 4.44) further demonstrates these dynamics, exhibiting a less smooth path compared to longer Δt scenarios, which are analyzed later in this section.

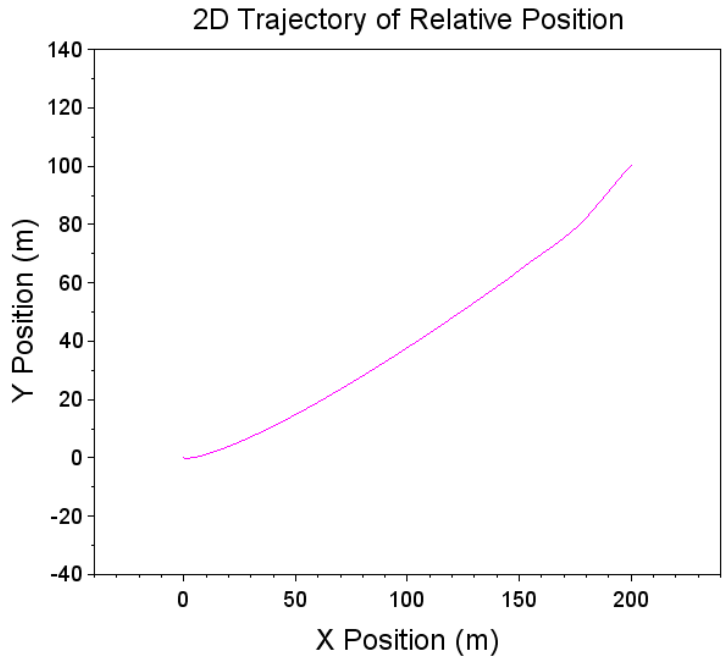

Figure 4.44.: XY Plane Trajectory of Relative Position for Test Case 2 ($\Delta t = 100$ seconds), illustrating the complex path due to frequent adjustments.

2. **Positional Dynamics:** The position time plots for the X axis (Figure 4.45), Y axis (Figure 4.46), and Z axis (Figure 4.47) indicate more frequent adjustments,

with the spacecraft taking longer to stabilize compared to scenarios with longer Δt.

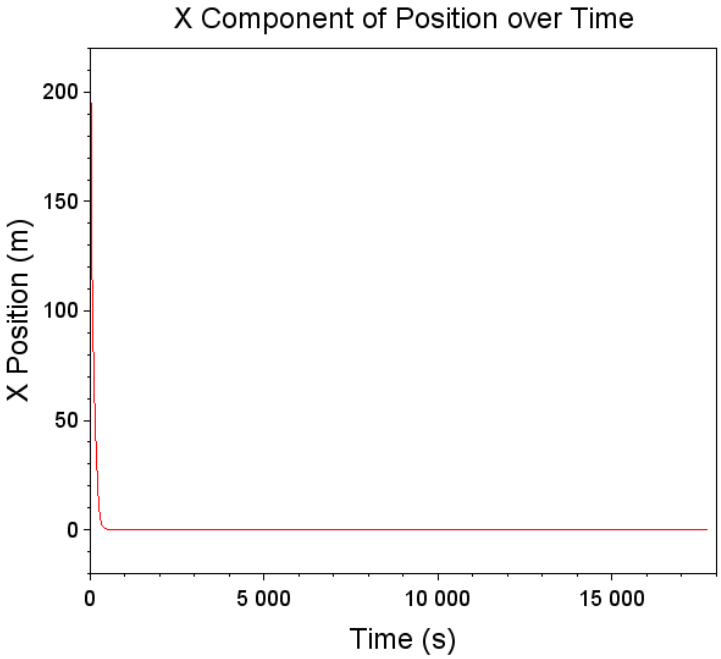

Figure 4.45.: X Component of Position over Time for Test Case 2 ($\Delta t = 100$ seconds), highlighting how control inputs are adjusted

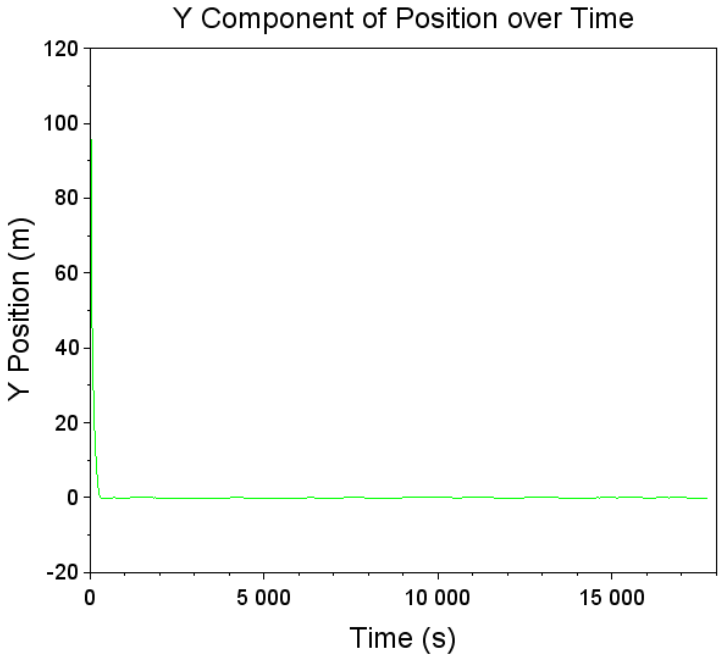

Figure 4.46.: Y Component of Position over Time for Test Case 2 ($\Delta t = 100$ seconds).

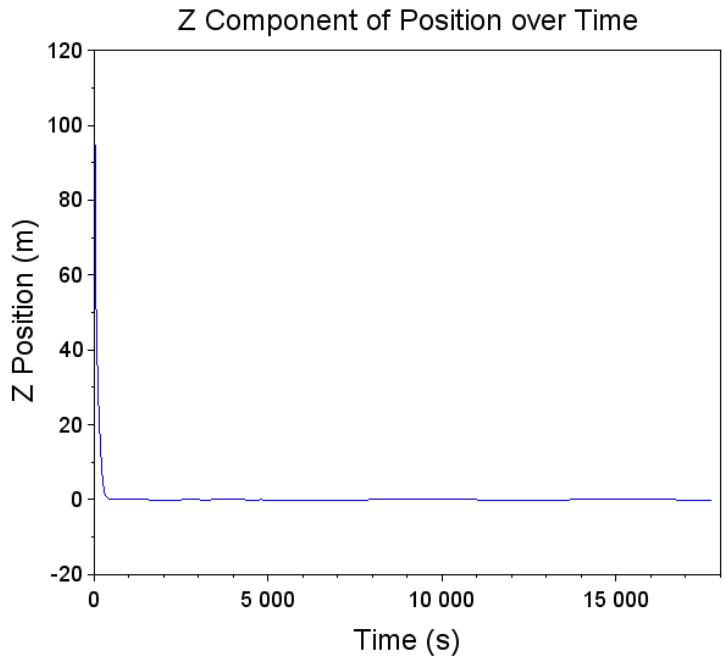

Figure 4.47.: Z Component of Position over Time for Test Case 2 ($\Delta t = 100$ seconds), demonstrating the effect of infrequent adjustments on vertical stability.

3. **Velocity Control:** The XY plane trajectory of relative velocity (Figure 4.48) displays greater variance and less predictable behavior, reflecting the challenges of maintaining stable velocity control with frequent adjustments.

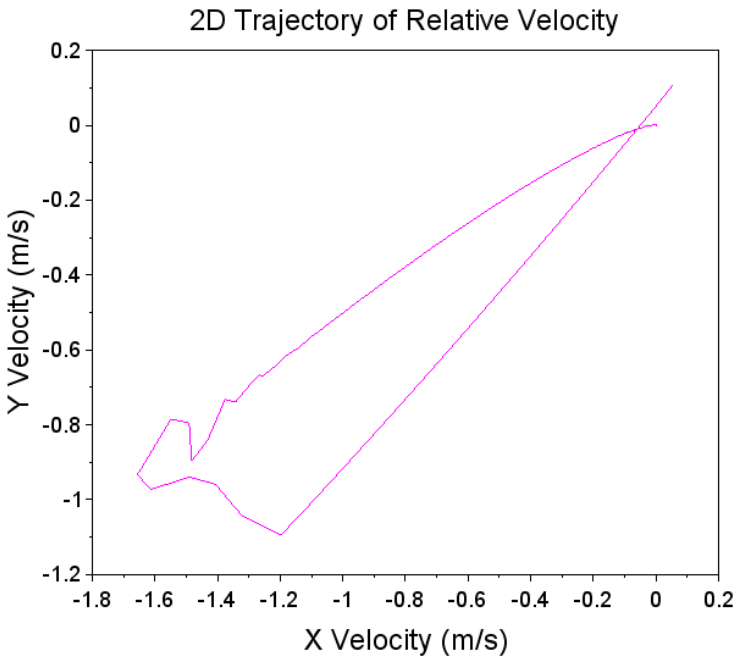

Figure 4.48.: XY Plane Trajectory of Relative Velocity for Test Case 2 ($\Delta t = 100$ seconds), showing greater variance due to shorter control intervals.

4. **Thruster Activity:** The bar plot showing thruster activations (Figure 4.49) reveals an increased number of firings, especially for Thruster 1 (positive x-direction) with 107 activations, followed by Thruster 2 (negative x-direction) and Thruster 3 (positive y-direction) with 77 and 66 firings, respectively. The combined activations for all six thrusters reach a total of 360 firings, underscoring the heightened operational demands imposed by the shorter control intervals.

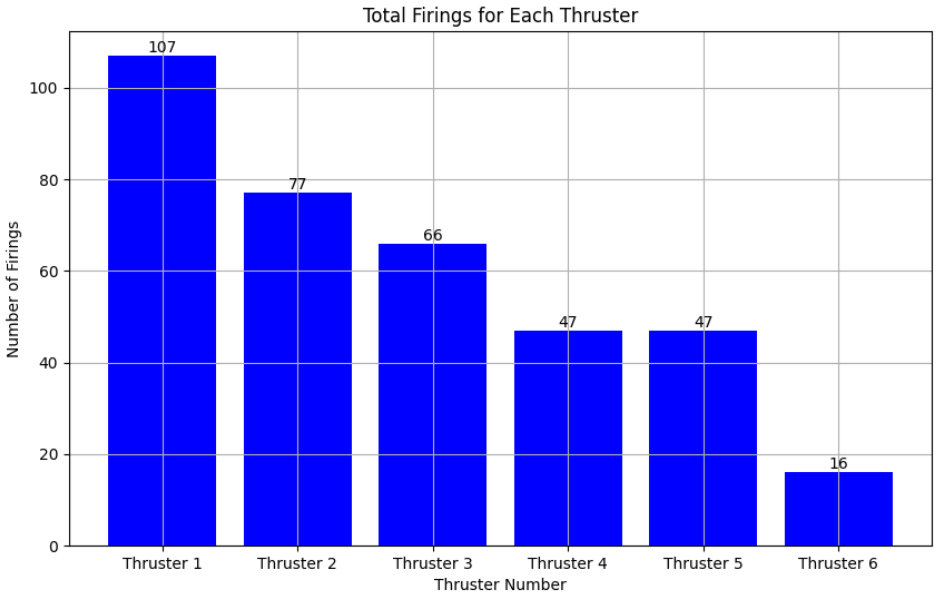

Figure 4.49.: Total Firings for Each Thruster for Test Case 2 ($\Delta t = 100$ seconds), illustrating the increased frequency of activations needed for shorter control periods.

5. **Fuel Efficiency:** In this test scenario, fuel consumption is lower than in the previous case (Test case 1 with $\Delta t = 10$ seconds) but higher than in tests with longer control intervals, totaling 0.18472 kg. This increment in fuel usage can be attributed to the increased thruster activations necessary to maintain the desired trajectory within the shorter control periods.

Test Case 3 ($\Delta t = 500$ seconds)

With Δt increased to 500 seconds, the controller's strategy further adapts, favoring fuel efficiency and smooth trajectory control, which manifests as a spline motion toward the target. This extended duration reduces fuel consumption to a mere 0.0563865 kg, supporting the hypothesis that longer time-to-target parameters inversely correlate with fuel usage.

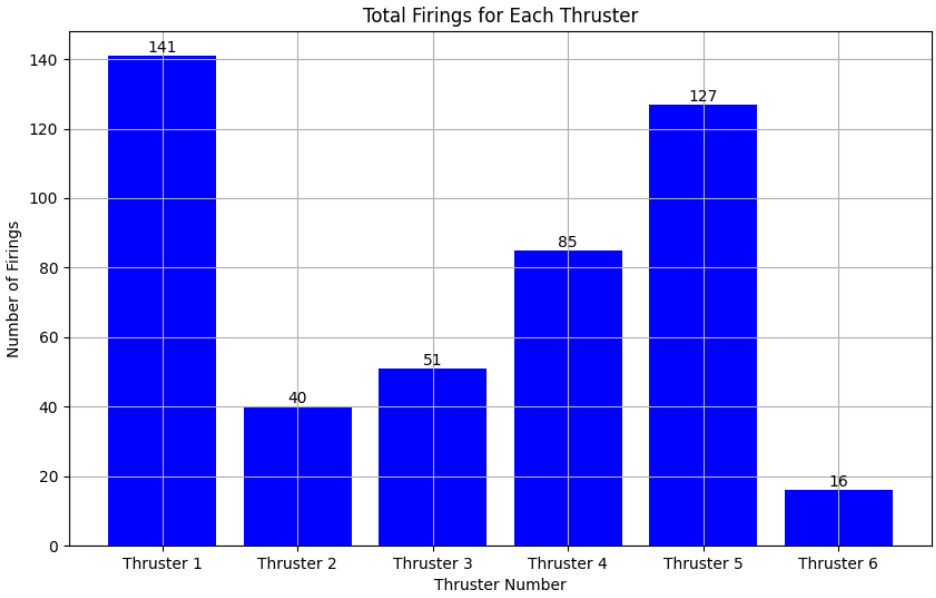

Figure 4.50.: Bar plot showing total firings for each thruster in Test Case 3 ($\Delta t = 500$ seconds), indicating a biased distribution of thruster usage with more frequent activations in specific thrusters.

As depicted in Figure 4.50, the firing frequency varies across thrusters. Thruster 1 (positive x-direction) leads with 141 activations, while Thrusters 5 (positive z-direction) and 4 (negative y-direction) follow with 127 and 85 firings, respectively. The less frequent activations of Thrusters 2 (negative x-direction), 3 (positive y-direction), and 6 (negative z-direction) illustrate a skewed distribution in thruster usage.

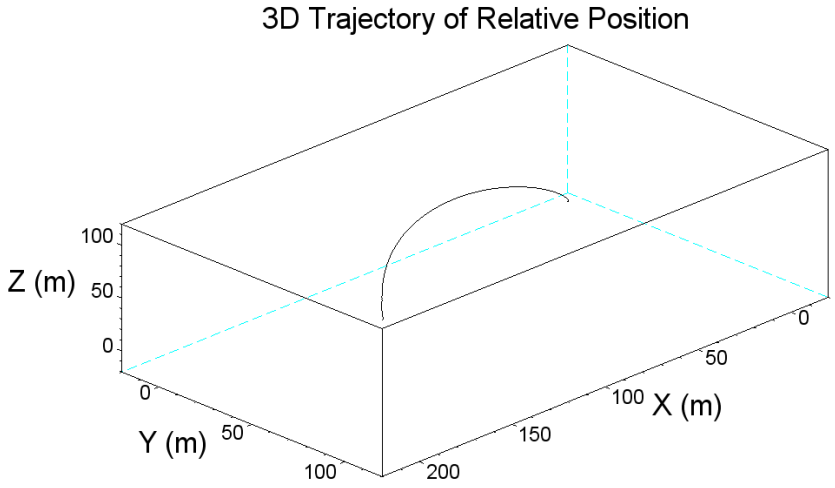

Figure 4.51.: 3D trajectory of relative position for Test Case 3 ($\Delta t = 500$ seconds), showcasing a smooth and controlled approach towards the target.

The 3D trajectory plot (Figure 4.51) shows a smooth and curved path towards the target. This suggests that the controller efficiently manages the satellite's movement over an extended period, ensuring a gradual and controlled approach.

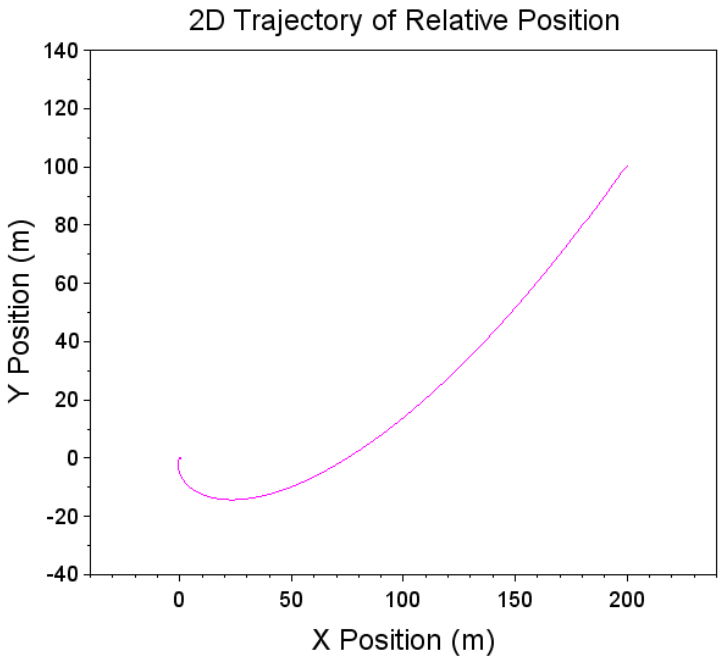

(a) XY plane trajectory of relative position for Test Case 3 ($\Delta t = 500$ seconds), illustrating a smooth, spiral-like path that ensures efficient maneuvering.

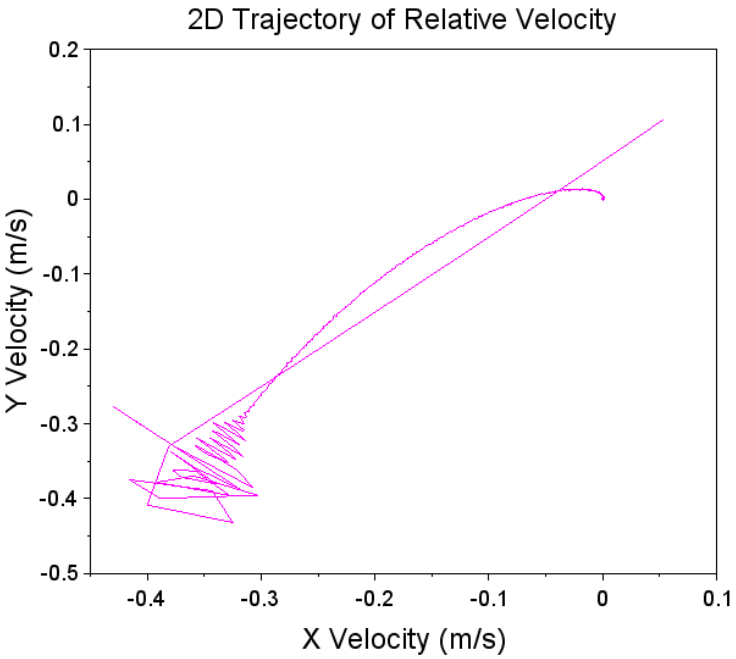

(b) XY plane trajectory of relative velocity for Test Case 3 ($\Delta t = 500$ seconds), showing complex path dynamics with initial oscillations that stabilize over time.

Figure 4.52.: Trajectory analyses in the XY plane for relative position and velocity in Test Case 3 ($\Delta t = 500$ seconds), highlighting the spacecraft's dynamic response to control inputs.

Figure 4.52a shows a smooth, spiral-like path in the XY plane trajectory, indicating efficient maneuvering in two dimensions. This trajectory ensures minimal oscillations and a direct approach towards the target.

Figure 4.52b illustrates the XY plane velocity trajectory, showing a complex path with initial oscillations that gradually stabilize. This indicates the controller's efforts to manage speed and direction efficiently, achieving a steady approach velocity toward the target.

The X component plot (Figure 4.53) indicates a rapid initial decrease followed by a stabilization period, which aligns with the expected behavior of the satellite adjusting its position quickly and then maintaining a steady state as it approaches the target.

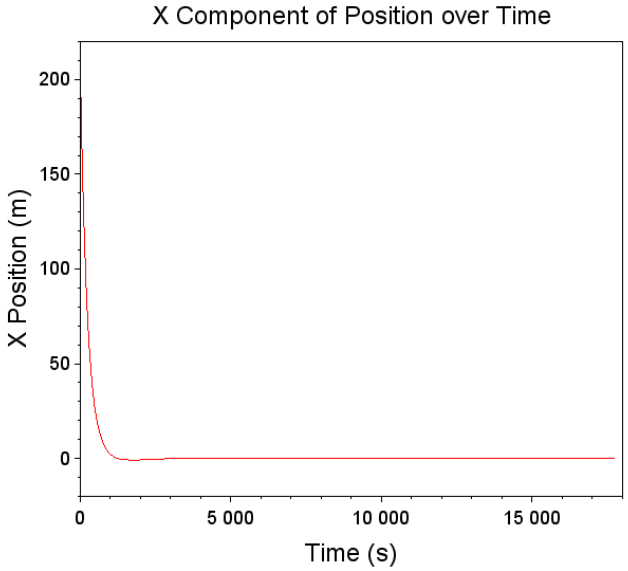

Figure 4.53.: X-axis position over time for Test Case 3 ($\Delta t = 500$ seconds), showing rapid initial decrease followed by stabilization.

The Y component plot (Figure 4.54) shows an initial drop followed by stabilization, similar to the X component. This behavior indicates that the controller manages the Y-axis adjustments effectively to bring the satellite into the desired trajectory.

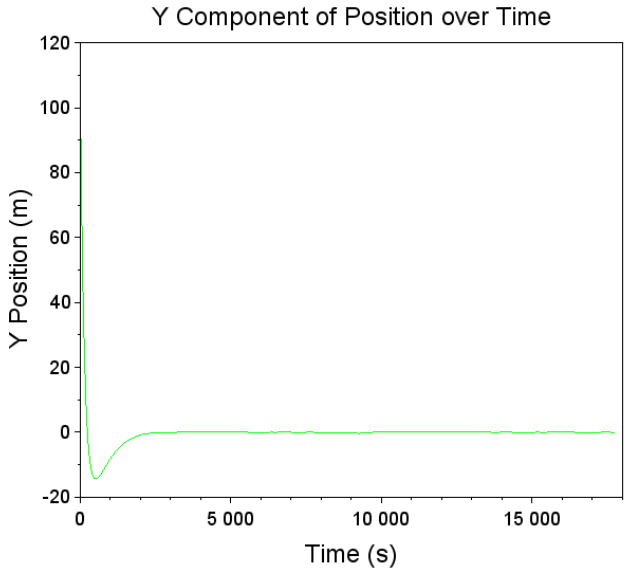

Figure 4.54.: Y-axis position over time for Test Case 3 ($\Delta t = 500$ seconds), depicting initial adjustments leading to steady positioning.

The Z component plot (Figure 4.55) reveals a continuous decrease and eventual stabilization, suggesting effective control in the vertical axis, ensuring the satellite maintains its intended altitude.

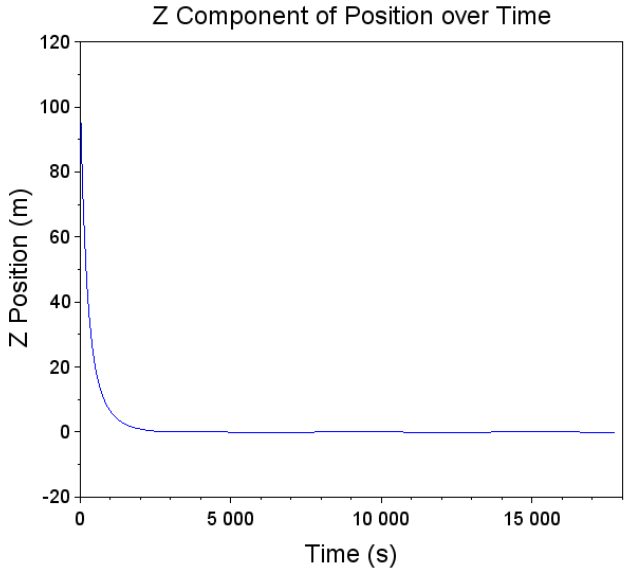

Figure 4.55.: Z-axis position over time for Test Case 3 ($\Delta t = 500$ seconds), reveals a gradual decrease and eventual stabilization.

Test Case 3 demonstrates that increasing the Δt to 500 seconds improves the control

system's efficiency by allowing more time for each control action to affect the spacecraft's trajectory, thereby reducing the frequency and intensity of thruster activations required. This methodical approach to control not only ensures precision in trajectory following but also significantly enhances fuel efficiency and operational stability.

Test Case 4 ($\Delta t = 1000$ seconds)

In this test case, the control interval Δt is set to 1000 seconds. This extended duration considerably alters the control strategy, emphasizing fuel efficiency and trajectory smoothness. This approach is evident from the observations and plots described. Notably, the 2D velocity plot(see figure 4.59a) reveals a complex path with initial oscillations, which gradually stabilize as the spacecraft approaches the target.

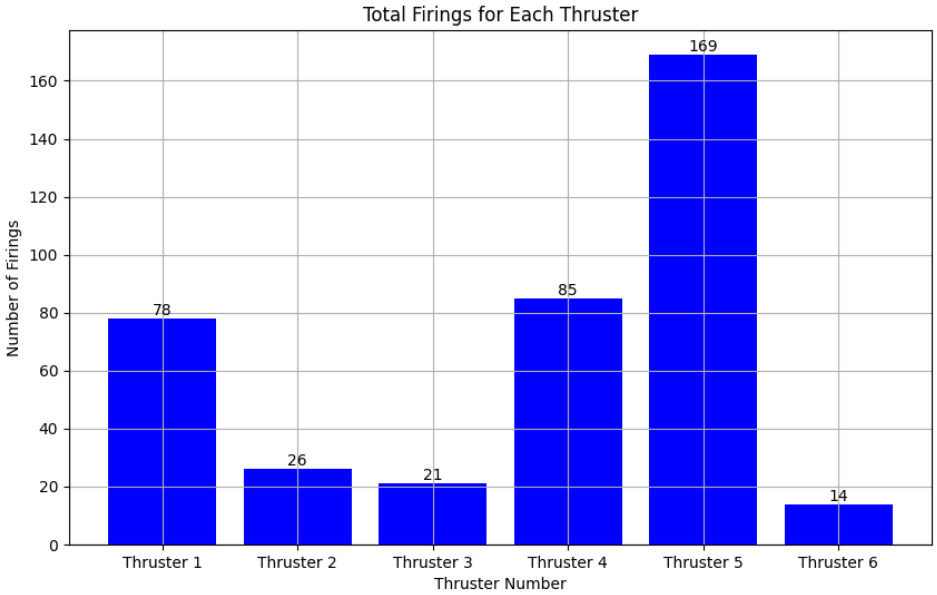

Figure 4.56.: Total firings for each thruster in Test Case 4 ($\Delta t = 1000$ seconds), showing a biased distribution of thruster usage with fewer activations, indicative of smoother control.

Figure 4.56 illustrates the frequency of activations for each thruster during this test case. Thruster 1 (positive x-direction) exhibits the highest frequency with 107 firings. It is followed by Thrusters 2 (negative x-direction) and 3 (positive y-direction) with 77 and 66 firings, respectively. Thrusters 4 (negative y-direction), 5 (positive z-direction), and 6 (negative z-direction) show significantly fewer activations, reflecting a biased utilization of thrusters in controlling the spacecraft's trajectory.

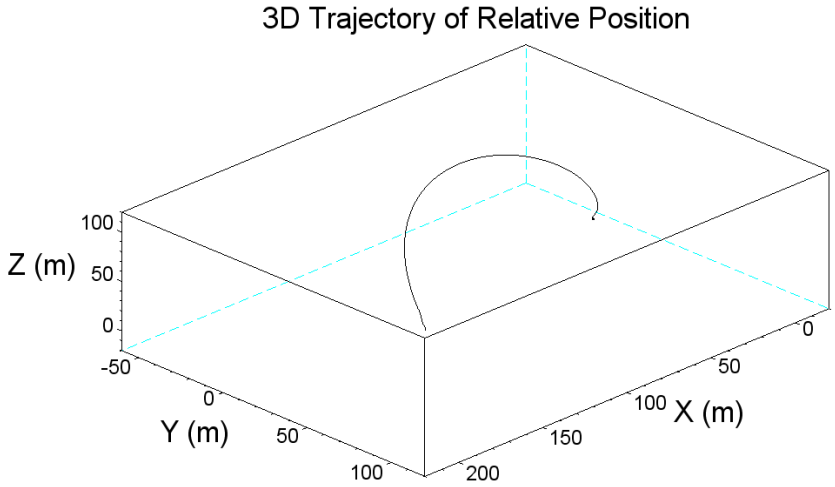

Figure 4.57.: 3D trajectory of relative position for Test Case 4 ($\Delta t = 1000$ seconds), illustrating a controlled and smooth path towards the target, highlighting the efficiency of extended duration control.

The 3D trajectory plot (Figure 4.57) shows a smooth and curved path towards the target, suggesting that the controller efficiently manages the satellite's movement over an extended period, ensuring a gradual and controlled approach.

Figure 4.58 shows a smooth, spiral-like path in the XY plane trajectory, indicating efficient maneuvering in two dimensions. This trajectory ensures minimal oscillations and a direct approach towards the target.

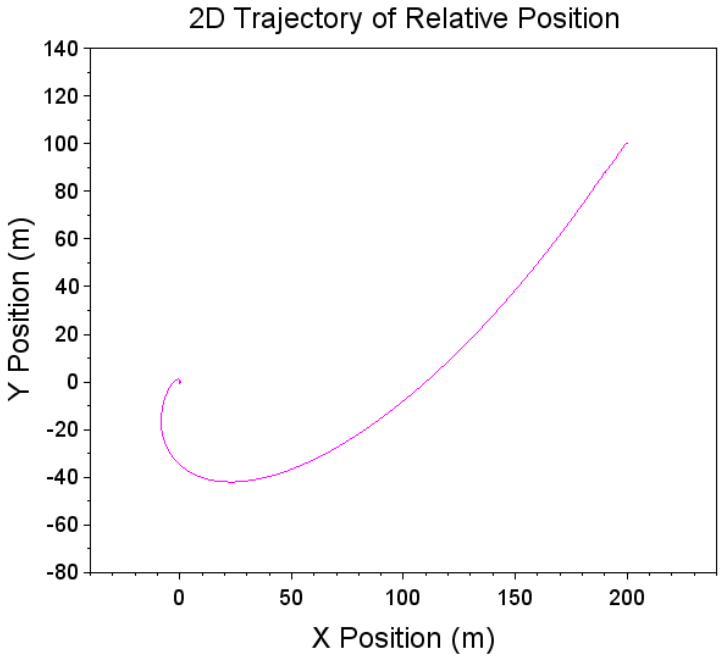

Figure 4.58.: XY plane trajectory of relative position for Test Case 4 ($\Delta t = 1000$ seconds).

Figure 4.59a displays the XY plane velocity trajectory, revealing a complex path with initial oscillations that gradually stabilize, demonstrating the controller's capability to effectively manage speed and direction, achieving a steady approach velocity toward the target. The initial oscillatory trajectory is attributed to the sampling time of 1 second set for the CW-based controller, as detailed in section 4.2.2. When δt(sampling time) is increased to 2 seconds, the trajectory becomes significantly smoother, as shown in Figure 4.59b. This adjustment results in fewer thruster activations while maintaining similar fuel efficiency. The fuel consumption for δt of 2 seconds is 0.0426394 kg, comparably close to the 0.042330 kg consumed when δt is 1 second.

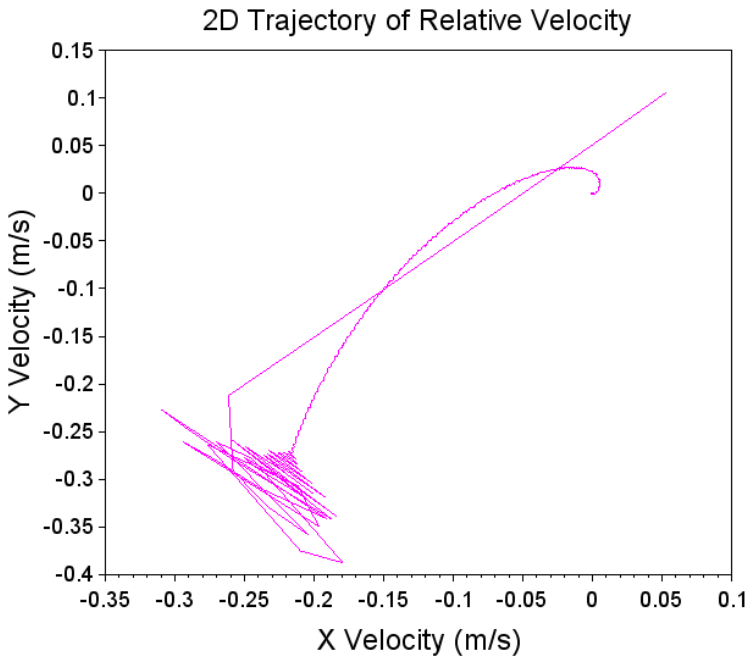

(a) XY plane trajectory of relative velocity for Test Case 4 with with sampling time of 1 second.

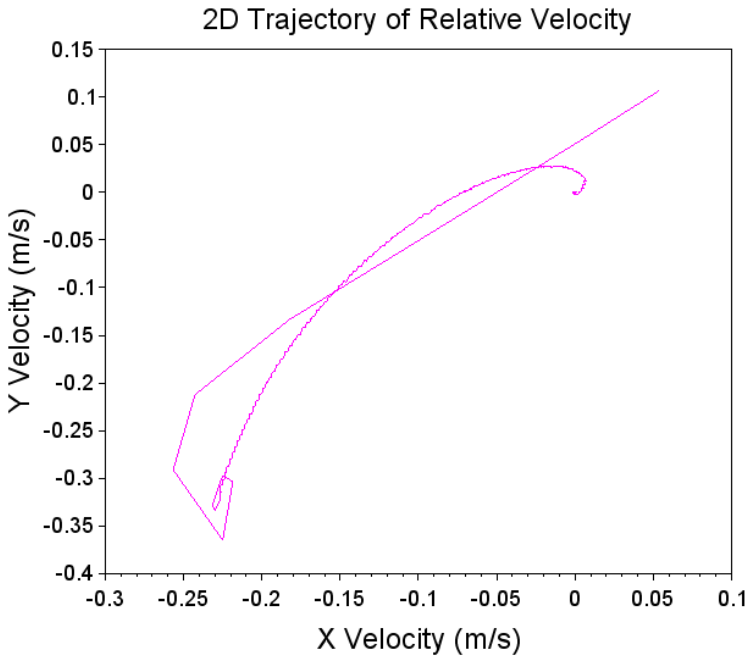

(b) XY plane trajectory of relative velocity for Test Case 4 with increased sampling time of 2 seconds, showcasing a smoother trajectory.

Figure 4.59.: Comparative analysis of XY plane trajectories of relative velocity for Test Case 4 under different sampling conditions, emphasizing the impact of $\Delta t = 1000$ seconds.

The X component plot (Figure 4.60) indicates a rapid initial decrease followed by a stabilization period, which aligns with the expected behavior of the satellite adjusting its position quickly and then maintaining a steady state as it approaches the target.

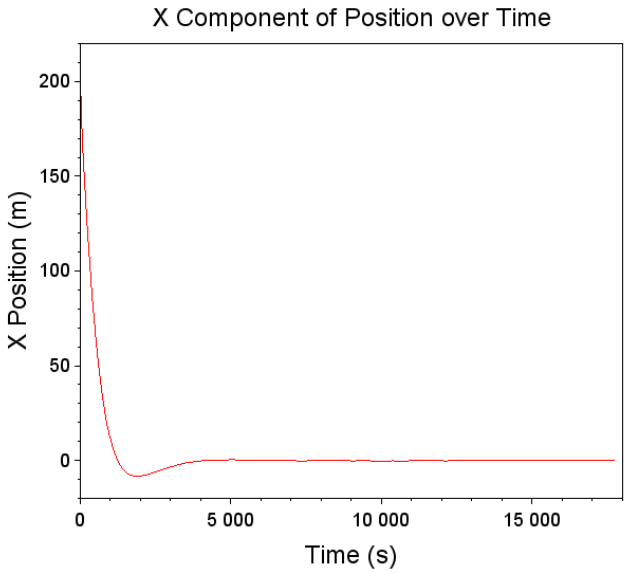

Figure 4.60.: X-axis position over time for Test Case 4 ($\Delta t = 1000$ seconds) demonstrates a rapid initial decrease followed by a stable approach towards the target, showcasing efficient directional control.

The Y component plot (Figure 4.61) shows an initial drop followed by stabilization, similar to the X component. This behavior indicates that the controller manages the Y-axis adjustments effectively to bring the satellite into the desired trajectory. The satellite reaches the target in just over 5000 seconds.

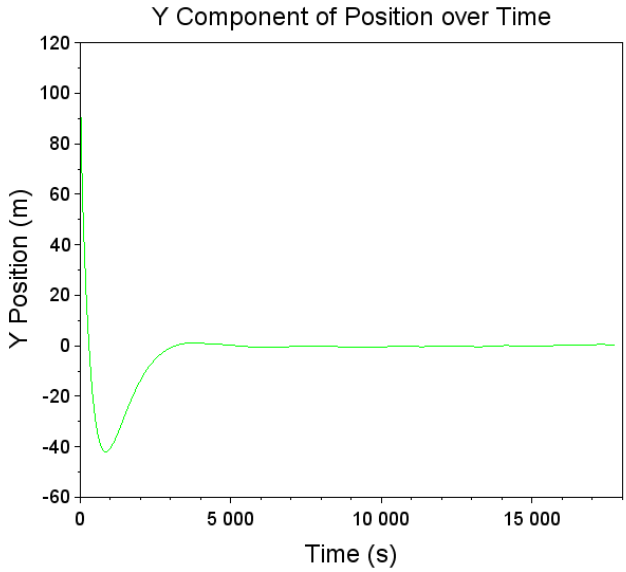

Figure 4.61.: Y-axis position over time for Test Case 4 ($\Delta t = 1000$ seconds) shows an initial drop and subsequent stabilization.

The Z component plot (Figure 4.62) reveals a continuous decrease and eventual stabilization, suggesting effective control in the vertical axis, ensuring the satellite maintains its intended altitude.

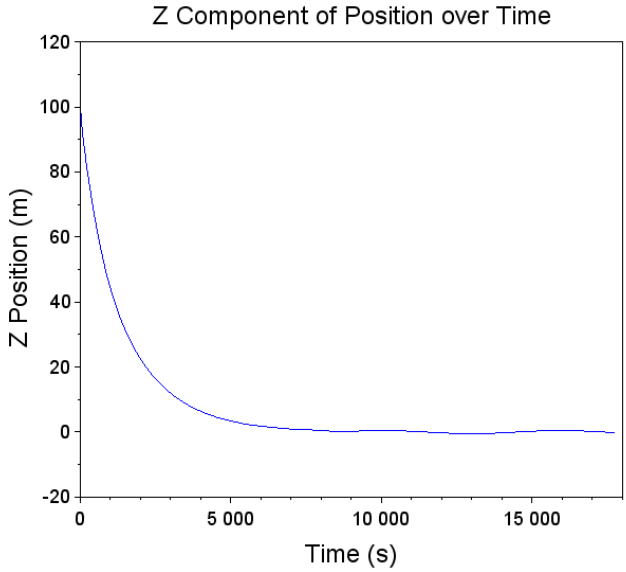

Figure 4.62.: Z-axis position over time for Test Case 4 ($\Delta t = 1000$ seconds) illustrates a continuous decrease and stabilization.

Overall, the results from the fourth test case demonstrate that an increased Δt of

1000 seconds allows the controller to optimize for fuel efficiency and smooth trajectory adjustments, corroborating the hypothesis that longer durations result in lower fuel consumption and controlled maneuvering.

Test Case 5 ($\Delta t = 2000$ seconds)

Test Case 5 investigates the effects of an extended control interval (Δt) of 2000 seconds on trajectory precision, fuel usage, and thruster operation, aiming to evaluate the controller's ability to maintain accuracy over prolonged durations with reduced operational demands. This test, which took approximately 8200 seconds to align the spacecraft with its target, recorded the lowest fuel consumption at 0.041085 kg across all scenarios tested. This underscores the efficiency of the controller in managing long-term trajectory adjustments. The forthcoming figures will provide a detailed visualization of position and velocity, offering a comprehensive view of the extensive control efforts employed in this test case.

Observations and Results:

1. **Trajectory Analysis:** The 3D trajectory plot (Figure 4.63) indicates a smooth and controlled path with minimal deviations, suggesting effective trajectory management by the controller.

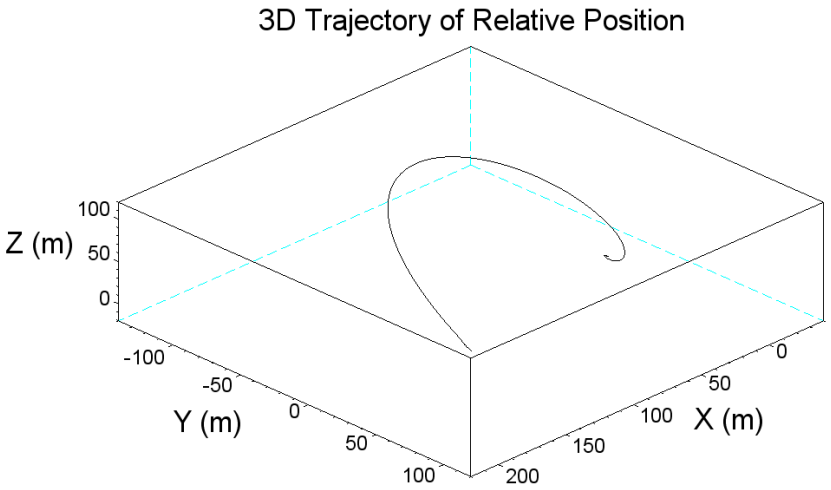

Figure 4.63.: 3D trajectory of relative position for Test Case 5 ($\Delta t = 2000$ seconds), illustrating a smoothly controlled path towards the target with minimal deviations.

The XY plane trajectory plot (Figure 4.64) supports this observation by showing a clear and consistent curvilinear path, reflecting the spacecraft's adherence to its intended trajectory.

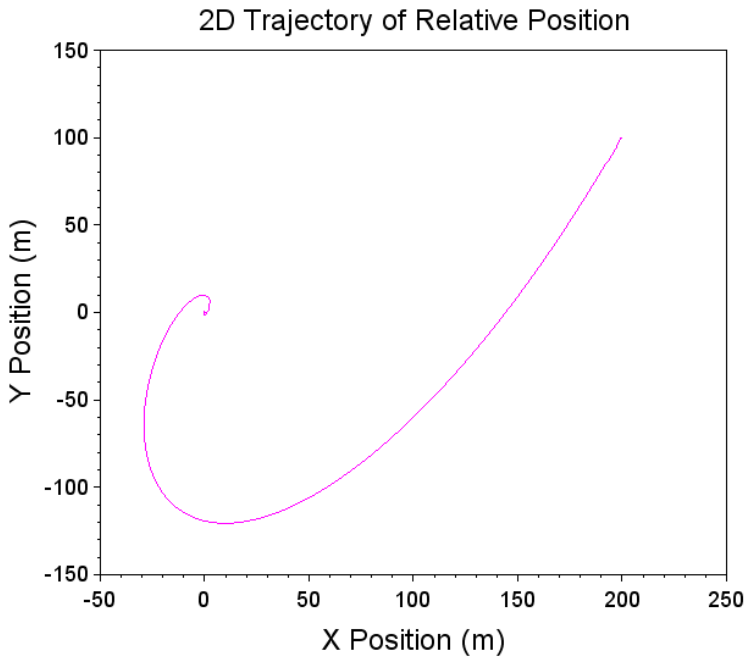

Figure 4.64.: XY plane trajectory of relative position for Test Case 5 ($\Delta t = 2000$ seconds), demonstrating a consistent curvilinear.

2. **Positional Dynamics:** The position time plots for the X axis (Figure 4.65a), Y axis (Figure 4.65b), and Z axis (Figure 4.66) demonstrate a gradual and steady convergence towards the target positions. The extended control period allows for smoother transitions and reduces the need for abrupt adjustments, thereby enhancing the overall stability of the system.

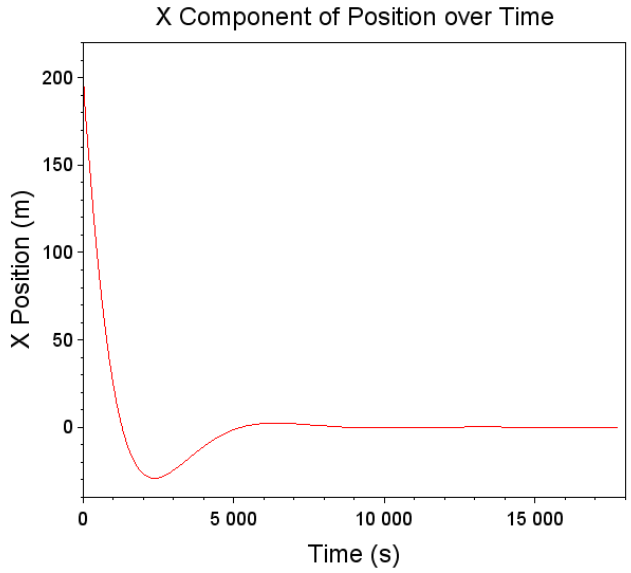

(a) X-axis position over time depicting gradual and steady adjustments toward the target, emphasizing the control strategy's long-term stability.

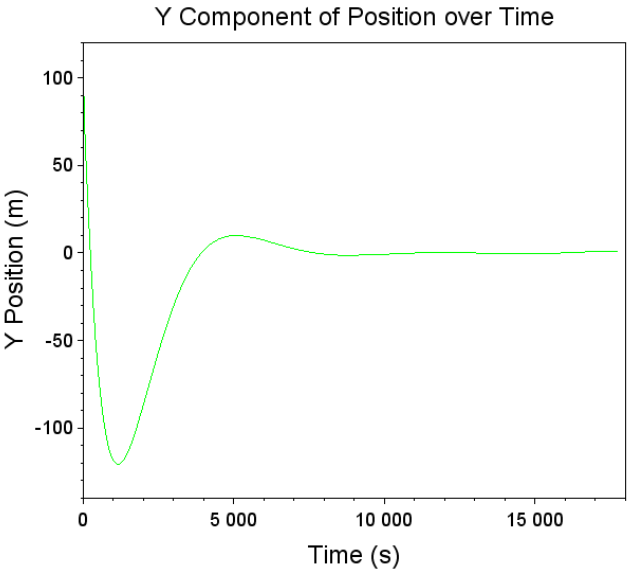

(b) Y-axis position over time showing slow and consistent trajectory adjustments.

Figure 4.65.: Comparative analysis of X and Y-axis position over time in Test Case 5, demonstrating the controller's ability to manage gradual trajectory corrections over a prolonged interval ($\Delta t = 2000$ seconds).

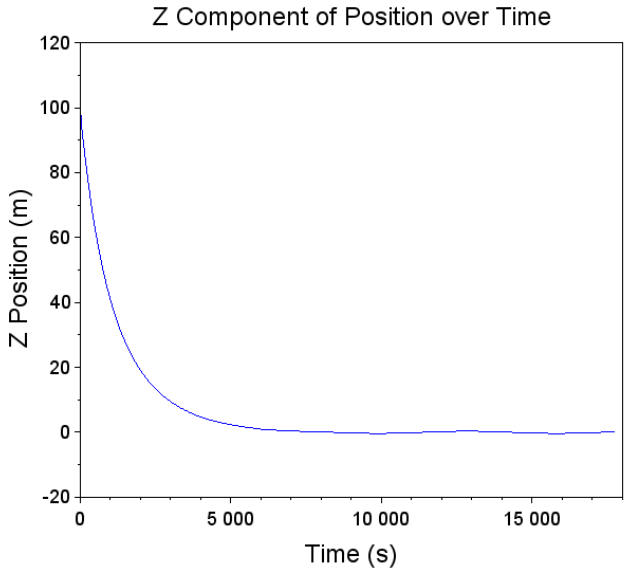

Figure 4.66.: Z-axis position over time for Test Case 5 ($\Delta t = 2000$ seconds), illustrating gradual altitude corrections and stabilization.

3. **Velocity Control:** In the XY plane, the trajectory of relative velocity (Figure 4.67a) presents a stable velocity profile with fewer oscillations compared to the previous test setup. This stabilization is more pronounced when the sampling time is extended to 2 seconds, leading to a smoother trajectory, as illustrated in the figure 4.67b. The fuel consumption for the two sampling durations remains relatively consistent, similar to earlier observations. Specifically, with a 1-second sampling interval, the fuel consumption is 0.4108 kg, while for a 2-second interval, it decreases slightly to 0.0416195 kg. Additionally, there is a notable reduction in thruster activations, dropping from 367 at 1 second to 323 at 2 seconds.

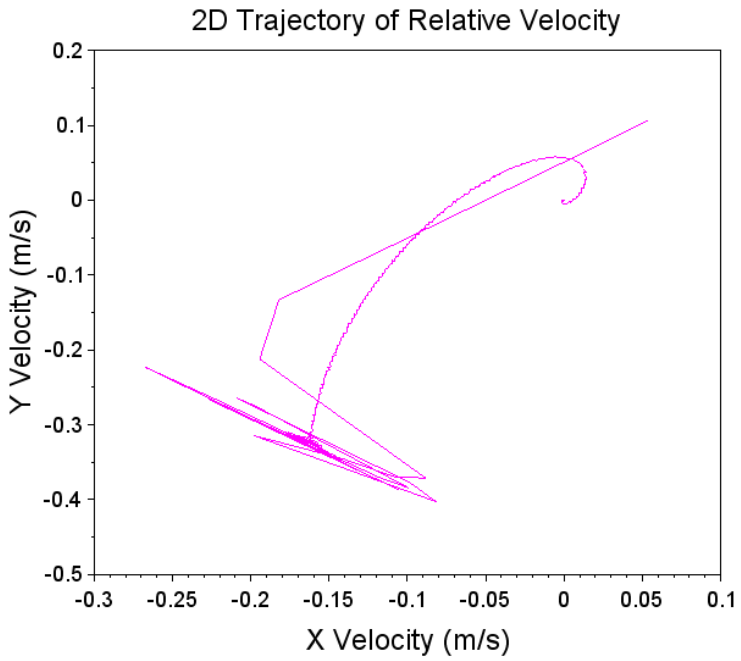

(a) With sampling time of 1 second, displaying regulated velocity.

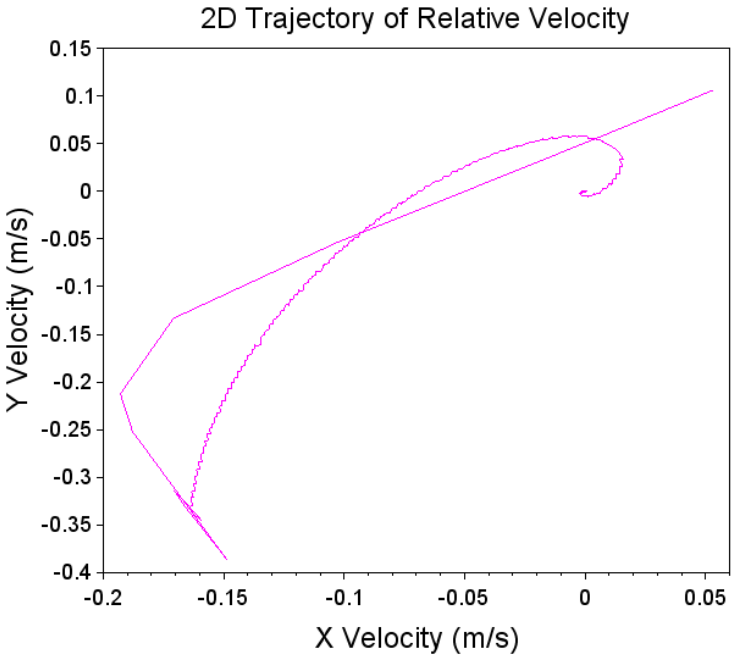

(b) With a 2-second sampling time, showcasing smoother dynamics.

Figure 4.67.: Comparative analysis of XY plane trajectories of relative velocity for Test Case 5 ($\Delta t = 2000$ seconds), illustrating the effect of different sampling times on velocity control.

4. **Thruster Activity:** The bar plot of thruster firings (Figure 4.68) shows Thruster 5(positive z-direction) as the most frequently used with 161 firings, and a total of 367 firings across all thrusters. This distribution demonstrates the controller's ability to optimize thruster usage, effectively balancing fuel consumption and mechanical wear.

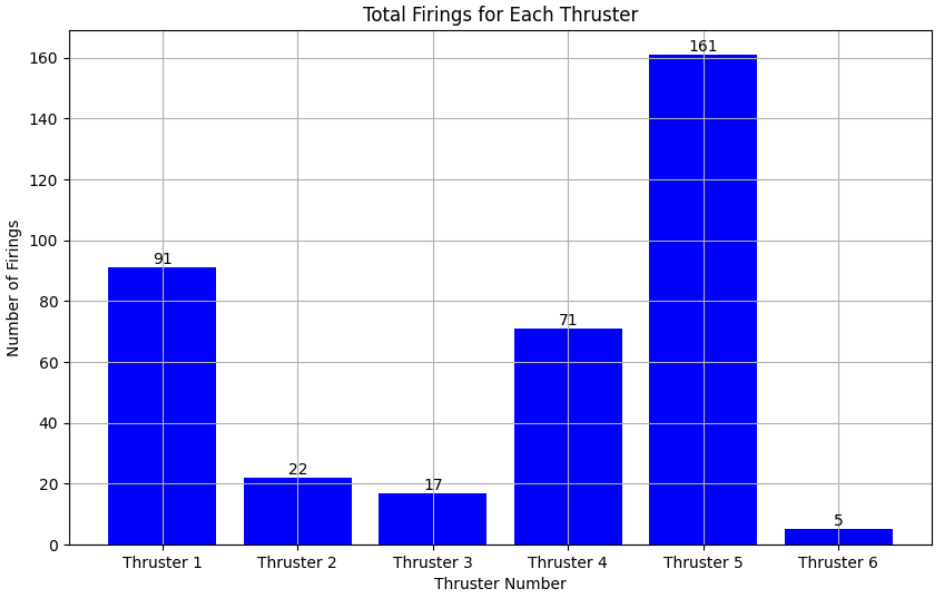

Figure 4.68.: Distribution of thruster firings for Test Case 5 ($\Delta t = 2000$ seconds.

5. **Fuel Efficiency:** The test resulted in the lowest fuel consumption among all scenarios, totaling 0.041085 kg. This significant reduction in fuel usage demonstrates the effectiveness of the extended Δt in minimizing operational costs while maintaining precision in control. Furthermore, the efficient control strategy reduces the frequency of thruster activations, leading to lower fuel usage and more efficient mission operations.

Test Case 5 illustrates that further increasing Δt to 2000 seconds enhances the control system's performance by allowing even more time for each control action to influence the spacecraft's trajectory. This reduction in the frequency and intensity of thruster activations not only ensures precise trajectory following but also significantly lowers fuel consumption and operational complexity. The findings support the hypothesis that longer control intervals contribute to more efficient and stable space mission operations.

Summary of Trajectory Control Tests

The summarized outcomes of the tests, as detailed in Table 4.2, reveal insightful trends and performance metrics across various control durations (Δt). In Test Case 1, with a highly aggressive control interval of just 10 seconds, the spacecraft consumed 1.25467 kg

of fuel and required 1428 thruster firings, underscoring the operational demands of such frequent adjustments. As Δt increased to 100 seconds in Test Case 2, there was a marked decrease in both fuel consumption and thruster usage, demonstrating improved efficiency with longer control intervals. This trend continued in subsequent tests; Test Cases 3 and 4 showed further reductions in fuel consumption with increasing Δt, reflecting the controller's ability to optimize performance over longer intervals. Notably, Test Case 5, with the longest Δt of 2000 seconds, achieved the lowest fuel consumption and a relatively lower number of thruster firings, highlighting the potential benefits of extended control durations for long-term space missions. These results underscore the significance of choosing appropriate control intervals to balance fuel efficiency, operational complexity, and trajectory precision.

Test Case	Δt **(seconds)**	**Fuel Consumption (kg)**	**Total Thruster Firings**
1	10	1.25467	1428
2	100	0.18472	360
3	500	0.0563865	460
4	1000	0.0423301	393
5	2000	0.041085	367

Table 4.2.: Comparative Analysis of Fuel Consumption and Thruster Firings Across Different Control Durations (Δt) in Trajectory Control Tests.

4.5.4. Observations on LQR and CW Controller Performance

The comparative analysis of the LQR and CW controllers reveals their respective strengths and applications in space missions, focusing on scenarios such as station-keeping and rendezvous.

- **Fuel Efficiency and Control Precision:** The LQR controller showcases exemplary fuel efficiency in Test Case 4, consuming merely 0.0733 kg of fuel. This exceptional efficiency, combined with its high control precision, renders it highly suitable for station-keeping missions where minimal deviation is critical. In contrast, the CW controller demonstrated in Test Case 2 uses more fuel (0.4 kg) but facilitates smoother velocity adjustments, ideal for the initial phases of rendezvous missions where gradual trajectory alignment is beneficial.
- **Thruster Activity and Operational Demand:** In Test Case 1, the LQR controller required the highest thruster firings (1605), suitable for complex maneuvers such as rendezvous, where precise and rapid positioning is crucial. The CW controller, while less demanding in thruster use, supports extended station-keeping with fewer activations, evident from its performance in Test Case 2 with only 179 firings.

- **Mission Suitability:** The rapid responsiveness of the LQR controller, particularly noted in Test Case 1, suits short-duration, high-precision tasks such as docking or complex orbital insertions. Conversely, the CW controller, with its gentler adjustment capabilities shown in Test Case 2, is better for long-term missions such as Earth observation or geostationary orbit maintenance, where stability and fuel efficiency are prioritized.
- **Additional Mission Contexts:** Beyond station-keeping and rendezvous, the LQR controller could be effectively used in debris avoidance maneuvers and emergency corrections due to its quick action capabilities. The CW controller, offering steady and predictable control, might better serve in scientific missions requiring stable platforms or in deploying satellite constellations where consistent inter-satellite spacing must be maintained.

The choice between LQR and CW controllers should be guided by the specific requirements of the mission, considering factors like the urgency of maneuver execution, the precision needed in trajectory control, and the duration over which the spacecraft must maintain its position or trajectory. This thoughtful selection will ensure that mission objectives are met efficiently and effectively.

4.6. Monte Carlo Simulations for Controller Evaluation

Monte Carlo simulations are indispensable in the analysis and design of control systems. These simulations employ random sampling techniques to generate numerous scenarios, reflecting the probabilistic variations in input parameters that a system may encounter. This approach is particularly valuable in control systems engineering for evaluating the robustness and effectiveness of controllers, such as the LQR, under diverse and uncertain conditions.

Simulation Setup and Controller Testing

This subsection details the simulation parameters and outcomes from evaluating different control strategies on an orbital chaser spacecraft. The simulations encompass three full orbits, amounting to 17,752.26 seconds, with both the target and the chaser positioned in a 700 km orbit above Earth. Initial conditions for the simulations are chosen to reflect typical mission scenarios, including orbital altitude at 700 km and specific orbital elements and velocity parameters.

4.6.1. Applying Monte Carlo Simulations in LQR Evaluation

In this study, Monte Carlo simulations are utilized to assess the performance of the LQR controller across a spectrum of initial conditions and disturbances. By simulating initial conditions ranging from -2500 m to $+2500$ m for position and velocity vectors, these tests replicate realistic operational uncertainties that the spacecraft might face during extended missions.

Controller Configuration The LQR controller's responsiveness to variations in initial conditions is critically evaluated by adjusting the weight matrices Q and R. These

matrices balance the minimization of state errors and control effort, thereby influencing the system's overall stability and fuel efficiency.

Test Case 1: High Initial Condition Variability

Controller Setup In Test Case 1, the LQR controller is configured to handle high variability in initial conditions, critical for missions requiring robust control under significant disturbances. The weight matrices are set as follows:

$$Q = \begin{bmatrix} 10 & 0 & 0 & 0 & 0 & 0 \\ 0 & 10 & 0 & 0 & 0 & 0 \\ 0 & 0 & 10 & 0 & 0 & 0 \\ 0 & 0 & 0 & 1 & 0 & 0 \\ 0 & 0 & 0 & 0 & 1 & 0 \\ 0 & 0 & 0 & 0 & 0 & 1 \end{bmatrix} \qquad R = \begin{bmatrix} 1000 & 0 & 0 \\ 0 & 1000 & 0 \\ 0 & 0 & 1000 \end{bmatrix}$$

This configuration aims to achieve an optimal balance between position accuracy and fuel economy.

Observations from Extended and Standard Initial Conditions The Monte Carlo simulations reveal distinct behaviors under two sets of initial conditions:

- **Extended Range ($[-2500, 2500]$ m):** This scenario includes a notable test where the system did not converge, with the chaser drifting significantly from the target along the X and Y axes. This behavior, illustrated in Figures 4.69a and 4.70a, suggests potential instabilities under large initial perturbations.

- **Standard Range ($[-1500, 1500]$ m):** Contrarily, tests within this range generally showed consistent convergence and effective control. The robustness of the controller in maintaining stability is evident from Figures 4.69b and 4.70b.

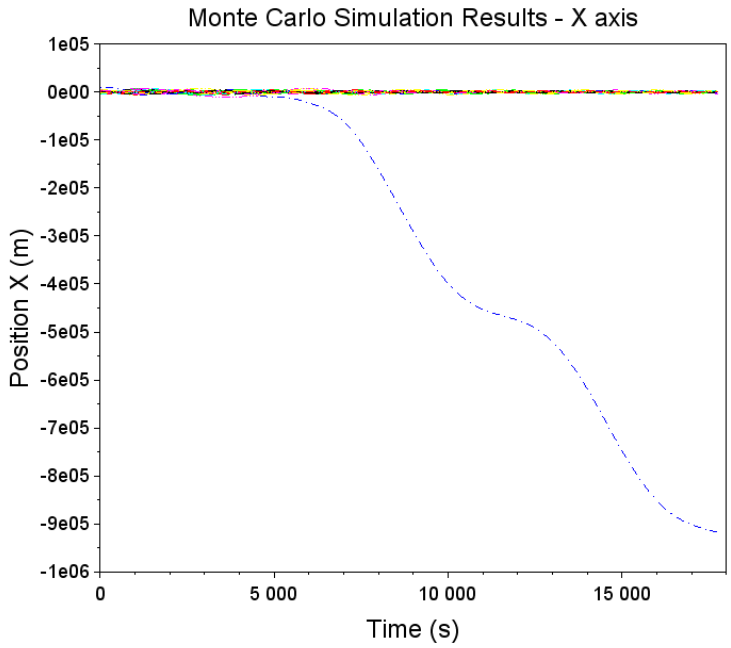

(a) X-axis performance under extended conditions, illustrating instances of non-convergence.

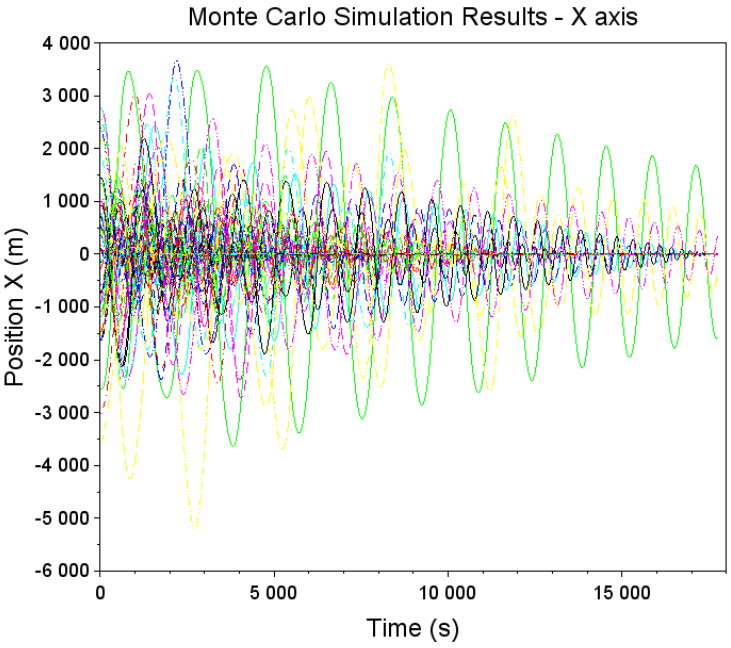

(b) X-axis performance under standard conditions, showing consistent convergence.

Figure 4.69.: Comparison of X-axis position tracking under varied initial conditions. (Test Case 1, LQR)

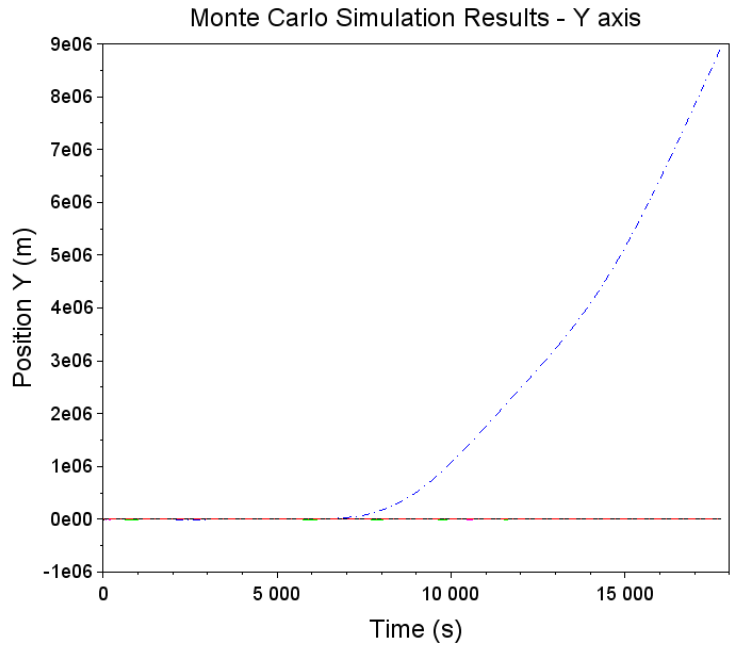

(a) Y-axis performance under extended conditions, indicating potential instabilities.

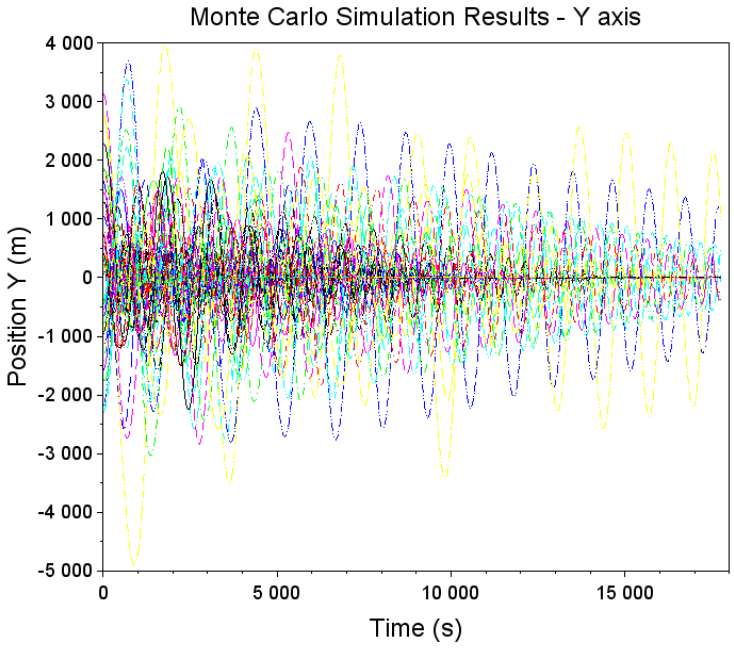

(b) Y-axis performance under standard conditions, confirming stability.

Figure 4.70.: Comparison of Y-axis position tracking under different initial conditions. (Test Case 1, LQR)

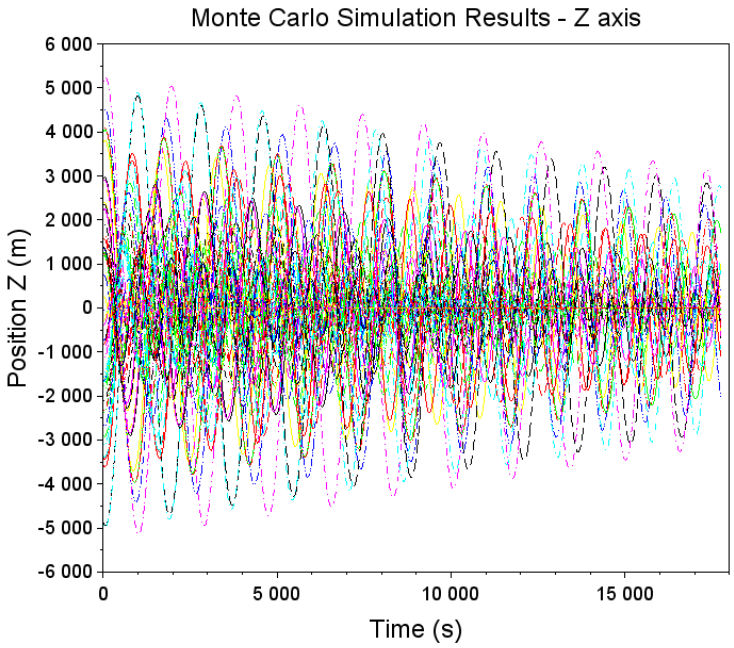

(a) Z-axis performance with extended initial conditions showing non-convergence.

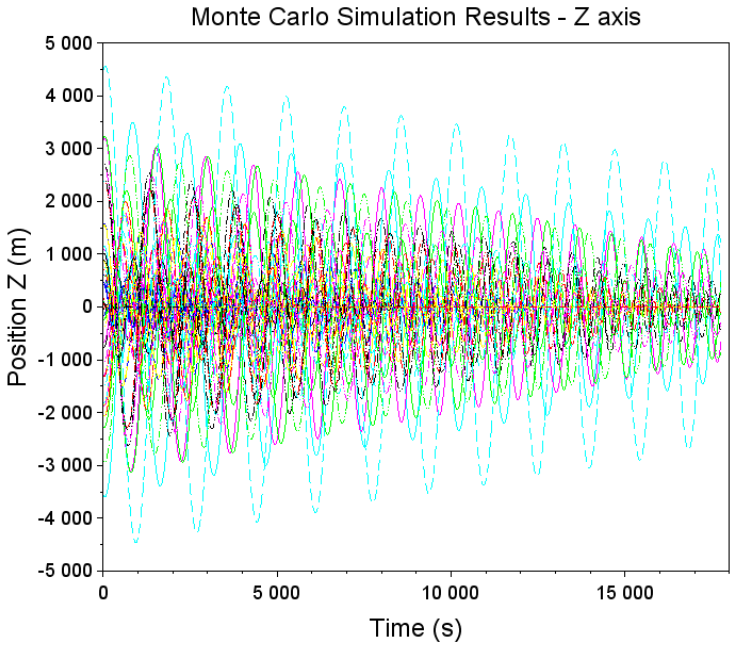

(b) Z-axis performance with standard initial conditions demonstrating stability in comparision to the extended initial contiditions.

Figure 4.71.: Comparison of Z-axis position tracking under varied initial conditions. (Test Case 1, LQR)

Thruster Activity Analysis The analysis of thruster firings provides insights into the control efforts and optimization strategies employed by the controller. Figure 4.72 illustrates the thruster firings across all tests, highlighting the minimum and maximum firings for each thruster.

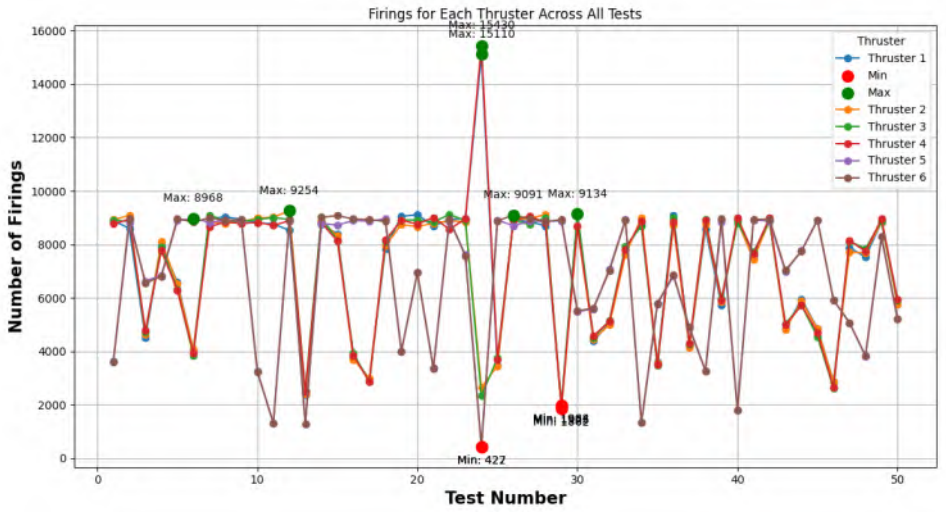

Figure 4.72.: Thruster firing frequency across all tests, highlighting optimization and control effort. (Test Case 1, LQR)

The plot reveals a varied distribution of thruster usage. Notably, Thruster 4 shows the highest number of firings, with a maximum of 15,430 firings for the 25^{th} test in the Monte Carlo simulation. Conversely, the minimum number of firings is observed for Thruster 6, with only 422 firings for test number 24. This distribution underscores the controller's optimization in thruster activation, balancing fuel consumption and mechanical wear across the different thrusters.

Test Case 2: Moderate Emphasis on Velocity and Control Weights

Controller Setup
In Test Case 2, the LQR controller is configured with a moderate emphasis on velocity

and control weights rather than position. The weight matrices are adjusted as follows:

$$Q = \begin{bmatrix} 10 & 0 & 0 & 0 & 0 & 0 \\ 0 & 10 & 0 & 0 & 0 & 0 \\ 0 & 0 & 10 & 0 & 0 & 0 \\ 0 & 0 & 0 & 100 & 0 & 0 \\ 0 & 0 & 0 & 0 & 100 & 0 \\ 0 & 0 & 0 & 0 & 0 & 100 \end{bmatrix}, \quad R = \begin{bmatrix} 100 & 0 & 0 \\ 0 & 100 & 0 \\ 0 & 0 & 100 \end{bmatrix}$$

This setup aims to achieve a balanced approach between maintaining velocity control and minimizing fuel usage.

Observations and Results:

Position Control Analysis: The Monte Carlo simulations show the X-axis position results (Figure 4.73a) indicating that the controller manages to stabilize the position with minimal oscillations around the zero position. The Y-axis results (Figure 4.73b) depict a similar trend with slightly higher oscillations initially that dampen over time. The Z-axis (Figure 4.74) also shows effective stabilization, confirming the controller's ability to handle three-dimensional control requirements efficiently.

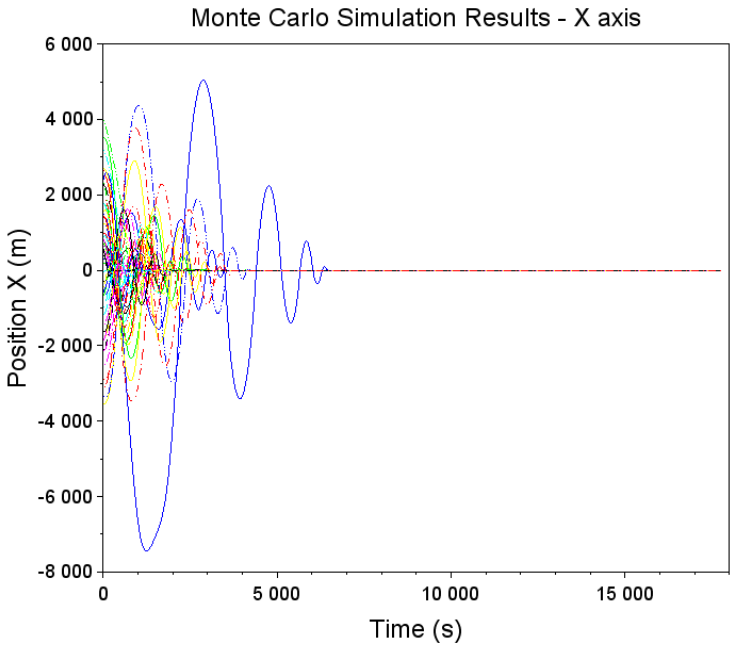

(a) X-axis Position Control: This plot displays the controller's response to diverse initial conditions, with most test cases converging to the target by 8000 seconds.

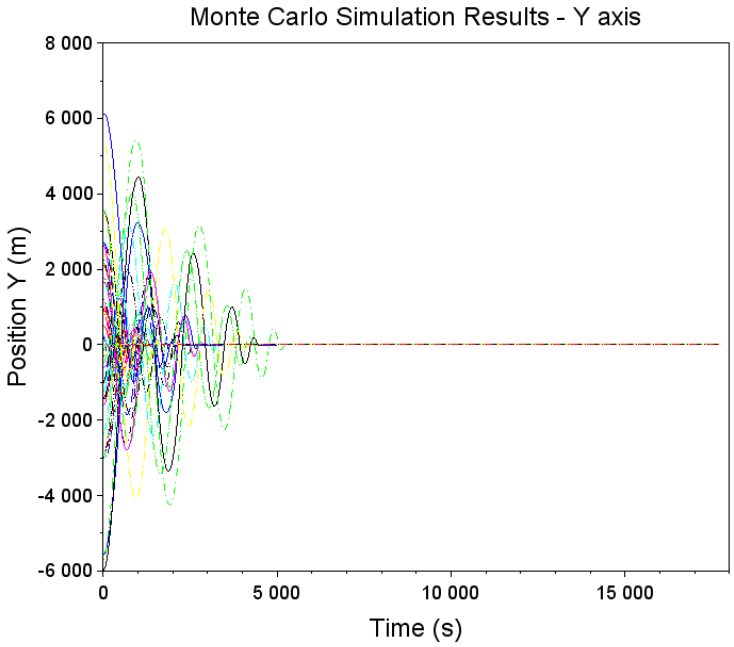

(b) Y-axis Position Control: The results demonstrate effective lateral control, typically achieving stability near the target around 8000 seconds.

Figure 4.73.: Comparative Monte Carlo simulation results for the X and Y axes in Test Case 2, showcasing the LQR controller's stabilization effectiveness.

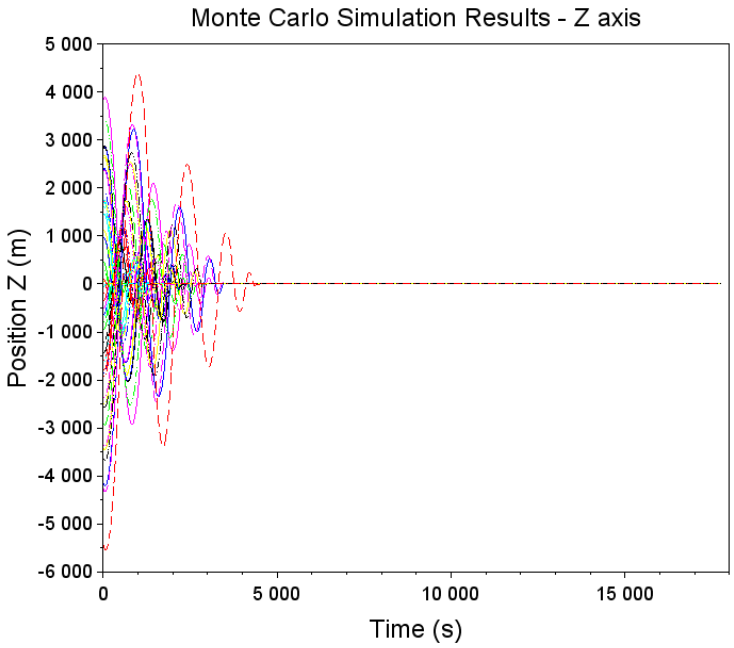

Figure 4.74.: Test Case 2, LQR Controller - Monte Carlo Simulation Results for Z-axis Position Control: The plot indicates a quicker stabilization in the vertical dimension, with most simulations converging to the target by 5000 seconds.

Thruster Activity: The distribution and frequency of thruster activations are detailed in Figure 4.75. Notably, the thruster for the positive x-direction exhibits the highest activity, firing a total of 3687 times. Conversely, the least frequent activations occur with the positive z-direction thruster, which fires only 44 times. This pattern indicates a generally balanced thruster use, although some disparities exist, demonstrating how the controller adapts to sustain the spacecraft's position and velocity within the required parameters.

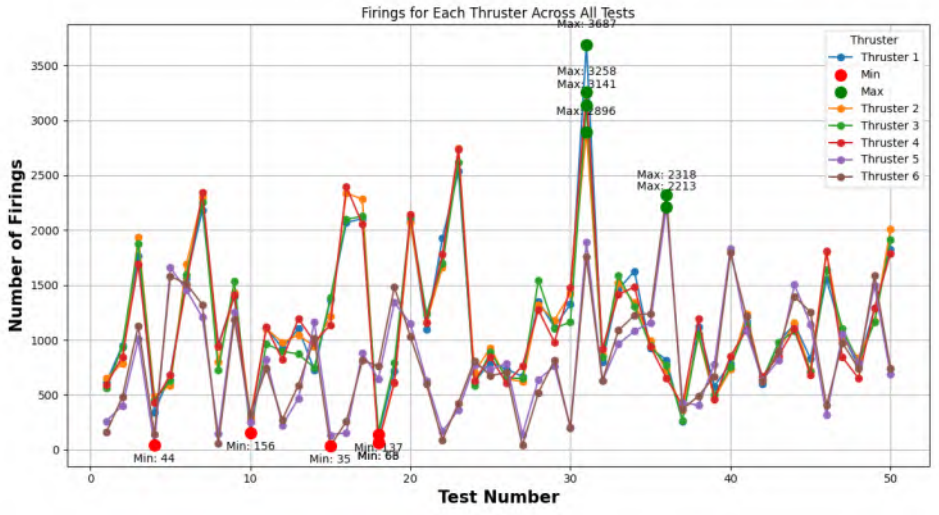

Figure 4.75.: Test Case 2, LQR Controller - Thruster Firings Distribution: This chart illustrates the thruster usage, with Thruster 4 exhibiting the highest activity, peaking at 17,331 firings, and Thruster 6 showing the least, with only 161 firings across the tests.

The Monte Carlo simulations for Test Case 2 demonstrate the LQR controller's robustness and efficiency in maintaining precise position control. The results highlight the controller's effectiveness in stabilizing the spacecraft's trajectory with optimized thruster activity, thereby ensuring minimal fuel consumption while achieving the desired control objectives.

Test Case 3: Emphasis on High-Control and Velocity Weights

Test Case 3 explores the performance of the control system with significantly high weights assigned to control efforts and velocity components. This configuration aims to investigate the system's behavior under a setup that strongly prioritizes minimizing control actions and maintaining strict velocity regulation.

$$Q = \begin{bmatrix} 0 & 0 & 0 & 0 & 0 & 0 \\ 0 & 0 & 0 & 0 & 0 & 0 \\ 0 & 0 & 0 & 0 & 0 & 0 \\ 0 & 0 & 0 & 100000 & 0 & 0 \\ 0 & 0 & 0 & 0 & 100000 & 0 \\ 0 & 0 & 0 & 0 & 0 & 100000 \end{bmatrix}, \quad R = \begin{bmatrix} 100000 & 0 & 0 \\ 0 & 100000 & 0 \\ 0 & 0 & 100000 \end{bmatrix}$$

The analysis of the Monte Carlo simulations for Test Case 3, as depicted in Figures 4.76, 4.77a, and 4.77b, reveals notable observations in terms of position tracking performance across the X, Y, and Z axes. Each plot represents the variations in the respective axis positions over time under the influence of the given weight matrices.

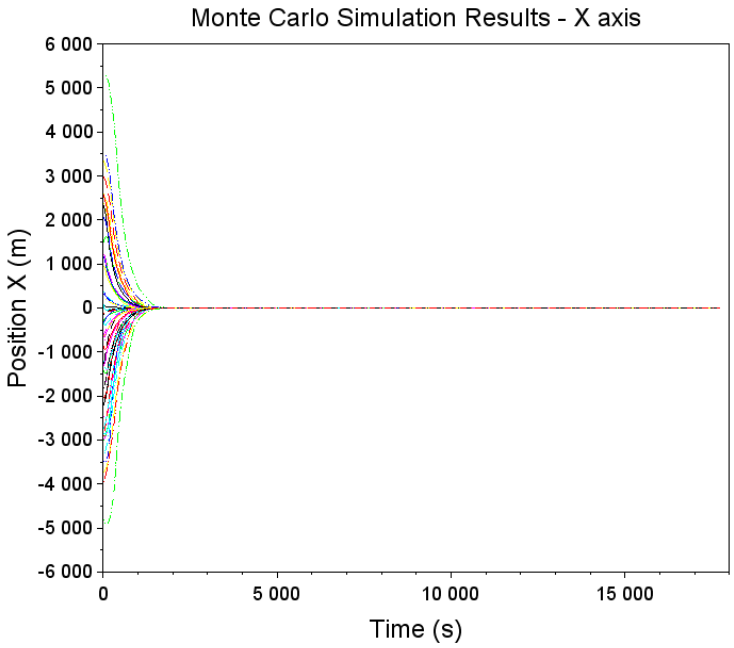

Figure 4.76.: Monte Carlo simulation results for the X-axis in Test Case 3 (LQR controller): The system stabilizes to the target position by approximately 2,000 seconds, demonstrating rapid convergence under high-control and velocity weights.

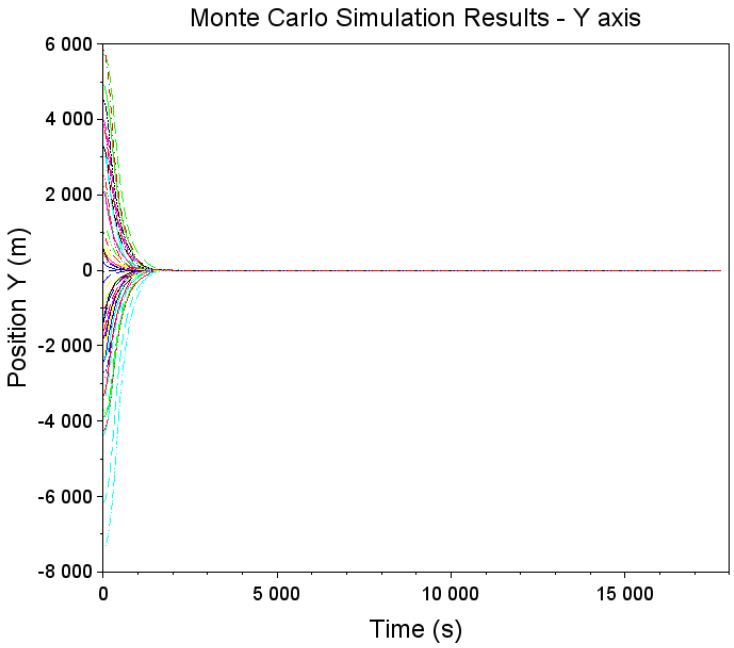

(a) The Y-axis converges to stability around 2,000 seconds similar to the X-axis.

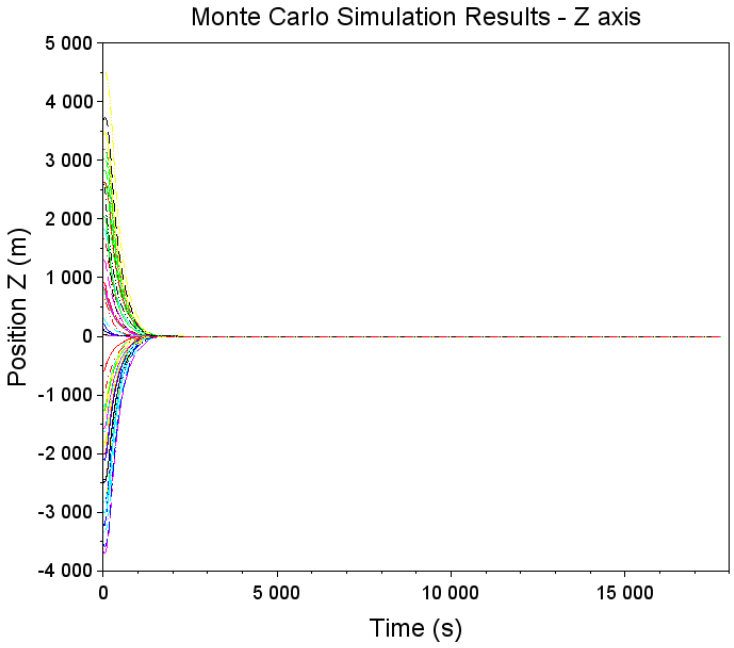

(b) The Z-axis shows slightly quicker stabilization, converging by approximately 1,900 seconds, indicating a slightly faster response in vertical control.

Figure 4.77.: Comparative Monte Carlo simulation results for the Y and Z axes in Test Case 3.

Thruster Firings: The thruster firing activity across all simulations is illustrated in Figure 4.78. This figure highlights the frequency and distribution of firings for each thruster, indicating the controller's strategy in balancing control efforts while maintaining the desired trajectory. The maximum and minimum firing annotations provide insight into the variability and demand of each thruster.

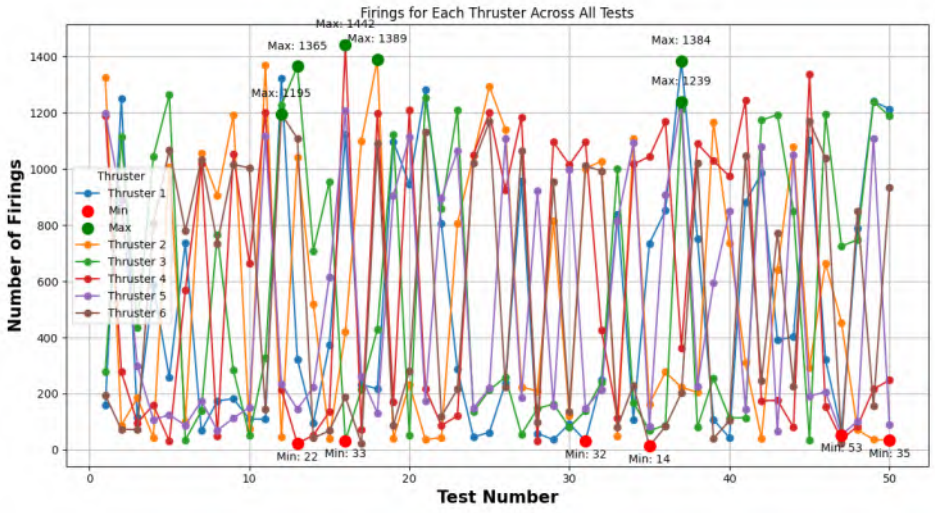

Figure 4.78.: Thruster firings for Test Case 3 (LQR controller) across all Monte Carlo tests with min/max annotations: This bar graph illustrates the variable thruster activity with a maximum of 1,484 firings for Thruster 2 and a minimum of 24 firings for Thruster 6, indicating the variability in control demands across different tests.

Observations:

- **Position Tracking:** The simulations demonstrate that with high control and velocity weights, the system achieves precise position control with minimal oscillations. This indicates strong convergence and stability, underscoring the effectiveness of the control parameters in maintaining accurate trajectory adherence.

- **Thruster Firings:** Analysis indicates a highly concentrated distribution of thruster firings, with some thrusters experiencing significantly higher usage. Despite this concentration, the overall number of firings is relatively low compared to previous test cases. The maximum observed was 1442 firings for the negative y-direction thruster in test case 16, while the minimum was just 14 firings for the negative z-direction thruster.

The Figure 4.79 illustrates a 3D plot from Monte Carlo simulations for test case 3. This visualization demonstrates how various initial conditions of the spacecraft converge towards a common point — the target or origin.

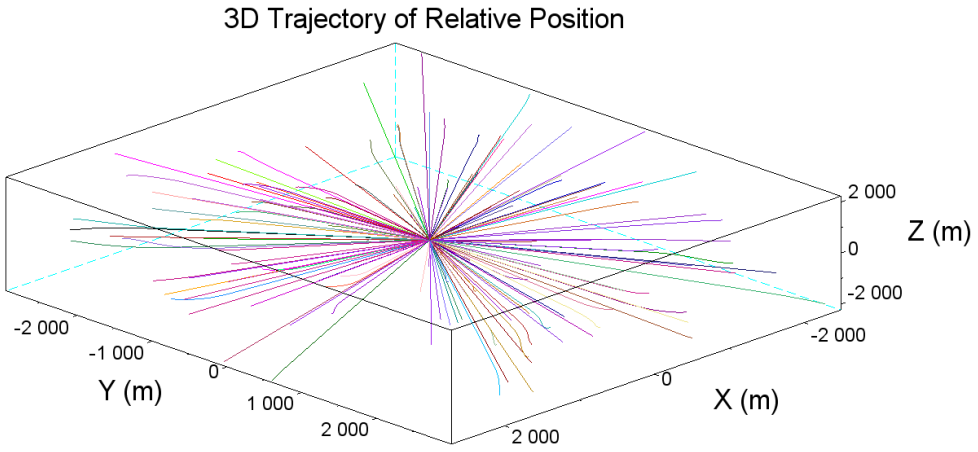

Figure 4.79.: 3D visualization of trajectories converging to the target, demonstrating the control system's capability to correct deviations and guide the spacecraft accurately despite varying initial states.

Observations from Monte Carlo Simulations

Test Case 1: High Initial Condition Variability

- **Observations**: The controller faced challenges in achieving convergence with extreme initial condition variations ($[-2500, 2500]$ m). Instability was noted along the X and Y axes, suggesting suboptimal settings for missions with large disturbances.
- **Recommendations**: This configuration may require adjustments for station-keeping missions and is less suited for complex rendezvous operations requiring high adaptability.

Test Case 2: Moderate Emphasis on Velocity and Control Weights

- **Observations**: Demonstrated stability with minimal oscillations, effectively balancing fuel efficiency and control effectiveness.
- **Recommendations**: Suitable for typical station-keeping and early-stage rendezvous operations where drastic maneuvers are not required.

Test Case 3: Emphasis on High-Control and Velocity Weights

- **Observations**: Showed robust performance with quick convergence and minimal oscillations, enhancing system responsiveness.
- **Recommendations**: Ideal for critical rendezvous phases and emergency maneuvers in orbit requiring rapid stabilization.

Thruster Activity Analysis

Lower thruster firings indicated more efficient control strategies, which reduces wear and operational costs. Notably, Test Case 3, despite its aggressive control strategy, demonstrated efficient use of thrusters compared to Test Case 1.

Fuel Efficiency and Mission Suitability

- **General Trend**: Fewer thruster firings correlated with better fuel efficiency, essential for long-duration missions.
- **Specific Recommendations**: Test Case 2's moderate control weights offer a balanced approach for extended station-keeping or Earth observation missions.

Concluding Recommendations

- **For High Precision and Quick Response**: Use settings similar to Test Case 3.
- **For Fuel Efficiency and Moderate Control**: Prefer settings used in Test Case 2.
- **For Large Disturbances**: Further tuning of Test Case 1 or consider alternative strategies.

This analysis emphasizes the importance of aligning control strategies with specific space mission demands to optimize both control performance and resource utilization.

4.6.2. Monte Carlo Evaluation of CW Based Controllers

This section presents the Monte Carlo tests conducted to evaluate the trajectory control using the controller based on CW feedback. These tests are critical for assessing the robustness and reliability of the controller under varied initial conditions. The primary variable in these tests is the time to target (Δt), ranging from 10 seconds to 2000 seconds, exploring the system's response across different time scales and operational scenarios.

Test Case 1: Rapid Maneuvering with $\Delta t = 10$ seconds

The objective of this test case was to evaluate the controller response within an extremely short time frame ($\Delta t = 10$ seconds), challenging the controller's ability to stabilize the spacecraft swiftly. The simulations were conducted with initial position and velocity vectors randomized within a range of $[-2500, 2500]$ meters to test the system under stressful conditions.

Standard Test Range Results The results from the standard test range of $[-1500, 1500]$ meters showed a better convergence towards the target coordinates within the allotted time in comparision to the extended test range, as expected under less extreme conditions. Figures 4.80a, 4.81a, and 4.82 illustrate these trajectories, demonstrating the system's capability to efficiently manage typical operational disturbances.

Extended Test Range Results Expanding the test range to $[-2500, 2500]$ meters. As shown in Figures 4.80b, 4.81b, and 4.83, the system failed to achieve convergence within the 10-second window. These outcomes underline the limitations when exposed to wider parameter variances, particularly noticeable in the x and y axes where significant divergences occurred.

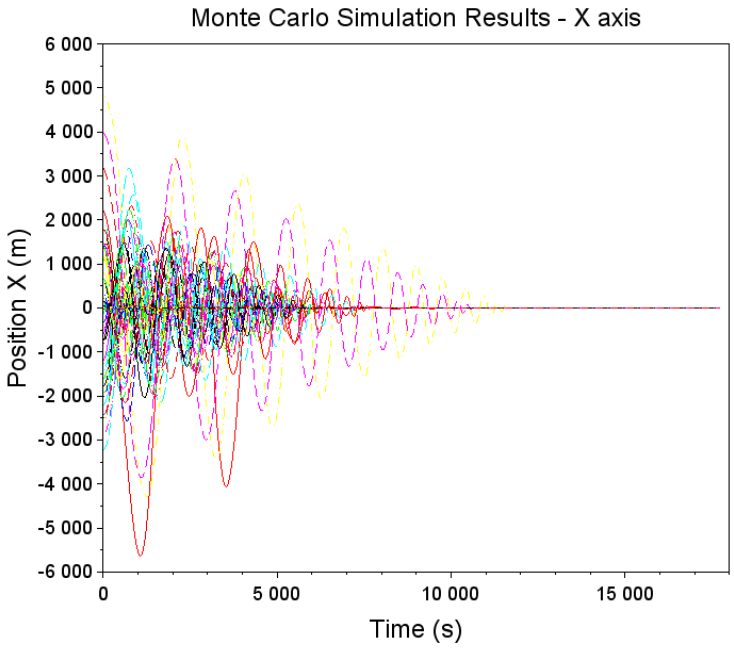

(a) Results under standard initial conditions, demonstrating convergence in most cases over a three-orbit simulation period.

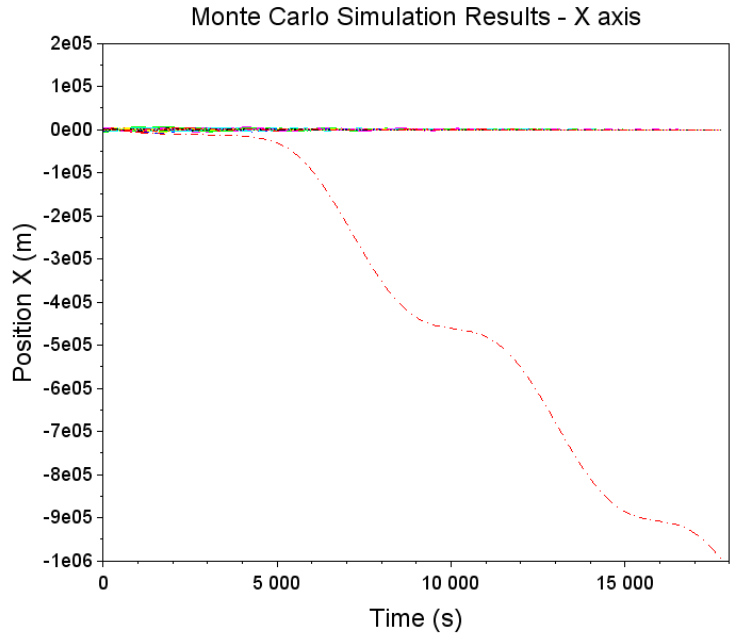

(b) Extended range results illustrating control challenges, with notable divergence observed in one specific test.

Figure 4.80.: Test Case 1 ($\Delta t = 10$ seconds): Monte Carlo simulation results for the x-axis under different initial condition ranges.

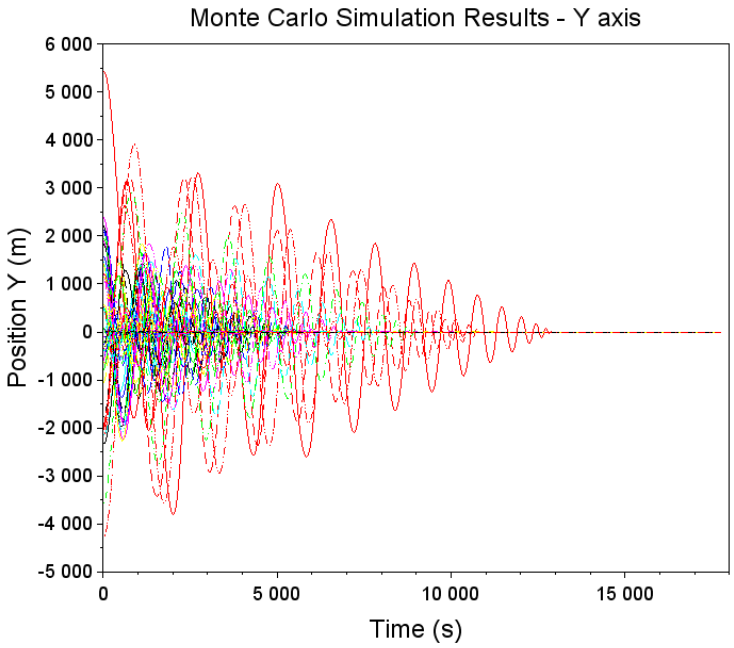

(a) Results under standard initial conditions depicting convergence across most simulations for a 3-orbit duration.

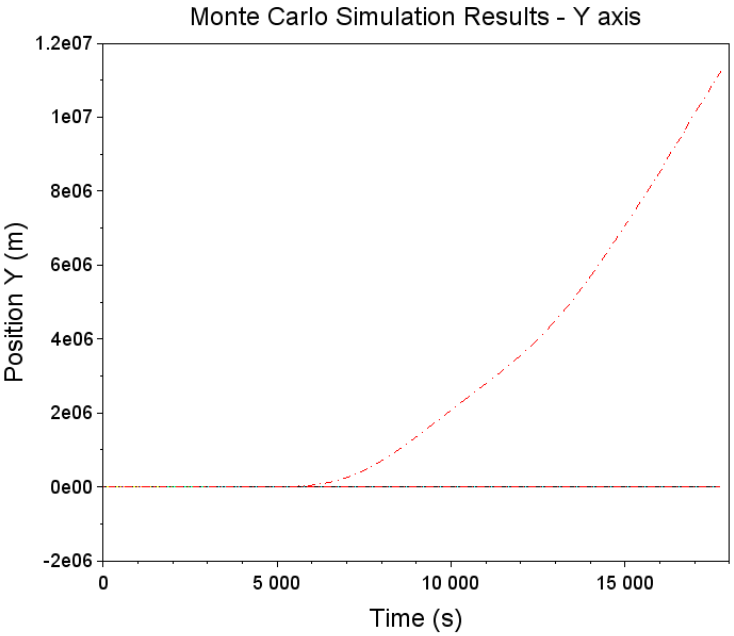

(b) Extended range results illustrating control challenges, with notable divergence observed in one specific test.

Figure 4.81.: Trajectory analyses of spacecraft y-axis position in Monte Carlo simulations for Test Case 1 with $\Delta t = 10$ seconds.

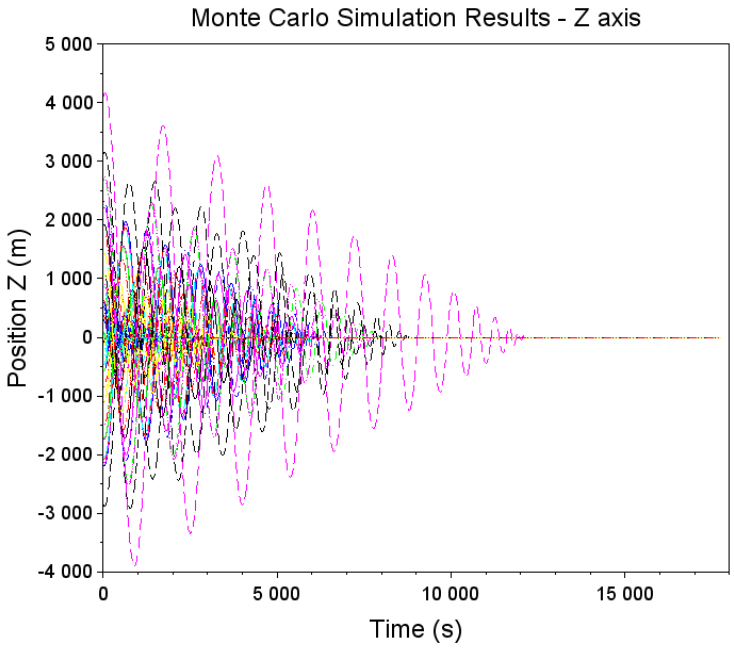

Figure 4.82.: Results under standard initial conditions showing convergence across most simulations for a 3-orbit period.

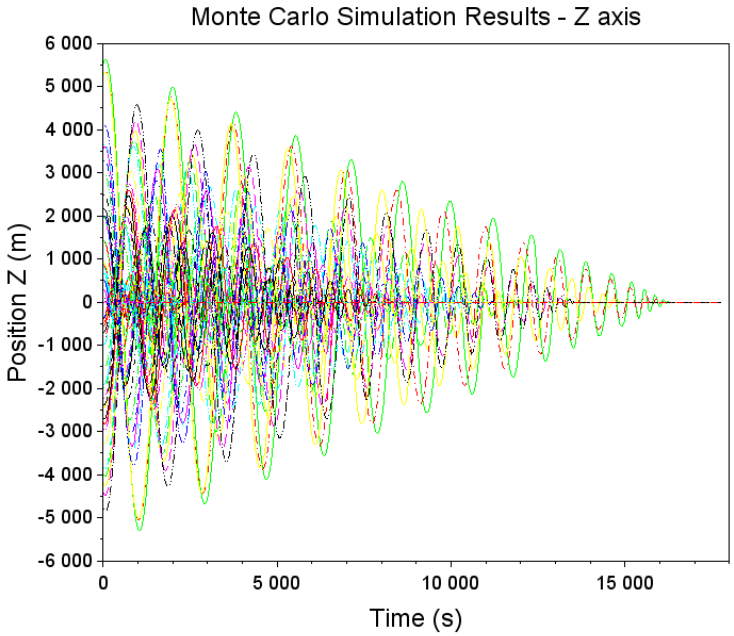

Figure 4.83.: Results under extended initial conditions also demonstrating convergence for most cases.

Figure 4.84.: Comparison of Monte Carlo simulation results for the z-axis, showing the effects of standard and increased initial conditions at $\Delta t = 10$ seconds.

Analysis of Thruster Firings Complementary to trajectory analyses, thruster firing patterns were also recorded, offering insights into control effort distribution and intensity. The standard range tests depicted consistent thruster usage, while the extended range tests, as shown in Figure 4.85, highlighted increased and erratic thruster activity, indicating higher control efforts to counteract larger initial perturbations.

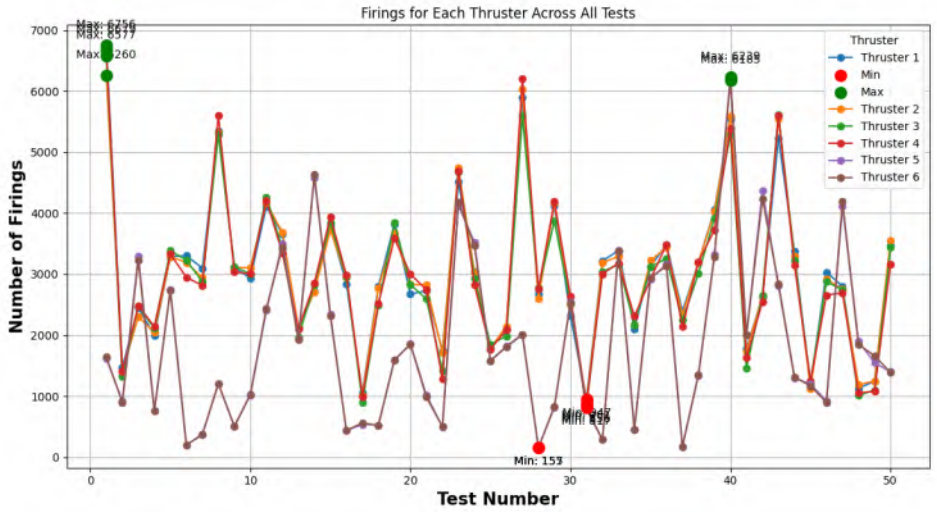

Figure 4.85.: Test Case 1 ($\Delta t = 10$ seconds): Thruster firing patterns reflecting increased control efforts during extended range tests, with higher and more erratic thruster activity evident.

Overall, the results from Test Case 1 with $\Delta t = 10$ seconds reveal the challenges of achieving rapid convergence under varied initial conditions. The high thruster activity and occasional divergence highlight the need for careful tuning of control parameters to ensure robustness and reliability in fast-response scenarios.

Test Case 2: $\Delta t = 500$ seconds

In this test scenario, the target time was extended to 500 seconds to assess the system's ability to stabilize and converge to the target position within a significantly longer time frame. This test provides insight into the controller's efficiency over extended periods, particularly analyzing its impact on fuel consumption and thruster activations under prolonged maneuver conditions.

X-axis Trajectory Analysis The X-axis Monte Carlo simulation results display a diverse spread of trajectories that show significant initial deviations from the target line, starting with values as high as 6,000 meters. These trajectories converge towards zero within approximately 2500 seconds. This indicates that the control strategy effectively counters initial displacements over time, stabilizing the chaser's position relative to the target along the X-axis. The convergence pattern suggests robust control dynamics capable of handling large initial errors in the X-direction (see Figure 4.86a).

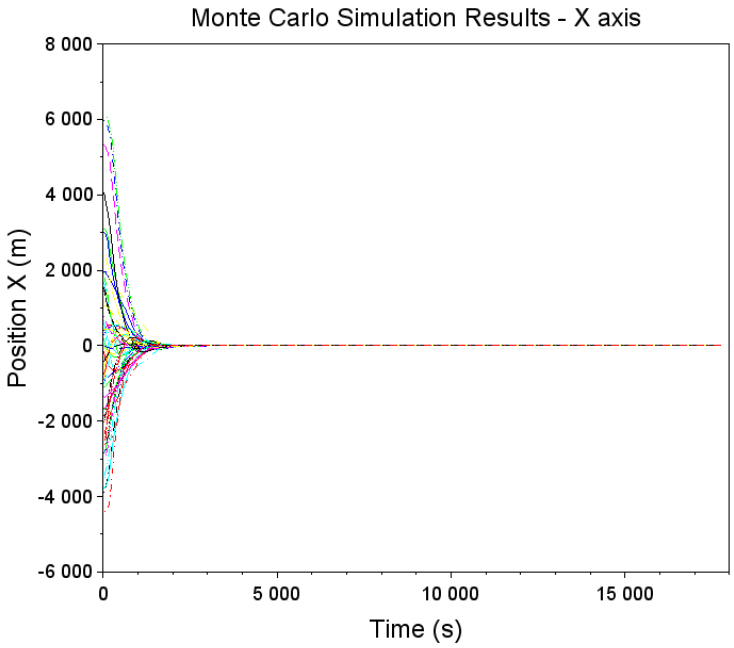

(a) X-axis trajectory analysis showing convergence by approximately 2500 seconds ($\Delta t = 500$ seconds).

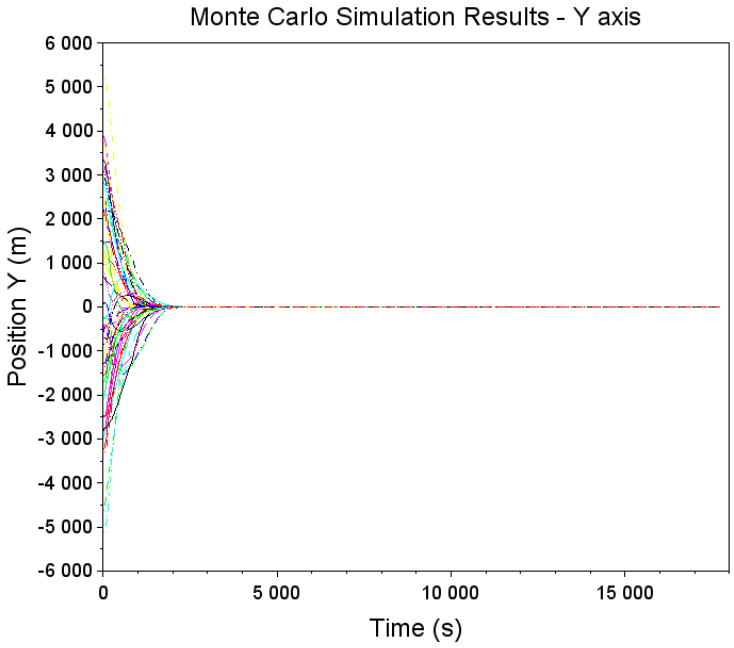

(b) Y-axis trajectory analysis showing convergence by approximately 2500 seconds ($\Delta t = 500$ seconds).

Figure 4.86.: Trajectory analyses for $\Delta t = 500$ seconds, demonstrating convergence on the x and y axes.

Y-axis Trajectory Analysis For the Y-axis, the simulation results again show a spread of trajectories with initial deviations that converge towards the target trajectory over time. Starting from positions up to approximately 5,500 meters away from the target, these trajectories stabilize around the zero mark by 2500 seconds similar to the X-axis. This pattern of convergence is consistent with the control strategy's ability to efficiently correct deviations, ensuring that the chaser remains on course relative to the target (see Figure 4.86b).

Z-axis Trajectory Analysis The Z-axis trajectories exhibit a similar trend to the X and Y axes, with initial positions starting off far from zero but rapidly converging towards the target trajectory within the same time frame of about 2500 seconds. The maximum initial offset appears slightly higher than in the X and Y simulations, suggesting a slightly greater initial instability in the Z-direction. However, the control strategy quickly compensates for these deviations, bringing the trajectories into alignment with the target, demonstrating effective control across all spatial dimensions (see Figure 4.87).

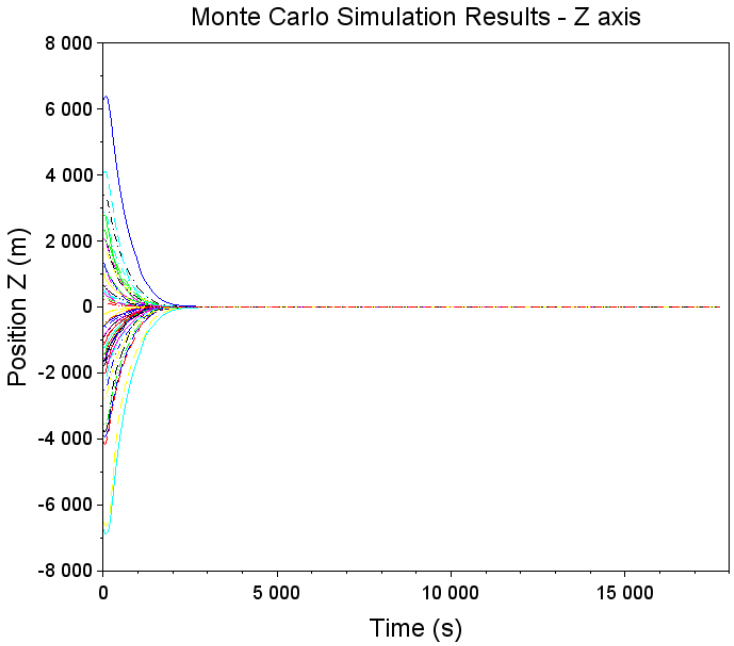

Figure 4.87.: Z-axis trajectory analysis showing convergence by approximately 2500 seconds ($\Delta t = 500$ seconds).

Thruster Activity Analysis The thruster firing data, showed a consistent pattern of activity, necessary to maintain and correct the spacecraft's trajectory. Figure 4.88 details the number of firings for each thruster throughout the test duration. This test case reveals how the controller effectively utilizes the thrusters to maintain a stable course, optimizing fuel consumption while ensuring precise maneuverability.

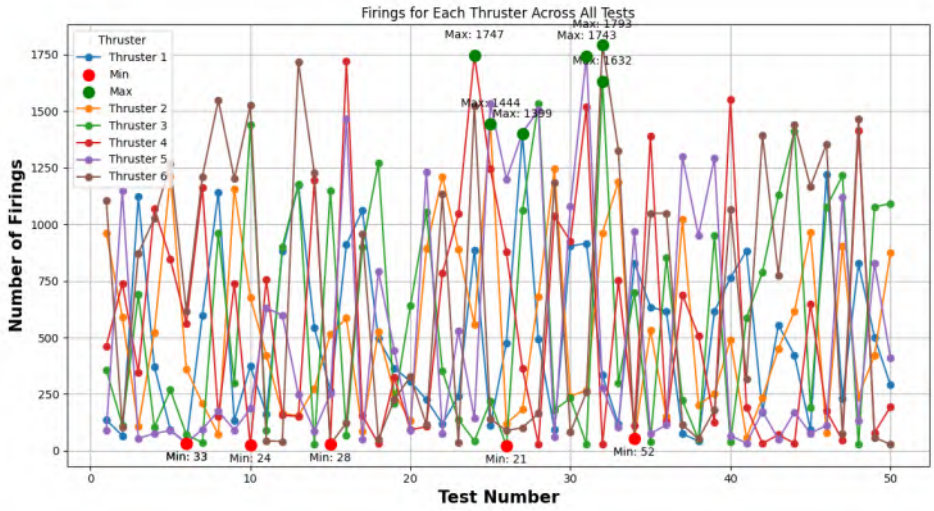

Figure 4.88.: Distribution of thruster firings throughout the $\Delta t = 500$ seconds test, showing a spectrum of activation intensities. Thruster 6 was the most active, peaking at 1793 firings, while Thruster 3 was utilized the least, with only 16 activations. This pattern highlights the differential roles of each thruster in maintaining trajectory control under varied conditions.

Test Case 2 confirms the controller's capability to effectively manage long-duration flights, showing a reliable stabilization of trajectory over extended periods. The consistent thruster activity and successful trajectory alignment within approximately half an orbit underscore the robustness of the CW-based controller under extended operational scenarios. This test not only validates the controller's effectiveness but also emphasizes its potential for mission-critical operations where time-extended maneuvers are required.

Test Case 3: $\Delta t = 2000$ seconds

The extended target time of 2000 seconds in Test Case 3 allows for a comprehensive evaluation of the controller's efficiency under sustained operational conditions. This test is crucial for understanding the control dynamics over longer periods, particularly in terms of fuel consumption and thruster usage efficiency.

Trajectory and Position Stability Figures 4.90a, 4.90b, and 4.91 illustrate the trajectory responses in the x, y, and z axes respectively. Each figure demonstrates that the system, despite initial variances, tends to stabilize and converge towards the target coordinates over time. The extended duration allows the system to counteract initial disturbances more effectively, leading to smoother trajectory corrections and less aggressive maneuvers as the control actions are spread out over a longer time frame.

Thruster Activity Analysis As depicted in Figure 4.89, the number of thruster firings is considerably lower in this test case compared to others with shorter Δt settings. This is indicative of the control system's ability to make more efficient use of thruster firings, optimizing fuel consumption and reducing wear on the thrusters over time. The maximum

and minimum firings across all tests provide insights into the operational demands placed on each thruster, showcasing a significant reduction in peak firings which correlates with improved fuel efficiency.

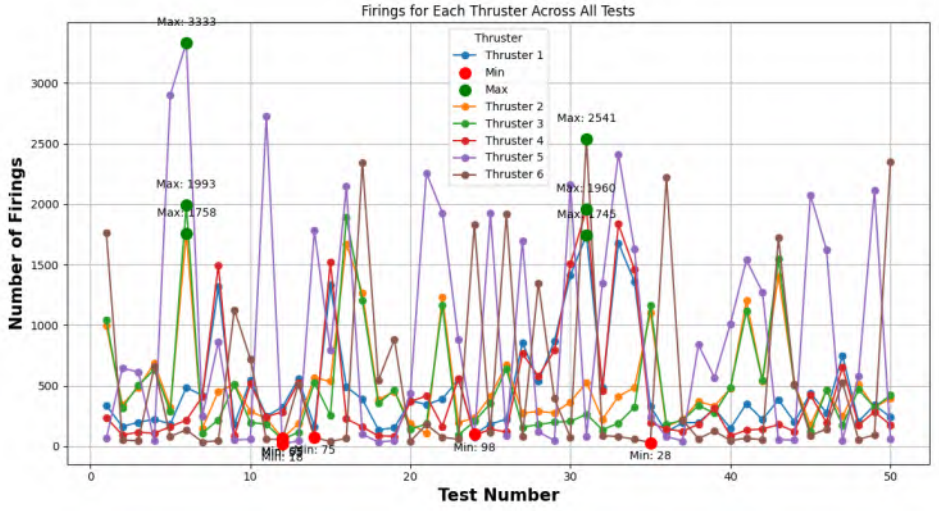

Figure 4.89.: Detailed analysis of thruster firings over the extended duration of Test Case 3 ($\Delta t = 2000$ seconds), showing a significant decrease in firing frequency. The most intensive use was by Thruster 5 with a peak at 3333 firings, while the least was also Thruster 5 with only 18 firing.

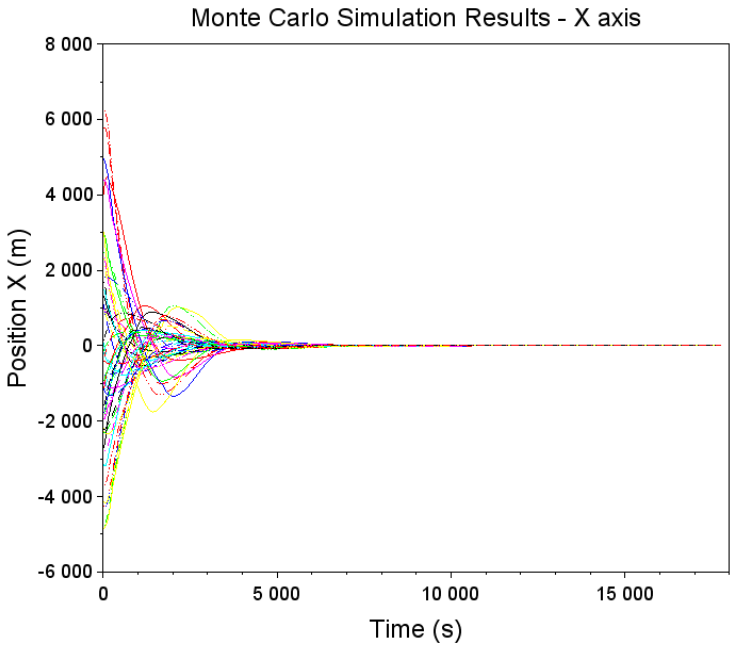

(a) Monte Carlo simulation results for the x-axis, illustrating convergence before 7000 seconds (Test case 3).

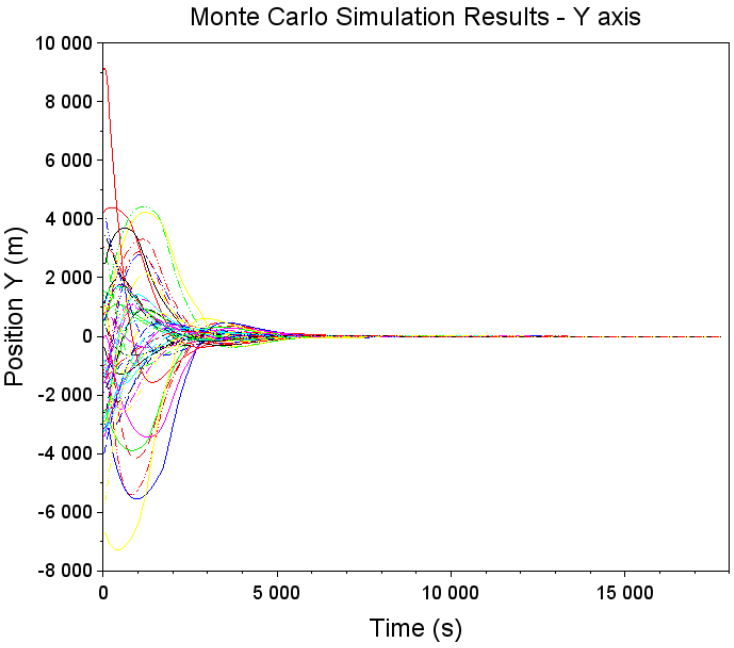

(b) Monte Carlo simulation results for the y-axis, showing trajectory stabilization before 9000 seconds (Test case 3).

Figure 4.90.: Monte Carlo simulation results for x and y axes ($\Delta t = 2000$ seconds).

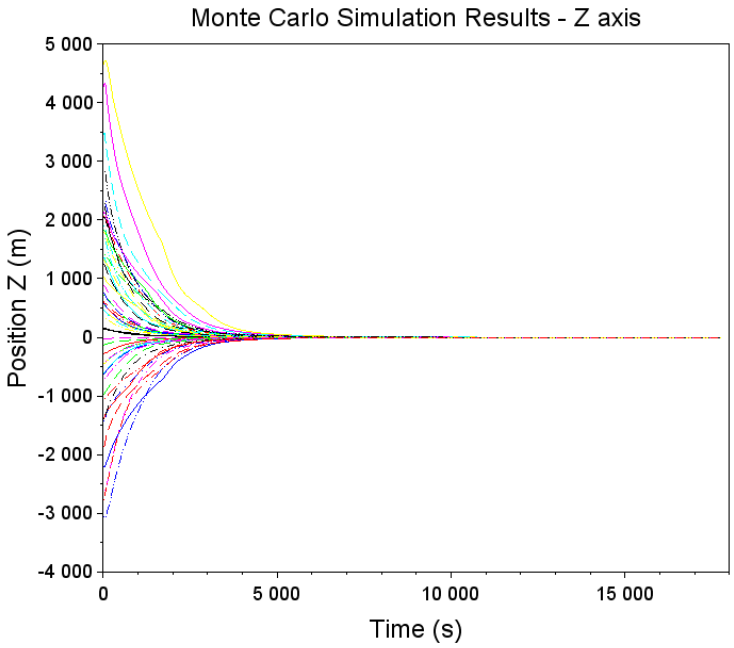

Figure 4.91.: Monte Carlo simulation results for the z-axis, demonstrating convergence before 6000 seconds ($\Delta t = 2000$ seconds).

Overall, the results from Test Case 3 demonstrate the capability of the control system to efficiently manage longer-duration missions, optimizing resource usage while maintaining high precision in trajectory alignment.

Observations from CW Based Controller Simulations

Overview of CW Controller Performance Monte Carlo simulations were conducted across various test cases with differing time-to-target (Δt) settings to evaluate the CW controller's performance under diverse operational conditions.

Test Case 1: Rapid Maneuvering ($\Delta t = 10$ seconds)

- **Observations**: The controller exhibited rapid response capabilities, stabilizing the spacecraft swiftly under standard test conditions ($[-1500, 1500]$ meters). However, under extended test conditions ($[-2500, 2500]$ meters), the system failed to converge within the short 10-second window, particularly in the x and y axes.
- **Recommendations**: This setting is suitable for short-duration missions requiring quick adjustments, such as debris avoidance maneuvers. However, for missions demanding high accuracy under variable conditions, like complex docking operations, adjustments to control parameters or alternative strategies might be necessary.

Test Case 2: Extended Duration ($\Delta t = 500$ seconds)

- **Observations**: With a longer time-to-target, the controller showed improved convergence and stability across all axes, indicating better handling of initial disturbances and a more measured control effort.
- **Recommendations**: Well-suited for station-keeping or intermediate rendezvous phases where gradual and precise adjustments are necessary. This setting helps minimize fuel consumption and thruster wear, advantageous for long-term orbital operations.

Test Case 3: Long-Duration Stability ($\Delta t = 2000$ seconds)

- **Observations**: Demonstrated high precision in maintaining trajectory with significantly reduced thruster firings, leading to enhanced fuel efficiency. Trajectory convergence was achieved smoothly, reflecting the system's robustness over extended durations.
- **Recommendations**: Ideal for deep-space missions and long-duration Earth observation where maintaining a precise orbit is crucial. The reduced thruster activity also suggests suitability for life-extension missions of satellites, where conserving onboard resources is critical.

General Insights

- **Fuel Efficiency**: Across all test cases, the CW controller's capability to reduce thruster firings correlated with better fuel economy, essential for sustainable long-term missions.
- **Control Precision**: Achieved effective stabilization and trajectory correction across all tests, demonstrating the controller's capability to handle a range of operational scenarios with varying degrees of complexity.

Concluding Remarks The CW based trajectory controller has proven effective across various time scales, with optimal performance observed in longer-duration tests. For mission planners, selecting the appropriate Δt based on mission goals and expected environmental conditions will be crucial to maximize performance and resource efficiency.

This analysis underscores the importance of aligning control strategies with specific mission demands to optimize both control performance and resource utilization.

4.6.3. Comparative Analysis of LQR and CW Based Controllers

This section presents a comparative analysis of the observations from the Monte Carlo simulations of LQR and CW-based trajectory controllers, highlighting their strengths and limitations in different operational scenarios.

Rapid Response and High-Variability Handling

LQR Controller:

- **Observations**: In high variability settings ($[-2500, 2500]$ m), the LQR controller struggled with convergence, particularly along the X and Y axes, suggesting limits in handling sudden, large disturbances.
- **Implications**: While LQR provides precise control, its effectiveness is reduced under extreme conditions, making it less ideal for missions where unpredictable disturbances are common.

CW Controller:

- **Observations**: Similar to the LQR, the CW controller faced challenges in the 10-second rapid maneuvering scenario, failing to converge within the short time frame under extended conditions.
- **Implications**: The CW controller, though quick to respond, requires fine-tuning of control parameters to enhance adaptability in fast-response or emergency scenarios.

Stability and Efficiency in Extended Missions

LQR Controller:

- **Observations**: Demonstrated stability with moderate emphasis on velocity and control weights, making it well-suited for typical station-keeping and early-stage rendezvous where extreme maneuvers are not required.
- **Recommendations**: Ideal for extended missions requiring smooth, incremental adjustments, due to its efficient handling of control dynamics and fuel resources.

CW Controller:

- **Observations**: In longer duration settings ($\Delta t = 500$ and 2000 seconds), the CW controller showed excellent trajectory stability and significantly reduced thruster firings, leading to enhanced fuel efficiency.
- **Recommendations**: Ideal for deep-space missions and extended Earth observation, where maintaining a precise orbit with minimal resource expenditure is crucial.

Overall Performance and Suitability

General Insights: Both controllers perform effectively across different timescales. However, the CW controller exhibits a slight edge in longer-duration tests due to its ability to maintain trajectory control with fewer resources, which is crucial for sustainability in long-term missions.

4.7. Implementation of LQR Controller in a Non-linear Test Environment

The positioning and velocities for the chaser and target are configured as follows:

- **Target:** Position = [7071000, 0, 0] meters, Velocity = [0, 7508.07270064, 0] meters per second.

- **Chaser:** Position = [7070600, 300, 100] meters, Velocity = [0, 7508.281, 0] meters per second.

This setup positions the chaser 400 meters away in the x-direction, 300 meters in the y-direction, and 100 meters in the z-direction from the target. The orbit radius is 7071000 meters. The simulation duration corresponds to one orbit, or 5917.42 seconds, to confirm the controller's efficacy in real conditions.

The non-linear testing framework, illustrated in Figure 4.92, mimics complex orbital dynamics, challenging the traditional linear modeling approaches. It evaluates the adaptability of the LQR controller to these realistic, fluctuating scenarios.

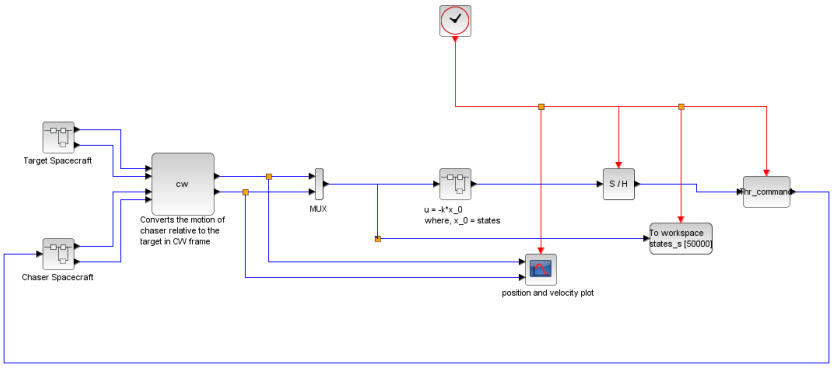

Figure 4.92.: Illustration of the non-linear test environment setup for assessing the LQR controller's performance under realistic orbital dynamics.

The 2D and 3D trajectory visualizations, as shown in Figures 4.93 and 4.94, offer detailed insights into how the spacecraft modifies its trajectory. These analyses affirm the LQR controller's precision in adhering to set paths despite the non-linear conditions.

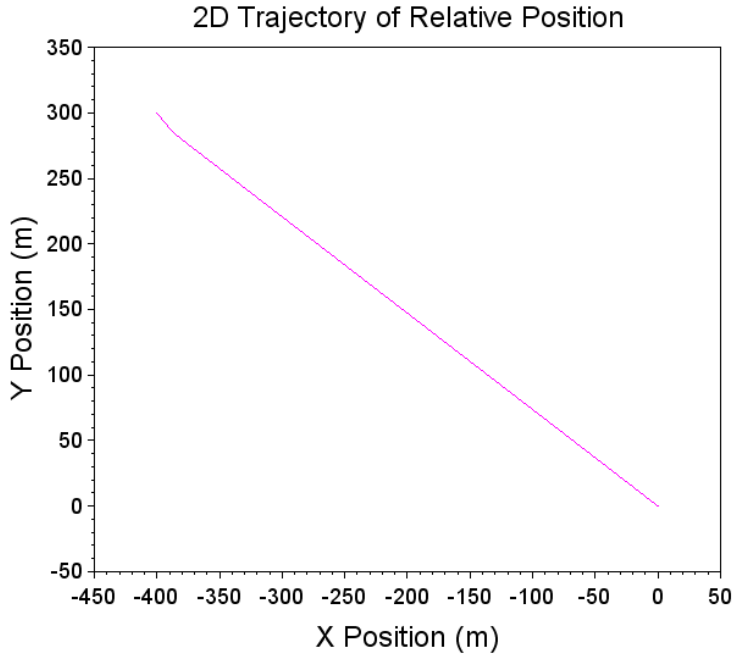

(a) Two-dimensional trajectory of the spacecraft under the CLSS block simulation, comparing path consistency with the LQR control.

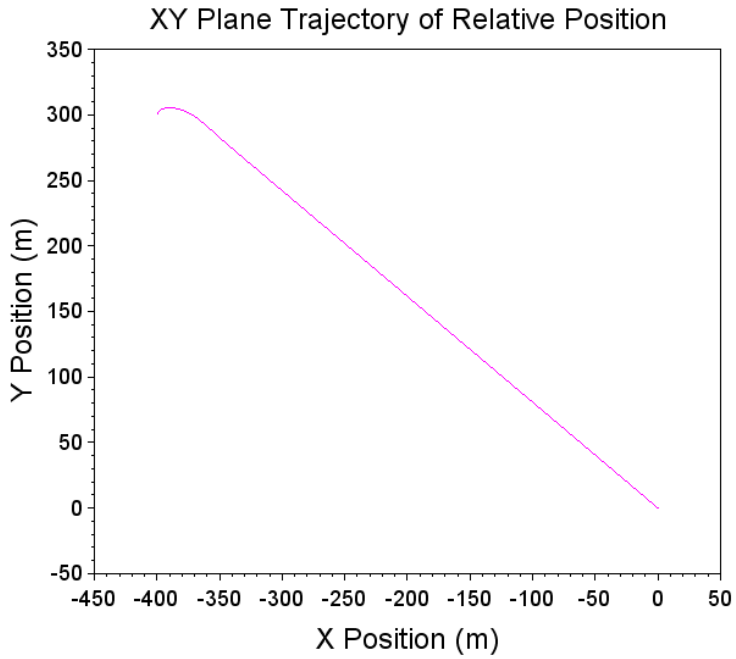

(b) Two-dimensional trajectory of the spacecraft under the non-linear test setup, demonstrating the path influenced by LQR control.

Figure 4.93.: Comparative analysis of two-dimensional trajectories using CLSS block and non-linear test setup under identical initial conditions, highlighting the LQR system's control effects.

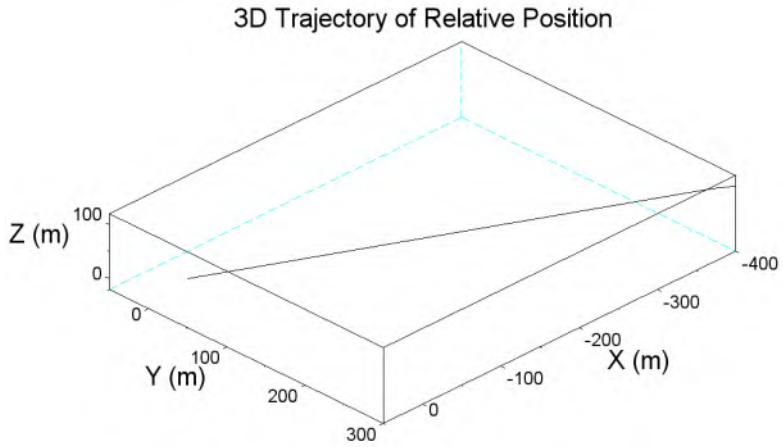

(a) Three-dimensional trajectory visualization of the spacecraft using the CLSS block, illustrating detailed spatial movements under control.

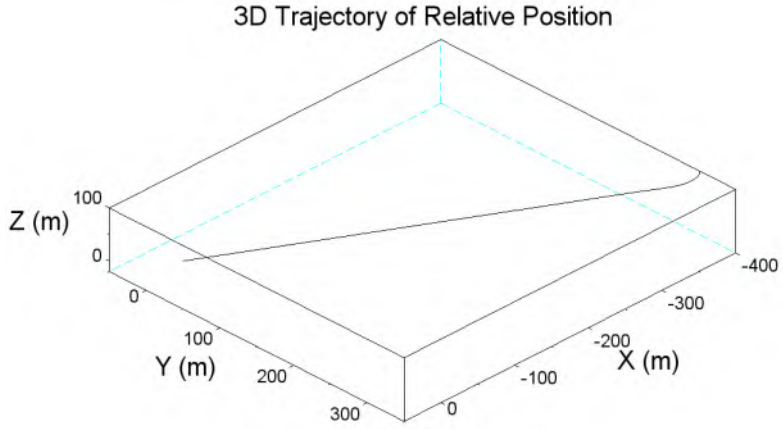

(b) Three-dimensional trajectory visualization of the spacecraft in a non-linear setup, displaying the dynamic response to LQR control.

Figure 4.94.: Analysis of three-dimensional spacecraft trajectories, comparing performance in CLSS block and non-linear test setups.

Figure 4.95b presents the thruster activation frequencies, with the positive y-direction thruster being the most engaged, firing 139 times, contributing to a total of 418 activations during the test. Similarly, for the CLSS block simulation, the same thruster also recorded the highest activity, albeit with a slightly higher overall activation count of 433, as depicted in Figure 4.95a.

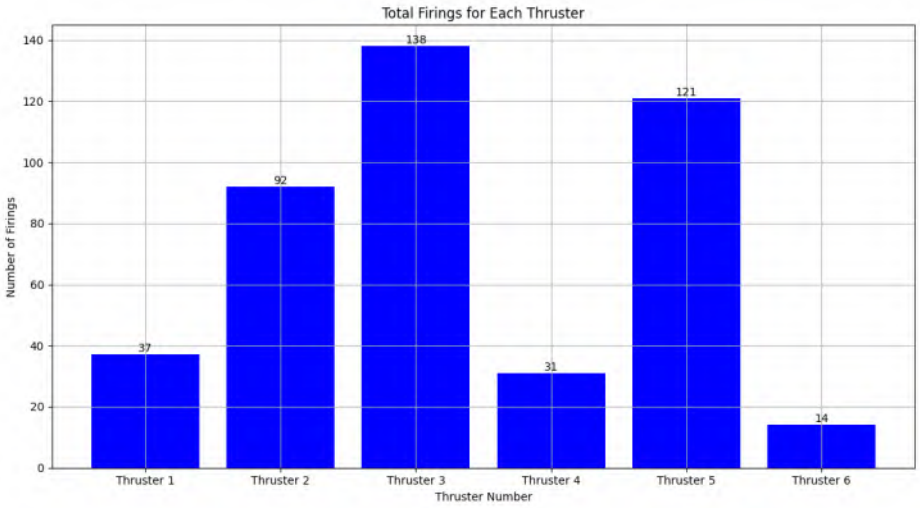

(a) CLSS block test: Highlights the most frequently used thruster in the y-direction with 138 firings out of a total of 433 activations.

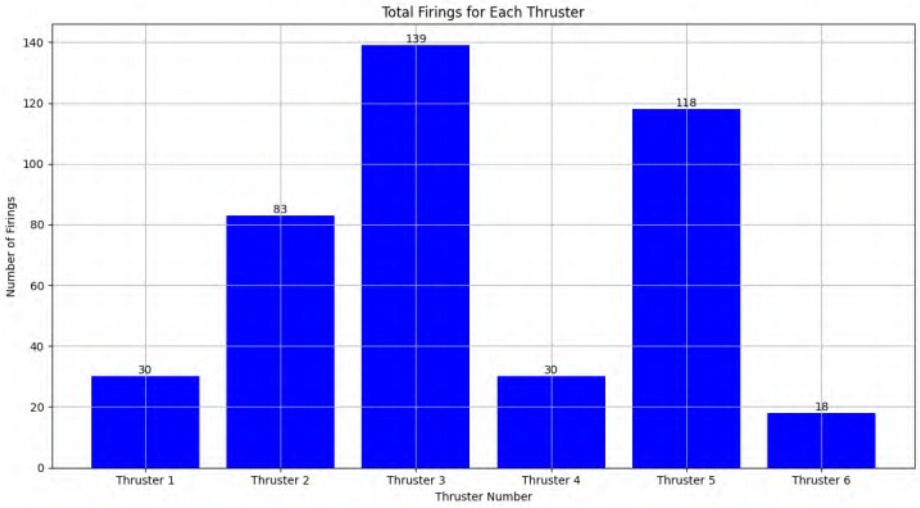

(b) Non-linear test: Echoes similar thruster activation patterns with 139 firings in the y-direction out of 418 total activations.

Figure 4.95.: Comparative analysis of thruster activations in the CLSS and non-linear test setups, indicating targeted control efforts to manage trajectory deviations.

Figures 4.96b, 4.97b, and 4.98b illustrate the spacecraft's positional adjustments along the X, Y, and Z axes. The stabilization occurs approximately within 1200-1300 seconds for the X-axis, 1400 seconds for the Y-axis, and 3000 seconds for the Z-axis. A comparative analysis between the simulations of the CLSS block and the non-linear test setup indicates remarkably similar behaviors across the X, Y, and Z axes in both setups.

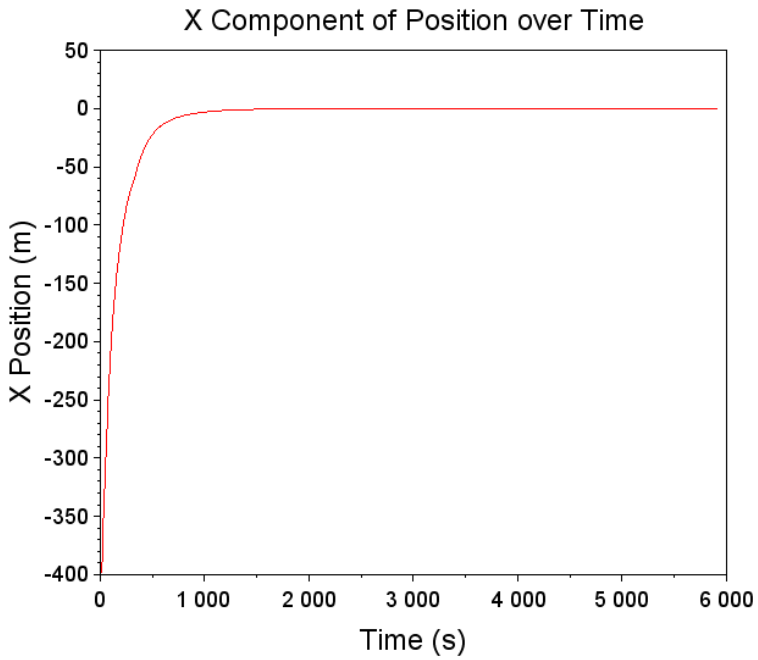

(a) Spacecraft X-axis position analysis using the CLSS block simulation, illustrating the response dynamics.

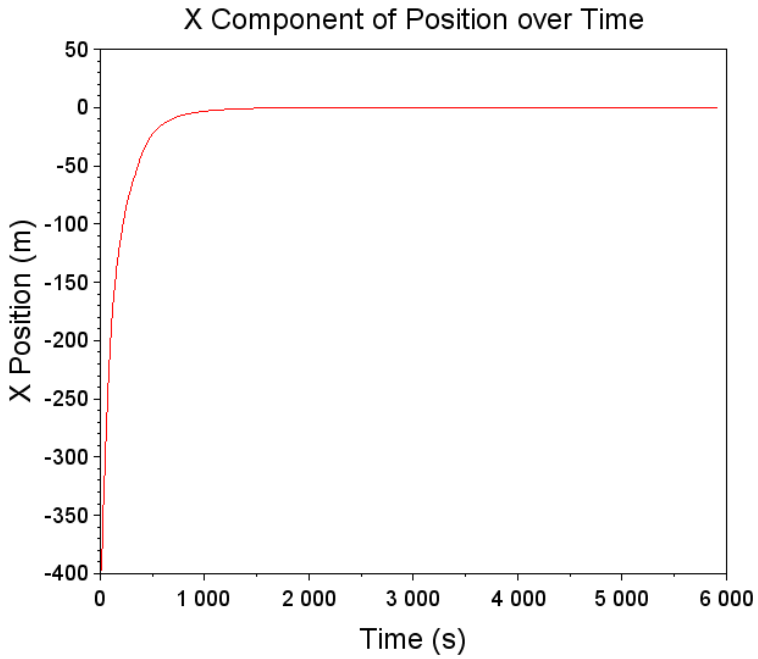

(b) Spacecraft X-axis position analysis in the non-linear model, highlighting rapid stabilization within 1200-1300 seconds.

Figure 4.96.: Comparative analysis of the spacecraft's X-axis position using CLSS block and non-linear simulations under the same initial conditions.

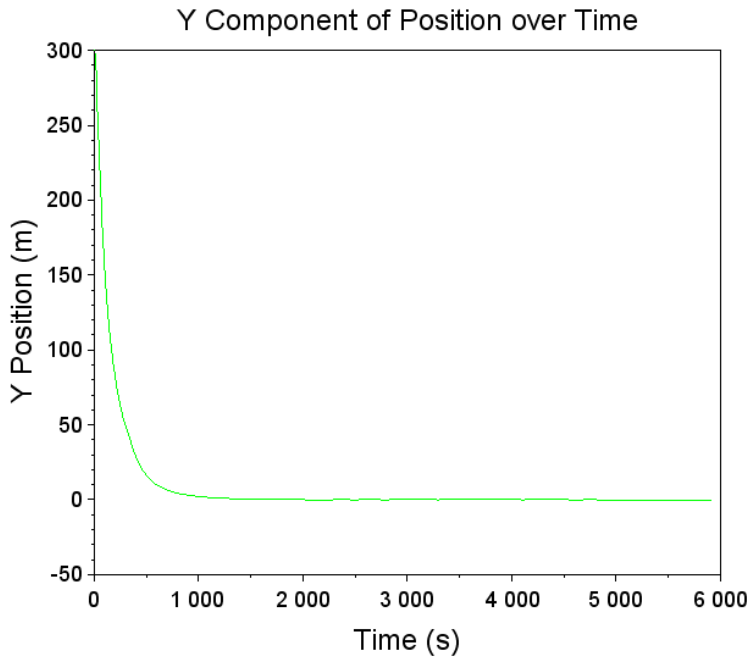

(a) Y-axis trajectory control using the CLSS block, showcasing path consistency under controlled conditions.

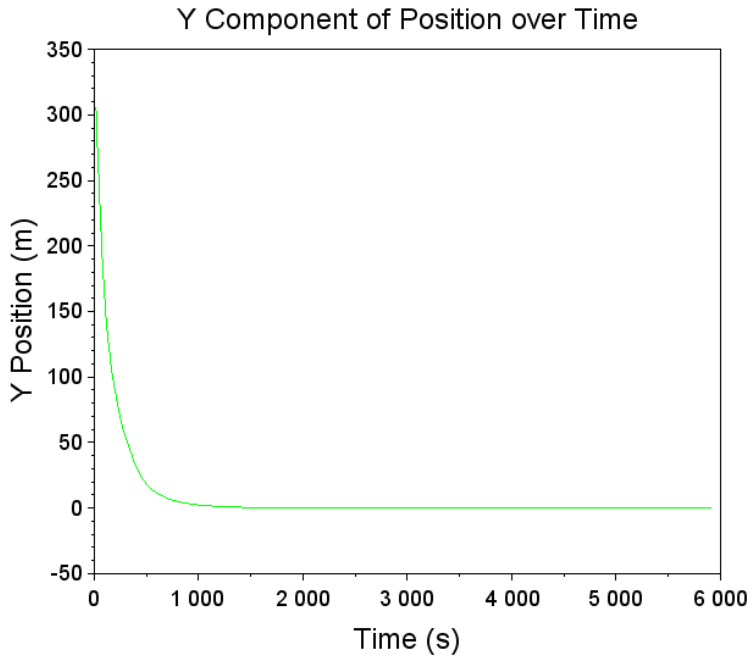

(b) Y-axis trajectory under the non-linear setup, achieving lateral stabilization by the 1400-second mark.

Figure 4.97.: Comparative analysis of Y-axis trajectory control in CLSS block and non-linear test setups, demonstrating the system's response to identical initial conditions.

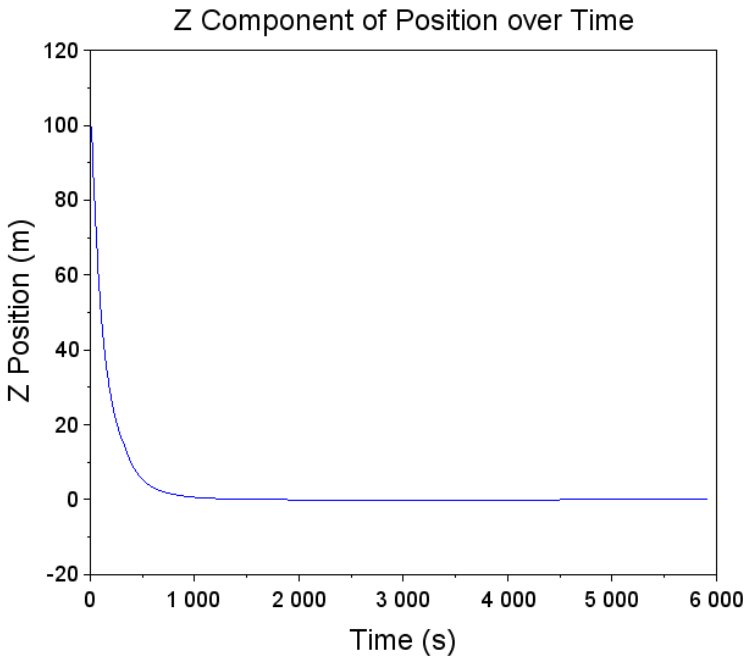

(a) Control stability along the Z-axis using the CLSS block, under given initial conditions.

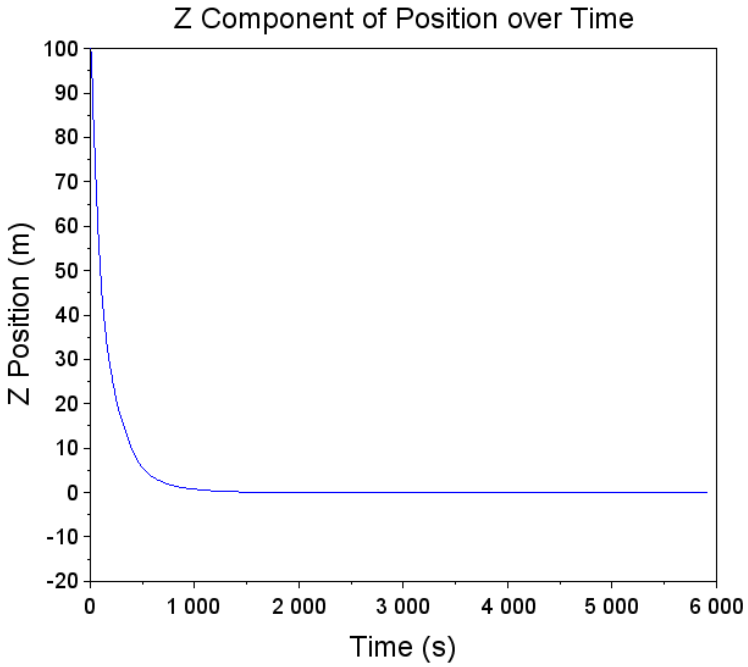

(b) Control stability along the Z-axis in the non-linear model, reaching stabilization within about 3000 seconds.

Figure 4.98.: Comparative analysis of Z-axis trajectory control in CLSS block and non-linear test setups.

The XY plane velocity trajectory, presented in Figure 4.99b, illustrates the spacecraft's velocity adaptations in response to control adjustments, underscoring the dynamic interaction between navigational commands and spacecraft responses.

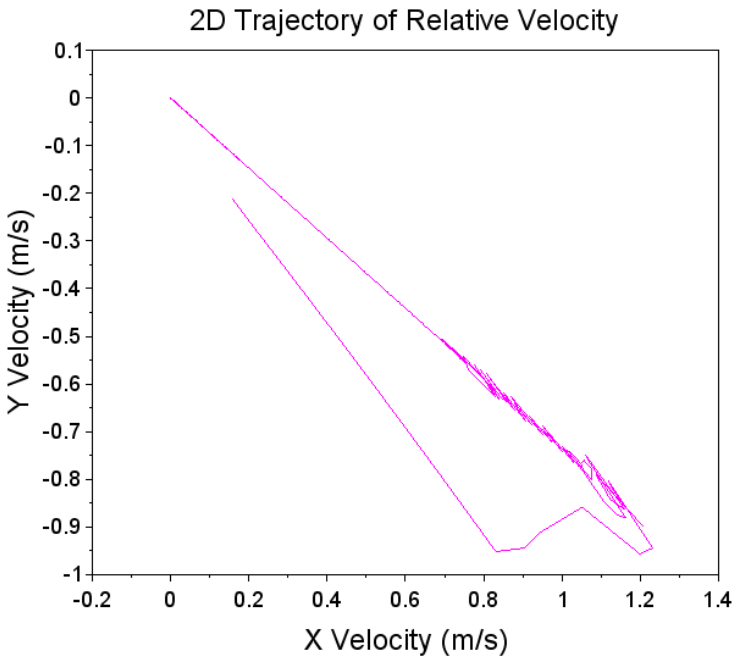

(a) Velocity adjustments in the XY plane using the CLSS block, highlighting dynamic response under initial test conditions.

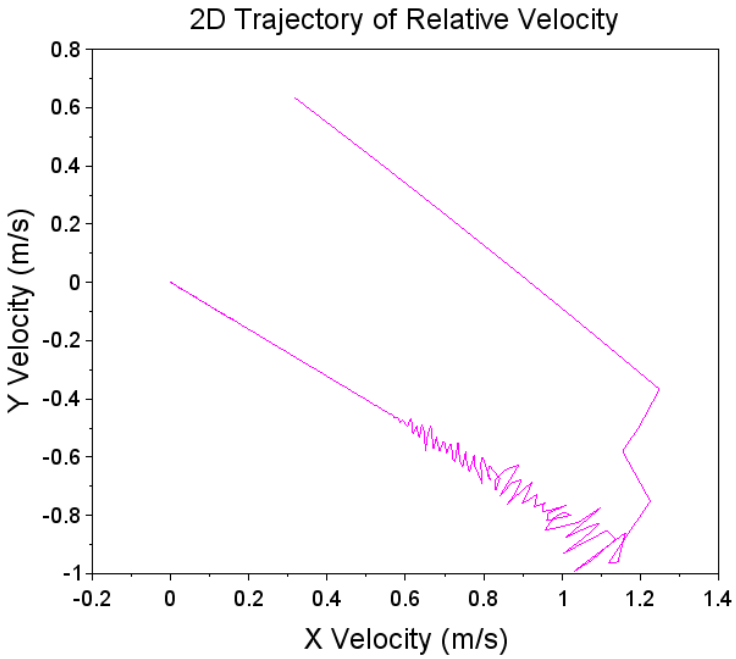

(b) Velocity adjustments in the XY plane using a non-linear LQR control model, demonstrating the system's dynamic response capabilities.

Figure 4.99.: Comparative analysis of dynamic velocity adjustments in the XY plane, illustrating the system responses in CLSS block and non-linear LQR control setups.

Comparative Analysis of Simulation Outcomes

Thruster Activation and Fuel Consumption: In the comparative analysis of the LQR controller's performance in the non-linear setup versus the CLSS block simulation, the total number of thruster firings was slightly higher in the CLSS block, totaling 433, compared to 418 in the non-linear setup. This suggests a marginally increased control effort in the CLSS scenario. Additionally, the fuel consumption data indicates a close parity between the two setups, with the non-linear simulation consuming 0.2908966 kg of fuel and the CLSS block simulation slightly higher at 0.2947 kg.

Trajectory Analysis: The trajectory analysis for position across both simulations revealed similar paths, confirming the effectiveness of the control strategies in maintaining the desired trajectory. However, the velocity trajectories exhibited some variations, indicating differential dynamics in response to control inputs between the non-linear and CLSS block simulations. This variation in velocity trajectories suggests that while both controllers achieve their positional targets effectively, their control tactics in velocity management differ slightly, impacting the dynamic response of the spacecraft.

4.8. CW Based Trajectory Controller for the Non-linear Test Setup

This section evaluates the implementation of the CW-based trajectory controller on the non-linear test setup, highlighting its performance over an extended simulation period. The primary objective is to observe the controller's effectiveness in guiding a chaser spacecraft to a designated target within a specified delta time of 100 seconds.

The simulation setup involves the following initial position and velocity parameters for the target and the chaser spacecraft:

- **Target:** Position = [7071000, 0, 0] meters, Velocity = [0, 7508.07270064, 0] meters per second.
- **Chaser:** Position = [7070600, 300, 100] meters, Velocity = [0, 7508.281, 0] meters per second.

These settings position the chaser in an orbit with a radius of 7071000 meters, maintaining a proximity of 400 meters in the x-direction, 300 meters in the y-direction, and 100 meters in the z-direction relative to the target. The simulation runs for one orbit, equivalent to 5917.42 seconds, to validate the controller's effectiveness in a real-world scenario.

Figure 4.100b displays the CW-based system's control of the chaser spacecraft's trajectory over a single orbital period within both the CLSS and non-linear simulations. Although the position trajectories for both simulations are not identical, they exhibit noticeable similarities. The results shown in Figure 4.100 indicate that the chaser successfully reaches its designated target, thereby demonstrating the effective application and operational reliability of the CW-based trajectory controller in a complex, non-linear simulation environment.

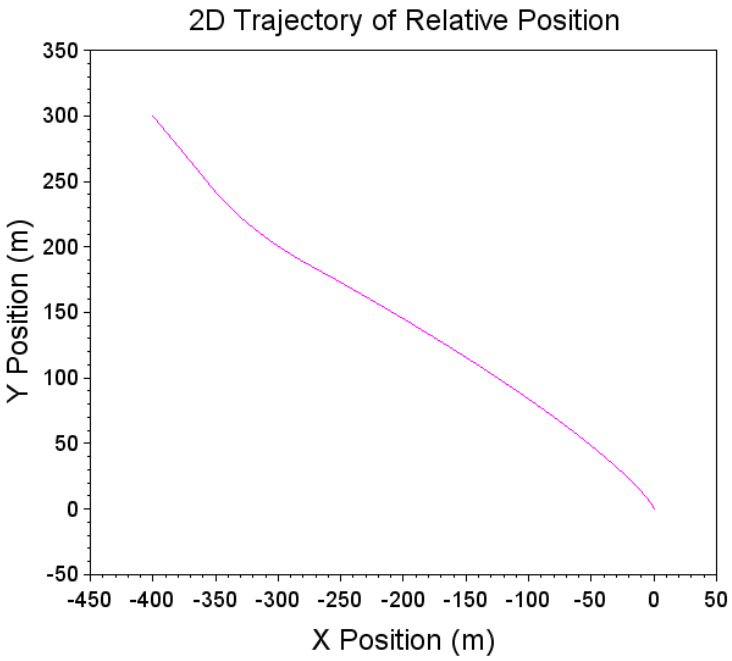

(a) Two-dimensional trajectory of the spacecraft under CW control within the CLSS simulation, illustrating path dynamics over time.

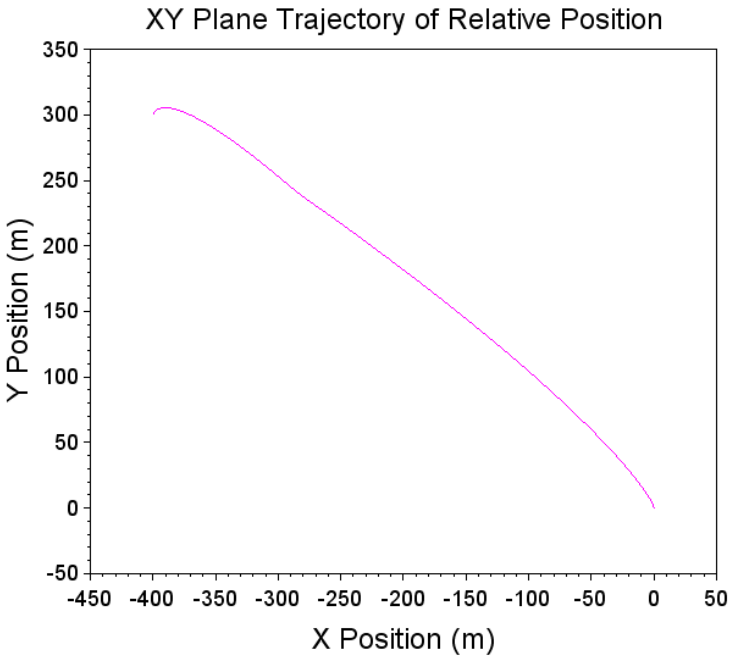

(b) Two-dimensional trajectory of the spacecraft under CW control in the non-linear test setup, highlighting effective trajectory management and target acquisition within 1000 seconds.

Figure 4.100.: Comparative analysis of the two-dimensional trajectories in the CLSS and non-linear simulations, demonstrating the spacecraft's response under CW control.

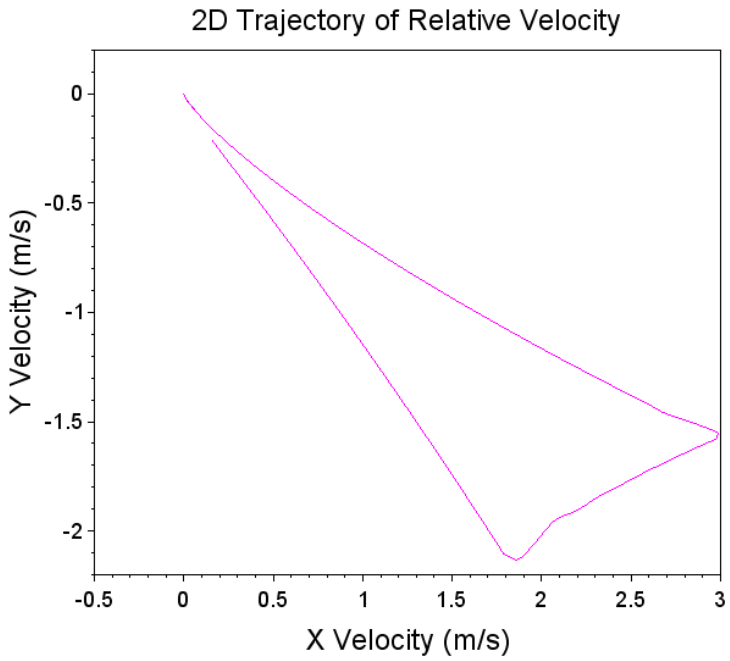

(a) Two-dimensional velocity trajectory of the spacecraft under the CLSS simulation, displaying the path dynamics influenced by velocity control adjustments.

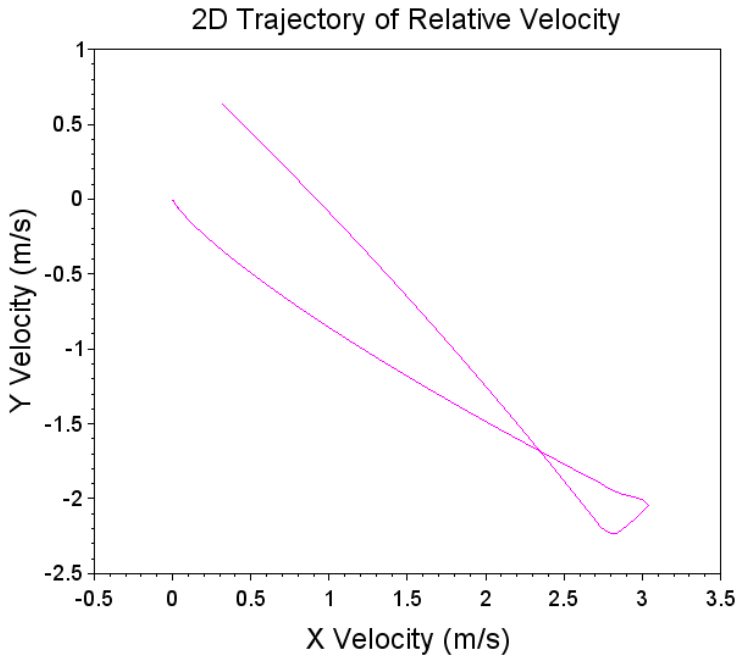

(b) Two-dimensional velocity trajectory of the spacecraft in the non-linear test setup, showing the CW-based controller's response in aligning with the target velocity path effectively.

Figure 4.101.: Comparative analysis of the two-dimensional velocity trajectories under the CLSS and non-linear simulations, showcasing how different control setups influence spacecraft dynamics.

Figure 4.102 provides a detailed examination of thruster use throughout the mission for both the CLSS and non-linear simulations. For the CLSS simulation, thrusters oriented in the positive y-direction were the most frequently used, activating 56 times, while those in the negative z-direction were least used. The total activations for all six thrusters were 203. In contrast, the non-linear simulation saw the most frequent use of the positive z-axis thrusters, with 47 firings. The aggregate number of activations for all thrusters in this simulation was 171 over the course of the orbit.

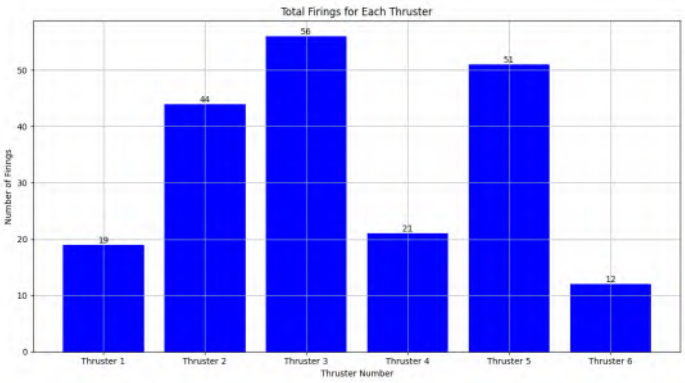

(a) Thruster activation profile for the CLSS simulation, highlighting the dominant use of y-axis thrusters which fired 56 times to aid in spacecraft's stabilization and alignment.

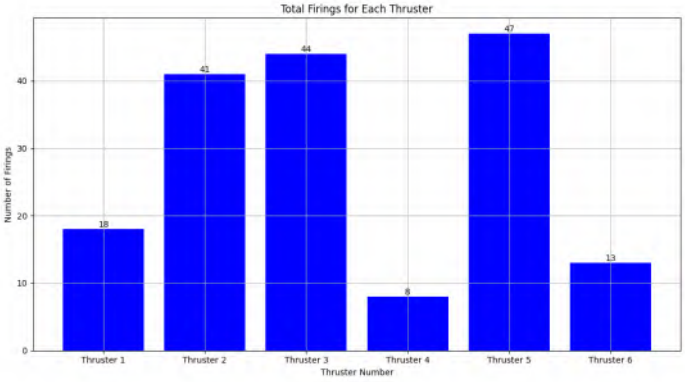

(b) Thruster activation profile for the non-linear test setup, where z-axis thrusters were the most utilized, firing 47 times to achieve precise spacecraft alignment and control.

Figure 4.102.: Comparative analysis of thruster activation profiles across the CLSS and non-linear simulations, demonstrating differences in control strategies and their impact on spacecraft trajectory corrections.

The fuel consumption for the non-linear setup was measured at 0.3232 kilograms. In comparison, the CLSS simulation showed slightly lower consumption at 0.31601 kg, with the small discrepancy being considered negligible.

4.8.1. Comparative Analysis of CW Controller Performance: CLSS vs. Non-linear Simulations

This section provides a comparative analysis of the CW-based trajectory controller's performance between CLSS and non-linear simulation setups. These comparisons help evaluate the controller's robustness, precision, and resource management under different simulation conditions.

Simulation Setup and Conditions

The CW controller was tested under two different setups: the CLSS block and a more complex non-linear simulation. Both scenarios used identical initial conditions for the chaser and target spacecraft, ensuring a controlled comparison of the controller's performance:

- **Initial Setup:** Both simulations initiated with the chaser positioned 400 meters x-directionally, 300 meters y-directionally, and 100 meters z-directionally from the target.

Trajectory Analysis

The trajectory control and stabilization outcomes of the CW controller varied subtly between the two setups:

- **Position and Velocity Trajectories:** The CLSS simulation typically showed a slightly more conservative approach to trajectory correction, resulting in marginally smoother but slower target alignment compared to the non-linear setup. This was evidenced by the controller's efficient management of both position and velocity adjustments in the non-linear model, which aggressively but accurately achieved the designated target within the specified delta time of 100 seconds.

Thruster Activity and Fuel Efficiency

The CW controller's operation across different test environments provided insights into its functional dynamics:

- **Thruster Usage:** In the non-linear simulation, thrusters oriented towards the positive z-axis were activated more frequently, which contrasted with the CLSS simulation where the y-axis thrusters saw more use. This indicates that the non-linear setup required more dynamic adjustments to maintain or change altitude compared to lateral movements in the CLSS block.
- **Fuel Consumption:** The non-linear test setup demonstrated a slightly higher fuel consumption rate (0.3232 kg) compared to the CLSS block (0.31601 kg). This marginal increase can be attributed to the non-linear dynamics requiring more frequent and varied thruster activations to counteract the complex interactions of forces acting on the spacecraft.

This comparative analysis reveals that while both setups validated the CW controller's capability, the non-linear simulation highlighted its potential to handle more complex and dynamically challenging environments efficiently.

4.9. Analysis of Controllers for higher LEO orbits

This section extends the scope of simulation and testing into higher orbits, focusing on the evaluation of two distinct controller configurations. To expedite computations, the CLSS block is utilized, previously validated as a computationally efficient substitute for the non-linear test configuration.

4.9.1. Test Case 1: Analysis of Orbital Characteristics at 7871 km Altitude

Initial Conditions This scenario is set with a semi-major axis of 7871000 meters. The simulation covers two complete orbits, totaling a duration of 13899.08 seconds. To evaluate system robustness, initial position and velocity vectors for the chaser spacecraft are randomized within $[-5000, 5000]$ meters.

LQR Controller Implementation

Monte Carlo simulations affirm the effectiveness of the LQR controller in higher orbit settings within LEO. This subsection details the positional, velocity, and thruster firing dynamics, accompanied by fuel consumption metrics for the specified orbital radius.

As noted in Section 4.5.1, the tuning parameters Q and R remain unchanged. The figures below depict the spacecraft's trajectories along the x, y, and z axes, illustrating convergence towards the target within approximately 2000 seconds for all dimensions in the test scenarios. The fuel consumption remains minimal, peaking at 0.3115 kg for the farthest test scenario, which is within operational limits.

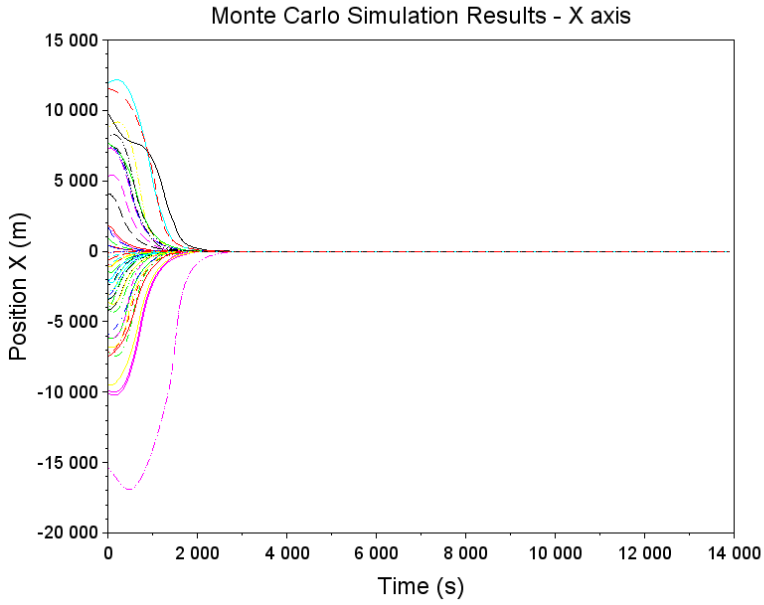

(a) X-Axis trajectories from Monte Carlo simulations, achieving target convergence within 2000 seconds, showcasing the LQR controller's precision under extended high-altitude conditions.

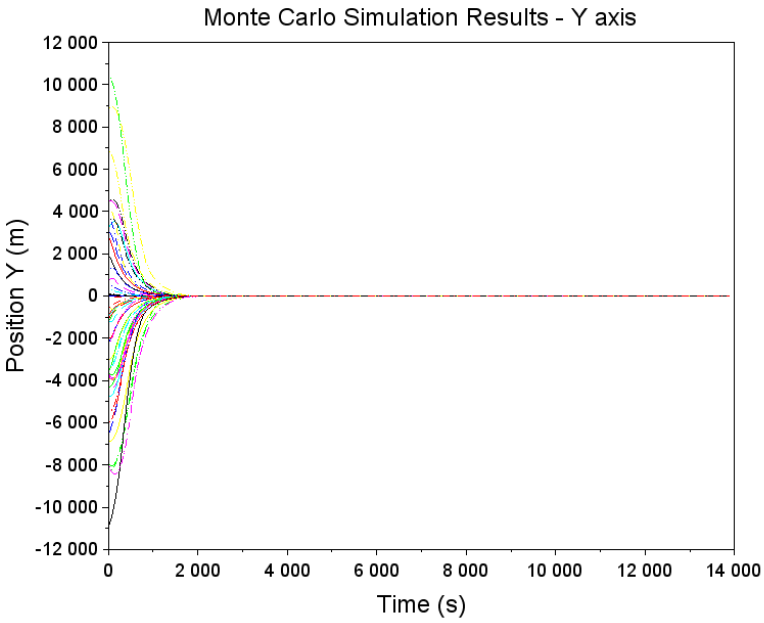

(b) Y-Axis trajectory performance indicating swift and consistent alignment with target coordinates, confirming the LQR controller's effectiveness at maintaining course under varied initial conditions.

Figure 4.103.: Monte Carlo simulations of the LQR controller's performance in high-altitude orbits: (a) X-Axis trajectory and (b) Y-Axis trajectory, demonstrating precision and effectiveness in target alignment.

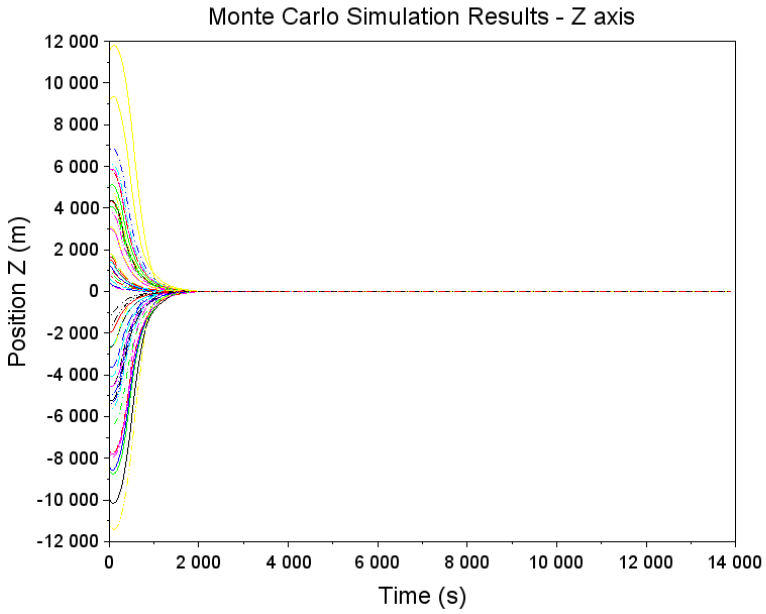

Figure 4.104.: Monte Carlo simulations for the Z-Axis, illustrating rapid and controlled trajectory convergence, managed by the LQR controller within 2000 seconds.

Thruster Activity Analysis The detailed analysis of thruster activations is illustrated in the subsequent figure, documenting the firing frequency for each of the six thrusters used throughout various simulation scenarios. Notably, the thruster directed towards the negative y-direction exhibited the highest number of firings, reflecting its significant role in maintaining orbital stability and trajectory corrections under the tested conditions. Conversely, the least number of activations was recorded for the thruster oriented towards the positive y-direction, indicating less frequent need for corrective maneuvers in that particular direction. This asymmetry in thruster usage underscores the dynamic nature of space navigation and control challenges faced in higher orbits. Figure 4.105 provides a visual representation of these findings, highlighting the disparities in thruster usage.

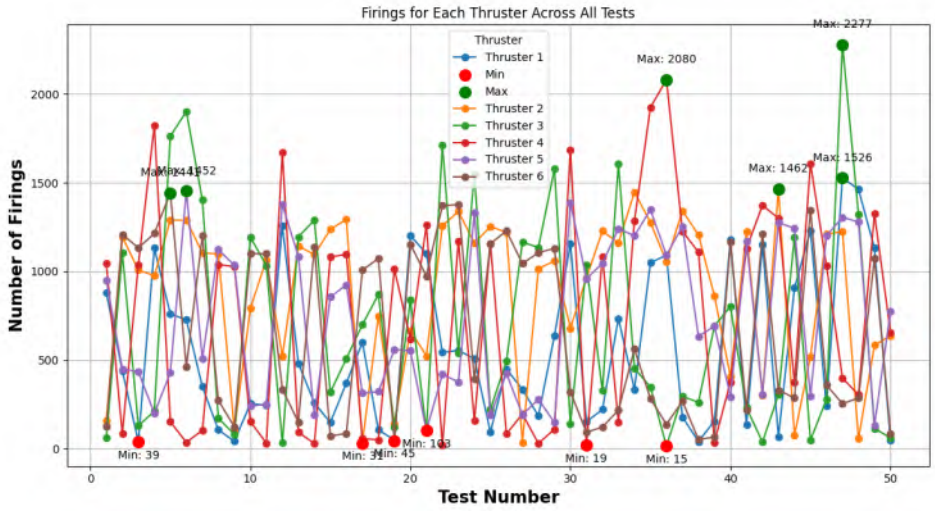

Figure 4.105.: Comprehensive thruster activation data across all simulations, highlighting efficient use of propulsion with a focus on the negative y-direction thruster, which activated 1745 times to maintain precise navigation and trajectory adjustments.

Analysis of CW-based Trajectory Controller in Higher Orbits

This section examines the CW based trajectory controller's performance in higher orbits, emphasizing its functionality when the control interval, Δt, is set to 1000 seconds. This setting tests the controller's efficacy over extended periods, which is crucial for long-term space missions.

The simulations deploy the CLSS block, chosen for its computational efficiency, to simulate conditions at a semi-major axis of 7871000 meters. Each simulation spans two orbits, totaling 13899.08 seconds, with initial state vectors for the chaser spacecraft randomized within $[-5000, 5000]$ meters.

CW-based Controller Implementation

Monte Carlo simulations validate the CW-based trajectory controller under these extensive orbital conditions. This section details positional corrections, thruster activities, and fuel usage, demonstrating the controller's adaptability to higher orbits.

Figures 4.106a, 4.106b, and 4.107 display the spacecraft's adjustments in the X, Y, and Z axes over time. These plots underscore the CW controller's capacity to accurately manage the spacecraft's trajectory towards a designated target within approximately 2000 seconds, affirming its effectiveness even with the extended Δt of 1000 seconds.

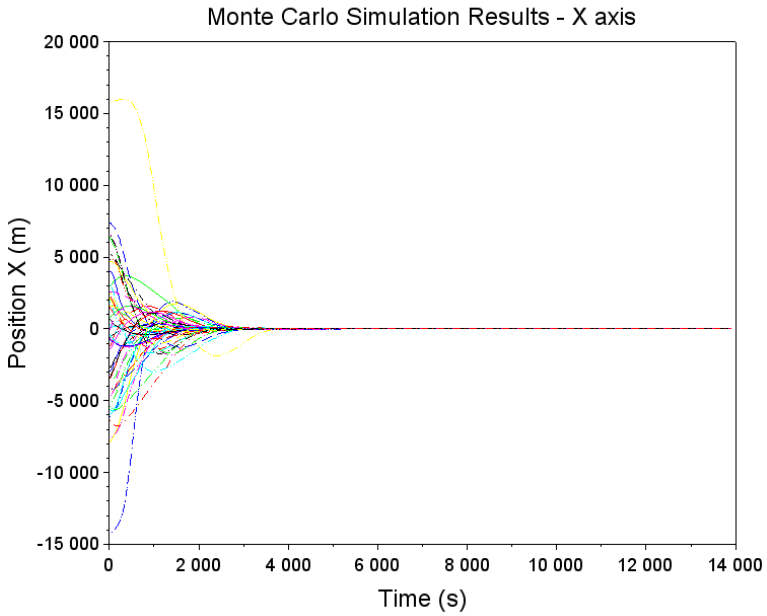

(a) Monte Carlo simulation results depicting trajectory adjustment in the X-axis within a 1000-second control interval, demonstrating effective positional control under extended CW-based system operation.

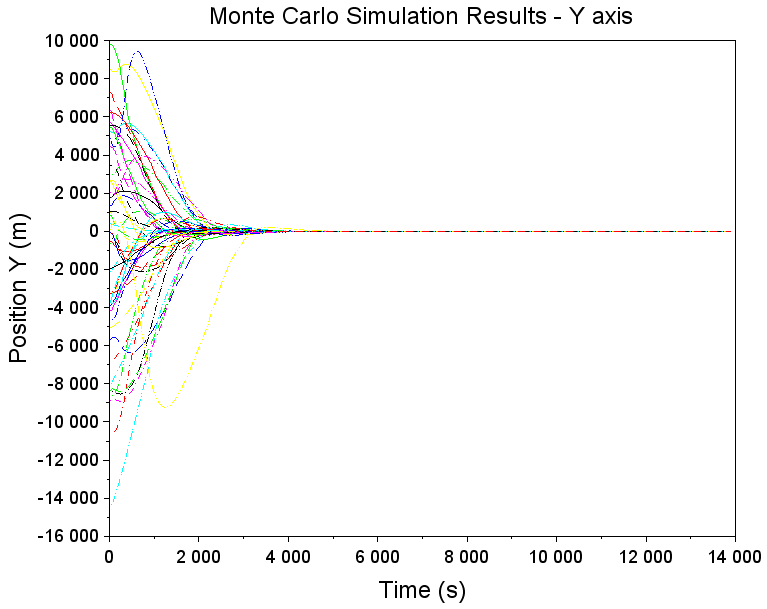

(b) Graphical analysis of the Y-axis positional corrections over the course of 1000 seconds, illustrating the CW-based controller's robustness in managing higher orbit dynamics.

Figure 4.106.: Comparative analysis of the X and Y axis trajectory adjustments in higher orbits over a 1000-second control interval using the CW-based controller, showcasing the system's effectiveness and robustness.

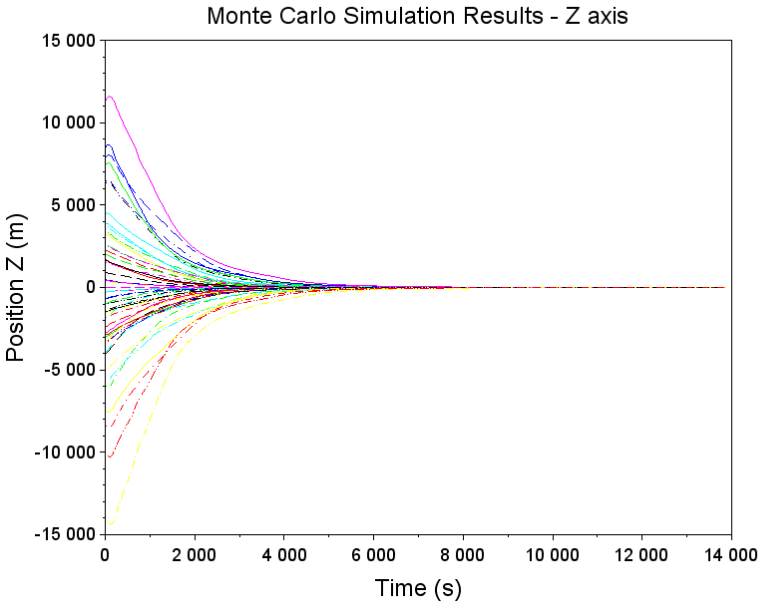

Figure 4.107.: Z-axis adjustments from Monte Carlo simulations, highlighting trajectory control with a 1000-second Δt.

Figure 4.108 presents a comprehensive analysis of the thruster activation patterns, which is critical for evaluating the operational efficiency and fuel consumption of the control system. The data highlights a significant variation in thruster usage, with the maximum activations reaching 4720 for the negative z-direction thruster. Conversely, the minimum number of activations recorded was as low as 5, also for the negative z-direction thruster. This variation underscores the controller's adaptive response to dynamic conditions, with the majority of thruster firings clustering at the lower end of the spectrum, indicating a conservative approach to fuel management and mechanical wear.

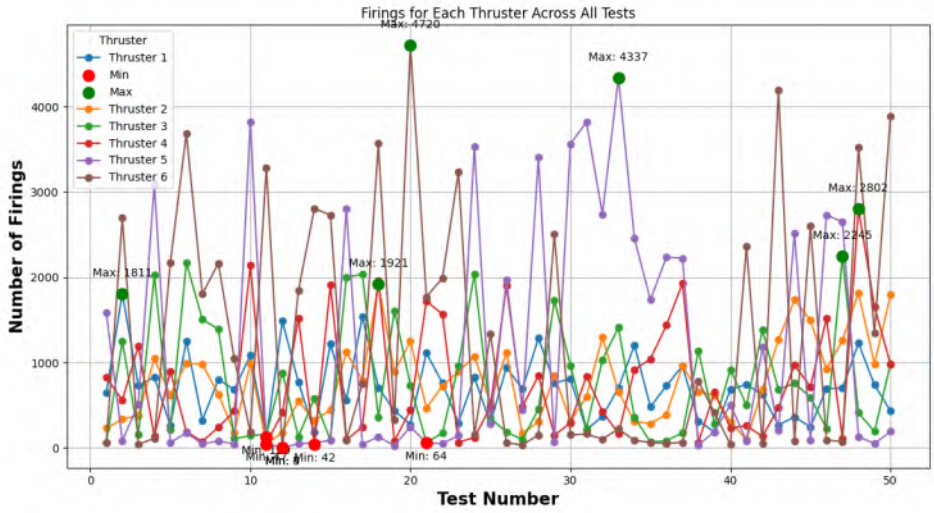

Figure 4.108.: Comprehensive analysis of thruster firings across multiple tests, highlighting propulsion management and sustained control exertions in a 1000-second Δt CW-based system.

Fuel consumption is maintained at an efficient level, totaling only 0.16428 kg, which falls within anticipated parameters. This demonstrates the controller's prudent use of resources, especially notable with the extended Δt setting, and highlights improved efficiency over the LQR controller implementation.

The performance analysis of the CW-based trajectory controller at higher orbital altitudes with a 1000-second Δt confirms its capability for precise and efficient navigation in space missions. This controller not only meets the demands of accurate trajectory management but also supports sustainable fuel consumption, a vital attribute for the success of long-duration missions.

4.9.2. Test Case 2: Scenario Analysis for an 8371 km Orbital Radius

Initial Conditions For Test Case 2, the scenario employs a semi-major axis of 8371000 meters, with each simulation covering two full orbits, resulting in a total duration of 15244.3 seconds. Initial position and velocity vectors for the chaser spacecraft again varied within $[-5000, 5000]$ meters to test controller adaptability at this increased altitude.

LQR Controller Implementation

This test confirms the efficiency of the LQR controller in a higher orbit of 8371000 meters radius. Similar to the previous test case, the controller parameters Q and R remain unchanged (see section 4.9.1). The following figures showcase the controller's performance in aligning the spacecraft along the x, y, and z axes, meeting the target within 2000 to 3000 seconds, illustrating the consistent reliability of the LQR settings across varying orbital altitudes.

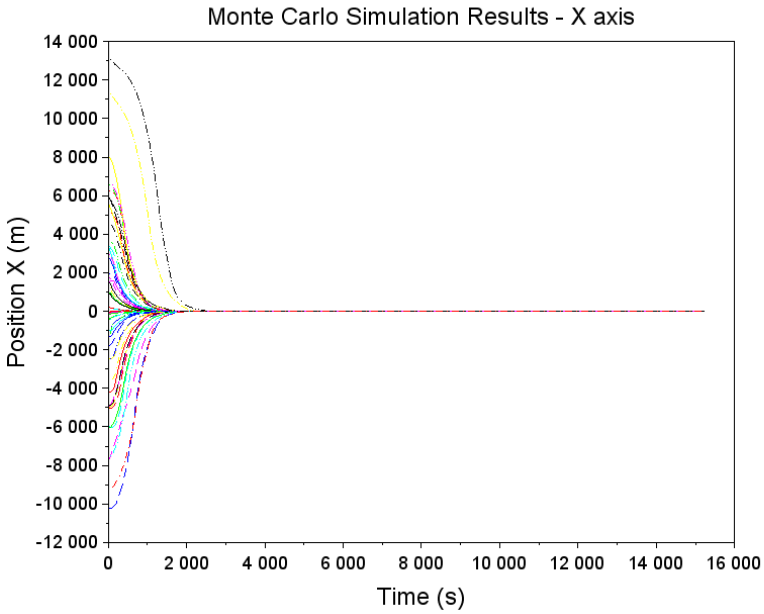

(a) LQR-controlled X-axis trajectory alignment at an altitude of 8371000 meters, achieving target precision within 3000 seconds.

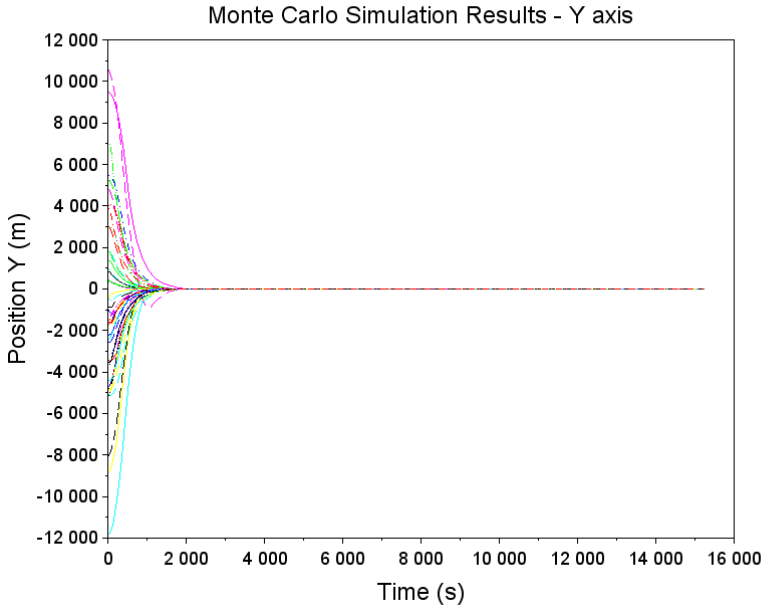

(b) Control efficacy in the Y-axis at 8371000 meters altitude, under LQR settings, demonstrating effective trajectory stabilization.

Figure 4.109.: Trajectory analyses at 8371000 meters altitude showing LQR controller effectiveness in X and Y-axis alignments within a simulation environment.

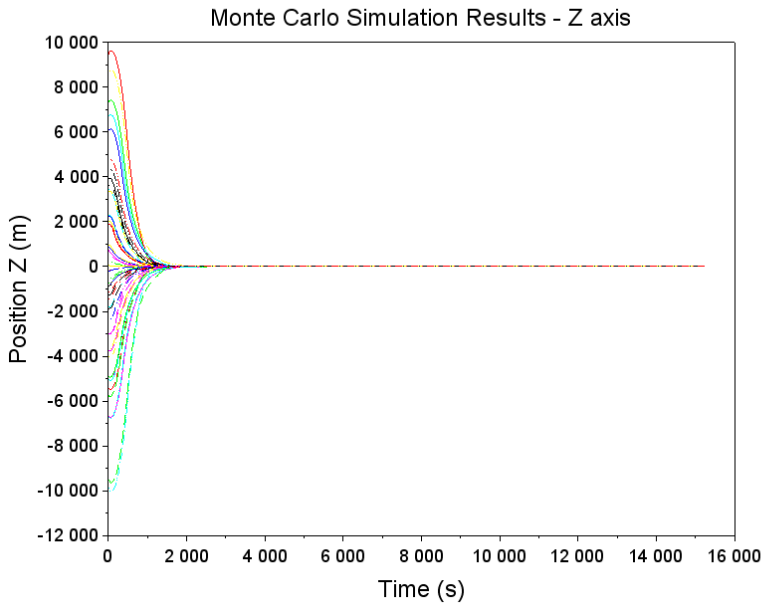

Figure 4.110.: Z-Axis adjustment within higher orbital parameters showing rapid stabilization capabilities of the LQR controller within 2000 seconds.

Thruster Activity Analysis Figure 4.111 presents a detailed analysis of the thruster usage across various test runs within Test Case 2, set at an orbital radius of 8371000 meters. The thruster firing data reveal significant variability in usage patterns, crucial for assessing the propulsion system's efficiency and responsiveness under extended orbital conditions. The most frequent activations occurred in the negative y-direction with a peak of 2205 firings for a particular test scenario, indicating high control demands in this orientation. Conversely, the minimum usage was recorded for the positive y-direction thruster, with only 15 firings, reflecting less need for corrective actions in that direction. Additionally, a specific test case with initial conditions set at

$$[x_0; y_0; z_0] = [1000; 700; 300]$$

meters, demonstrated a minimal fuel consumption of only 0.3134 kg, underscoring the controller's efficacy and fuel efficiency in maintaining the spacecraft's trajectory within the specified parameters.

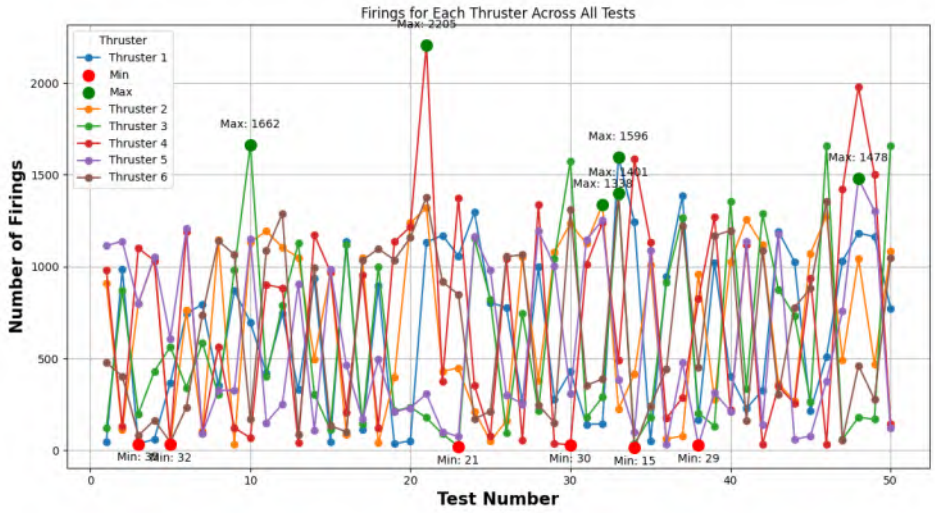

Figure 4.111.: Frequency of thruster activations during Test Case 2, demonstrating the dynamic control response and fuel efficiency at an orbital radius of 8371000 meters. Maximum and minimum firings illustrate the range of control efforts required under varying conditions.

CW-based Controller Implementation

The second test case also assesses the CW-based trajectory controller with a Δt of 2000 seconds. The extended control interval tests the controller's efficiency over longer periods crucial for deep-space missions.

The CW-based controller's effectiveness is evaluated across different axes under extended operational conditions. Convergence times for the x-axis varied: most scenarios achieved target alignment around 6000 seconds, while a few extended to about 9000 seconds, showcasing the controller's adaptability and resilience under varied dynamic inputs, as shown in Figure 4.112a. For the y-axis, convergence was typically achieved around 5500 seconds, with some tests requiring up to 10000 seconds, as detailed in Figure 4.112b. The z-axis demonstrated the most consistent and rapid convergence, with all tests aligning before 5000 seconds, indicating a robust control mechanism effectively compensating for vertical positional variances, illustrated in Figure 4.113.

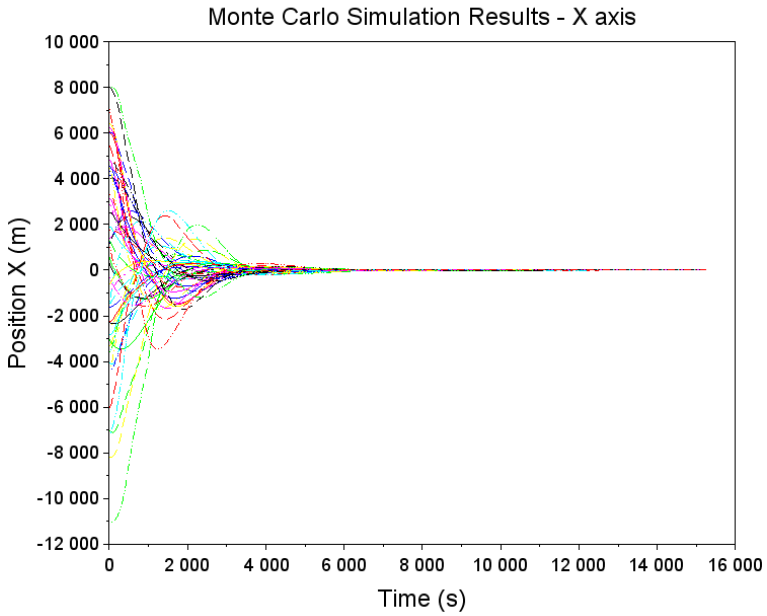

(a) X-axis trajectory adjustments under CW control at 8371000 meters altitude, demonstrating convergence within 6000 to 9000 seconds ($\Delta t = 2000$ seconds).

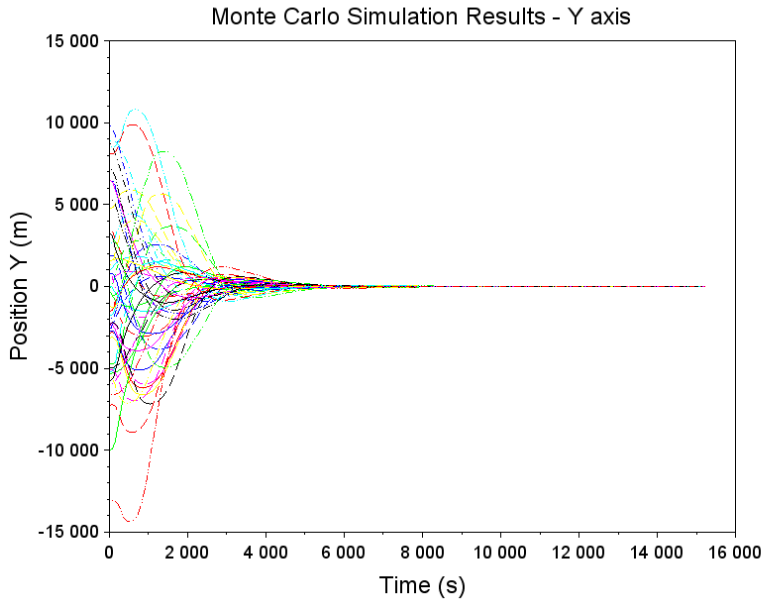

(b) Y-axis performance under CW control in higher orbits, with convergence times ranging from 5500 to 10000 seconds ($\Delta t = 2000$ seconds).

Figure 4.112.: Test Case 2: Comparative analysis of X and Y-axis trajectory adjustments in a high orbit of 8371000 meters, under extended CW control, demonstrating the controller's effectiveness over prolonged intervals.

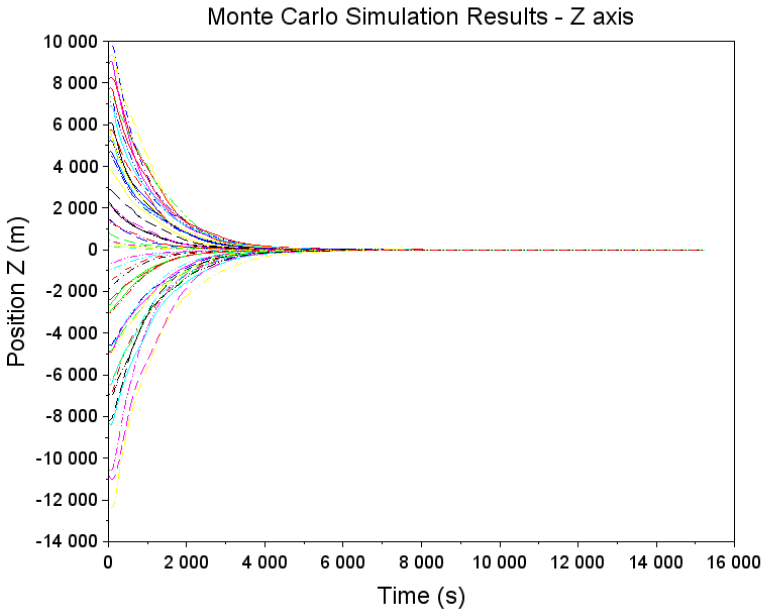

Figure 4.113.: Test Case 2: Control dynamics along the Z-axis under the CW controller, achieving rapid stabilization across all test scenarios within 5000 seconds ($\Delta t = 2000$ seconds).

Thruster Activity and Fuel Consumption The thruster firing data provide crucial insights into the operational demands and efficiency of the CW controller. Analysis reveals the maximum and minimum thruster activations, noting the most significant demand on the z-direction thruster with a peak of 3821 firings in one test, while the minimal activity was also in the z-direction with only 37 firings in another scenario. These extremes are indicative of the controller's responsiveness to varying dynamic conditions.

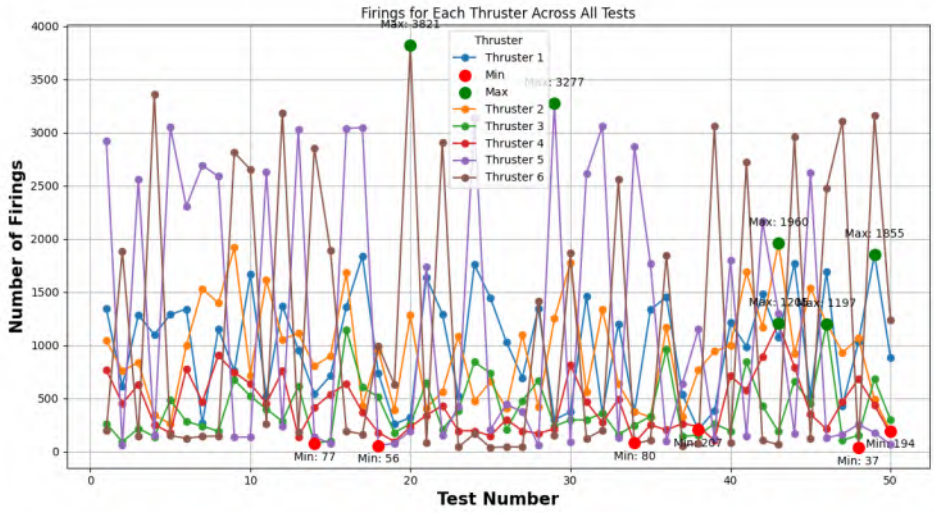

Figure 4.114.: Test Case 2: Comprehensive thruster firing data, indicating efficient resource utilization under the CW controller with a Δt of 2000 seconds, in higher orbital scenarios.

4.10. Observations on Controller Performance in Higher LEO Orbits

This section outlines key observations from the performance analysis of LQR and CW-based controllers.

LQR Controller Observations

Performance Metrics

The LQR controller demonstrated robust capabilities in maintaining precise control over the spacecraft's trajectory, with successful convergence to target positions within approximately 2000 seconds across all tested axes (x, y, and z). This rapid stabilization is indicative of the LQR's reliability and precision in higher orbital environments. Fuel consumption remained within acceptable limits, peaking at 0.3115 kg for scenarios involving the furthest orbital positions, thereby underscoring the LQR's efficiency.

Thruster Activity

Analysis of thruster firing patterns revealed a higher demand on the thruster directed towards the negative y-direction, which was activated up to 1745 times to counteract orbital perturbations and maintain trajectory alignment. This suggests a robust response mechanism to dynamic orbital conditions, with minimal activations noted for the positive y-direction, indicating less frequent corrective requirements in that orientation.

CW-based Controller Observations

Extended Control Efficiency

The CW-based controller, tested with a Δt of 1000 seconds, showcased effective management of spacecraft trajectories across all axes within a control interval significantly longer than typical settings. The controller adeptly handled initial state variances, steering the spacecraft towards its target within a span of 2000 seconds for most tests. Such performance highlights the controller's potential for long-duration missions where sustained trajectory control is crucial.

Adaptability and Fuel Efficiency

In terms of adaptability, the CW controller adjusted to a range of dynamic inputs, efficiently managing trajectory corrections with extended control intervals. Fuel consumption was notably efficient, with a recorded use of only 0.16428 kg, emphasizing the controller's capability to optimize resource usage effectively over prolonged operational periods.

Thruster Utilization

The thruster usage data offered further insights into the operational dynamics under the CW-based control system. The controller exhibited a strategic use of thrusters, particularly maximizing the efficiency of z-direction thrusters, which were heavily utilized in one scenario with up to 3821 firings. In contrast, minimal firings were observed in the same directional axis under less demanding conditions, illustrating the controller's ability to scale its response based on real-time navigational requirements.

Comparative Analysis

The comparative analysis between the LQR and CW-based controllers indicates that both systems are highly capable of navigating higher orbit scenarios effectively. However, the LQR controller tends to achieve quicker stabilization across all axes, which might be preferable in scenarios where rapid response is critical. Conversely, the CW-based controller excels in scenarios requiring sustained control over extended periods, potentially making it more suitable for long-term missions where fuel efficiency and adaptive response are prioritized.

Overall, the detailed evaluation of these controllers in higher LEO orbits demonstrates their suitability for advanced space mission scenarios, with each controller having distinct advantages that can be leveraged depending on specific mission requirements.

5. Conclusion

The objective of this thesis was to design and model an orbital control system for station keeping, utilizing Scilab 5.5.2 and Xcos to create models of a spacecraft. The models tested and combined in Xcos included the Translation Motion, Thruster, GNSS Receiver, and Orbit Determination models, culminating in a comprehensive simulation of spacecraft motion. The functionality of the Thruster model has been thoroughly tested and validated, as discussed in Section 3.4.

This research focused on the development and implementation of orbit control systems for satellites in LEO, based on CW principles. It involved the design and comparative analysis of two controllers, evaluating them based on thruster usage and fuel consumption, with the aim of enhancing the efficiency of station-keeping and rendezvous maneuvers.

A detailed evaluation of two control strategies—LQR and CW-based controllers—was conducted across various operational environments and test cases. The analysis included both low and higher Earth orbits and employed Monte Carlo simulations to accommodate initial condition variability and to evaluate the controllers' robustness under stochastic effects.

In specific tests, the LQR controller demonstrated high precision and fuel efficiency when configured with high control weights. Notably, in Test Case 4, it minimized fuel usage to 0.0733 kg, effectively maintaining trajectory control (see Subection 4.5.1). This configuration was optimal for scenarios requiring precise control with minimal fuel usage. Conversely, the CW-based controller excelled during extended control durations ($\Delta t = 2000$ seconds), achieving the lowest fuel consumption of 0.041085 kg in all test scenarios, highlighting its suitability for long-duration missions (refer to Subection 4.5.3).

Thruster activity varied significantly across scenarios. The most aggressive control strategy was observed in Test Case 1 under LQR control(see Subection 4.5.1), which required 1605 activations to maintain accurate trajectory paths. Meanwhile, the CW-based controller used a more balanced approach, with the fewest thruster firings (367) in a scenario that emphasized velocity control and operational efficiency.

Monte Carlo simulations underscored the adaptability of both controllers. The LQR controller exhibited superior performance across extended ranges of initial conditions, ensuring consistent effectiveness despite significant perturbations. However, the CW controller faced challenges in rapid maneuver scenarios, particularly in Test Case 1 with $\Delta t = 10$ seconds, where it struggled to converge under extended initial condition ranges.

5.1. Adaptation to Higher Orbital Altitudes

Investigations conducted at higher orbital altitudes, specifically at 7871 km and 8371 km, provided valuable insights into the scalability and adaptability of control strategies. Both the LQR and CW-based controllers were rigorously tested, unveiling particular challenges related to control effort and fuel efficiency as orbital altitudes increased. The LQR controller exhibited robust performance with minimal adjustments required, affirming its reliability in higher orbits. Conversely, the CW-based controller demonstrated significant fuel efficiency, especially at 8371 km with a Δt of 2000 seconds, rendering it suitable for extended missions where fuel economy is a priority.

5.2. Comparative Analysis and Final Remarks

The LQR controller consistently delivered better precision and faster convergence, aligning well with mission requirements that demand high accuracy and quick responsiveness. On the other hand, the CW-based controller was more effective in scenarios prioritizing fuel efficiency and operational simplicity, making it ideal for longer-duration missions where conserving fuel is crucial.

In conclusion, the choice between LQR and CW-based controllers should be guided by specific mission criteria: LQR is preferable for missions requiring high precision and stability against disturbances, while CW is better suited for missions that focus on fuel efficiency and simpler long-term control. Future research could explore hybrid strategies that combine the strengths of both controllers, potentially enhancing adaptive control systems for space missions.

5.3. Summary of Key Findings

The tests involving direct thrust applications in designated orbital directions predominantly corroborated the theoretical models, with precise outcomes in the alteration of orbital parameters such as semi-major axis and eccentricity due to controlled thrust applications. For example, the tests involving direct thrust in specific orbital directions (Tests 1 through 4) demonstrated how closely the simulation aligned with expected changes in orbital characteristics, reinforcing the reliability of the models employed:

- **Predictive Accuracy:** The slight variances observed between expected and actual outcomes in parameters like the semi-major axis underline the challenges in perfectly replicating the complex dynamics of space within a simulated environment. These discrepancies, though minor, provide critical data that can be used to refine the models further.
- **Operational Implications:** The findings highlight the sensitivity of orbital dynamics to operational conditions and control inputs, suggesting that even small misalignments or timing delays in thruster operations can significantly impact the spacecraft's trajectory and stability.

This study highlighted several significant insights as discussed in Section 4.5.1, and 4.5.3:

- The development and simulation of orbit control models using LQR and CW trajectory control strategies significantly enhanced the precision of satellite maneuvers, particularly in terms of fuel efficiency and maneuver accuracy.
- Validation of these strategies within a simulated Scilab environment confirmed their robustness and effectiveness in maintaining desired satellite trajectories.
- Comparative analysis with existing control systems underscored that the proposed models both support and extend the findings of previous research, offering new perspectives on the practical challenges of orbit maintenance in LEO.

The Monte Carlo simulations provided a detailed evaluation under a variety of initial conditions, shedding light on the distinct capabilities and limitations of each controller:

- The LQR controller exhibited excellent performance in scenarios with moderate variability in initial conditions, achieving stable control and efficient trajectory convergence. Nevertheless, vulnerabilities emerged under certain configurations, notably when low weights were assigned to position and velocity relative to control efforts, leading to non-convergence in some instances, particularly in the X and Y axes, as detailed in Section 4.6.1.
- The CW controller consistently excelled under standard operational conditions, defined within the range $[-1500, 1500]$ meters. This solid performance confirms its suitability for routine satellite operations. However, it also faced challenges under extended conditions $[-2500, 2500]$ meters, particularly in tests with very short control intervals Δ_t, exposing its limitations under rapidly changing conditions, as discussed in Section 4.6.2.

5.4. Discussion of the Implications

The findings of this thesis have broad implications for both theory and practice:

- **Enhanced Model Fidelity:** The insights gained from the testing scenarios involving directional thrust(Section 3.4) advocate for the continuous improvement of simulation models to more accurately mirror real-world conditions, which is vital for the planning and execution of complex satellite operations.
- **Fuel Efficiency and Control Optimization:** By fine-tuning the control algorithms based on the validated models, future missions can achieve greater fuel efficiency and cost-effectiveness, essential for long-duration space missions and extensive satellite networks.
- **Theoretical Framework:** This research enriches the theoretical foundations of satellite dynamics and control by refining models used for predicting and adjusting satellite trajectories, thereby contributing significantly to the academic literature.
- **Practical Applications:** The developed control systems have the potential to enhance the longevity and reliability of satellite missions by reducing fuel consumption and providing precise control commands, thereby increasing the operational efficiency of satellites.

- **Future Technological Developments:** The integration of these advanced control strategies could lead to the development of more autonomous satellite systems, potentially revolutionizing future space technology and operations.

5.5. Limitations of the Study

While the results are promising, this study is not without limitations:

- The validation process relied primarily on simulated scenarios, which may not fully capture all the physical and external variables affecting satellites in actual space conditions.
- There is a compelling need for future research to focus on implementing these control strategies in actual flight missions to gather real-world data. Such data would provide a more definitive validation of the simulation outcomes and help refine the controllers further.
- Extending the application of these controllers to missions beyond LEO, including Medium Earth Orbit (MEO) and Geostationary Orbit (GEO), would significantly broaden their applicability and utility, enhancing overall mission flexibility.

5.6. Recommendations for Future Research

Based on the findings and limitations identified, further research could explore several promising areas:

- **Incorporation of External Perturbations:** Future simulations should include factors such as atmospheric drag, solar radiation pressure, and other perturbations to enhance the realism and predictive power of the models.
- Adapting and testing the proposed control strategies for satellites in MEO and GEO to assess their effectiveness across different orbital environments.
- Integrating emerging technologies such as artificial intelligence and machine learning to further enhance the autonomy and operational efficiency of orbit control systems.
- Conducting empirical tests of the developed models in real-world satellite missions to refine the control strategies based on operational data and direct feedback.
- Exploring different thruster technologies such as hot gas, cold gas, and ion thrusters in conjunction with the designed controllers to enhance versatility and performance.

Bibliography

AI Solutions. (n.d.). Attitude reference frames [Accessed on 2023-07-10].

Anderson, B. D., & Moore, J. B. (2005). *Optimal control: Linear quadratic methods* (1st). Prentice Hall.

Armstrong, M. (2022, September). *From sputnik to starlink - earth's orbit is getting crowded [digital image]* [Retrieved February 26, 2024, from]. https://www.statista.com/chart/28308/satellite-payloads-launched-into-space-timeline/

Bate, R. R., Mueller, D. D., & White, J. E. (1971). *Fundamentals of astrodynamics*. Dover Publications.

Breger, L., & How, J. P. (2008). New state transition matrix for relative motion on an arbitrary elliptical orbit. *Journal of Guidance, Control, and Dynamics*, *31*(2), 290–302.

Brown, A., & Smith, K. (2019). Integrating lqr and cw control for efficient satellite docking. *IEEE Transactions on Aerospace and Electronic Systems*, *55*(4), 1805–1816.

Choueiri, E. Y. (2009). New dawn for electric rockets. *Scientific American*, *300*(2), 58–65.

Clohessy, W. H., & Wiltshire, R. S. (1960a). Terminal guidance system for satellite rendezvous. *Journal of the Aerospace Sciences*, *27*(9), 653–658.

Clohessy, W. H., & Wiltshire, R. S. (1960b). Terminal guidance system for satellite rendezvous. *Journal of the Aerospace Sciences*, *27*(9), 653–658. https://doi.org/10.2514/8.8704

Curtis, H. D. (2013). *Orbital mechanics for engineering students* (3rd). Elsevier.

Curtis, H. D. (2014). *Orbital mechanics for engineering students* (3rd). Elsevier.

Damico, G., et al. (2015). Dynamic modeling and efficient control strategies for spacecraft rendezvous. *Journal of Guidance, Control, and Dynamics*, *38*(7), 1286–1302.

de Bruijn, F. J. (2016). Orbit maneuver for responsive coverage using electric propulsion. *Journal of Spacecraft and Rockets*, *53*(4), 635–645.

Du, X., Richter, H., & Guo, Y. (2016). Multivariable sliding-mode strategy with output constraints for aeroengine propulsion control. *Journal of Guidance, Control, and Dynamics*, *39*(7), 1631–1642. https://doi.org/10.2514/1.g001802

Eaton, J. W., Bateman, D., Hauberg, S., & Wehbring, R. (2013). Gnu octave manual version 4 [Available online: https://www.gnu.org/software/octave/doc/interpreter/].

Eickhoff, J. (2012). *Onboard computers, onboard software and satellite operations: An introduction*. Springer. https://doi.org/10.1007/978-3-642-25170-2

Enterprises, S. (2021). Scilab: Free and open source software for numerical computation [Retrieved from https://www.scilab.org].

Fortescue, P., Stark, J., & Swinerd, G. (2011). *Spacecraft systems engineering* (4th). John Wiley Sons.

Franklin, G., Powell, J., & Emami-Naeini, A. (2010). *Feedback control of dynamic systems* (Vol. 7). Prentice Hall.

Gatlin, B. (2019). *Satellite constellation design and management*. John Wiley & Sons.

Gelb, A. (1974). *Applied optimal estimation*. The MIT Press.

Goebel, D. M., & Katz, I. (2008). *Fundamentals of electric propulsion: Ion and hall thrusters*. John Wiley Sons.

Goldstein, H., Poole, C. P., & Safko, J. L. (2002). *Classical mechanics* (3rd). Addison Wesley.

Guan, X., Xu, X., & Li, P. (2022). Fault diagnosis and isolation for aerospace systems: A survey of recent developments. *IEEE Transactions on Aerospace and Electronic Systems*, *59*(3), 1954–1972.

Gurfil, P. (2013). *Spacecraft attitude determination and control*. Cambridge University Press.

Hill, G. W. (1878). Researches in the lunar theory. *American Journal of Mathematics*, *1*(1), 5–26. https://doi.org/10.2307/2369430

Hofmann-Wellenhof, B., Lichtenegger, H., & Collins, J. (2008). *Global positioning system: Theory and practice* (Vol. 5). Springer-Verlag Wien.

Iqbal, M., Ali, Z., & Javaid, N. (2020). A survey of recent advancements in satellite propulsion technologies. *Advances in Space Research*, *66*(8), 2598–2620.

Julier, S. J., & Uhlmann, J. K. (1997). A new extension of the kalman filter to nonlinear systems. *Int. Symp. Aerospace/Defense Sensing, Simul. and Controls*.

Kumar, V. (2011). Design of autonomous orbit control systems for satellites. *Journal of Aerospace Engineering*, *24*(1), 127–138.

Lee, D., & Richards, A. (2018). Hybrid control strategies for satellite proximity operations. *Acta Astronautica*, *143*, 372–380.

Leick, A. (2004). *Gps satellite surveying* (2nd). John Wiley & Sons.

Levine, W. S. (1996). *The control handbook*. CRC Press.

Li, B., Li, P., Liu, Y., & Sun, C. (2018). Fuel-efficient orbit control for multiple satellites using deep reinforcement learning. *IEEE Transactions on Aerospace and Electronic Systems*, *55*(1), 371–384.

Li, M., et al. (2019). Review of real-time multi-gnss precise orbit determination based on the filter method. *Satellite Navigation*, *2*, 1–13. https://doi.org/10.1186/s43020-019-0002-2

Luo, Y., Wu, J., Liu, Z., & Liu, F. (2020). Learning-based adaptive attitude control for spacecraft with actuator saturation. *IEEE Transactions on Industrial Electronics*, *68*(7), 6205–6215.

Matsumoto, C. (2016). *Guidance, navigation, and control of small satellite attitude using micro-thrusters* [Master's thesis]. University of Hawai'i at Manoa.

Maybeck, P. S. (1979). *Stochastic models, estimation, and control: Vol. 1*. Academic Press.

Michael, G. J., & Farrar, F. (1974). *Development of optimal control modes for advanced technology propulsion systems* (tech. rep.). United Aircraft Research Laboratories. East Hartford, CT, USA.

Montenbruck, O., & Gill, E. (2000). *Satellite orbits: Models, methods, and applications*. Springer.

Montenbruck, O., & Gill, E. (2018). *Satellite orbits: Models, methods and applications* (2nd). Springer. https://doi.org/10.1007/978-3-662-58351-3

Mottelet, S. (2012). Customizing xcos with new blocks and palette [Retrieved from http://www.scilab.org/scilab/xcos].

Ogata, K. (1998). *Modern control engineering*. Prentice-Hall.

Oppenheim, A. V., & Schafer, R. W. (1999). *Discrete-time signal processing* (2nd). Prentice Hall.

Overton, M. L. (2015). Numerical computing with matlab [Retrieved from https://www.mathworks.com/moler/index$_n$*cm.html*].

Pisacane, V. L. (2005). *Fundamentals of space systems* (2nd). Oxford University Press.

Proakis, J. G., & Manolakis, D. K. (2007). *Digital signal processing: Principles, algorithms, and applications* (4th). Prentice Hall.

Qin, S., & Badgwell, T. (2003). A survey of robust control methods for spacecraft attitude control. *IEEE Transactions on Aerospace and Electronic Systems*, *39*(3), 595–628.

Ren, W., Beard, R., & Atkins, E. (2018). Distributed consensus algorithms in a multi-vehicle system with non-switching directed topology. *Control Theory and Applications*, *164*(2), 126–140.

Richter, H. (2011). A multi-regulator sliding mode control strategy for output-constrained systems. *Automatica*, *47*(10), 2251–2259. https://doi.org/10.1016/j.automatica.2011.08.003

Schaub, H., & Junkins, J. L. (2004). *Analytical mechanics of space systems*. AIAA.

Selvan, K., Siemuri, A., Prol, F., Välisuo, P., Bhuiyan, M. Z. H., & Kuusniemi, H. (2023). Precise orbit determination of leo satellites: A systematic review. *GPS Solutions*, *27*. https://doi.org/10.1007/s10291-023-01520-7

Starek, J. A., Schmerling, E., Maher, G. D., Barbee, B. W., & Pavone, M. (2017). Fast, safe, propellant-efficient spacecraft motion planning under clohessy–wiltshire–hill dynamics. *Journal of Guidance, Control, and Dynamics*, *40*(2), 418–438. https://doi.org/10.2514/1.G001913

Sullivan, J., & Atkins, E. (2013). Real-time trajectory redesign for satellite formation flying using cw equations. *Journal of Guidance, Control, and Dynamics*, *36*(2), 430–441.

Sutton, G. P., & Biblarz, O. (2010). *Rocket propulsion elements* (8th). John Wiley & Sons.

Team, F. (2020). Scilab toolbox development [Retrieved from https://fossee.in/scilab-toolbox].

Teunissen, P. J. G., & Montenbruck, O. (2017). Springer handbook of global navigation satellite systems. https://doi.org/10.1007/978-3-319-42928-1

Turner, M. J. L. (2008). *Rocket and spacecraft propulsion: Principles, practice and new developments* (3rd). Springer-Praxis.

Vaddiparty, K., & Chandrasekhar, S. (2017). Autonomous orbit control systems: A review of the state-of-the-art and future trends. *Acta Astronautica*, *134*, 112–126.

Vallado, D. A. (2013). *Fundamentals of astrodynamics and applications* (4th). Microcosm Press.

Vallado, D. A., & McClain, W. D. (2017). *Fundamentals of astrodynamics and applications* (4th). McGraw-Hill Education.

Wang, H., et al. (2019). Advanced control techniques for spacecraft. *Journal of Geophysical Research: Solid Earth*, *124*(3), 2894–2906.

Wertz, J. R. (2011). *Orbit and constellation design and management* (Extended). Microcosm Press.

Wertz, J. R., & Larson, W. J. (2011). *Spacecraft mission design* (2nd). Microcosm Press.

Wikipedia contributors. (2024). Moving average — Wikipedia, the free encyclopedia [[Online; accessed 5-March-2024]]. https://en.wikipedia.org/w/index.php?title=Moving_average&oldid=1211755357

Wu, F., & Chen, J. (2010). Adaptive lqr control using real-time dynamic programming. *International Journal of Control*, *83*(3), 600–608.

Acknowledgments

I am profoundly grateful for the guidance and support of my supervisor and mentor, Dr. Stephan Theil. His insights and expertise have been invaluable throughout this research journey, shaping both the direction and execution of this thesis.

I owe a special debt of gratitude to my family, whose unyielding support and belief in my abilities have been my foundation. To my sister, who has been a pillar of emotional and financial support, and to the rest of my family, who encouraged me every step of the way, thank you from the bottom of my heart.

I would also like to extend my thanks to my friends, whose enduring support and encouragement have played a crucial role in my personal and academic life during this challenging and rewarding time.

This thesis would not have been possible without the collective support, encouragement, and inspiration from all mentioned above, and for this, I am eternally grateful.

A. Appendix A: Additional Data and Graphs

A.1. Python code for analytical calculations

A.1.1. Calculation of orbital elements from position and velocity in Cartesian coordinates

This section describes the Python function `CL_oe_car2kep` which calculates orbital elements from given position and velocity vectors in Cartesian coordinates. The function uses NumPy for vector operations and calculations.

```
import numpy as np

def CL_oe_car2kep(pos, vel, mu=3.986004418e14):
    r = np.array(pos)
    v = np.array(vel)

    # Calculate specific angular momentum
    h = np.cross(r, v)
    n_mag = np.linalg.norm(h)

    # Calculate node vector
    N = np.cross([0, 0, 1], h)
    N_mag = np.linalg.norm(N)

    # Calculate eccentricity vector
    e_vec = (np.cross(v, h) / mu) - (r / np.linalg.norm(r))
    e = np.linalg.norm(e_vec)

    # Calculate semi-major axis
    a = 1 / ((2 / np.linalg.norm(r)) - (np.linalg.norm(v)**2 / mu))

    # Calculate inclination
    i = np.arccos(h[2] / n_mag)

    # Calculate right ascension of the ascending node (Omega)
    if N_mag > 1e-8:
        Omega = np.arctan2(N[1], N[0])
    else:
        Omega = 0  # Undefined for zero inclination
```

```
    # Calculate argument of periapsis (omega)
    if e > 1e-8 and N_mag > 1e-8:
        omega = np.arctan2(np.dot(np.cross(N, e_vec), h) / n_mag,
                           np.dot(N, e_vec) / N_mag)
    else:
        omega = 0  # Undefined for circular orbits or zero inclination

    # Calculate true anomaly (nu)
    if e > 1e-8:
        nu = np.arctan2(np.dot(np.cross(e_vec, r), h) / n_mag,
                        np.dot(e_vec, r) / e)
    else:
        nu = np.arctan2(r[1], r[0])  # True anomaly is the angle
in the plane for circular orbits

    return np.array([a, e, i, omega, Omega, nu])

# Example usage
pos = np.array([7071000, 0, 0])
vel = np.array([0, 7512.06853975, 0])
kep_elements = CL_oe_car2kep(pos, vel)
print("Keplerian Elements:", kep_elements)

def true_to_mean_anomaly(true_anomaly, eccentricity):
    if eccentricity < 1e-8:
        return true_anomaly  # For circular orbits,
mean anomaly approximates the true anomaly
    # Calculate eccentric anomaly
    eccentric_anomaly = 2 * np.arctan(np.sqrt((1 - eccentricity) /
(1 + eccentricity)) * np.tan(true_anomaly / 2))
    # Calculate mean anomaly
    mean_anomaly = eccentric_anomaly - eccentricity *
np.sin(eccentric_anomaly)
    return mean_anomaly

# Convert true anomaly back to mean anomaly for testing
true_anomaly = kep_elements[5]
eccentricity = kep_elements[1]
mean_anomaly = true_to_mean_anomaly(true_anomaly, eccentricity)
print("Mean Anomaly:", mean_anomaly)
```

In this function, various orbital elements such as the semi-major axis, eccentricity, inclination, right ascension of the ascending node, argument of periapsis, and true anomaly are computed from position and velocity vectors. These elements are essential for detailed orbital analysis and satellite mission planning.

A.1.2. Calculating position and velocity in Cartesian coordinates from the classical orbital elements

This section presents a Python function to calculate position and velocity in Cartesian coordinates from classical orbital elements. The calculations are performed using NumPy, and the conversion involves solving Kepler's equation and transforming coordinates from the perifocal to the Earth-Centered Inertial (ECI) frame.

```
import numpy as np

def kepler_equation(M, e, tolerance=1e-10):
    E = M
    delta = 1
    while delta > tolerance:
        delta_E = (E - e * np.sin(E) - M) / (1 - e * np.cos(E))
        E -= delta_E
        delta = abs(delta_E)
    return E

def orbital_elements_to_cartesian(a, e, i, omega, Omega, M, mu=3.986004418e14):
    E = kepler_equation(M, e)
    nu = 2 * np.arctan2(np.sqrt(1 + e) * np.sin(E / 2), np.sqrt(1 - e) *
np.cos(E / 2))

    p = a * (1 - e**2)
    r = p / (1 + e * np.cos(nu))
    r_perifocal = np.array([r * np.cos(nu), r * np.sin(nu), 0])

    v_perifocal = np.array([-np.sqrt(mu/p) * np.sin(nu),
                            np.sqrt(mu/p) * (e + np.cos(nu)),
                            0])

    R3_Omega = np.array([[np.cos(Omega), -np.sin(Omega), 0],
                         [np.sin(Omega), np.cos(Omega), 0],
                         [0, 0, 1]])

    R1_i = np.array([[1, 0, 0],
                     [0, np.cos(i), -np.sin(i)],
                     [0, np.sin(i), np.cos(i)]])

    R3_omega = np.array([[np.cos(omega), -np.sin(omega), 0],
                         [np.sin(omega), np.cos(omega), 0],
                         [0, 0, 1]])

    rotation_matrix = R3_Omega @ R1_i @ R3_omega
    r_eci = rotation_matrix @ r_perifocal
    v_eci = rotation_matrix @ v_perifocal
```

```
    return r_eci, v_eci

# Given orbital elements
a_t = 7071000  # Semi-major axis in meters
e_t = 0.00001  # Eccentricity
i_t = 0  # Inclination in radians
pom_t = 0  # Argument of perigee in radians
RAAN_t = 0  # Right ascension of ascending node in radians
M_t = 0  # Mean anomaly in radians

# Convert to Cartesian coordinates
pos, vel = orbital_elements_to_cartesian(a_t, e_t, i_t, pom_t, RAAN_t, M_t)
print("Position (ECI):", pos)
print("Velocity (ECI):", vel)
```

The code snippet above uses the classical orbital elements to compute the position and velocity of a satellite.

A.2. Orbit determination model: filtering

The simulation setup, as illustrated in Figure 3.4, incorporates random generator blocks designed to introduce noise into the position and velocity vectors. Utilizing the Celestlab function `CL_oe_car2kep`, these vectors are converted into orbital elements. The addition of noise to the position and velocity vectors results in the derivation of noisy (or unfiltered) orbital elements. This process is critical for demonstrating the functionality and necessity of implementing a filtering algorithm within the orbit determination model.

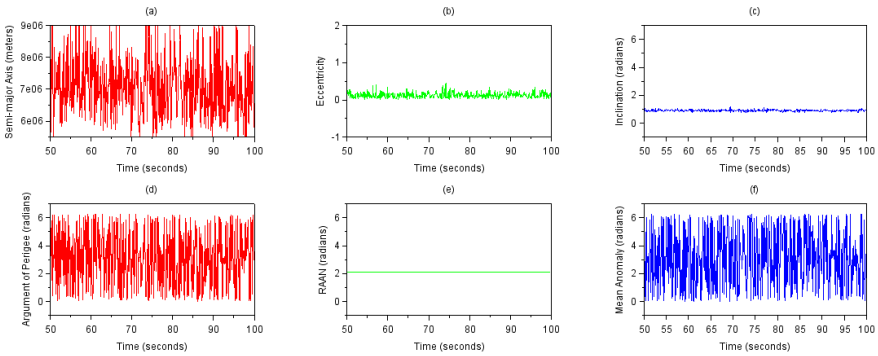

Figure A.1.: Unfiltered orbital elements as obtained from Celestlab's `CL_oe_car2kep` function

In practical scenarios, when a satellite orbits the Earth, its position and velocity are subject to fluctuations, leading to variations in the orbital elements. These fluctuations can subsequently induce imperfect control over the satellite, manifesting as unpredictable thrust applications or inaccuracies in the orbital element determinations.

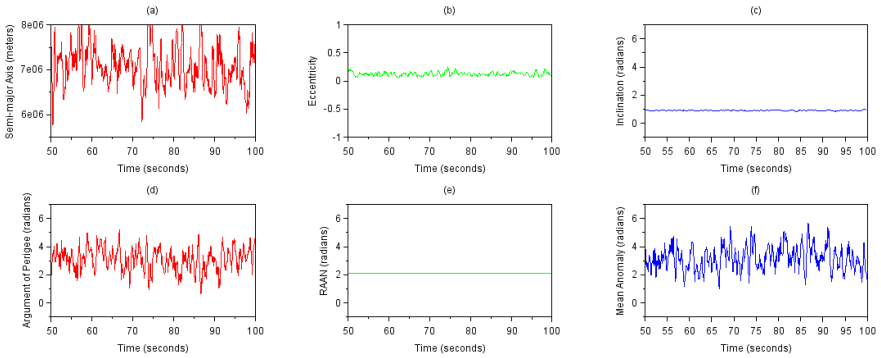

Figure A.2.: Orbital elements obtained with fifth order SMA filtering

The observed enhancements in the smoothness of the semi-major axis, as evidenced by the comparison between Figures A.1 and A.2, underscore the efficacy of the fifth-order SMA filtering algorithm. This comparison vividly demonstrates the algorithm's capability to mitigate noise within the orbital elements, thereby affirming its utility in enhancing the accuracy of satellite control through improved orbital element determination.

A comparison with a first-order filter revealed its relatively inferior smoothing effect, highly dependent on the filter coefficient (α) An α value of 1 results in minimal smoothing, closely mirroring the unfiltered scenario figure A.1, whereas an α of 0.01 provides a slight improvement in data smoothness.

This observation prompted the exploration and subsequent implementation of the SMA filter algorithm, culminating in significantly smoother orbital elements, as evidenced in Figure A.2. This enhancement substantiates the SMA filter's utility in refining the fidelity of simulated orbital data.

A.3. Additional Monte carlo test cases

A.3.1. Test Case 6: $\Delta t = 2500$ seconds

In this scenario, extending the time to target to 2500 seconds allowed for an extensive evaluation of the system's long-term trajectory correction capabilities. The prolonged period provided ample time for the controller to adjust the spacecraft's trajectory, which significantly reduced the frequency and intensity of thruster activations necessary to

maintain the desired path. The Monte Carlo simulation results for the x, y, and z axes, as seen in Figures A.4a, A.4b, and A.5, depict this extended alignment phase. The associated thruster firing data, presented in Figure A.3, further elucidates the minimal thruster activity, indicative of the reduced fuel consumption and enhanced efficiency achieved in this test.

The simulation results demonstrate the spacecraft's trajectory across the x, y, and z axes over time. Notably, the x-axis shows a tight convergence, with all trajectories closely following each other and stabilizing near the target position. Similarly, the y-axis and z-axis results illustrate a gradual alignment towards the desired coordinates, with minimal deviations post-convergence, suggesting a stable and controlled approach.

Thruster Activity Analysis of thruster firings reveals a marked decrease in activity, particularly highlighting the system's efficiency in utilizing minimal maneuvers to achieve and maintain alignment. The specific thruster data (Figure A.3) indicates that maximum and minimum firings across tests significantly vary, underscoring the adaptive response of the thruster system to the extended time frame provided for trajectory corrections.

Figure A.3.: Thruster firing statistics for Test Case 6 with $\Delta t = 2500$ seconds.

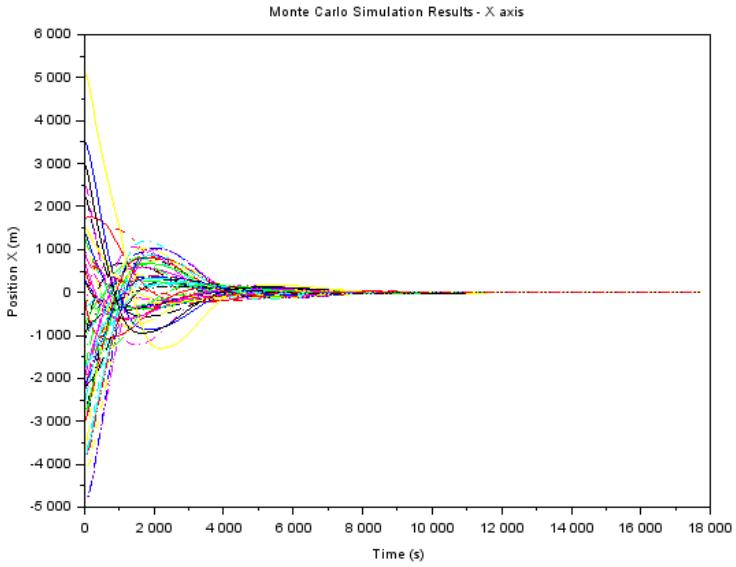

(a) Monte Carlo simulation results for the x-axis at $\Delta t = 2500$ seconds, showing trajectory behavior.

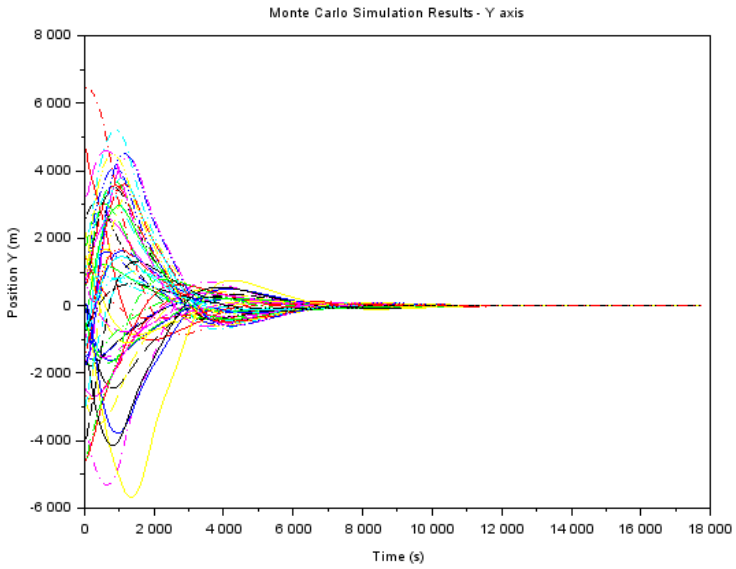

(b) Monte Carlo simulation results for the y-axis at $\Delta t = 2500$ seconds, detailing control performance.

Figure A.4.: Comparative Monte Carlo simulation results for the x-axis and y-axis at $\Delta t = 2500$ seconds, illustrating the system's dynamic response under extended control intervals.

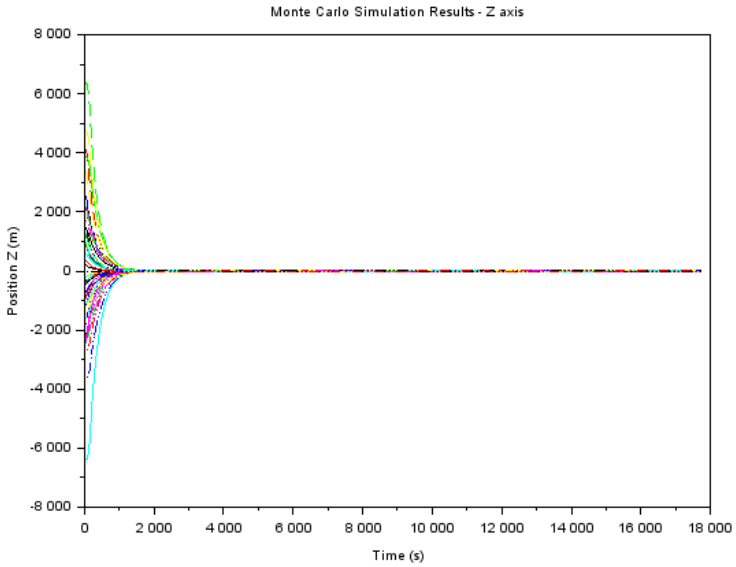

Figure A.5.: Monte Carlo simulation results for the z-axis at $\Delta t = 2500$ seconds.

A.3.2. Test Case 2: $\Delta t = 100$ seconds

In Test Case 2, the control system was challenged with a target time of $\Delta t = 100$ seconds to evaluate the controller's efficacy over an intermediate duration before reaching stabilization. This test case offers insight into the dynamic adjustments and control robustness necessary for effective trajectory alignment over approximately 2000 to 2500 seconds, which was the typical time frame observed for achieving proximity to the target across the x, y, and z axes.

Trajectory Analysis The Monte Carlo simulations for the x-axis (Figure A.6) show a significant initial overshoot before converging towards the target position, highlighting the controller's aggressive initial response and subsequent stabilization. The figure below illustrates these dynamics:

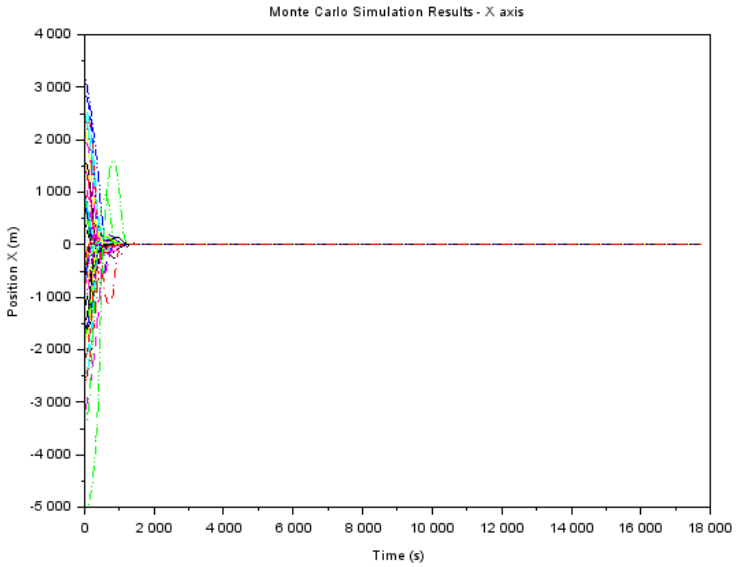

Figure A.6.: Monte Carlo simulation results for the x-axis indicating convergence times and stability patterns over the duration of the test.

Similarly, the y-axis results (Figure A.7) display a gradual descent, with the position values eventually aligning closely to the target trajectory. The behavior is captured in the following figure:

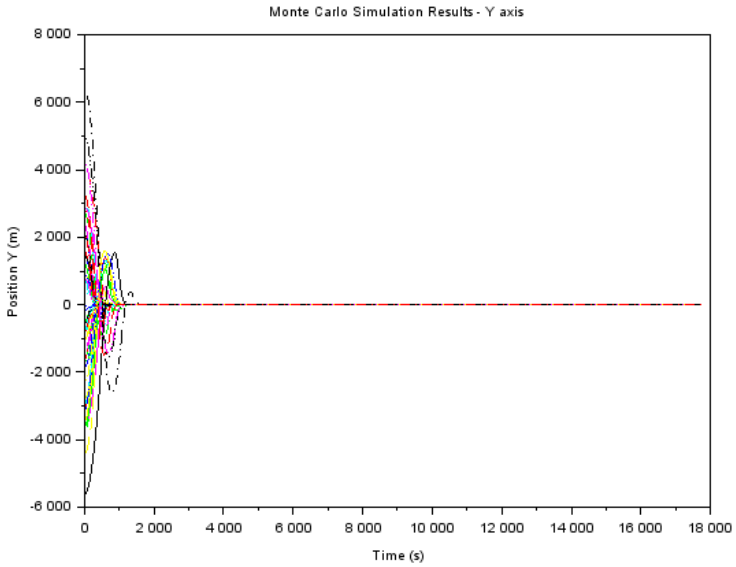

Figure A.7.: Trajectory results on the y-axis, illustrating the control system's ability to adjust and align the trajectory towards the target position.

The z-axis behavior (Figure A.8) is characterized by high-frequency oscillations, indicating a constant adjustment by the controller to maintain the trajectory within the desired bounds. This is detailed in the figure below:

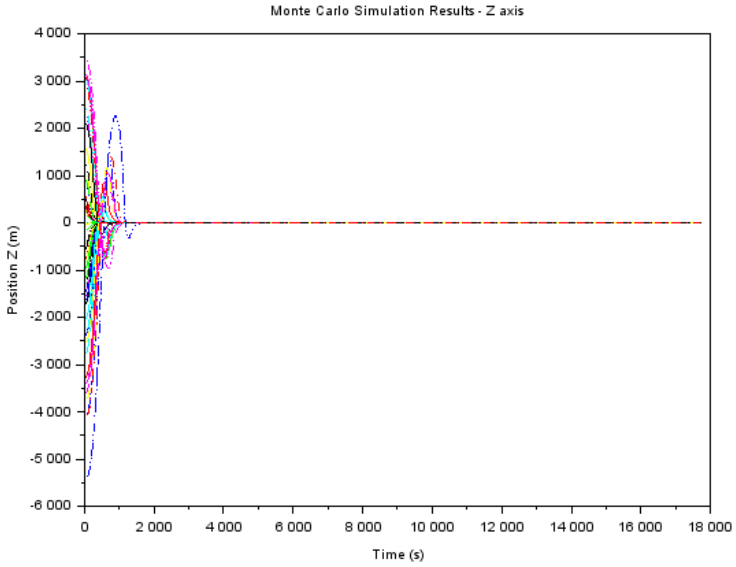

Figure A.8.: Z-axis results showing persistent oscillations as the system attempts to stabilize the spacecraft's position relative to the target.

The analysis of thruster firings is critical for understanding the control efforts required to maintain the trajectory. In this test, the thruster activity (Figure A.9) varied significantly, with a notable peak in the 28th test where the thruster for the positive x-direction was activated 1114 times. This high level of activity underscores the challenges in maintaining trajectory alignment within the set time frame and the resultant high demand on the control system. The following figure provides a detailed overview:

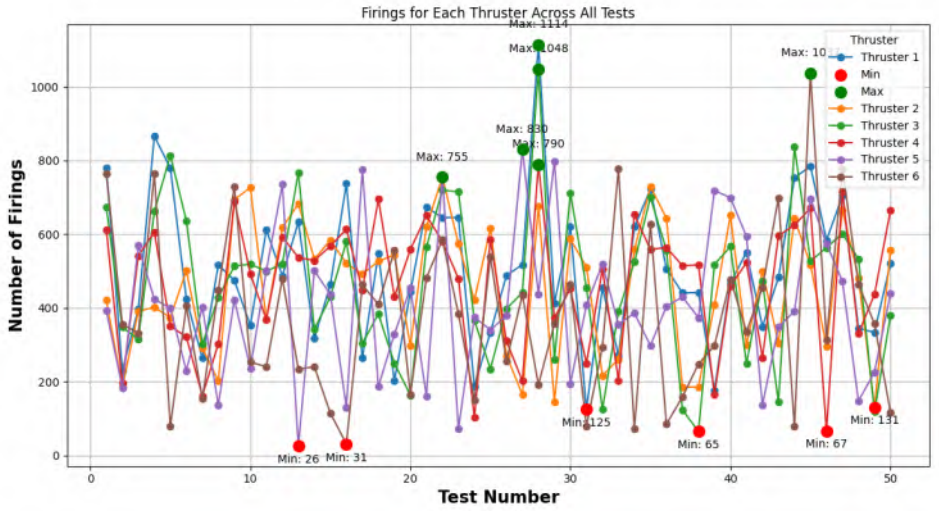

Figure A.9.: Detailed overview of thruster activity throughout the test, highlighting the variability and maximum firing instances necessary for trajectory correction.

A.3.3. Test Case 4: $\Delta t = 1000$ seconds

For a target time of 1000 seconds, reaching the target in the z-direction took slightly more than one orbit, while the x and y axes were aligned in about 5000 seconds. The thruster firing statistics, shown in Figure A.10, highlight increased activity in both the positive and negative z-direction thrusters compared to those for the x and y directions.

Thruster Activity Analysis The firing patterns of the thrusters are critical in evaluating the efficiency and effectiveness of the control strategy employed. Figure A.10 presents the number of firings for each thruster across all tests, where variability in the firing rate indicates the response to different trajectory corrections needed over the test duration.

Trajectory Control Analysis

- **X-axis:** As depicted in Figure A.11, trajectories quickly converge to the target, demonstrating the controller's capability to effectively manage lateral deviations.
- **Y-axis:** Figure A.12 shows the trajectory alignment along the y-axis, where convergence is similarly achieved efficiently.
- **Z-axis:** The z-axis control, shown in Figure A.13, required a longer time to stabilize, indicating a more challenging control scenario in the vertical direction.

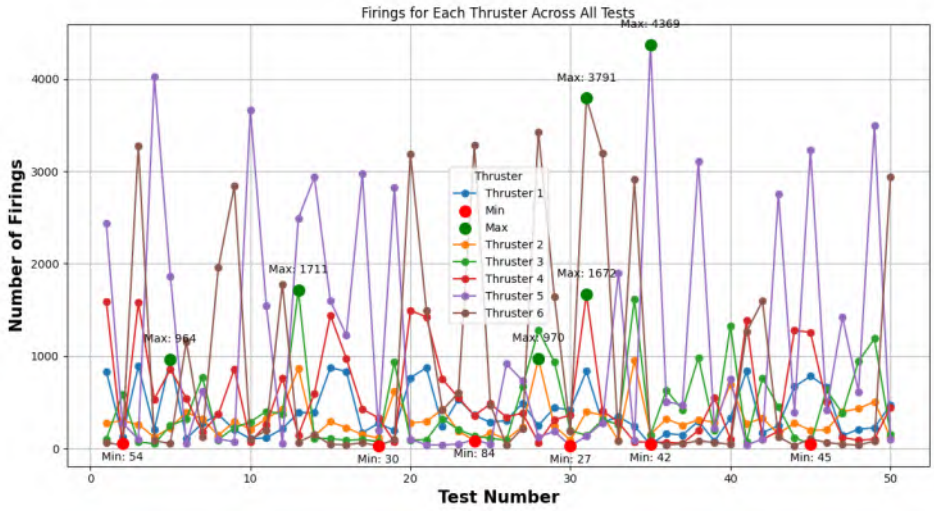

Figure A.10.: Thruster firings for each thruster across all tests with min/max annotations ($\Delta t = 1000$ seconds).

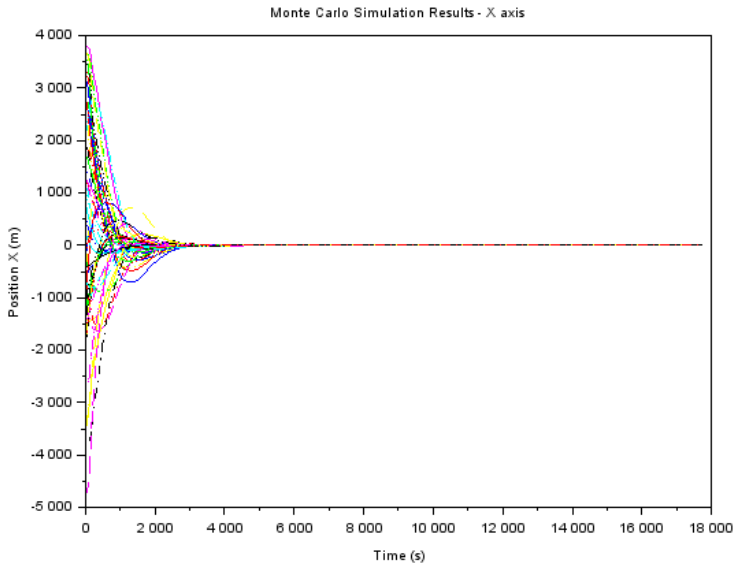

Figure A.11.: Monte Carlo Simulation Results - X axis.

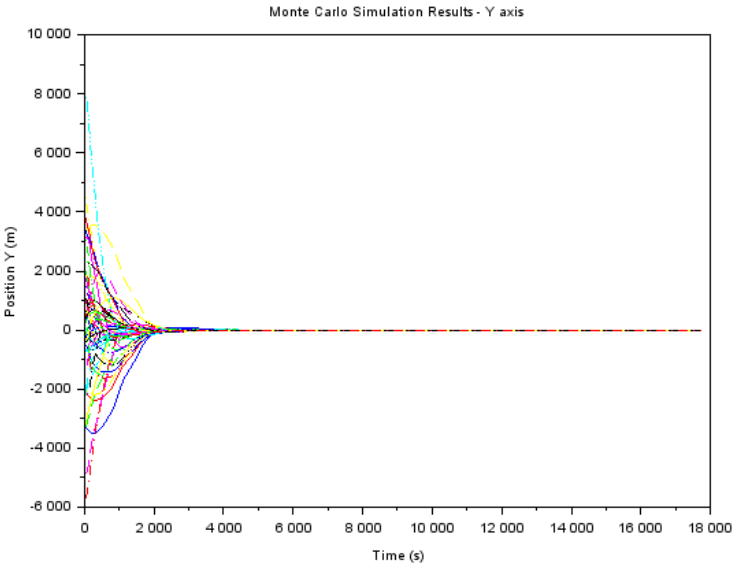

Figure A.12.: Monte Carlo Simulation Results - Y axis.

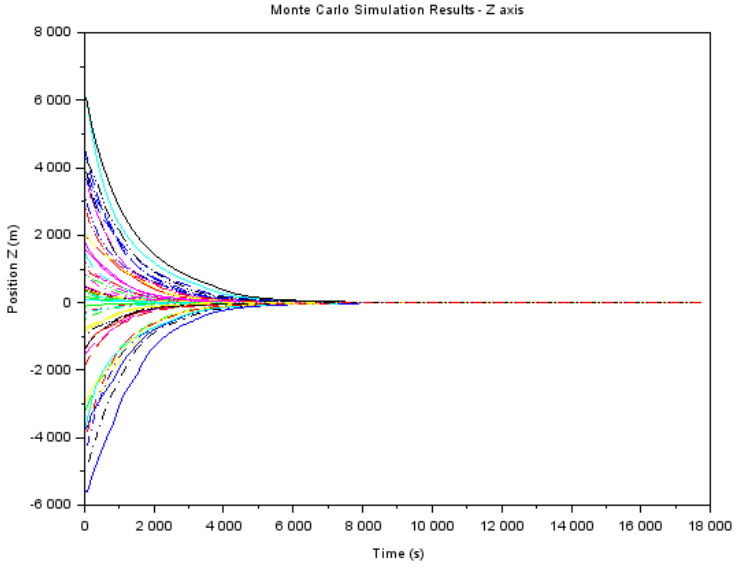

Figure A.13.: Monte Carlo Simulation Results - Z axis.

This analysis provides insights into the control system's performance, revealing both its strengths and areas for potential improvement in managing long-duration trajectories.

A.3.4. Test Case 4(LQR): Emphasis on Position Control with Moderate Control Effort

Test Case 4 examines the performance of the LQR controller with a focus on position control while applying moderate control effort. The weight matrices used in this configuration are:

$$Q = \begin{bmatrix} 10 & 0 & 0 & 0 & 0 & 0 \\ 0 & 10 & 0 & 0 & 0 & 0 \\ 0 & 0 & 10 & 0 & 0 & 0 \\ 0 & 0 & 0 & 10000 & 0 & 0 \\ 0 & 0 & 0 & 0 & 10000 & 0 \\ 0 & 0 & 0 & 0 & 0 & 10000 \end{bmatrix}, \quad R = \begin{bmatrix} 100 & 0 & 0 \\ 0 & 100 & 0 \\ 0 & 0 & 100 \end{bmatrix}$$

This configuration seeks a balance between maintaining precise position control and minimizing control effort.

Observations and Results:

1. **X-Axis Position Tracking:** The Monte Carlo simulation results for the X-axis position tracking (Figure A.14) show that the system stabilizes with minimal oscillations, achieving a steady state around the zero position mark. This indicates effective control with high precision over the extended simulation period.

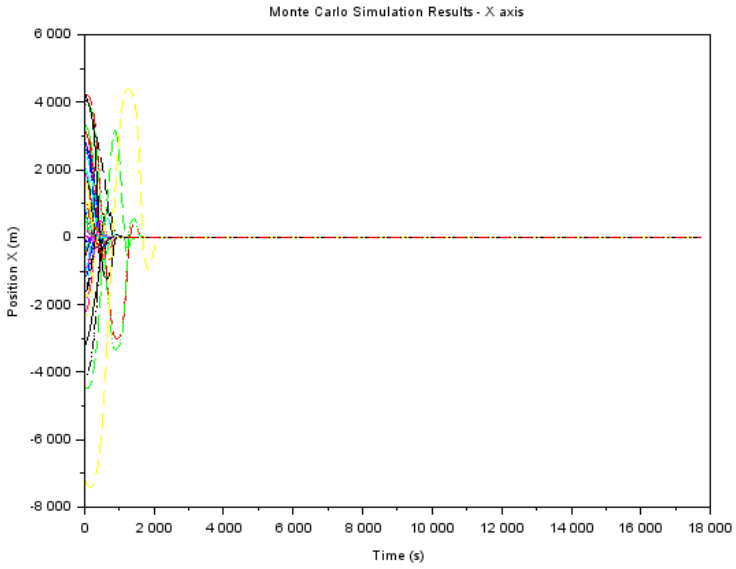

Figure A.14.: Monte Carlo Simulation Results - X axis

2. **Y-Axis Position Tracking:** The Y-axis results (Figure A.15) mirror the X-axis behavior, with the system reaching a stable state with minimal residual oscillations. This confirms the controller's robustness in maintaining position control under varying initial conditions.

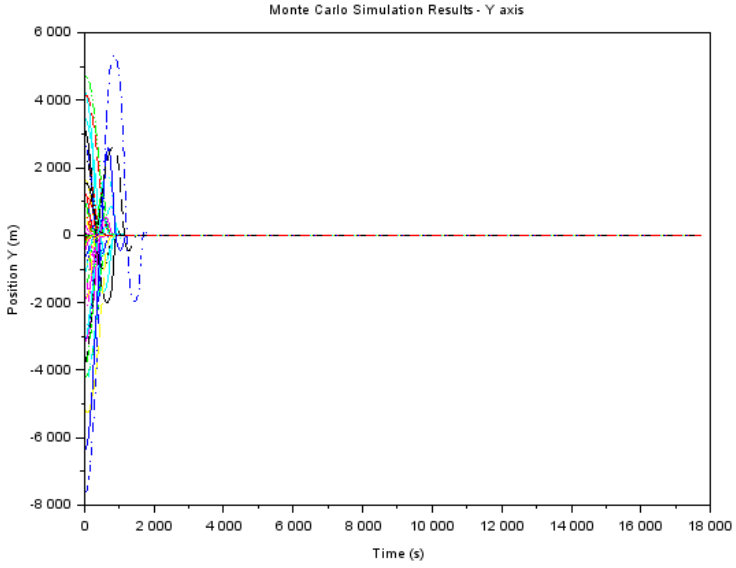

Figure A.15.: Monte Carlo Simulation Results - Y axis

3. **Z-Axis Position Tracking:** Similar to the X and Y axes, the Z-axis position

tracking (Figure A.16) demonstrates the controller's ability to stabilize the system effectively, with convergence to the desired state observed across all simulations.

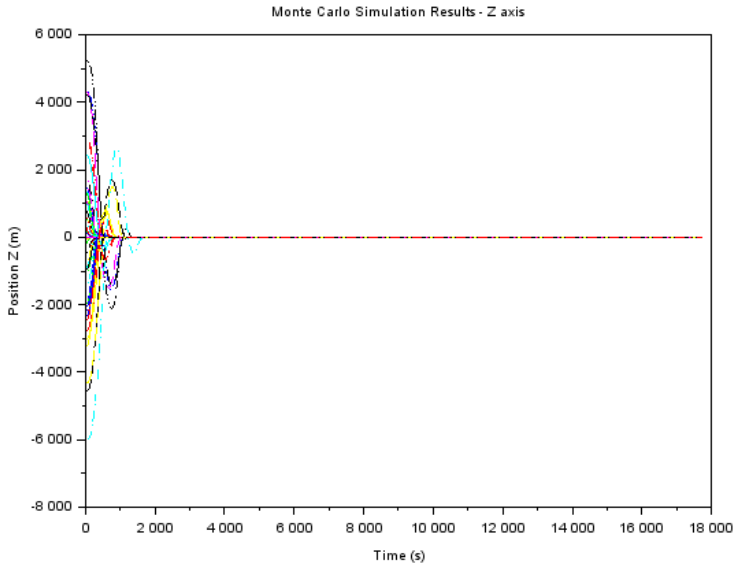

Figure A.16.: Monte Carlo Simulation Results - Z axis

4. **Thruster Activity Analysis:** The distribution of thruster firings across all test scenarios is shown in Figure A.17. The observations are:

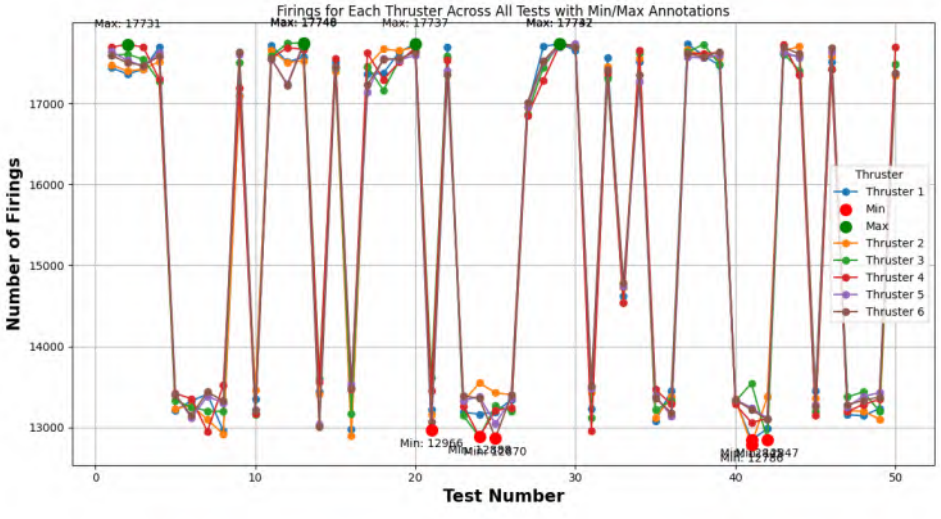

Figure A.17.: Firings for Each Thruster Across All Tests with Min/Max Annotations

- **Firings Distribution:** The plot shows a consistent pattern of thruster activations, with maximum firings reaching up to 17,748 for Thruster 1 and

a minimum of 12,966 for Thruster 6. The thruster activity appears well-distributed, reflecting balanced control efforts.

- **Optimization:** The results indicate an effective utilization of thrusters, ensuring that fuel consumption and mechanical wear are optimized while maintaining precise control over the spacecraft's trajectory.

Test Case 4 demonstrates that the chosen weight configuration in the LQR controller effectively balances position control accuracy and control effort. The Monte Carlo simulations validate the controller's robustness and stability across a range of initial conditions, confirming its suitability for extended space missions with stringent position control requirements. The thruster activity analysis further underscores the efficiency of the control strategy in maintaining optimal performance while minimizing operational costs.